

<https://doi.org/10.15388/vu.thesis.670>

<https://orcid.org/0000-0001-5629-8545>

VILNIUS UNIVERSITY

CENTER FOR PHYSICAL SCIENCES AND TECHNOLOGY

Justinas Jorudas

# Optical and Electrical Investigation of GaN-based HEMT and Graphene Structures for Applications in THz Detection

**DOCTORAL DISSERTATION**

Natural Sciences,  
Physics (N 002)

VILNIUS 2024

The dissertation was prepared between 2019 and 2024 at the Center for Physical Sciences and Technology. The research was supported by Research Council of Lithuania with grant for academic achievements P-DAP-22-199.

**Academic supervisor** – Dr. Irmantas Kašalynas (Center for Physical Sciences and Technology, Natural Sciences, Physics – N 002).

This doctoral dissertation will be defended in a public meeting of the Dissertation Defense Panel:

**Chairman** – Prof. Habil. Dr. Gintautas Tamulaitis (Vilnius University, Natural Sciences, Physics, N 002).

**Members:**

Doc. Dr. Renata Butkutė (Center for Physical Sciences and Technology, Technological Sciences, Materials Engineering, T 008),

Prof. Dr. Harri Lipsanen (Aalto University, Espoo, Finland, Natural Sciences, Physics, N 002).

Dr. Šarūnas Meškinis (Kaunas University of Technology, Technological Sciences, Materials Engineering, T 008),

Prof. Dr. Roland Tamošiūnas (Vilnius University, Natural Sciences, Physics, N 002).

The dissertation shall be defended at a public meeting of the Dissertation Defense Panel at 3PM on 24<sup>th</sup> of September 2024 in auditorium A101 of the Center for Physical Sciences and Technology.

Address: Saulėtekio ave. 3, A101, Vilnius, Lithuania

Tel. +370 5 264 8884; e-mail: office@ftmc.lt

The text of this dissertation can be accessed at the libraries of Center for Physical Sciences and Technology and Vilnius University, as well as on the website of Vilnius University:

<https://www.vu.lt/naujienos/ivykiu-kalendorius>

<https://doi.org/10.15388/vu.thesis.670>

<https://orcid.org/0000-0001-5629-8545>

VILNIAUS UNIVERSITETAS  
FIZINIŲ IR TECHNOLOGIJOS MOKSLŲ CENTRAS

Justinas Jorudas

# GaN-pagrindu HEMT ir grafeno struktūrų, skirtų THz detektavimui, optinių ir elektrinių savybių tyrimas

**DAKTARO DISERTACIJA**

Gamtos mokslai,  
Fizika (N 002)

VILNIUS 2024

Disertacija rengta 2019–2024 metais Fizinių ir technologijos mokslų centre. Mokslinius tyrimus rėmė Lietuvos mokslo taryba – skyrė paramą už akademinį pasiekimą P-DAP-22-199.

**Mokslinis vadovas** – dr. Irmantas Kašalynas (Fizinių ir technologijų mokslų centras, gamtos mokslai, fizika, N 002).

Gynimo taryba:

**Pirmininkas** – prof. habil. dr. Gintautas Tamulaitis (Vilniaus universitetas, gamtos mokslai, fizika, N 002).

**Nariai:**

doc. dr. Renata Butkutė (Fizinių ir technologijos mokslų centras, technologijos mokslai, medžiagų inžinerija, T 008),

prof. dr. Harri Lipsanen (Aalto universitetas, Espoo, Suomija, gamtos mokslai, fizika, N 002).

dr. Šarūnas Meškiniš (Kauno technologijos universitetas, technologijos mokslai, medžiagų inžinerija, T 008),

prof. dr. Roland Tomašiūnas (Vilniaus universitetas, gamtos mokslai, fizika, N 002).

Disertacija ginama viešame Gynimo tarybos posėdyje 2024 m. rugsėjo mėn. 24 d. 15 val. Fizinių ir technologijos mokslų centro A101 auditorijoje. Adresas: Saulėtekio al. 3, A101, Vilnius, Lietuva. tel. +370 5 264 8884; el. paštas office@ftmc.lt.

Disertaciją galima peržiūrėti Fizinių ir technologijos mokslų centro bei VU bibliotekose ir VU interneto svetainėje adresu:

<https://www.vu.lt/naujienos/ivykiu-kalendorius>

## ACKNOWLEDGEMENTS

This thesis wouldn't have been possible without the support and guidance of many. I'm thankful to my academic supervisor, Irmantas Kašalynas, whose expertise and advice were crucial throughout this journey. With his support and encouragement, I have been able to widen my skillset during many conferences, work trips, and traineeships in Lithuania and abroad.

A big shoutout to my lab mates past and present from THz Atelier (Terahertz Photonics Laboratory), whom there are too many to individually to address. The collaborative spirit of our lab not only propelled our research forward but also created a wonderful collaborative environment and made the lab a great place to learn and grow.

The opportunity to collaborate with researchers has been one of the highlights of my PhD journey. I extend my heartfelt thanks to FTMC colleagues: Andrius Bičiūnas (Photonic Technologies and Devices Laboratory, Optoelectronics department), Andrzej Urbanowicz (Photonic Technologies and Devices Laboratory, Optoelectronics department), Vitalij Kovalevskij (Experimental Nuclear Physics Laboratory, Department of Nuclear Research), Simonas Indrišiūnas (Laser Microfabrication Laboratory, Department of Laser Technologies), Artūr Šimukovič and Emilis Šermukšnis (Fluctuation Research Laboratory, Department of Fundamental Research), Ilja Ignatjev and Gediminas Niaura (Laboratory of Spectroelectrochemistry, Department of Organic Chemistry) and others.

Also, thanks to my international collaborators from Institute of High Pressure Physics PAS (Warsaw, Poland) at Laboratory of Semiconductor Characterization (Paweł Prysawko, Jacek Kacperski, many others) and CENTERA (Sergey L. Rumyantsev, Maciej Sakowicz, Dmytro B. But, Pavlo Sai, Maksym Dub and others) (Warsaw, Poland). Also, colleagues from Department of Physics and Mathematics from University of Eastern Finland (group of Polina Kuzhir) (Joensuu, Finland). These collaborations not only enriched my thesis but also provided me with a global perspective on scientific inquiry.

To everyone who contributed to this thesis directly or indirectly, in ways big or small, thank you. This work reflects not just my efforts but the support and encouragement I received from each one of you.

## CONTENTS

ACKNOWLEDGEMENTS .....	5
ABBREVIATIONS.....	9
INTRODUCTION.....	10
MAJOR GOAL .....	15
TASKS OF THIS WORK .....	15
SCIENTIFIC NOVELTY .....	15
STATEMENTS FOR DEFENSE .....	17
AUTHOR CONTRIBUTION .....	17
PARTICIPATION IN PROJECTS.....	18
SECONDMENTS .....	18
LIST OF PUBLICATIONS.....	19
ON DISSERTATION TOPIC .....	19
NOT INCLUDED IN DISSERTATION.....	20
Conference list.....	22
PRESENTED BY THE AUTHOR.....	22
PRESENTED BY CO-AUTHORS .....	25
1. SAMPLES AND METHODS .....	29
1.1. SAMPLES .....	29
1.1.1. GaN-based heterostructures.....	29
1.1.2. Graphene .....	34
1.1.3. Pyrolytic carbon films .....	36
1.1.4. Electric contacts .....	37
1.2. METHODS AND MODELS.....	38
1.2.1. THz time domain spectroscopy (THz-TDS) method .....	38
1.2.2. Fourier transform infrared (FTIR) spectroscopy method .	39
1.2.3. Drude conductivity modelling and THz transmission spectroscopy of thin conductive layers.....	39
1.2.4. Van der Pauw method and Hall experiment.....	40

1.2.5.	Band-diagram calculation model (Nextnano++ and Snider)	42
1.2.6.	Transfer length method (TLM)	43
1.2.7.	Low frequency noise and McWhorter model for estimation of charge trap-density	45
2.	RESULTS	46
2.1.	DEVELOPMENT OF THE GaN-BASED HETEROSTRUCTURES	46
2.1.1.	Thin AlGa <sub>N</sub> /Ga <sub>N</sub> HEMT structure	46
2.1.2.	Lattice matched InAlGa <sub>N</sub> barrier HEMT structures	48
2.1.3.	Trap density in typical AlGa <sub>N</sub> /Ga <sub>N</sub> HEMT structures	52
SUMMARY		56
2.2.	PERFORMANCE OF AlGa <sub>N</sub> /Ga <sub>N</sub> HEMT STRUCTURES UNDER HIGH ELECTRIC FIELD AND CURRENT DENSITY	57
2.2.1.	Self-heating of electric contact resistance and 2DEG layer resistance	57
2.2.2.	Bow-tie diode THz sensor	61
2.2.3.	Bow-tie bolometric THz sensor	63
SUMMARY		68
2.3.	GRAPHENE	69
SUMMARY		75
2.4.	PYROLYTIC CARBON THIN-FILMS	76
SUMMARY		82
	MAIN RESULTS AND CONCLUSIONS	83
	SANTRAUKA	85
	SANTRUMPOS	85
	ĮVADAS	86
	DARBO TIKSLAS	89
	DARBO UŽDAVINIAI	89
	DARBO NAUJUMAS	90

GINAMIEJI TEIGINIAI .....	91
AUTORIAUS INDĒLIS .....	92
DALYVAVIMAS PROJEKTUOSE.....	92
STAŽUOTĒS.....	93
REZULTATŲ APŽVALGA.....	93
1. GaN pagrindu sukurtų HEMT struktūrų vystymas .....	93
2. AlGaIn/GaN HEMT struktūros dideliuose elektriniuose laukuose ir srovės tankiuose .....	95
3. Grafenas .....	97
4. Ploni pirolitinės anglies sluoksniai.....	99
IŠVADOS .....	101
REFERENCES .....	103
CURRICULUM VITAE .....	120
REPRINTED PUBLICATIONS .....	122



## ABBREVIATIONS

2DEG	Two-dimensional electron gas
BT	Bow-tie
CVD	Chemical vapor deposition
DC	Direct current
FET	Field-effect transistor
GaN	Gallium Nitride
HEMT	High electron mobility transistor
IV	Current-voltage characteristics
MOCVD	Metalorganic chemical vapor deposition
NEP	Noise equivalent power
PPF	Pyrolytic photoresist film
PMMA	Polymethyl methacrylate
PyC	Pyrolytic carbon
RF	Radio frequency
SEM	Scanning electron microscopy
SBD	Schottky barrier diode
Si	Silicon
SiC	Silicon carbide
SIMS	Secondary ion mass spectroscopy
TDS	Time-domain spectroscopy
THz	Terahertz
TLM	Transmission line method
UID	Unintentionally doped

## INTRODUCTION

The landscape of electronic devices has witnessed a transformative change, driven by the pursuit of enhanced performance, efficiency, and miniaturization. Recently, GaN has emerged as a material platform, promising to push the boundaries of electronic device capabilities. GaN is a direct bandgap III-V group compound semiconductor, garnered significant attention over the last decades due to its exceptional material properties, listed and compared to other important semiconductor materials in Table 1. Compared to industry standard Si, GaN exhibits 3.1 times wider bandgap (at 3.4 eV), more than 2 times higher electron saturation velocity and up to 12 times larger critical electric field, making it extremely suited for light-emitting diodes (LEDs) [1]–[3] and RF and power conversion applications [4], such as high voltage blocking and high power switching devices [5], [6]. Due to its properties GaN allows for high efficiency (>99%), fast switching ( $\gg 1$  MHz) devices, that can safely operate at higher temperatures (>400°C). Due to high breakdown field, vertical devices can be significantly thinner than Si counterparts at the same performance class, leading to more energy-efficient and compact devices. Alternative SiC has a similar wide-bandgap (3.3 eV) and superior thermal conductivity, which offers an advantage in lower frequency higher power/voltage blocking applications. Using Baliga high-frequency figure of merit (BHFFoM) that quantifies switching losses in a

Table 1. Properties of Si, 4H-SiC, GaN and graphene semiconductors at the room temperature [15]–[17].

Material	Si	4H-SiC	GaN	CVD graphene
<b>Bandgap <math>E_g</math> (eV)</b>	1.1	3.3	3.4	—
<b>Carrier mobility <math>\mu</math> (<math>\text{cm}^2\text{V}^{-1}\text{s}^{-1}</math>)</b>	1400	900	1250	$2 \times 10^5$
<b>Electron saturation velocity <math>v_s</math> (<math>10^7</math> cm/s)</b>	1.0	2.0	2.2	~6.0
<b>Critical breakdown field <math>E_{cr}</math> (MV/cm)</b>	0.3	2.2	3.3	—
<b>Thermal conductivity <math>\lambda</math> (<math>\text{W cm}^{-1}\text{K}^{-1}</math>)</b>	1.5	1.5	1.3	50 <sup>a</sup>
<b>BHFFoM (normalized to Si)</b>	1	35	108	—

<sup>a</sup> Thermal conductivity in plane of graphene sheet;

material:  $BHFFoM = 1/2 \mu E_{cr} U_G^{1/2} U_{br}^{-3/2}$ , where  $\mu$  is carrier mobility,  $E_{cr}$  is critical breakdown field,  $U_G$  is gate voltage,  $U_{br}$  is breakdown voltage [7]. According to this, value of GaN stands out of the rest for high frequency applications. Furthermore, GaN epilayers and structures grown on Si allow for significantly lower cost per device compared to SiC, due to low cost and large sizes of Si substrates. Recently GaN-on-Si up to 300 mm in diameter became available [8]–[10].

GaN based heterostructures with conductive channel of high density and mobility 2D electron gas (2DEG) are used to overcome bulk GaN mobility limitation of around  $1250 \text{ cm}^2\text{V}^{-1}\text{s}^{-1}$ . For this reason, a thin barrier layer with larger bandgap (AlGa<sub>x</sub>N, AlIn<sub>x</sub>N or AlInGa<sub>x</sub>N) is used on a GaN channel layer along the [0001] crystallographic direction. At the interface of AlGa<sub>x</sub>N and GaN layers, an energy discontinuity appears in the band diagram due to bandgap mismatch. The lattice mismatch between GaN and Al<sub>x</sub>Ga<sub>1-x</sub>N or Al<sub>x</sub>In<sub>1-x</sub>N induces a tensile or compressive strain in the barrier layer to compensate for the in-plane lattice mismatch. The calculated lattice constants for ternary Al<sub>x</sub>Ga<sub>1-x</sub>N and Al<sub>x</sub>In<sub>1-x</sub>N alloys are shown in Figure 1a. In the case of Al<sub>x</sub>Ga<sub>1-x</sub>N barrier, the spontaneous and piezoelectric polarizations add up in the layer and the polarization dipole between the AlGa<sub>x</sub>N surface and the AlGa<sub>x</sub>N/GaN interface is compensated by the formation of 2DEG. The band diagram and electron distribution for typical HEMT structure with 25 nm thick Al<sub>0.25</sub>Ga<sub>0.75</sub>N barrier on GaN is shown in Figure 1b. The electron mobility in 2DEG layer in a typical AlGa<sub>x</sub>N/GaN HEMT structure is high, exhibiting values up to  $2400 \text{ cm}^2\text{V}^{-1}\text{s}^{-1}$  under high carrier density of around

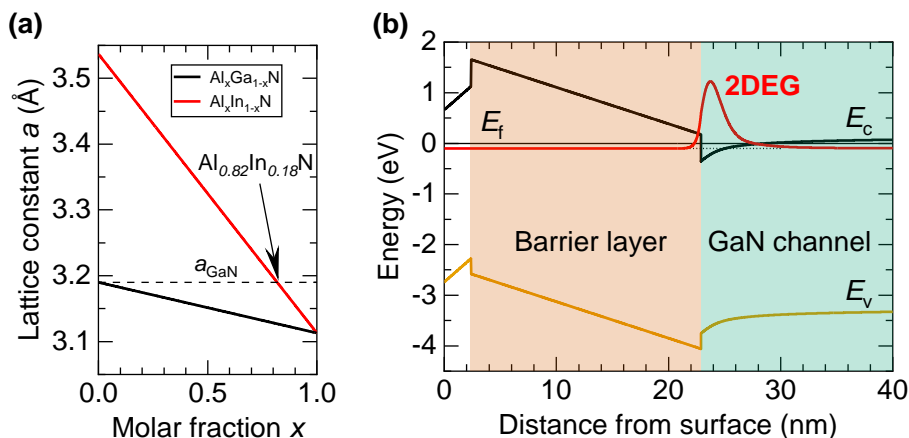


Figure 1. (a), Lattice constants for Al<sub>x</sub>Ga<sub>1-x</sub>N and Al<sub>x</sub>In<sub>1-x</sub>N as function of Al molar fraction  $x$ . (b) Band diagram of Al<sub>0.25</sub>Ga<sub>0.75</sub>N/GaN heterostructure with 2DEG region shown by red color carrier distribution in the heterostructure. Dashed line marks lowest energy level in the formed quantum well.

$1 \times 10^{13} \text{ cm}^{-2}$  [11]. An alternative to  $\text{Al}_{0.25}\text{Ga}_{0.75}\text{N}$  can be  $\text{Al}_x\text{In}_{1-x}\text{N}$  barrier [12], [13], which at composition of  $x \approx 0.82$  is lattice-matched (LM) to GaN channel layer (Figure 1a) providing high mobility values due to reduced electron scattering at the interface. Furthermore, in energy diagram LM AlInN barrier is higher than  $\text{Al}_{0.25}\text{Ga}_{0.75}\text{N}$ , allowing to achieve higher 2DEG density of  $\sim 2.5 \times 10^{13} \text{ cm}^{-2}$  at same layer thickness, or the same carrier density of  $\sim 1 \times 10^{13} \text{ cm}^{-2}$  in a range of barrier thicknesses from 7-12 nm [12], [14].

The maturing AlGaN/GaN material platform over the last decade started to be studied more intensely outside typical GaN applications of solid-state lighting and power electronics. Some of these emerging applications are in photonics [18], [19], non-linear photonics [20], deep ultraviolet LEDs/laser diodes [21]–[23], THz plasmonics [24]–[26],[P12]–[P13],[P15], also THz detectors [27].

Most widespread AlGaN/GaN HEMT based THz detectors are field effect transistor (FET) coupled to THz-antenna, so called TeraFETs [27]–[32], operation of which is based on resistive self-mixing in the transistor channel, realizing regime of damped plasma waves [27]. The record sensitivity TeraFETs leverage relatively advanced GaN MMIC nodes of  $\leq 100 \text{ nm}$  [27], [33]. Recently novel type of AlGaN/GaN HEMT THz detectors were suggested with geometry similar to fin-shaped channel FET (FinFET), but with two lateral Schottky gates directly deposited to edges of transistor channel (called EdgeFETs) [34], [35]. The EdgeFET topology allows for electrical control of the width of 2DEG transistor channel and thus enhances resonant plasmonic detection mechanism. Historically, one of the most successful solid-state THz detectors are Schottky barrier diodes (SBDs), used for mixing and direct rectification of the incoming radiation via strongly nonlinear current-voltage characteristic of the contact, which were also fabricated of AlGaN/GaN heterostructures [36], [37]. Hot-electron microbolometers for THz detection has been realized also of 2DEG in AlGaN/GaN heterostructures [38], [39]. Generally, the push for higher efficiency/higher frequency in electronics and better THz responsivity of sensors are pursued through maturation and improvement of AlGaN/GaN HEMT platform [5]. The research for better performance is also achieved via novel heterostructure approaches such as InAlN/GaN [40]–[42], InAlGaN/GaN [43]–[45]. Indeed, InAlN or InAlGaN barriers allow to achieve comparable 2DEG parameters at smaller barrier thickness, which is important for high frequency HEMTs with short-channels used in RF electronics, 2D plasmonics, and TeraFETs.

Graphene, a two-dimensional carbon allotrope with atoms arranged in a hexagonal lattice and having zero bandgap has captivated the scientific community since its discovery in 2004 [46], [47]. Its remarkable properties,

such as unparalleled thermal conductivity (38 times larger than GaN) and extraordinary electrical conductivity [48], [49] (Table 1), position graphene as a transformative material for a wide range of applications such as RF transistors with  $f_T$  in THz range [50], magnetic or mechanical sensors [51], environmental gas sensors [52] and etc. Compared to GaN, graphene isn't applicable in power electronics due to its band structure with zero bandgap resulting in transistors with low on/off current ratio [53]. On the other hand, the ~97.7% transparency of the graphene in the visible range [54] offers unique opportunities for the development optoelectronic devices, like phototransistors for visible range image sensors [55] and etc. At longer wavelengths, like THz range, monolayer of graphene absorbs significantly more due to absorption of free charge carriers [56], [57]. Most commonly graphene FETs (GFETs) with integrated THz antenna are used as detectors [58]–[62] and their response is comprised of two components: the resistive self-mixing and photothermoelectric effect [63]. In GFET, resistive self-mixing arises from carrier density oscillations and rectification, while photothermoelectric effect is defined by carrier heating in the graphene. The bolometers for THz range have been developed of single layer graphene [64], [65], but the temperature coefficient of its resistance is found to be smaller than that for metal- and semiconductor-based bolometers [66], [67].

Integrating graphene with GaN semiconductors offers the potential to enhance device performance and explore novel applications. One of the more unique graphene-GaN integration cases is to use graphene coated substrate for epitaxial growth, which is called remote epitaxy [68]–[70]. Using this approach grown GaN epilayers or heterostructures can be detached and graphene coated substrate – reused. Usually though, graphene with GaN is integrated for device level applications. Graphene forms a Schottky contact to GaN [71], [72], but unlike all metals used for Schottky contacts – graphene is transparent up to visible spectrum range [57]. There have already been reported UV range graphene-GaN diodes [73], transistors [71], photodiodes [74], [75], and phototransistors [76]. Looking ahead, research is needed to address key challenges in the integration of graphene with GaN semiconductors. Challenges include scalability of fabrication techniques, processing engineering to minimize defects and improve device performance. Additionally, efforts to standardize characterization techniques [77] and develop predictive models for device behavior are essential for the commercialization of graphene devices.

If end-application does not require active electrical control with graphene electrode then other types of thin carbon-based films, such as pyrolytic carbon, can be considered. Two main types of pyrolytic carbon films are used:

pyrolytic carbon (PyC) produced through the pyrolytic decomposition of certain hydrocarbon gases [78], [79], and pyrolyzed photoresist films (PPFs) produced via pyrolyzation of resist films [80]–[82]. In both cases a film of disordered graphene-like nanocrystallites is formed [83], possessing high conductivity and chemical robustness. These properties make them an excellent alternative for graphene in various applications, one of which could be absorber layers in bolometric detection of radiation in the mid-infrared (MIR) or THz ranges [84]–[86].

To summarize, the integration of GaN and graphene presents a promising avenue for overcoming the limitations of current semiconductor technologies. The synergy between GaN high-power, high-frequency capabilities and exceptional properties of the graphene lead to the development of novel devices offering unique performance. This work is devoted to investigation of IR/THz-range optical and electrical properties of two different materials - GaN heterostructures and graphene structures for a possible integration in THz detection applications.

The main results presented in the thesis are discussed in 4 sub-chapters. First sub-chapter 2.1 is devoted to development of GaN-based HEMT structures and includes 3 parts. First part 2.1.1 is devoted to study of thin AlGaIn/GaN HEMT structure achieved through novel growth methods that improve thermal dissipation properties of the devices. Second part 2.1.2 is devoted to development and study of thin GaN-based HEMT structure with lattice matched InAlGaIn barrier of about 10 nm thickness only. Last part 2.1.3 is devoted to study of electrically active traps in a typical AlGaIn/GaN HEMT structure and in the thin AlGaIn/GaN HEMT structure.

Second sub-chapter 2.2 covers performance of AlGaIn/GaN HEMT structures under high electric fields and current densities. It includes part 2.2.1 which is devoted to investigation of charge carrier heating in 2DEG and Ohmic contact layers at high current densities and electric fields. Novel AlGaIn/GaN based THz detectors are developed investigating electron heating in the Ohmic contact to 2DEG layer and shaped 2DEG layer presented in parts 2.2.2 and 2.2.3, respectively.

Third sub-chapter 2.3 is devoted to the development of graphene processing to utilize low doping and high mobility charge carriers in wet-transferred CVD graphene on the substrate of Si and AlGaIn/GaN HEMT structure, both of which are important for integrated semiconductor applications.

Last sub-chapter 2.4 is devoted to investigation of thin pyrolytic carbon films as a possible alternative for graphene in the THz range.

## MAJOR GOAL

To study novel GaN-based semiconductors and integrated devices in tandem with graphene and pyrolytic carbon films, which are suitable for THz detection applications.

## TASKS OF THIS WORK

1. Development and research of thin GaN-based heterostructures with aim to provide high electron mobility and density in the 2DEG channel used for the development of HEMTs and sensitive THz detectors.
2. Identify electron heating effects in contact layer and in 2DEG channel of GaN-based HEMT structures, useful for the development of new THz detectors.
3. Development of graphene processing technologies to utilize high charge mobility in the graphene related materials for GaN-based THz detectors.

## SCIENTIFIC NOVELTY

1. Thin AlGaIn/GaN HEMT structure without thick GaN buffer layer was developed possessing thermally stable 2DEG layer with electron density and mobility values of  $1.0 \times 10^{13} \text{ cm}^{-2}$  and  $1.7 \times 10^3 \text{ cm}^2 \text{ V}^{-1} \text{ s}^{-1}$  at 300 K, respectively. Moreover, developed test SBDs demonstrated the breakdown field values up to 0.8 MV/cm. while output DC characteristics of HEMTs exhibited negligible reduction in drain current at high input power of  $\geq 2.5 \text{ W/mm}$ , due to improved thermal design of the heterostructure. RF performance of HEMTs was characterized by  $f_T = 1.33 \text{ GHz}$  and  $f_{\text{max}} = 6.7 \text{ GHz}$ , which results in the figure of merit  $f_T \times L_G$  of  $6.7 \text{ GHz} \times \mu\text{m}$ .
2. Quaternary InAlGaIn lattice-matched thin barrier layer of 9 nm thickness only was developed for GaN-based HEMT structure, allowing to reach comparable 2DEG density and mobility parameters of  $1.2 \times 10^{13} \text{ cm}^{-2}$  and  $1.6 \times 10^3 \text{ cm}^2 \text{ V}^{-1} \text{ s}^{-1}$  at 300 K to standard AlGaIn/GaN HEMT heterostructures but with barrier thickness of 20 nm or more.
3. Effective trap density of as low as  $10^{19} \text{ eV}^{-1} \text{ cm}^{-3}$  was extracted using McWhorter model from low frequency noise measurements of the AlGaIn/GaN HEMTs. This data was found to correlate to secondary ion mass spectroscopy results of uncompensated donor density and THz

electroluminescence spectroscopy measurements, proving that low-frequency noise is a sensitive method to estimate material quality in case of AlGaIn/GaN heterostructures.

4. Self-heating of Ohmic contact resistance and 2DEG channel resistance under high pulsed-current density was observed for AlGaIn/GaN and AlGaIn/AlN/GaN HEMT structures. Increase of contact resistance was up to 6 times for all studied samples, effect of which was larger than self-heating of channel resistance for currents above 0.6 A/mm.
5. Bow-tie diode and bow-tie bolometers based on asymmetrically shaped AlGaIn/GaN HEMT structures with Ohmic contacts were investigated as THz detectors at selected temperatures of 300 K and 80 K. Responsivities of up to 4 V/W with resulting noise equivalent power (NEP) of  $4 \text{ nW}/\sqrt{\text{Hz}}$  was obtained for BT diodes at the fundamental mode of THz antenna with frequency of 150 GHz. The responsivity scaled nonlinearly with the resistance of the BT diode, demonstrating that the tapering of the apex below the range of a few micrometers is ineffective in applications which require low NEP values.
6. A method for PMMA removal from CVD graphene surface has been developed, which involves photodegradation of PMMA under UV-C exposure (254 nm wavelength) and its removal in solvent mixture of isopropyl alcohol and water. High quality of the graphene after the removal of PMMA was confirmed with SEM, AFM, and Raman spectroscopy. Charge carrier performance was found from THz-TDS of the released graphene, revealing the low-field mobility values to be up to  $6900 \text{ cm}^2\text{V}^{-1}\text{s}^{-1}$ .
7. A method for patterning PMMA protected graphene using UV photolithography was developed. Using photoresist and the protective PMMA layer allows to avoid direct contact of graphene with the photoresist or its residues, avoiding also a chemical doping of the graphene.
8. PPF made by pyrolyzing AZ nLOF 2070 resist exhibited frequency independent conductivity of up to  $1.3 \times 10^4 \text{ S/m}$  in the frequency range from DC up to 1.5 THz.
9. Development of tens of nanometers thin conductive graphitic film on the suspended dielectric  $\text{Si}_3\text{N}_4$  membrane: a 20 nm thick graphitic film on  $\text{Si}_3\text{N}_4$  demonstrated the absorption values of 40% in the THz range and of from 10 till 40% in the NIR band, covering in total the ultrabroadband spectrum range of 0.5-200 THz.



## STATEMENTS FOR DEFENSE

1. Thin-film AlGaIn/GaN and lattice matched InAlGaIn/GaN HEMT structures are suitable to achieve high density (around  $10^{13} \text{ cm}^{-2}$ ) of 2D electrons with the mobility values above  $1700 \text{ cm}^2\text{V}^{-1}\text{s}^{-1}$  at room temperature.
2. Electron heating in Ohmic contact layer and in 2DEG channel can be identified in AlGaIn/GaN HEMT structures and implemented for the development of bow-tie diodes and bow-tie bolometric THz sensors, respectively.
3. Graphene with high mobility carriers ( $> 2900 \text{ cm}^2\text{V}^{-1}\text{s}^{-1}$ ) and small doping ( $\leq 3 \times 10^{12} \text{ cm}^{-2}$ ), suitable for integration with GaN structures, is achievable using two step polymethyl methacrylate cleaning and patterning process via UV-C photo exposure and removal in mixture of isopropanol:water (3:1).
4. Thin pyrolytic carbon on  $\text{Si}_3\text{N}_4$  films (20-160 nm) with sheet resistance of  $500 \text{ } \Omega/\text{sq}$ . can be realized in the THz range (frequencies  $\leq 10 \text{ THz}$ ) and used as an alternative to CVD graphene for THz application

## AUTHOR CONTRIBUTION

Most of the sample fabrication and experimental investigations were done in the Center for Physical Sciences and Technology (FTMC) (Vilnius, Lithuania). Part of the GaN semiconductor samples in articles [P1-P5, P10-P11] were processed in Institute of High Pressure Physics PAS (UNIPRESS, Warsaw, Poland, under supervision of Dr. Pawel Prystawko). The author designed UV photolithography masks and performed processing of GaN-based heterostructures to fabricate devices and test structures [P1-P5, P12-P13, P15-P16]. The author was involved partially in designing UV photolithography mask for *n*-GaN samples in articles [P10-P11] for Dr. Roman M. Balagula. The author performed DC electrical characterization of the van der Pauw and TLM/CTLM test structures, SBDs and HEMTs fully [P1-P5, P12-P13, P15-P16] and partially in articles [P10-P11, P14]. The author in cooperation with co-authors performed DC electrical and THz responsivity characterization plus data analysis of AlGaIn/GaN BT diodes in article [P5].

The author performed all sample fabrication (CVD graphene and PMMA samples), water contact angle measurements, detailed Raman spectroscopy data analysis and electrical van der Pauw characterization in article [P6] and

in patent application [P7]. Pyrolytic carbon samples in articles [P8-P9] were fabricated and electrically characterized by the author in University of Eastern Finland (Joensuu, Finland, under supervision of Prof. Polina Kuzhir and Dr. Georgy Fedorov), together with THz spectroscopy of PPFs in article [P8].

## PARTICIPATION IN PROJECTS

The author was also involved in the research projects:

1. Research Council of Lithuania (Lietuvos mokslo taryba) under the “TERAGANWIRE” project (grant No. S-LL-19-1), by the National Science Centre of Poland (grant no. 2017/27/L/ST7/03283)
2. Research Council of Lithuania (Lietuvos mokslo taryba) „Kompaktiški terahercinės spinduliuotės plazmoniniai emiteriai (KOTERA-PLAZA)” project (Nr. 01.2.2-LMT-K-718-01-0047)
3. Academy of Finland, Flagship Programme PREIN (Decision 320166)
4. Subproject of EU ATTRACT Phase 2 Research Infrastructure H2020 Project (grant no. 101004462) “Micromechanical Bolometers arrays for THz hyperspectral imaging (h-cube)”
5. Research Council of Lithuania (Lietuvos mokslo taryba) „T-HP” (T-HP)” project (Nr. 01.2.2-LMT-K-718-01-0096).

## SECONDMENTS

The author had secondments during a PhD period:

1. 2020 January 13-26<sup>th</sup> AlGa<sub>N</sub>/Ga<sub>N</sub> and InAlGa<sub>N</sub>/Ga<sub>N</sub> HEMT structure processing at High Pressure Physics Institute (UNIPRESS), Warsaw, Poland.
2. 2020 August July 31<sup>st</sup> – August 7<sup>th</sup> AlGa<sub>N</sub>/Ga<sub>N</sub> HEMT low-frequency noise measurements and bow-tie diode THz detector characterization at CENTERA of High Pressure Physics Institute (UNIPRESS), Warsaw, Poland.
3. 2022 August 1<sup>st</sup> – December 31<sup>st</sup> deposition and studies of pyrolytic carbon (PPF and PyC) in DC and THz frequency ranges. Learning to use Raith electron beam lithography equipment for AlGa<sub>N</sub>/Ga<sub>N</sub> plasmonic structure fabrication at University of Eastern Finland (UEF), Joensuu, Finland.
4. 2023 July 17<sup>th</sup> – August 18<sup>th</sup> processing of THz plasmonic structures on AlGa<sub>N</sub>/Ga<sub>N</sub> HEMT structures using electron beam lithography at University of Eastern Finland (UEF), Joensuu, Finland.

## LIST OF PUBLICATIONS

In this chapter, the author listed all articles published since the start of PhD studies in October 2019.

### ON DISSERTATION TOPIC

[P1] **Jorudas, J.**; Šimukovič, A.; Dub, M.; Sakowicz, M.; Prystawko, P.; Indrišiūnas, S.; Kovalevskij, V.; Romyantsev, S.; Knap, W.; Kašalynas, I. AlGaN/GaN on SiC Devices without a GaN Buffer Layer: Electrical and Noise Characteristics. *Micromachines* **2020**, *11*, 1131, doi:10.3390/mi11121131.

[P2] **Jorudas, J.**; Prystawko, P.; Šimukovič, A.; Aleksiejūnas, R.; Mickevičius, J.; Kryško, M.; Michałowski, P.P.; Kašalynas, I. Development of Quaternary InAlGaN Barrier Layer for High Electron Mobility Transistor Structures. *Materials (Basel)*. **2022**, *15*, 1118, doi:10.3390/ma15031118.

[P3] Sai, P.; **Jorudas, J.**; Dub, M.; Sakowicz, M.; Jakštas, V.; But, D.B.; Prystawko, P.; Cywinski, G.; Kašalynas, I.; Knap, W.; et al. Low Frequency Noise and Trap Density in GaN/AlGaN Field Effect Transistors. *Appl. Phys. Lett.* **2019**, *115*, 183501, doi:10.1063/1.5119227.

[P4] Šermukšnis, E.; **Jorudas, J.**; Šimukovič, A.; Kovalevskij, V.; Kašalynas, I. Self-Heating of Annealed Ti/Al/Ni/Au Contacts to Two-Dimensional Electron Gas in AlGaN/GaN Heterostructures. *Appl. Sci.* **2022**, *12*, 11079, doi:10.3390/app122111079.

[P5] **Jorudas, J.**; Seliuta, D.; Minkevičius, L.; Janonis, V.; Subačius, L.; Pashnev, D.; Pralgauskaitė, S.; Matukas, J.; Ikamas, K.; LISAUSKAS, A.; et al. Terahertz Bow-Tie Diode Based on Asymmetrically Shaped AlGaN/GaN Heterostructures. *Lith. J. Phys.* **2023**, *63*, doi:10.3952/physics.2023.63.4.1.

[P6] **Jorudas, J.**; Pashnev, D.; Kašalynas, I.; Ignatjev, I.; Niaura, G.; Selskis, A.; Astachov, V.; Alexeeva, N. Green Removal of DUV-Polarity-Modified PMMA for Wet Transfer of CVD Graphene. *Nanomaterials* **2022**, *12*, 4017, doi:10.3390/nano12224017.

[P7] Alexeeva, N.; **Jorudas, J.**; Kašalynas, I. Method for patterning graphene layers through photolithography for a scalable fabrication of graphene devices, EP23205083 (European Patent Office application), 2023-10-23.

[P8] **Jorudas, J.**; Rehman, H.; Fedorov, G.; Cojocari, M.; Karvinen, P.; Urbanowicz, A.; Kašalynas, I.; Matzui, L.Y.; Svirko, Y.; Kuzhir, P. Pyrolyzed Photoresist Thin Film: Effect of Electron Beam Patterning on DC and THz Conductivity. *Lith. J. Phys.* **2023**, *63*, doi:10.3952/physics.2023.63.3.6.

[P9] **Jorudas, J.**; Rehman, H.; Cojocari, M.; Pashnev, D.; Urbanovic, A.; Kašalynas, I.; Bertoni, B.; Vicarelli, L.; Pitanti, A.; Malykhin, S.; Svirko, Y.; Kuzhir, P.; Fedorov, G. Ultra-Broadband Absorbance of Nanometer-Thin Pyrolyzed-Carbon Film on Silicon Nitride Membrane. *Nanotechnology* **2024**. doi:10.1088/1361-6528/ad4157.

#### NOT INCLUDED IN DISSERTATION

[P10] Balagula, R.M.; Subačius, L.; **Jorudas, J.**; Janonis, V.; Prystawko, P.; Grabowski, M.; Kašalynas, I. High-Frequency and High-Power Performance of *n*-Type GaN Epilayers with Low Electron Density Grown on Native Substrate. *Materials (Basel)*. **2022**, *15*, 2066, doi:10.3390/ma15062066.

[P11] Balagula, R.M.; Subačius, L.; **Jorudas, J.**; Prystawko, P.; Grabowski, M.; Leszczyński, M.; Kašalynas, I. Space-Charge Domains in *n*-Type GaN Epilayers under Pulsed Electric Field. *Appl. Phys. Lett.* **2022**, *121*, doi:10.1063/5.0098951.

[P12] Pashnev, D.; Kaplas, T.; Korotyeyev, V.; Janonis, V.; Urbanowicz, A.; **Jorudas, J.**; Kašalynas, I. Terahertz Time-Domain Spectroscopy of Two-Dimensional Plasmons in AlGa<sub>N</sub>/Ga<sub>N</sub> Heterostructures. *Appl. Phys. Lett.* **2020**, *117*, 051105, doi:10.1063/5.0014977.

[P13] Pashnev, D.; Korotyeyev, V. V.; **Jorudas, J.**; Kaplas, T.; Janonis, V.; Urbanowicz, A.; Kašalynas, I. Experimental Evidence of Temperature Dependent Effective Mass in AlGa<sub>N</sub>/Ga<sub>N</sub> Heterostructures Observed via THz Spectroscopy of 2D Plasmons. *Appl. Phys. Lett.* **2020**, *117*, 162101,

doi:10.1063/5.0022600.

[P14] Adamov, R.B.; Pashnev, D.; Shalygin, V.A.; Moldavskaya, M.D.; Vinnichenko, M.Y.; Janonis, V.; **Jorudas, J.**; Tumėnas, S.; Prystawko, P.; Krysko, M.; et al. Optical Performance of Two Dimensional Electron Gas and GaN:C Buffer Layers in AlGaN/AlN/GaN Heterostructures on SiC Substrate. *Appl. Sci.* **2021**, *11*, 6053, doi:10.3390/app11136053.

[P15] Pashnev, D.; Korotyeyev, V. V.; **Jorudas, J.**; Urbanowicz, A.; Prystawko, P.; Janonis, V.; Kasalynas, I. Investigation of Electron Effective Mass in AlGaN/GaN Heterostructures by THz Spectroscopy of Drude Conductivity. *IEEE Trans. Electron Devices* **2022**, *69*, 3636–3640, doi:10.1109/TED.2022.3177388.

[P16] Indrišiūnas, S.; Svirplys, E.; **Jorudas, J.**; Kašalynas, I. Laser Processing of Transparent Wafers with a AlGaN/GaN Heterostructures and High-Electron Mobility Devices on a Backside. *Micromachines* **2021**, *12*, 407. doi: 10.3390/mi12040407

## CONFERENCE LIST

PRESENTED BY THE AUTHOR

[K1] **Jorudas, J.**; Malakauskaitė, J.; Subačius, L.; Janonis, V.; Jakštas, V.; Kovelevskij, V.; Kašalynas, I. Planarinių AlGa<sub>N</sub>/Ga<sub>N</sub> peteliškės tipo diodų kūrimas sub-THz detekcijai. In abstract book of the 43<sup>ioji</sup> Lietuvos Nacionalinė Fizikos Konferencija, 2019; pp. 94. ISBN 978-609-02-1638-5. <https://www.ebooks.ktu.lt/eb/1497/43-ioji-lietuvos-nacionaline-fizikos-konferencija-programa-ir-pranesimu-tezes/>. Oral presentation.

[K2] **Jorudas, J.**; Šimukovič, A.; Kašalynas. The performance of AlGa<sub>N</sub>/Ga<sub>N</sub> HEMTs without Ga<sub>N</sub> buffer layer. In abstract book of 10<sup>oji</sup> doktorantų ir jaunųjų mokslininkų konferencija „FizTech 2020“, 2020; [https://www.ftmc.lt/uploads/pdf/Dokumentai/doktorantura/tezes/FizTech2020\\_tezes.pdf](https://www.ftmc.lt/uploads/pdf/Dokumentai/doktorantura/tezes/FizTech2020_tezes.pdf). Oral presentation.

[K3] **Jorudas, J.**; Šimukovič, A.; Kašalynas, I. Electrical characteristics of “buffer-free” AlGa<sub>N</sub>/Ga<sub>N</sub> heterostructures. In abstract book of the 64<sup>th</sup> International conference for students of physics and natural sciences Open Readings 2021; pp. 46. ISBN 978-609-07-0590-2. URL: [http://www.openreadings.eu/wp-content/uploads/2021/03/Abstract\\_book\\_2021S.pdf](http://www.openreadings.eu/wp-content/uploads/2021/03/Abstract_book_2021S.pdf). Oral presentation.

[K4] **Jorudas, J.**; Prystawko, P.; Dub, M.; Skapas, M.; Selskis, A.; Sai, P.; Sakowicz, M.; Rumyantsev, S.; Knap, W.; Kašalynas, I. Structural and morphological analysis of the “buffer-free” AlGa<sub>N</sub>/Ga<sub>N</sub> heterostructures on SiC substrate. In 2021 Spring meeting of European Materials Research Society (E-MRS), Section M ALTECH 2021. URL: <https://www.european-mrs.com/altech-2021-analytical-techniques-precise-characterization-nano-materials-emrs>. Poster presentation.

[K5] **Jorudas, J.**; Prystawko, P.; Dub, M.; Skapas, M.; Selskis, A.; Sai, P.; Sakowicz, M.; Rumyantsev, S.; Knap, W.; Kašalynas, I. Structural and electrical investigation of the “Buffer-Free” AlGa<sub>N</sub>/Ga<sub>N</sub> heterostructures on SiC substrate. In abstract book of the 23<sup>rd</sup> International Conference-School Advanced Materials and Technologies, 2021 pp. 112 DOI: 10.5755/e01.2669-1930.2021 URL: <https://www.ebooks.ktu.lt/einfo/1561/advanced-materials->

[and-technologies-book-of-abstracts-of-23rd-international-conference-school/](#). Poster presentation.

[K6] **Jorudas, J.**; Prystawko, P.; Dub, M.; Skapas, M.; Selskis, A.; Sai, P.; Sakowicz, M.; Rumyantsev, S.; Knap, W.; Kašalynas, I. Structural and electrical investigation of the “Buffer-Free” AlGaN/GaN heterostructures on SiC substrate. In abstract book of the 49<sup>th</sup> “Jaszowiec” 2021 International School & Conference on the Physics of Semiconductors, pp. 205 URL: <https://www.jaszowiec.edu.pl/files/Jaszowiec2021-book.pdf>. <https://d.docs.live.net/7951bc93a89c8828/Laboratorija/DOKTORANTAURA/Thesis/a> Poster presentation.

[K7] **Jorudas, J.**; Pashnev, D.; Alexeeva, N.; Ignatjev, I.; Urbanowicz, A.; Kašalynas, I. Characterization of Graphene Drude Conductivity by Terahertz and Infrared Spectroscopy Methods. In Proceedings of the 2021 46<sup>th</sup> International Conference on Infrared, Millimeter and Terahertz Waves (IRMMW-THz); IEEE, August 29 2021; pp. 1–2. doi: 10.1109/IRMMW-THz50926.2021.9567542; <https://ieeexplore.ieee.org/document/9567542/>. Poster presentation.

[K8] **Jorudas, J.**; Pashnev, D.; Ignatjev, I.; Kašalynas, I. Characterization of graphene electrical properties by combined terahertz and infrared spectroscopy methods. In abstract book of 11<sup>oji</sup> doktorantų ir jaunųjų mokslininkų konferencija „FizTech 2021“, 2021; <https://www.ftmc.lt/uploads/images/pages/doktorantura/FizTeCh2021/TEZIU%20RINKINYS%202021.pdf>. Oral presentation.

[K9] **Jorudas, J.**; Pashnev, D.; Alexeeva, N.; Ignatjev, I.; Urbanowicz, A.; Balagula, R.M.; Kašalynas, I. Characterization of Graphene Using Contactless Terahertz Spectroscopy Methods. In abstract book of the 2021 International conference on carbon chemistry and materials (CCM-2021); pp. 14. [https://carbon.unitedscientificgroup.org/2021/pdfs/CCM\\_2021\\_Book.pdf](https://carbon.unitedscientificgroup.org/2021/pdfs/CCM_2021_Book.pdf). Oral presentation.

[K10] **Jorudas, J.**; Kašalynas, I. Sub-THz responsivity of AlGaN/GaN bow-tie diodes at the temperatures of 295 K and 80 K. In abstract book of the 2022 French-German THz conference; pp. 45; La Grande Motte, France; May 18, 2022. <https://terahertz2022.sciencesconf.org/>. Poster presentation.

[K11] **Jorudas, J.**; Kašalynas, I. Terahertz Responsivity of AlGa<sub>N</sub>/Ga<sub>N</sub> Bow-Tie Diode Detectors at the Temperatures of 295 K and 80 K. In Proceedings of the 2022 47<sup>th</sup> International Conference on Infrared, Millimeter and Terahertz Waves (IRMMW-THz); IEEE, August 28 2022; pp. 1–2. doi: 10.1109/IRMMW-THz50927.2022.9895472;

<https://ieeexplore.ieee.org/document/9895472/>. Poster presentation.

[K12] **Jorudas, J.**; Šimukovič, A.; Prystawko, P.; Kašalynas, I. Comparison of InAlGa<sub>N</sub> and AlGa<sub>N</sub> HEMT Structures. In abstract book of the Advanced Properties and Processes in Optoelectronic Materials and Systems (APROPOS 18); Vilnius, Lithuania, 2022. pp. 75;

[https://www.ftmc.lt/uploads/APROPOS18/APROPOS18\\_abstract\\_book\\_ISBN\\_978-609-96355-0-7.pdf](https://www.ftmc.lt/uploads/APROPOS18/APROPOS18_abstract_book_ISBN_978-609-96355-0-7.pdf). Poster presentation.

[K13] **Jorudas, J.**; Šimukovič, A.; Prystawko, P.; Kašalynas, I. Comparison of InAlGa<sub>N</sub> and AlGa<sub>N</sub> HEMT Structures for RF Applications. In abstract book of the International Workshop on Nitride Semiconductors; Berlin, Germany, 2022. pp. 498

[https://www.iwn2022.org/fileadmin/congress/media/iwn2022/pdf/TWN22\\_Abstract\\_book.pdf](https://www.iwn2022.org/fileadmin/congress/media/iwn2022/pdf/TWN22_Abstract_book.pdf). Poster presentation.

[K14] **Jorudas, J.**; Kašalynas, I. Sub-THz responsivity of AlGa<sub>N</sub>/Ga<sub>N</sub> bow-tie diodes at the temperatures of 295K and 80K. In abstract book of 12<sup>oji</sup> doktorantų ir jaunųjų mokslininkų konferencija „FizTech 2022“, 2022;

<https://www.ftmc.lt/uploads/news/id1192/FizTeCh%202022%20teziu%20rinkinys.pdf>. Oral presentation.

[K15] **Jorudas, J.**; Rehman, H.; Fedorov, G.; Cojocari, M.; Karvinen, P.; Urbanowicz, A.; Pashnev, D.; Kašalynas, I.; Svirko, Y.; Kuzhir, P. Terahertz and Dc Conductivity of Pyrolyzed Photoresist Films. In Proceedings of the 2023 48<sup>th</sup> International Conference on Infrared, Millimeter, and Terahertz Waves (IRMMW-THz); IEEE, September 17 2023; pp. 1–2. doi: 10.1109/IRMMW-THz57677.2023.10299151;

<https://ieeexplore.ieee.org/document/10299151/>. Poster presentation.

[K16] **Jorudas, J.**; Kašalynas, I. AlGa<sub>N</sub>/Ga<sub>N</sub> peteliškės tipo (BT) jutiklių tyrimas 300 K ir 80 K temperatūrose teraherciniame dažnių ruože. In abstract book of the 45<sup>oji</sup> Lietuvos nacionalinė fizikos konferencija; Vilnius, Lithuania,



2023. <https://ff.vu.lt/external/ff/files/LNFK45/Programa/PROGRAMA-LNFK45-final.pdf>. Oral presentation.

PRESENTED BY CO-AUTHORS

[K17] Janonis, V.; Pashnev, D.; Grigelionis, I.; Korotieiev, V.; Balagula, R.M.; Minkevicius, L.; **Jorudas, J.**; Alexeeva, N.; Subacius, L.; Valušis, G.; et al. Electrically-Pumped THz Emitters Based on Plasma Waves Excitation in III-Nitride Structures. In Proceedings of the Terahertz Emitters, Receivers, and Applications XI; Razeghi, M., Baranov, A.N., Eds.; SPIE, September 2020; Vol. 11499, p. 8. doi:10.1117/12.2569261; <https://www.spiedigitallibrary.org/conference-proceedings-of-spie/11499/2569261/Electrically-pumped-THz-emitters-based-on-plasma-waves-excitation-in/10.1117/12.2569261.short>

[K18] Pashnev, D.; Kaplas, T.; Korotyeyev, V.; Janonis, V.; Grigelionis, I.; Urbanowicz, A.; **Jorudas, J.**; Indrisiunas, S.; Alexeeva, N.; Kasalynas, I. Investigation of two-dimensional plasmons in grating-gated AlGa<sub>N</sub>/Ga<sub>N</sub> heterostructures with terahertz time domain spectrometer. In Proceedings of the 2020 45<sup>th</sup> International Conference on Infrared, Millimeter, and Terahertz Waves (IRMMW-THz); IEEE, 2020; pp. 1–1. doi:10.1109/IRMMW-THz46771.2020.9370916; <https://ieeexplore.ieee.org/document/9370916/>

[K19] Dub, M.; Sai, P.; But, D.B.; **Jorudas, J.**; Kašalynas, I.; Sakowicz, M.; Cywinski, G.; Rumyantsev, S.; Knap, W. Anomalous Sub-THz Detection by GaN/AlGa<sub>N</sub> FinFETs. In Proceedings of the 2020 23<sup>rd</sup> International Microwave and Radar Conference (MIKON); IEEE: Vilnius, October 5 2020; pp. 297–299. doi: 10.23919/MIKON48703.2020.9253898; <https://ieeexplore.ieee.org/document/9253898/>

[K20] Pashnev, D.; Kaplas, T.; Korotyeyev, V.; Janonis, V.; Urbanowicz, A.; **Jorudas, J.**; Kašalynas, I. Temperature dependent electron effective mass in AlGa<sub>N</sub>/GAN heterostructures measured via THz spectroscopy of 2D plasmons. In Abstract book of the 64<sup>th</sup> International conference for students of physics and natural sciences Open Readings 2021; pp. 45. ISBN 978-609-07-0590-2. [http://www.openreadings.eu/wp-content/uploads/2021/03/Abstract\\_book\\_2021S.pdf](http://www.openreadings.eu/wp-content/uploads/2021/03/Abstract_book_2021S.pdf)

[K21] Pashnev, D.; **Jorudas, J.**; Balagula, R.M.; Urbanowicz, A.; Kašalynas, I. Modeling transmission spectra for a thin conductive layer on a semi-insulating substrate. In abstract book of the 49<sup>th</sup> “Jaszowiec” 2021 International School & Conference on the Physics of Semiconductors, pp. 133 <https://www.jaszowiec.edu.pl/files/Jaszowiec2021-book.pdf>

[K22] Pashnev, D.; **Jorudas, J.**; Balagula, R.M.; Urbanowicz, A.; Kašalynas, I. Investigation of THz transmission through semi-insulating substrate with a thin conductive layer. In Proceedings of the 2021 46<sup>th</sup> International Conference on Infrared, Millimeter and Terahertz Waves (IRMMW-THz); IEEE, 2021; pp. 1–2. doi: 10.1109/IRMMW-THz50926.2021.9567456; <https://ieeexplore.ieee.org/document/9567456/>

[K23] Balagula, R.M.; Subačius, L.; **Jorudas, J.**; Prystawko, Kašalynas, I. High-frequency characterization of GaN epilayers on native semi-insulating substrate. In 2021 Fall meeting of European Materials Research Society (EMRS), Symposium P Wide band gap (WBG) materials 2021. <https://www.european-mrs.com/wide-band-gap-wbg-materials-theory-growth-characterization-and-applications-emrs-0>

[K24] **Jorudas, J.**; Janonis, V.; Pashnev, D.; Balagula, R.M.; Grigelionis, I.; Subačius, L.; Indrišiūnas, S.; Kašalynas, I. Semiconductor GaN structures for terahertz and infrared spectrum ranges. In abstract book of the 44<sup>oji</sup> Lietuvos nacionalinė fizikos konferencija; Vilnius, Lithuania, 2021. <http://Infk.ftmc.lt/wp-content/uploads/2021/11/LNFK-44-pranesimu-medziaga-2021-spaliu-6-8-Vilnius.pdf>

[K25] Pashnev, D.; Balagula, R.M.; Dub, M.; Sakowicz, M.; **Jorudas, J.**; Janonis, V.; Subačius, L.; Sai, P.; Cywinski, G.; Kašalynas, I. "Terahertz spectroscopy of two-dimensional plasmons in grating-gated AlGa<sub>N</sub>/Ga<sub>N</sub> heterostructures," in 2022 International Conference on Free Electron Laser Applications in Infrared and THz Studies of New States of Matter, Warsaw, Poland (2022).

[K26] Pashnev, D.; Balagula, R. M.; **Jorudas, J.**; Subačius, L.; Dub, M.; Sakowicz, M.; Sai, P.; Cywinski, G.; Kašalynas, I. "THz emission spectra of 2D plasmons excited in grating-gated AlGa<sub>N</sub>/Ga<sub>N</sub> heterostructures," In abstract book of the 24<sup>th</sup> International Conference-School Advanced Materials and Technologies, 2022 pp. 76 doi: 10.5755/e01.2669-1930.2022;

<https://www.ebooks.ktu.lt/einfo/1600/advanced-materials-and-technologies-book-of-abstracts-of-24th-international-conference-school/>

[K27] Pashnev, D.; Balagula, R.M.; Dub, M.; Sakowicz, M.; **Jorudas, J.**; Subačius, L.; Sai, P.; Cywinski, G.; Kašalynas, I. Optimization of 2D Plasmons Excitation in Grating-Gated AlGa<sub>N</sub>/Ga<sub>N</sub> High Electron Mobility Transistor Structures. In Proceedings of the International Workshop on Nitride Semiconductors; Berlin, Germany, 2022. pp. 116; [https://www.iwn2022.org/fileadmin/congress/media/iwn2022/pdf/IWN22\\_Abstract\\_book.pdf](https://www.iwn2022.org/fileadmin/congress/media/iwn2022/pdf/IWN22_Abstract_book.pdf)

[K28] Pashnev, D.; Balagula, R.M.; Dub, M.; Sakowicz, M.; **Jorudas, J.**; Subačius, L.; Sai, P.; Cywinski, G.; Kašalynas, I. Optimization of 2D Plasmons Excitation in Grating-Gated AlGa<sub>N</sub>/Ga<sub>N</sub> High Electron Mobility Transistor Structures. In abstract book of the Advanced Properties and Processes in Optoelectronic Materials and Systems (APROPOS 18); Vilnius, Lithuania, 2022. pp. 35; [https://www.ftmc.lt/uploads/APROPOS18/APROPOS18\\_abstract\\_book\\_ISBN\\_978-609-96355-0-7.pdf](https://www.ftmc.lt/uploads/APROPOS18/APROPOS18_abstract_book_ISBN_978-609-96355-0-7.pdf)

[K29] Dub, M.; But, D. B.; **Jorudas, J.**; Sai, P.; Cywinski, G.; Kašalynas, I.; Rumyantsev, S.L.; Knap, W. Low frequency noise as a quality control of novel AlGa<sub>N</sub>/Ga<sub>N</sub> devices. In abstract book of the Advanced Properties and Processes in Optoelectronic Materials and Systems (APROPOS 18); Vilnius, Lithuania, 2022. pp. 33; [https://www.ftmc.lt/uploads/APROPOS18/APROPOS18\\_abstract\\_book\\_ISBN\\_978-609-96355-0-7.pdf](https://www.ftmc.lt/uploads/APROPOS18/APROPOS18_abstract_book_ISBN_978-609-96355-0-7.pdf)

[K30] Sakowicz, M.; Dub, M.; Sai, P.; But, D.B.; Cywinski, G.; **Jorudas, J.**; Šimukovic, A.; Prystawko, P.; Indrišiunas, S.; Kovalevskij, V.; et al. Towards Terahertz Optopair Based on AlGa<sub>N</sub>/Ga<sub>N</sub> HEMTs. In Proceedings of the Terahertz Emitters, Receivers, and Applications XIII; Razeghi, M., Baranov, A.N., Eds.; SPIE, October 3 2022; p. 4. doi: 10.1117/12.2632980; <https://www.spiedigitallibrary.org/conference-proceedings-of-spie/12230/2632980/Towards-terahertz-optopair-based-on-AlGaNGaN-HEMTs/10.1117/12.2632980.full>

[K31] Pashnev, D.; **Jorudas, J.**; Janonis, V.; Urbanowicz, A.; Kašalynas, I. Excitation and Control of Two-Dimensional Plasmons in Grating-Gated

AlGaIn/GaN Heterostructures under Applied Electric Fields. In Optics and Photonics Days; Joensuu, Finland, 2023.

[K32] Moscotin, M.; **Jorudas, J.**; Saniuk, M.; Prystawko, P.; Romyantsev, S.L.; Knap, W.; Cywiński, G.; Kašalynas, I. THz Detection Optimization of Antenna Coupled AlGaIn/GaN High Electron Mobility Transistors. In Proceedings of the 48<sup>th</sup> International Conference on Infrared, Millimeter, and Terahertz Waves, IRMMW-THz; Montreal, Canada, 2023. doi: 10.1109/irmmw-thz57677.2023.10299032; <https://ieeexplore.ieee.org/abstract/document/10299032>

[K33] Saniuk, M.; Moscotin, M.; **Jorudas, J.**; Kašalynas, I. Antonomis Susieti AlGaIn/GaN Didelio Elektronų Judrio Tranzistoriai THz Dažnio Bangoms Detektuoti. In abstract book of the 45-oji Lietuvos nacionalinė fizikos konferencija; Vilnius, Lithuania, 2023. <https://ff.vu.lt/external/ff/files/LNFK45/Programa/PROGRAMA-LNFK45-final.pdf>

[K34] Pashnev, D.; **Jorudas, J.**; Subačius, L.; Janonis, V.; Urbanowicz, A.; Kašalynas, I. Moduliavimas Amplitudės Ir Fazės THz Spektrų Su 2D Plazmonais AlGaIn/GaN Heterostruktūrose Veikiamose Nuolatine Įtampa. In abstract book of the 45<sup>oji</sup> Lietuvos nacionalinė fizikos konferencija; Vilnius, Lithuania, 2023. <https://ff.vu.lt/external/ff/files/LNFK45/Programa/PROGRAMA-LNFK45-final.pdf>

[K35] Mura, M. La.; Lamberti, P.; Tucci, V.; **Jorudas, J.**; Cojocari, M.; Fedorov, G.; Kuzhir, P. Exploring the Impact of Absorber Material on the Performance of a Terahertz Microbolometer by Finite Element Analysis. In Proceedings of the 2023 IEEE Nanotechnology Materials and Devices Conference (NMDC); IEEE, October 22 2023; pp. 520–524. doi: 10.1109/NMDC57951.2023.10343843; <https://ieeexplore.ieee.org/document/10343843/>

# 1. SAMPLES AND METHODS

## 1.1. SAMPLES

In the following chapter 1.1.1, a description of the investigated GaN-based heterostructures is presented with discussion of their layout and material differences. CVD graphene and graphitic film processing techniques and sample properties are discussed in chapters 1.1.2 and 1.1.3, respectively.

### 1.1.1. GaN-based heterostructures

Three types of GaN-based heterostructures are investigated in the thesis. Their layer layouts are summarized in Table 1.1. A schematic layer layout of a typical AlGa<sub>x</sub>Ga<sub>1-x</sub>N (x = 0.2–0.3) barrier layer, ~1 nm of AlN spacer layer and up to 1 μm of UID GaN channel layer. These top layers usually are grown on a thick 1–3 μm buffer layer of GaN compensated with iron (Fe) or carbon (C) which are grown on the substrate with the nucleation layer of GaN or AlN of tens to hundreds of nanometers thickness [87]. Four of the studied heterostructures in thesis are considered typical – HEMT A, HEMT B, HEMT C and HEMT E.

In the case of heteroepitaxy, the heterostructures differ by the substrate on which they are grown on. Commonly sapphire (Al<sub>2</sub>O<sub>3</sub>) has been used extensively due to its low price, but large lattice mismatch to GaN of 16% [88] introduces large amounts of defects. Three heterostructures investigated in the thesis are grown on Al<sub>2</sub>O<sub>3</sub> substrates – HEMT A, HEMT B, HEMT F. More expensive SiC substrates are used to grow high quality GaN-based heterostructures for high performance applications, since SiC have small lattice mismatch of 3.5% to GaN and very high thermal conductivity [87]. Three samples of heterostructures grown on SiC substrates are HEMT C, HEMT E and HEMT D.

In the AlGa<sub>x</sub>N barrier/GaN channel interface the 2DEG is formed as seen in Figure 1d. The AlN spacer layer between barrier and channel layers (orange colored layer in Figure 2) is often used to distance the formed 2DEG layer from the AlGa<sub>x</sub>N barrier to mitigate the alloy disorder scattering, thus improving electron mobility in the 2DEG layer [89]–[91]. Though recently due to the maturation of the AlGa<sub>x</sub>N/GaN HEMT technology high mobility of >2000 cm<sup>2</sup>V<sup>-1</sup>s<sup>-1</sup> is achieved without the use of spacer layer [92], [93]. In the

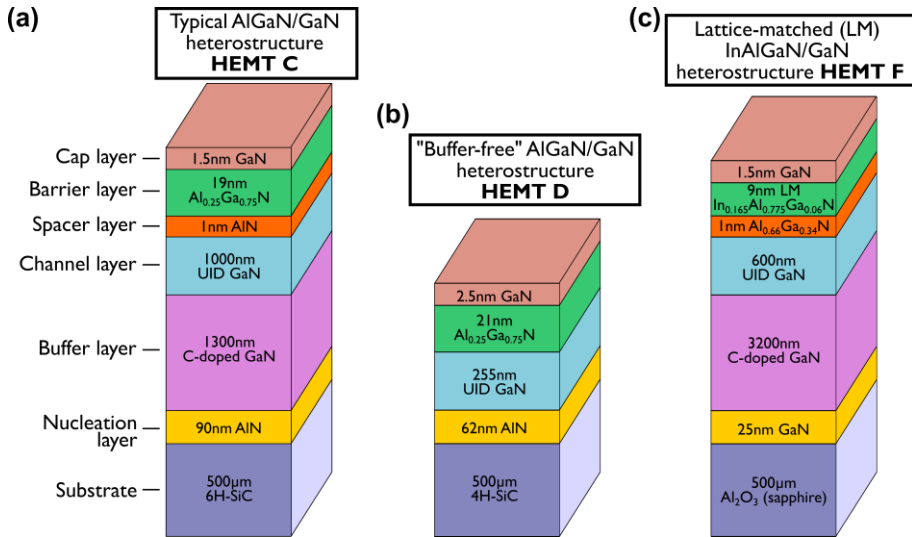


Figure 2. Schematic layouts of some investigated GaN-based heterostructures. (a) Typical AlGaIn/GaN heterostructure - HEMT C. (b) Thin AlGaIn/GaN heterostructure - HEMT D. (c) Thin barrier lattice-matched InAlGaIn/GaN heterostructure - HEMT F.

thesis two of the studied heterostructures do not use spacer layers in their layout – HEMT E and HEMT D.

Above the nucleation layer and below the UID GaN channel layer, a  $\sim 1\text{-}3\ \mu\text{m}$  thick buffer layer of GaN compensated with Fe or C (shown in Figure 2 by purple color) is used to reduce the number of threading dislocations in the top layers of the heterostructure [94], [95] and to achieve semi-insulating layer below channel layer. Furthermore, Fe or C compensated GaN buffers have been found to improve RF and DC off-state performance of HEMTs [96], [97]. Recently, novel approach to grow high quality AlN nucleation layer directly on SiC substrate was developed, that allows to skip GaN buffer layer completely [98], [99]. One of the studied heterostructures in the thesis, HEMT D shown in Figure 2b, was grown using this method without GaN buffer layer and was investigated in [P1].

Another approach to improve GaN-based HEMT heterostructures is to change typical AlGaIn barrier layer with other nitride material, such as InAlN [40], [42], [100], [101] or InAlGaIn [43], [102]–[105]. These barrier materials allow to achieve the same 2DEG performance with significantly thinner barrier layers, which allows to achieve lower pinch-off voltages for devices and mitigate short channel effects in deeply scaled HEMTs [106]. One of the studied heterostructures in the thesis, HEMT F, uses novel InAlGaIn barrier layer of 9 nm thickness and was investigated in [P2].

Using cloverleaf type van der Pauw test structures and performing Hall measurements, the main properties of the 2DEGs were obtained at the temperatures of 300 K and 77 K for the investigated heterostructures. The results are summarized in Table 1.2.

Table 1.1 Layout of layers and composition of the investigated AlGaIn/GaN and InAlGaIn HEMT structures grown on SiC and Al<sub>2</sub>O<sub>3</sub> substrates

	HEMT A	HEMT B	HEMT C	HEMT D	HEMT E	HEMT F
<b>GaN cap</b>	—	—	2 nm	2.5 nm	1.5 nm	0.5 nm
<b>Barrier</b>	Al <sub>0.20</sub> Ga <sub>0.80</sub> N 25 nm	Al <sub>0.23</sub> Ga <sub>0.77</sub> N 27 nm	Al <sub>0.25</sub> Ga <sub>0.75</sub> N 19 nm	Al <sub>0.25</sub> Ga <sub>0.75</sub> N 20.5 nm	Al <sub>0.25</sub> Ga <sub>0.75</sub> N 21 nm	In <sub>0.165</sub> Al <sub>0.775</sub> Ga <sub>0.06</sub> N 8.7 nm
<b>Spacer</b>	AlN 1 nm	AlN 1 nm	AlN 1 nm	—	—	Al <sub>0.66</sub> Ga <sub>0.34</sub> N 1.2 nm
<b>UID-GaN channel</b>	500 nm	500 nm	1000 nm	255 nm	200 nm	600 nm
<b>GaN buffer</b>	1000 nm	1000 nm	1300 nm	—	1800 nm	3200 nm
<b>Nucleation layer</b>	n.d.	n.d.	90 nm	AlN 62 nm	AlN 50 nm	GaN 25 nm
<b>Substrate</b>	Al <sub>2</sub> O <sub>3</sub>	Al <sub>2</sub> O <sub>3</sub>	6H-SiC	4H-SiC	4H-SiC	Al <sub>2</sub> O <sub>3</sub>

n.d. — no data.



Table 1.2 Mean and standard deviation values for electrical parameters of the 2DEGs in GaN-based heterostructures obtained from Hall experiment using van der Pauw structures.

		HEMT A	HEMT B	HEMT C	HEMT D	HEMT E	HEMT F
Sheet electron density $N_s$ ( $\times 10^{13} \text{ cm}^{-2}$ )	300 K	0.92	0.73	$0.80 \pm 0.05$	$1.00 \pm 0.01$	$0.95 \pm 0.05$	$1.23 \pm 0.01$
	77 K	n.d.	n.d.	$0.73 \pm 0.03$	$0.96 \pm 0.01$	$0.86 \pm 0.06$	$1.20 \pm 0.01$
Mobility $\mu$ ( $\text{cm}^2 \text{V}^{-1} \text{s}^{-1}$ )	300 K	$1.3 \times 10^3$	$1.4 \times 10^3$	$(1.9 \pm 0.2) \times 10^3$	$(1.7 \pm 0.1) \times 10^3$	$(1.8 \pm 0.1) \times 10^3$	$(1.6 \pm 0.1) \times 10^3$
	77 K	$4.2 \times 10^3$	n.d.	$(1.5 \pm 0.2) \times 10^4$	$(1.0 \pm 0.1) \times 10^4$	$(1.8 \pm 0.2) \times 10^4$	$(8.8 \pm 0.1) \times 10^3$
Sheet resistance $R_{\text{sh}}$ ( $\Omega/\text{sq.}$ )	300 K	510	630	$420 \pm 30$	$380 \pm 2$	$360 \pm 20$	$320 \pm 10$
	77 K	n.d.	n.d.	$60 \pm 6$	$60 \pm 1$	$40 \pm 3$	$60 \pm 1$

n.d. – no data.

### 1.1.2. Graphene

Graphene samples on high resistivity Si ( $>10\text{ k}\Omega\text{ cm}$ ) and AlGaN/GaN heterostructures were fabricated of commercial monolayer CVD graphene on a copper foil protected by 60 nm PMMA coating (Graphenea).

CVD graphene was transferred to substrates using standard wet transfer method using native PMMA as support layer [107], [108]. Transfer process is schematically shown in Figure 3. First, PMMA coated graphene on Cu foil is placed on the surface of dilute  $\text{H}_2\text{O}/\text{HCl}/\text{H}_2\text{O}_2$  at volumetric ratio 60:5:2 to etch Cu foil. The translucent PMMA/graphene stack from step 2 is transferred to deionized (DI) water bath in step 3 to dilute the transferred etching solution with graphene. Step 3 of transferring PMMA/graphene into clean DI bath is repeated 3 times to ensure that no etching solution at relevant concentration is left. Next, in step 4 PMMA/graphene stack is wet transferred onto substrate of choice (hydrophilic substrates make this easier) and after wet transfer substrate with PMMA/graphene is dried in an oven at  $130^\circ\text{C}$  in step 5. Afterwards, the dry sample is exposed to 254 nm DUV light for 3 hours (sample to DUV lamp distance approximately 16 cm) to modify PMMA making it more soluble in the remover (step 6). The exposed PMMA is removed in IPA/DI water (volumetric ratio 7:3) rapidly in 30 seconds (step 7), to finally obtain a clean graphene sample on desired substrate (step 8).

Multiple samples of PMMA/graphene were wet transferred on HR Si and AlGaN/GaN heterostructure substrates following steps 1 through 5 (see Figure 3). The DUV exposure — IPA/DI removal procedure was compared to more typical purely chemical removal of PMMA with acetone and chloroform (in both cases 18 hours at the room temperature). The quality of the graphene after

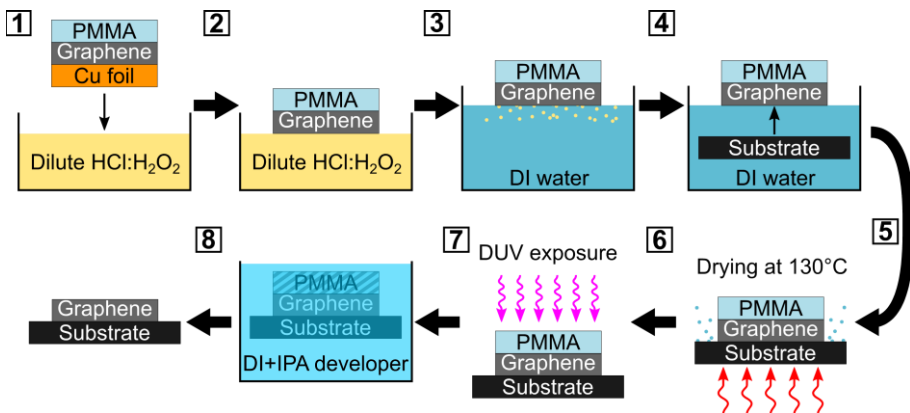


Figure 3. Wet transfer process protocol used to transfer CVD graphene to required substrate.

Table 1.3 Raman spectroscopy statistics of wet-transferred CVD graphene on AlGaIn/GaN HEMT structure and Si substrates

Sample	$I_{2D}/I_G$	2D FWHM ( $\text{cm}^{-1}$ )	Processing run
GaN-IP	$2.57 \pm 0.19$	$32.3 \pm 1.9$	#1
Si-IP1	$2.74 \pm 0.31$	$30.2 \pm 1.3$	#1
Si-IP2	$3.00 \pm 0.41$	$27.8 \pm 1.0$	#1
Si-IP3	$2.90 \pm 0.22$	$27.9 \pm 1.3$	#2
Si-C1	$2.45 \pm 0.35$	$29.5 \pm 2.2$	#2
Si-A	$3.13 \pm 0.36$	$31.4 \pm 1.2$	#2

wet transfer and PMMA removal was immediately investigated using Raman spectroscopy. The results are summarized in Table 1.3.

As soon as possible after Raman spectroscopy measurements, conductivity of the graphene samples was investigated from THz transmission spectra measured using THz-TDS system (chapter 1.2.1). The spectra were analyzed in a frame of Drude conductivity model (chapter 1.2.3). Summary of the conductivity results obtained by the remote characterization is given in Table 1.4.

Table 1.4 Electrical parameters of wet-transferred CVD graphene on AlGaIn/GaN HEMT structure and Si substrates extracted from remote characterization using THz-TDS system

Sample	Sheet resistance $R_{sh}$ ( $\Omega/\text{sq.}$ )	Carrier density $N_s$ ( $\times 10^{12} \text{ cm}^{-2}$ )	Carrier mobility $\mu$ ( $\text{cm}^2 \text{V}^{-1} \text{s}^{-1}$ )	Processing run
GaN-IP	670	3.2	2960	#1
Si-IP1	670	2.5	3720	#1
Si-IP2	840	2	3650	#1
Si-IP3	1110	0.8	6910	#2
Si-C1	850	1.3	5890	#2
Si-A	850	3.1	2410	#2

### 1.1.3. Pyrolytic carbon films

Pyrolytic carbon films are comprised of disordered graphene-like nanocrystallites [83], resulting in high conductivity and chemical robustness of the films. In particular, the conductivity of pyrolytic carbon films can reach up to  $\sim 10^5$  S/m, value of which is a couple orders of magnitude lower than conductivity of metals at  $\sim 10^7$  S/m. Main advantage of pyrolytic carbon is easier and more reproducible fabrication path to fabricate conductive film of desired sheet resistance. Pyrolytic carbon films are also robust, which makes them good alternative to graphene, processing of which can be difficult. These properties motivated the research and development of the pyrolytic carbon films in the thesis.

One type of pyrolytic carbon films are pyrolyzed polymer films (PPFs), which are made by annealing photoresist at high temperatures ( $>700^\circ\text{C}$ ) in an oxygen free environment [80]–[82], [109], [110]. The PPF samples were developed on  $525\ \mu\text{m}$  thick *p*-doped Si wafers coated with  $3\ \mu\text{m}$  of  $\text{SiO}_2$  and  $300\ \text{nm}$  of  $\text{Si}_3\text{N}_4$ . The photoresist AZ nLOF 2070 was spin-coated at different speeds obtaining the desired thickness of photoresist precursor. The pyrolysis was performed in a vacuum tube furnace under a vacuum of  $0.1\ \text{mBar}$  at different temperatures from  $800$  to  $1100^\circ\text{C}$  for  $60\ \text{min}$ . Depending on the pyrolysis temperature film thickness decreased from  $5.3$  to  $8.3$  times from original photoresist thickness after pyrolysis at the temperatures of  $900^\circ\text{C}$  to  $1100^\circ\text{C}$ , respectively. The crosslinked resist samples were named PPFe (exposed to e-beam before pyrolysis), and the non-crosslinked resist samples were named PPFu (unexposed to e-beam before pyrolysis). A few sets of the PPF samples were prepared at different annealing temperatures. The results of PPF thickness with DC-conductivity parameters are summarized in Table 1.5.

Another type of pyrolytic carbon films studied are CVD deposited pyrolytic carbon (PyC) films, which are produced through the pyrolytic decomposition of hydrocarbon gases like methane [78], [79], [111]. The PyC was deposited on both sides of a  $250\ \mu\text{m}$  thick silicon wafer coated with  $300\ \text{nm}$  of high stress  $\text{Si}_3\text{N}_4$ . A 1:4 hydrogen-methane gas mixture for decomposition to a pressure of  $25\ \text{mBar}$  was introduced in the vacuum tube furnace chamber at  $700^\circ\text{C}$ . The chamber was heated up to  $1100^\circ\text{C}$  and kept at this temperature for  $5\ \text{min}$  and cooled back down to  $700^\circ\text{C}$  and then to room temperature. After the whole CVD process, the thickness of resulting PyC film using profilometer was measured to be  $20\ \text{nm}$ . Van der Pauw sheet resistance measurements on the as-grown film revealed the sheet resistance of  $600\ \Omega/\text{sq.}$ , which results in DC conductivity value of about  $8 \times 10^4\ \text{S/m}$ . To obtain a  $1 \times 1\ \text{mm}^2$  PyC/ $\text{Si}_3\text{N}_4$  freestanding membrane, a square opening was realized in

Table 1.5. PPF thickness and dc-conductivity properties for of the PPF<sub>e</sub> and PPF<sub>u</sub> samples studied in this work.

Sample	Process temperature (°C)	Final thickness $d$ (nm)	Shrinkage $D/d$	Sheet resistance ( $\Omega/\text{sq.}$ )	Resistivity ( $\text{m}\Omega \text{ cm}$ )
PPF1u	900	42	6.2	1800	7.6
PPF1e				1550	6.6
PPF2u		150	5.3	570	8.5
PPF2e		157	470	7.4	
PPF3u	1000	35	7.7	3940	13.8
PPF3e				2620	9.1
PPF4e	1100	32	8.3	5140	16.1
PyC	1100	20	—	600	1.2

the Si<sub>3</sub>N<sub>4</sub> film on the back side of the Si wafer using UV photolithography and fluorine-based reactive ion etching, while Si wafer was removed using hot 30% KOH wet etching (NEST, CNR – Istituto Nanoscienze, Pisa Italy). After all the processing steps sheet resistance of the PyC film remained close to as-grown value at  $500\pm 50 \Omega/\text{sq.}$ . The results of PyC films are summarized in Table 1.5.

#### 1.1.4. Electric contacts

Electric Ohmic contacts for all GaN-based heterostructure samples were formed of e-beam evaporated metal stacks Ti/Al/Ni/Au with thicknesses of 30/90/20/100 nm, respectively. To form Ohmic contact to the 2DEG layer, the semiconductor die with metal stack was rapidly annealed at 830°C temperature for 30 seconds in inert nitrogen ambient. Averaging over more than thirty processed dies, ohmic contact resistance was found to be in the range of  $1.0\pm 0.5 \Omega \text{ mm}$ .

To provide Schottky contact to the 2DEG layer, a Ni/Au metal stack (25/300 nm) was evaporated using e-beam on a top side of the GaN-based heterostructures using UV photolithography.

## 1.2. METHODS AND MODELS

### 1.2.1. THz time domain spectroscopy (THz-TDS) method

Terahertz time-domain spectroscopy (THz-TDS) is a powerful and versatile technique used to investigate the properties of materials usually in the lower part of the terahertz frequency range ( $\sim 0.1$ – $4$  THz). THz-TDS can be used to measure complex refractive index of dielectric material [112] and electrical conductivity [113] of metallic films [114] and various 2D systems such as graphene [115]–[118] or GaN-based heterostructures with 2DEG [119], [P12-P15].

For a typical THz-TDS system a femtosecond laser beam is split into two: one for terahertz generation and another for THz detection, as shown in Figure 4. Photoconductive antennas are one of most common approaches to generate and detect THz pulses in THz-TDS systems, proposed for the first time in the late 80s [120], [121].

The key feature of THz-TDS system is its ability to capture the temporal evolution of terahertz pulses via the usage of the delay line. By moving mirror in the delay line between the THz generation and optical probe pulses, a THz pulse trace is recorded. In transmission experiment, the THz pulse will contain information about the sample after propagating through it. A fast Fourier transformation (FFT) of THz pulse trace is performed, resulting in frequency domain data of amplitude and phase [122].

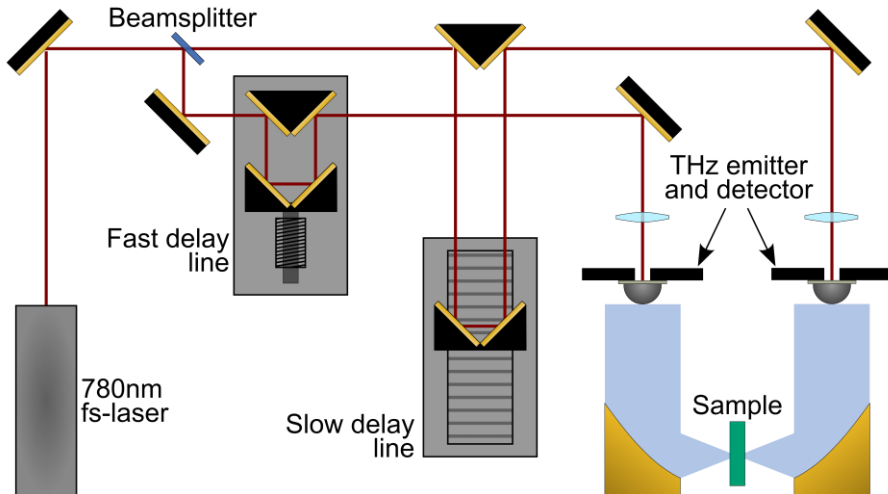


Figure 4. Schematic of THz time domain spectrometer in transmission geometry

### 1.2.2. Fourier transform infrared (FTIR) spectroscopy method

To investigate sample properties in the upped THz region FTIR spectroscopy is usually employed, which can cover the range from ~2-3 THz up to MIR and even further changing the detector and beamsplitter used in the system. FTIR spectroscopy in the terahertz range provides valuable information about the vibrational and rotational modes of molecules [123]–[125], as well as the collective excitations of the crystal lattice (phonons) of various semiconductors [126], [127], electronic band structure and carrier dynamics [56], [128].

A typical FTIR spectrometer setup is based on Michelson interferometer, principle of operation of which in transmission geometry is shown in Figure 5. It consists of a radiation source (usually thermal for THz range), detector (usually pyroelectric), beamsplitter (solid state such as Si or thin film), flat mirrors required for Michelson interferometer and focusing mirrors for sample investigation. By moving one of the mirrors in the interferometer, the interference conditions on the beamsplitter for various wavelengths are changed, which allows to record signal dependence on mirror position – interferogram. The main highest intensity peak in the interferogram corresponds to zero path difference in the interferometer arms. To obtain a spectrum, an FFT is performed on the recorded interferogram signal.

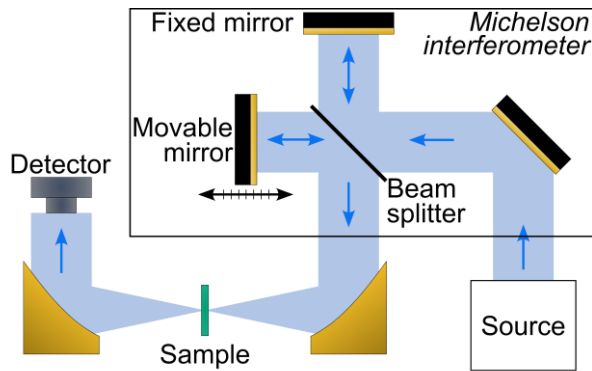


Figure 5. Setup of the Fourier transform infrared spectrometer based on Michelson interferometer.

### 1.2.3. Drude conductivity modelling and THz transmission spectroscopy of thin conductive layers

Contactless characterization of thin conductive films, such as free-standing graphitic films, metallic films and especially graphene deposited on a thick

dielectric substrate, is possible by usage of the THz spectroscopy techniques [77], [114]–[116], [129], [130]. Experimental transmission spectra  $T(\omega)$  in the THz range obtained by THz-TDS or FTIR spectroscopy can be fitted with analytical equations based on Drude conductivity model. Considering the sample as a dielectric substrate of thickness  $d_s$  with delta-thin conductive layer, Drude conductivity is used and the sheet conductivity  $\sigma_{sh}$  and scattering time  $\tau_{sc}$  are obtained from measured THz transmission spectrum [P15]:

$$T(\omega) = \left| \cos \theta_s - i \frac{\varepsilon_s + 1}{2\sqrt{\varepsilon_s}} \sin \theta_s + \frac{2\pi\sigma_{sh}}{c(1 - i\omega\tau_{sc})} \left( \cos \theta_s - i \frac{1}{\sqrt{\varepsilon_s}} \sin \theta_s \right) \right|^{-2}, \quad (1)$$

where  $\theta_s = \sqrt{\varepsilon_s} k_0 d_s$  is the phase shift for the electric field vector,  $k_0$  is the incident wave wavenumber,  $\varepsilon_s$  is the substrate dielectric permittivity,  $c$  is the speed of light.

Relevant electrical parameters such as sheet resistance  $R_{sh}$  is calculated from fitting parameters:

$$R_{sh} = \frac{1}{\sigma_{sh}}, \quad (2)$$

In the case of graphene, doping level  $N_s$  and carrier mobility  $\mu$  are obtained using:

$$N_s = \frac{\pi \hbar^2}{q v_f^2} \left( \frac{\sigma_{sh}}{\tau_{sc}} \right)^2, \quad (3)$$

$$\mu = \frac{N_s}{q \sigma_{sh}}, \quad (4)$$

where  $\hbar$  is the reduced Planck constant,  $v_f$  is the Fermi velocity and  $q$  is the elementary charge.

#### 1.2.4. Van der Pauw method and Hall experiment

The van der Pauw method allows to determine resistivity of 2D samples from resistance measurements without knowledge of samples physical dimensions and was developed in 1958 [131], [132]. It has become one of the most common methods used to measure semiconductor sheet resistance. With the use of external magnetic field carrier type, density, and mobility for arbitrary shaped samples can also be determined.



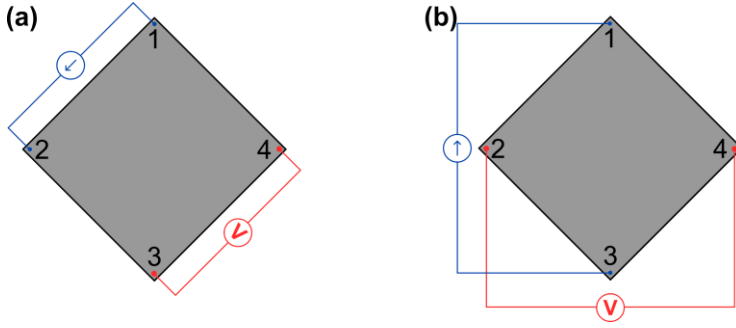


Figure 6. Van der Pauw measurement connections. (a) Example for resistivity measurements. (b) Example for Hall voltage measurements during Hall experiment.

Van der Pauw method requires four small diameter contacts on the edges of the sample as shown in Figure 6a. To obtain sheet resistance ( $R_{sh}$ ) eight resistance measurements need to be made. For example, connecting current source between contacts 2 and 1 and measuring voltage between contacts 3 and 4 for both current polarities we obtain resistance  $R_{21,34}$ . Repeating the same procedure for resistance  $R_{32,41}$  we can obtain sheet resistance:

$$R_{sh}^A = \frac{\pi f}{\ln(2)} \frac{R_{21,34} + R_{32,41}}{2}, \quad (5)$$

where  $f$  is a numerical solution to the equation:

$$\frac{q-1}{q+1} = \frac{f \cosh^{-1} e^{\frac{\ln 2}{f}}}{\ln(2)}, \quad (6)$$

where  $q = R_{21,34}/R_{32,41}$  or  $q = R_{32,41}/R_{21,34}$  (whichever is larger). For better accuracy, the same procedure is repeated for  $R_{43,12}$  and  $R_{14,23}$  to obtain  $R_{sh}^B$ . Final sheet resistance is calculated as  $R_{sh} = 0.5(R_{sh}^A + R_{sh}^B)$ .

The physical principle underlying the Hall effect is the Lorentz force, which acts on a charge carrier in a combination of crossed electric and magnetic fields. Charge carriers moving along applied electric field direction and perpendicular to the applied magnetic field experience a magnetic force and depending on the charge of the carrier different electric field will be induced. The integral of this induced electric field perpendicular to applied electric field is called Hall voltage ( $V_H$ ). Hall voltage measurement schematic using sample van der Pauw method is shown in Figure 6b. Connecting current source between diagonal contacts 1 and 3 and measuring voltage across another diagonal 4-2 for both current polarities and magnetic field polarities we obtain  $V_{13,42}^{B^+}$  and  $V_{13,42}^{B^-}$ . Initial Hall voltage is obtained as

$V_H^A = 0.5(V_{13,42}^{B+} - V_{13,42}^{B-})$ . Repeating the same procedure for the other contact pairs we obtain  $V_H^B$ . The same as for  $R_{sh}$ , final Hall voltage is calculated as  $V_H = 0.5(V_H^A + V_H^B)$ .

Using  $V_H$  with its polarity, the charge carrier type (sign) and density are obtained:

$$n_s = \frac{IB}{qV_H}, \quad (7)$$

where  $I$  is the current used,  $B$  is the magnetic field strength and  $q$  is the elementary charge. Using  $R_{sh}$  obtained from van der Pauw method, carrier mobility  $\mu$  can be obtained using:

$$\mu = \frac{1}{qn_s R_{sh}}. \quad (8)$$

Compact, cloverleaf type van der Pauw test structures (see Figure 7), were developed and used to characterize the GaN-based HEMT structure samples.

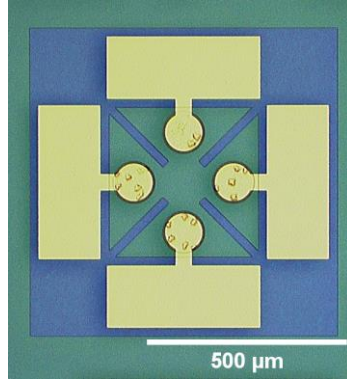


Figure 7. Microscope picture of the cloverleaf geometry van der Pauw structure used for Hall experiment to determine DC-conductivity parameters of 2DEGs in GaN-based HEMT structure samples.

#### 1.2.5. Band-diagram calculation model (Nextnano++ and Snider)

Poisson (eq.(9)) and Schrödinger (eq. (10)) equations are solved self-consistently to calculate the band-diagram and carrier distribution in a semiconductor structure [133], [134]:

$$\frac{d}{dx} \left( \epsilon_s(x) \frac{d}{dx} \right) \phi(x) = \frac{-q(N_d(x) - n(x))}{\epsilon_0}, \quad (9)$$

$$-\frac{\hbar^2}{2} \frac{d}{dx} \left( \frac{1}{m_{eff}(x)} \frac{d}{dx} \right) \psi(x) + V(x)\psi(x) = E\psi(x), \quad (10)$$

here  $\varphi$  is the electrostatic potential,  $N_d$  – ionized donor density,  $n$  – electron density,  $\psi$  – wavefunction,  $E$  – energy,  $V$  – potential energy,  $\hbar$  - reduced Planck constant,  $m_{\text{eff}}$  – effective carrier mass. In a quantum well the potential energy  $V$  is related to the electrostatic potential  $\varphi$  as:

$$V(x) = -q\varphi(x) + \Delta E_c(x), \quad (11)$$

where the  $\Delta E_c$  is the pseudopotential energy due to the band offset at heterointerface. The wave function  $\psi(x)$  in eq.(10) and the electron density  $n(x)$  in eq.(9) are connected by expression:

$$n(x) = \sum_{k=1}^m \psi_k^*(x) \psi_k(x) n_k, \quad (12)$$

where  $m$  is the number of bound states and  $n_k$  is the electron occupation for each state. The electron occupation for each state can be expressed with Fermi-Dirac distribution:

$$n_k = \frac{m^*}{\pi \hbar^2} \int_{E_k}^{\infty} \frac{1}{1 + e^{(E-E_F)/kT}} dE, \quad (13)$$

where  $E_k$  is the eigen energy of state  $m$  and  $E_F$  is Fermi energy [133].

The Poisson-Schrödinger solver (Nextnamo++ and Snider) combines the Poisson (eq.(9)) and the Schrödinger (eq.(10)) equations to simultaneously solve for the electrostatic potential  $\varphi$  and the electron and hole wave functions  $\psi$  within a semiconductor material in an iterative approach using finite-difference method [133], [134].

### 1.2.6. Transfer length method (TLM)

While there are various techniques to estimate contact resistance ( $R_c$ ), the transmission line method (TLM) is the most popular. Originally proposed by Shockley [135] and further extended by Berger [136], it provides a convenient method to determine resistive performance of the ohmic contacts together with sheet resistance ( $R_{\text{sh}}$ ) and transfer length ( $L_T$ ) estimation.

The method itself involves total resistance  $R_T$  measurements in the low-field regime on adjacent Ohmic contacts with variable spacing between them. Two most common test structures are shown in Figure 8. Usually, a simple linear array of Ohmic contacts of the same size, but placed at increasing distances  $L$ , on the semiconductor surface is used, as seen in Figure 8a. The total resistance  $R_T$  between any two contacts (of length  $d$  and width  $W$ ) separated by a distance  $L$  is measured and plotted as a function of  $L$ . The total resistance  $R_T$  dependence on contact separation distance  $L$  can be expressed as [137]:

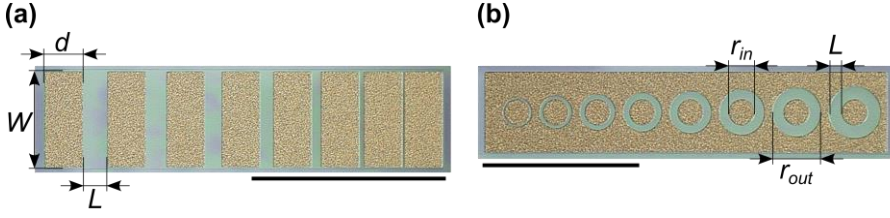


Figure 8. Photo of linear resistor array structures used for transmission line method with main geometry parameters: (a) rectangular shape (standard TLM) and (b) circular shape (CTLM) resistor arrays. Black scale bars – 500  $\mu\text{m}$ .

$$R_T = \frac{R_{sh}L}{W} + 2R_c \approx \frac{R_{sh}}{W}(L + 2L_T). \quad (14)$$

Thus, performing linear fit of the  $R_T(L)$  data allows to extract  $R_{sh}$  from the slope,  $2R_c$  is extracted from intersection with ordinate axis ( $R_T$  at  $L=0$ ) and  $2L_T$  is extracted from intersection with abscissa axis ( $L$  at  $R_T=0$ ).

Fabrication of the standard linear TLM resistor array (Figure 8a) requires two photolithography steps (mesa and ohmic metallization) and precise control of mesa width  $Z$ , value of which should be as close to  $W$  as possible. A circular TLM (CTLM) structure fabricated in a single photolithography step was proposed later [138]. Here, the size of inner contact with radius  $r_{in}$  is constant, but it is spaced out by a distance  $L$  to the concentric outer contact, radius of which is changing in array as  $r_{out}=r_{in}+2L$ . Picture of CTLM structure is shown in Figure 8b. In the case of CTLM the eq. (14) takes form of

$$R_T = \frac{R_{sh}}{2\pi r_{in}}(L + 2L_T)C, \quad (15)$$

where  $C$  is the correction factor

$$C = \frac{r_{in}}{L} \ln \left( 1 + \frac{L}{r_{in}} \right). \quad (16)$$

Detailed derivation of the formulas for the transmission line method was given elsewhere [137]–[140]. Note, that the contact width and length should be chosen according to sheet resistance of the semiconductor and expected contact resistivity to minimize systematic errors of measurements [141].

### 1.2.7. Low frequency noise and McWhorter model for estimation of charge trap-density

McWhorter model was originally developed to explain flicker low frequency noise ( $1/f$  noise) in germanium filaments under an assumption that noise is caused by fluctuation in number of carriers due to charge trapping and detrapping in surface states [142]. Model was further developed to characterize  $1/f$  noise in a MOSFET under an assumption that the noise in the device originates from electron tunneling from channel to oxide and their capture at different distances from the channel [143]. The AlGaIn/GaN HEMTs are quite similar to standard Si MOSFETs, since conductive 2DEG layer is distanced from the gate via AlGaIn barrier layer, which could be considered as dielectric material. Electrons tunnelling between gate and the 2DEG channel, through the AlGaIn layer can be captured by traps. Due to ability to extract trap density, the McWhorter model was applied to characterize AlGaIn/GaN transistors [144]–[146].

In the McWhorter model, spectral noise density of a drain current fluctuations  $S_I/I^2$  is determined by:

$$\frac{S_I}{I^2} = \frac{kTN_t}{\gamma fWL_g n_s^2}, \quad (17)$$

where  $k$  is the Boltzmann constant,  $T$  is the temperature,  $N_t$  is the effective trap density,  $f$  is the frequency,  $WL_g$  is the channel area,  $n_s$  is sheet carrier concentration and  $\gamma$  is the attenuation coefficient of the electron wave function under the barrier ( $10^8 \text{ cm}^{-1}$ ). Equation (17) does not consider the drain and source access resistances, which are sum of the contact resistance and resistance of the ungated parts of the channel. Using input gate voltage noise  $S_{U_g}=(S_I/I^2)/(g_m/I)^2$  the effective trap density can be estimated, neglecting the impact of access resistances, since  $S_{U_g}$  does not depend on them:

$$S_{U_g} = \frac{kTN_t q^2}{\gamma fWL_g C^2}, \quad (18)$$

where  $q$  is the electron charge,  $C$  is the gate capacitance per unit area. Note also, that in accordance with the McWhorter model,  $S_{U_g}$  does not depend on the carrier concentration in the channel, i.e., on the gate voltage.

## 2. RESULTS

### 2.1. DEVELOPMENT OF THE GaN-BASED HETEROSTRUCTURES

This chapter covers the research and development of novel GaN-based HEMT structures, namely: the development thin AlGa<sub>N</sub>/Ga<sub>N</sub> HEMT without thick Ga<sub>N</sub> buffer layer [P1] and lattice-matched InAlGa<sub>N</sub> thin barrier HEMT [P2] structures; also research of electrically active trap density characteristics for the AlGa<sub>N</sub>/Ga<sub>N</sub> HEMT structures [P3].

#### 2.1.1. Thin AlGa<sub>N</sub>/Ga<sub>N</sub> HEMT structure

A thin AlGa<sub>N</sub>/Ga<sub>N</sub> HEMT structure, based on a new approach of thin Ga<sub>N</sub>-AlN-SiC nucleation layer without a thick Ga<sub>N</sub> buffer was proposed [93], [99] and investigated in this work [P1]. The layer layout of the investigated sample HEMT D is shown in Figure 2b. Thin Schottky barrier diodes (T-SBDs) and thin HEMTs (T-HEMTs) were developed to study realistic devices under high DC voltages and in radio frequency (RF) regimes.

Measured 2DEG properties for HEMT D are summarized in Table 1.2. A thermally stable 2DEG density was obtained, with the mobility increased ~6 fold upon cooling to 77 K. The performance of 2DEG at the room temperature for this heterostructure is found to be comparable to typical AlGa<sub>N</sub>/Ga<sub>N</sub> HEMT structures.

The T-SBDs were developed and characterized, revealing standard values for threshold voltage to be of -3.1 V. In the reverse bias breakdown voltages of up to -780 V were achieved for contact spacing of 40 μm (see Figure 9a). Meanwhile, the largest breakdown field up to 0.8 MV/cm was measured in SBD samples with smallest spacing of 5 μm used (see Figure 9b). It is worth noting that similar thin Ga<sub>N</sub>-AlN-SiC structure demonstrated the breakdown field values up to 1.9 MV/cm for the same contact spacing but without 2DEG between contacts in such way eliminating dissipation of DC power [93].

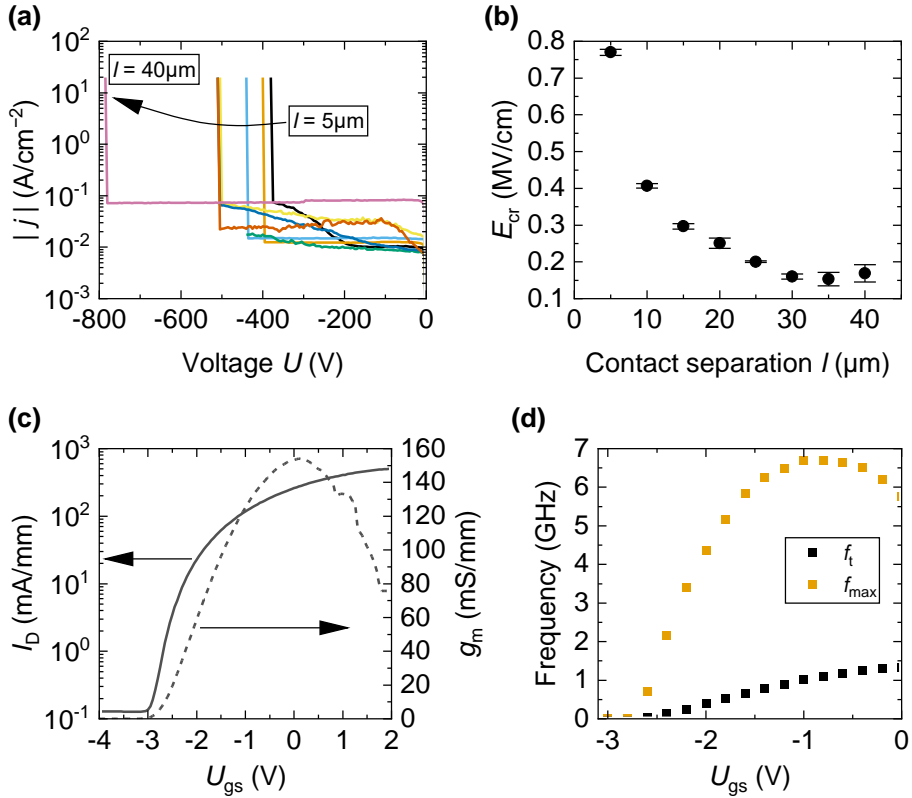


Figure 9. (a) Breakdown of various contact separation Schottky barrier diodes (SBDs) in the reverse bias and (b) critical breakdown field  $E_{\text{cr}}$  dependence on contact separation. (c) Transfer characteristics and transconductance  $g_m$  of HEMT at  $U_D=5$  V. (d) Unity current gain cut-off ( $f_t$ ) and unity maximum unilateral power gain ( $f_{\text{max}}$ ) frequencies for HEMT at  $U_D=7$  V.

Measured DC transfer characteristics of the representative T-HEMT sample are shown in Figure 9c. Maximum achieved drain current was 507 mA/mm, while maximum achieved transconductance was 154 mS/mm. Measuring output characteristics for the T-HEMTs (see [P1]) drain saturation level of 266 mA/mm was achieved at  $U_D=10$  V and  $U_{\text{gs}}=+1$  V, which translates to input power of 2.6 W/mm at a channel width of  $2 \times 0.2$  mm. The reduction of drain currents in the saturation region up to maximum input power was only by 1-2% for the various geometry of T-HEMT samples. Data indicates efficient heat dissipation from thin HEMT structure to the SiC substrate and heat sink. The RF characterization (Dr. Artūras Šimukovič, FTMC, Vilnius, Lithuania) of T-HEMTs allowed us to extract unity current cut-off ( $f_t$ ) and the unity maximum unilateral power gain ( $f_{\text{max}}$ ) frequencies. The results are shown in Figure 9d. The devices with  $2 \times 0.2$  mm channel width

( $L_G=5\ \mu\text{m}$ ;  $L_{SD}=14\ \mu\text{m}$ ) demonstrated the highest operational frequencies with values of  $f_T$  reaching up to 1.3 GHz and  $f_{\text{max}}$  values – up to 6.7 GHz, which translates in the figure of merit  $f_T \times L_G$  of 6.7 GHz $\times\mu\text{m}$ . The results are comparable to the best value of 9.2 GHz $\times\mu\text{m}$  reported in literature for the T-HEMTs but with significantly shorter gate length, being of 200 nm only [98]. The resolution of semiconductor processing technologies available at the FTMC during study period were only of 2-3  $\mu\text{m}$  and that was main bottleneck for the record performance of developed electronic devices (SBD, HEMT, etc.). To the authors knowledge these are first RF HEMTs designed and fabricated at the FTMC, Lithuania, with  $f_T$  and  $f_{\text{max}}$  above 1 GHz.

### 2.1.2. Lattice matched InAlGaN barrier HEMT structures

The lattice-matched (LM) InAlN/GaN HEMT structures are very attractive for the development of HEMTs as they possess no degradation due to mechanical stress and exhibit high chemical and thermal stability, with devices operation demonstrated up to 1000°C [13], [40], [147], [148]. Even more, the use of LM-InAlN barrier (demonstrated down to 3 nm thickness [14]) allows to achieve approximately two times higher 2DEG densities than that in the AlGaN/GaN HEMT structures with the same barrier thickness of 25 nm [149]. All reported features of the LM-InAl(Ga)N/GaN HEMT structures are attractive for the development of novel electronics and in particular THz plasmonic devices. The quaternary LM-In<sub>0.165</sub>Al<sub>0.775</sub>Ga<sub>0.06</sub>N barrier layer with thickness of 9 nm only was developed for GaN-based HEMT structures on sapphire substrate (HEMT F). The structural material properties, optical and electrical characteristics were investigated studying the test devices developed and fabricated in this work [P2].

The SIMS analysis revealed the oxygen, carbon, and silicon impurity concentrations in the GaN channel layer, which were found to be of  $(3.7\pm 1.3)\times 10^{16}\ \text{cm}^{-3}$ ,  $(5.1\pm 0.3)\times 10^{16}\ \text{cm}^{-3}$  and  $(1.0\pm 0.6)\times 10^{16}\ \text{cm}^{-3}$ , respectively. These values were comparable to ones obtained for typical AlGaN/GaN HEMT structures [P3]. The investigation of atomic fractions for the top layers of epi-structure also revealed a small amount of Ga in the barrier. Traces of Ga have been previously observed while trying to grow pure InAlN layers on GaN using MOCVD techniques [150]–[152]. The XRD measurements (Marcin Kryśko, UNIPRESS, Warsaw, Poland) revealed good crystal quality and allowed to estimate the layer thicknesses and barrier layer composition. The experimental and the fitted data are shown in Figure 10. Under the assumption that Ga fraction in barrier layer was 6%, the other concentrations were found to be of 16.5 $\pm$ 0.2% for In and 77.5 $\pm$ 0.2% for Al at



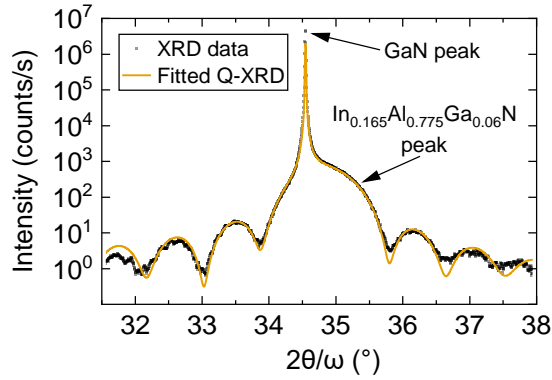


Figure 10. Experimental HR-XRD curve (black squares) and the best fit (line) of the heterostructure with quaternary barrier composition Q-XRD of  $16.5 \pm 0.2\%$ ,  $77.5 \pm 0.2\%$ , and  $6\%$  for In, Al, and Ga, respectively, and thickness of 8.6 nm.

barrier thickness of 8.6 nm. As seen from the XRD curve, there is no visible strain in the barrier layer, confirming the lattice matching for the InAlGaN layer.

The photoluminescence spectra of as-grown heterostructure HEMT F were measured (Jūras Mickevičius, Vilnius University, Vilnius, Lithuania) exciting with ns-pulses at 300 nm and at 250 nm wavelengths. The results are shown in Figure 11a,b. After pulsed laser excitation of 300 nm wavelength only electron-hole recombination in GaN layers was probed, demonstrating Lorentzian shape band at 3.43 eV with FWHM of 90 meV. At excitation wavelength of 250 nm a broad spectrum centered around 3.98 eV with

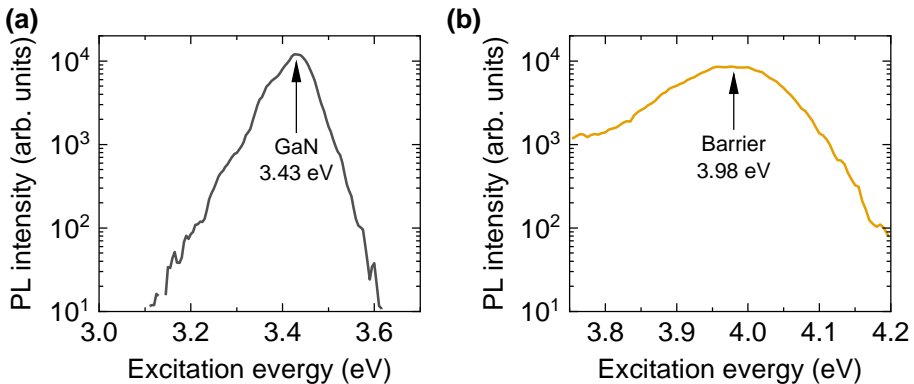


Figure 11. PL spectra of the heterostructure HEMT F measured using different excitation wavelengths: (a) 300 nm (black line) and (b) 250 nm (yellow line), respectively.

FWHM of 200 meV was observed in the PL spectrum, which was evidence of the InAlGaN barrier contribution [153]–[155].

The band diagrams and carrier distributions were numerically simulated using Nextnano++ software to determine the actual composition of grown barrier layer. Data of SIMS and XRD measurements as well as the growth protocol data of ternary InAlN barrier were considered. The band diagrams of three analyzed compositions are shown in Figure 12a-c. The considered composition cases were of nominal LM-ternary  $\text{In}_{0.18}\text{Al}_{0.82}\text{N}$ , quaternary  $\text{In}_{0.23}\text{Al}_{0.74}\text{Ga}_{0.03}\text{N}$  determined from SIMS (Q-SIMS), and LM-quaternary  $\text{In}_{0.165}\text{Al}_{0.775}\text{Ga}_{0.06}\text{N}$  determined from XRD fitting (Q-XRD). The 2DEG density, lattice matching and barrier bandgaps were calculated and compared with experimental 2DEG density and barrier-associated PL line position. The results are shown in Figure 12d,e. The SIMS measurements indicated some GaN incorporation in barrier layer, while XRD data demonstrated good lattice-matching between layers, thus significantly lower carrier density value than the experimental data seem to rule out Q-SIMS composition. Comparing the fitted quaternary barrier composition Q-XRD to that of the nominal ternary  $\text{In}_{0.18}\text{Al}_{0.82}\text{N}$ , not only the lattice matching condition is maintained, but also the resulting  $\text{In}_{0.165}\text{Al}_{0.775}\text{Ga}_{0.06}\text{N}$  bandgap of 4.36 eV is very close to 4.39 eV of ternary  $\text{In}_{0.18}\text{Al}_{0.82}\text{N}$  barrier. The 2DEG density for heterostructure with barrier Q-XRD was calculated to be  $1.6 \times 10^{13} \text{ cm}^{-2}$ , which was similar to experimentally determined from Hall measurements (see also Table 1.2). The 2DEG density was found to be stable to temperature changes, while the mobility increased from  $1590 \text{ cm}^2\text{V}^{-1}\text{s}^{-1}$  at 300 K to  $8830 \text{ cm}^2\text{V}^{-1}\text{s}^{-1}$  at 77 K. The discrepancy between the simulated and the experimental carrier density values was acceptable and in line with the material sensitivity to technological steps used in the HEMT device processing [156]–[158]. Regarding photoluminescence measurements, the PL line in our case red-shifted from the expected value by 0.4 eV, that is not large difference as Stokes shifts up to 1 eV were reported for InAlN barrier PL in the literature [153]–[155], [159], [160]. Various explanations of the Stokes shift were proposed such as the introduction of sub-band edge states near the band edge minima which induce strain and related alloy composition fluctuations [161], local variations of the number of Al and In atoms surrounding nitrogen atom [162], or radiative recombination between the electrons in the triangular quantum well (2DEG) and photoexcited holes efficiently transferred from InAlN to GaN via sub-band-gap states [155].

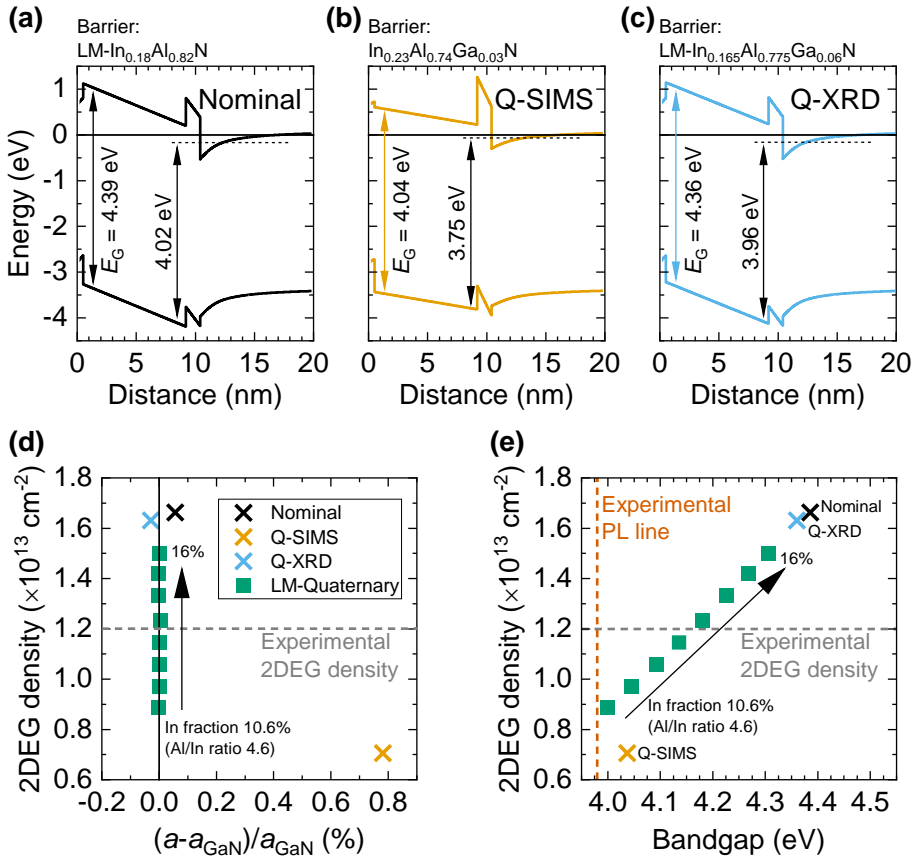


Figure 12. Modelling results (Nextnano++) for various compositions. Band diagrams for heterostructures with barrier layers: (a) nominal LM-ternary  $\text{In}_{0.18}\text{Al}_{0.82}\text{N}$ , (b) quaternary  $\text{In}_{0.23}\text{Al}_{0.74}\text{Ga}_{0.03}\text{N}$  determined from SIMS (Q-SIMS) and (c) LM-quaternary  $\text{In}_{0.165}\text{Al}_{0.775}\text{Ga}_{0.06}\text{N}$  determined from XRD fitting (Q-XRD). Bandgaps  $E_G$  and indirect energy gap from lowest 2DEG energy level to barrier valence band are given in the graphs. (d) 2DEG carrier densities in heterostructures calculated the barrier layers plotted versus lattice matching. (e) 2DEG carrier densities plotted against bandgaps of the barrier layers. Dashed lines in (d) and (e) show experimental 2DEG density and experimental PL line associated with barrier.

Finally, SBDs and HEMTs were fabricated out of the HEMT F heterostructure. Measurement and analysis of current-voltage characteristics of the SBDs, revealed the pinch-off voltage was only  $-1.74$  V [P2], while for standard AlGaN/GaN HEMT structures of similar  $R_{\text{sh}}$  was usually around  $-3$  V [P3]. To investigate breakdown field of this heterostructure SBDs with contact separations of  $40 \mu\text{m}$  and  $5 \mu\text{m}$  were reverse biased till breakdown. It was measured to occur at  $-230$  V and  $-200$  V, resulting in breakdown field of

0.05 MV/cm and 0.43 MV/cm for contact spacing of 40  $\mu\text{m}$  and 5  $\mu\text{m}$ , respectively. Such lowering of breakdown field was attributed to relatively high threading dislocation density present in the heterostructure grown on  $\text{Al}_2\text{O}_3$  substrate. It is worth to note that number of TDDs and other defects scales with an active area of the device. The leakage currents as large as 2 mA/mm prior to the breakdown indicated to the thermal breakdown as the most likely mechanism.

The HEMT samples were tested in both DC and RF regimes. The results are shown in Figure 13. As in SBDs, the low pinch-off voltage of  $-1.74$  V can be seen from the transfer characteristics measured at  $U_{\text{ds}}=5$  V (Figure 13a). The maximum achieved drain current was up to 200 mA/mm, while maximum achieved transconductance was 117 mS/mm. Due to relatively large leakage currents  $I_{\text{on}}/I_{\text{off}}$  ratio was limited to 26 dB. Following the same procedure as before,  $f_{\text{T}}$  and  $f_{\text{max}}$  frequencies were extracted (Dr. Artūrs Šimukovičs, FTMC, Vilnius, Lithuania) for HEMTs ( $W=2\times 0.2$  mm;  $L_{\text{G}}=5$   $\mu\text{m}$ ;  $L_{\text{SD}}=12$   $\mu\text{m}$ ). The results are shown in Figure 13b. The highest  $f_{\text{T}}$  and  $f_{\text{max}}$  values were obtained at  $U_{\text{ds}}=5$  V and  $U_{\text{gs}}=0.2$  V to be 1.0 GHz and 4.5 GHz, respectively. Using obtained  $f_{\text{T}}$  value, results in the figure of merit  $f_{\text{T}}\times L_{\text{G}}$  is 5.0 GHz $\times\mu\text{m}$ .

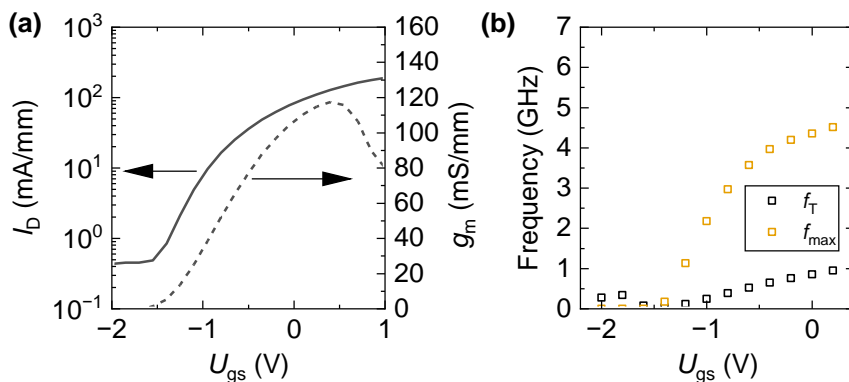


Figure 13. Performance of thin InAlGaN barrier (heterostructure HEMT F) HEMTs in DC and RF at  $U_{\text{ds}}=5$  V. (a) Transfer and transconductance  $g_{\text{m}}$  characteristics. (b) RF operational frequencies  $f_{\text{T}}$  and  $f_{\text{max}}$  as a function gate voltage  $U_{\text{gs}}$

### 2.1.3. Trap density in typical AlGaIn/GaN HEMT structures

Trap density was studied in a number of typical AlGaIn/GaN HEMT structures measuring the  $1/f$  current noise and current-voltage characteristics for HEMT devices at the room temperature. The trap density was estimated

by applying the McWhorter model in cooperation with prof. Sergey L. Rumyantsev (UNIPRESS, Warsaw, Poland) [P3].

The noise spectra were measured (Pavlo Sai, UNIPRESS, Warsaw, Poland) as a function of the drain,  $V_D$ , and gate,  $V_g$ , voltages with the source grounded. The voltage fluctuations,  $S_v$ , from the drain load resistance  $R_L=1-10\text{ k}\Omega$  were found using a dynamic signal analyzer. The short-circuit current fluctuations were calculated as  $S_i=S_v[(R_L+R_d)/(R_LR_d)]^2$ , where  $R_d$  is the drain to source resistance obtained from the experimental current-voltage characteristics. Fabricated HEMT samples demonstrated  $\sim 6$  orders of magnitude on/off ratio and the subthreshold slope of  $\eta=1.5-2$ , which is considered as good performance for high power electronic applications in general.

The noise spectra had the form of  $1/f^\alpha$  noise with  $\alpha=0.95-1.05$ . The dependences of noise on the gate voltage swing ( $U_g-U_t$ ) were investigated in the linear regime at frequency  $f=10\text{ Hz}$ . The results for the representative devices are shown in Figure 14a ( $U_t$  is the threshold voltage). The shape typical for the FETs was observed and at a high gate voltage, the noise slightly increased with the gate voltage, manifesting the noise contribution of the contacts [163]. At a lower gate voltage, noise decreases with the gate voltage increase steeper than McWhorter model prediction of  $1/(U_g-U_t)^2$ , which is often observed. The two most probable are the influence of the drain and source access resistances or the dependence of the trap density on energy. The trap density was extracted for three different standard AlGaIn/GaN heterostructures with HEMTs using formula (18). The results are shown in Figure 14b. It is important to note, that in McWhorter model trap density  $\underline{N}_t$  is trap density is assumed to be uniform in energy and in space, so is normalized to unit energy and unit volume (dimension of  $\text{eV}^{-1}\text{cm}^{-3}$ ).

The investigated AlGaIn/GaN HEMT structures had fairly similar epitaxial structures (see Table 1.1) and 2DEG sheet resistances (see Table 1.2), but the effective trap densities were quite different. Especially HEMT structure HEMT B exhibited up to two orders of magnitude higher trap density at high gate voltages. To investigate this SIMS measurements were ordered for all three heterostructures. The results are summarized in Table 2.1. Considering that oxygen and silicon act as shallow donors, while carbon is acceptor in GaN, the heterostructure HEMT B had the highest uncompensated donor density ( $N_D-N_A$ ). This and higher extracted trap density were further supported by the THz electroluminescence spectroscopy of shallow impurities at cryogenic temperatures [164], [165]. The same HEMT B (marked in ref. [164] as U28) had a 30% higher oxygen peak compared to HEMT A (marked in ref. [164] as U26). To compare overall, the obtained value

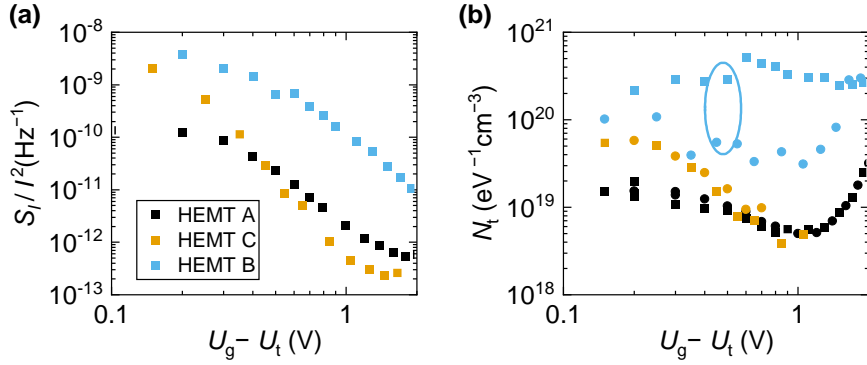


Figure 14. (Left) Dependences of noise on the gate voltage swing ( $U_g-U_t$ ) for the HEMTs on respective heterostructures;  $f=10$  Hz; and  $U_D=0.1$  V. (Right) Effective trap density  $N_t$  as a function of the gate voltage swing ( $U_g-U_t$ ) for same heterostructures.

$N_t \approx 10^{19} \text{ eV}^{-1} \text{ cm}^{-3}$  at high gate voltages, is similar or even smaller than the effective trap densities reported for Si MOSFETs[166]–[168] and in other works for AlGaIn/GaN HEMTs[169].

Effective trap density for the HEMTs fabricated of thin AlGaIn/GaN structures was also investigated [P1]. The results extracted from low-frequency current noise (Pavlo Sai, UNIPRESS, Warsaw, Poland) and current-voltage data are shown in Figure 15. Overall values were found to be in the range of  $10^{19}$ – $10^{20} \text{ eV}^{-1} \text{ cm}^{-3}$ . This is of similar level as the data for various typical AlGaIn/GaN HEMT structures with thick GaN buffer layers (see also Figure 14b). It demonstrates that avoiding a thick GaN buffer does not increase active (dislocation related) trap density in the GaN–AlN–SiC material heterostructures.

Table 2.1. Concentrations of oxygen, silicon and carbon atoms in GaN channel layers obtained from SIMS.

Heterostructure	Oxygen ( $\times 10^{16} \text{ cm}^{-3}$ )	Silicon ( $\times 10^{16} \text{ cm}^{-3}$ )	Carbon ( $\times 10^{16} \text{ cm}^{-3}$ )
HEMT A	$2.0 \pm 1.0$	$0.9 \pm 0.6$	$1.4 \pm 0.2$
HEMT B	$2.5 \pm 1.1$	$1.0 \pm 0.7$	$1.1 \pm 0.2$
HEMT C	$2.1 \pm 1.2$	$1.0 \pm 0.8$	$1.3 \pm 0.2$

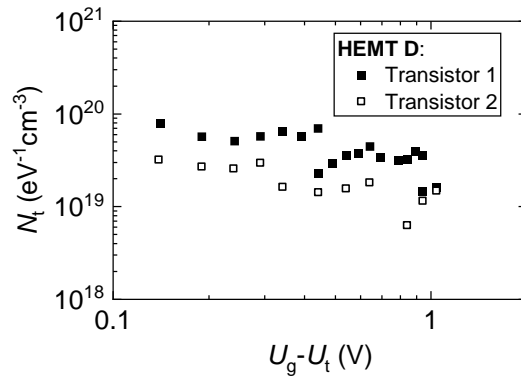


Figure 15. Effective trap density for extracted from 10 Hz frequency current noise measurements for two T-HEMTs (heterostructure HEMT D).

## SUMMARY

1. Thin AlGa<sub>N</sub>/Ga<sub>N</sub> on SiC heterostructure without thick Ga<sub>N</sub> buffer layers exhibits the 2DEG density up to  $1.0 \times 10^{13} \text{ cm}^{-2}$ , mobility up to  $1.0 \times 10^4 \text{ cm}^2 \text{ V}^{-1} \text{ s}^{-1}$ , breakdown field up to 0.8 MV/cm, which all allow to achieve good performance of HEMT-based devices. Results show that a thin heterostructure design does not compromise the quality of the HEMT structure which is suitable for development of devices with improved thermal dissipation and HEMTs with RF performance of  $f_T \times L_G = 6.7 \text{ GHz} \times \mu\text{m}$ .
2. A quaternary lattice-matched InAlGa<sub>N</sub> barrier layer of only 9 nm thickness was developed for Ga<sub>N</sub>-based HEMT structures. A detailed analysis of the structural, morphological, optical, and electrical properties revealed the composition of the barrier layer to be  $16.5 \pm 0.2\%$  of In,  $77.5 \pm 0.2\%$  of Al, and 6% of Ga. The thermally stable density of the 2DEG was experimentally confirmed to be of  $1.2 \times 10^{13} \text{ cm}^{-2}$ . The fabricated SBDs demonstrated the pinch-off voltage values to be of  $-1.74 \text{ V}$  and breakdown field to be 0.4 MV/cm for this heterostructure. The HEMTs fabricated of this heterostructure were tested both in DC and RF regimes demonstrating as good performance as that of typical AlGa<sub>N</sub>/Ga<sub>N</sub> HEMTs.
3. The effective trap density in various AlGa<sub>N</sub>/Ga<sub>N</sub> HEMTs was extracted from the low frequency noise measurement demonstrating values to be below  $10^{19} \text{ eV}^{-1} \text{ cm}^{-3}$ . It was found that the high effective trap density correlates with the data of SIMS and THz electroluminescence spectroscopies showing higher concentration of uncompensated donors. The effective trap density for AlGa<sub>N</sub>/Ga<sub>N</sub> on SiC heterostructure without Ga<sub>N</sub> buffer layers was found below the level of  $10^{19} \text{ eV}^{-1} \text{ cm}^{-3}$ , which was similar to trap densities in heterostructures grown on thick Ga<sub>N</sub>:C buffers.



## 2.2. PERFORMANCE OF AlGa<sub>N</sub>/Ga<sub>N</sub> HEMT STRUCTURES UNDER HIGH ELECTRIC FIELD AND CURRENT DENSITY

This chapter covers the effects in conductive channels of the AlGa<sub>N</sub>/Ga<sub>N</sub> HEMT structures being operated under high current densities and electric fields. Investigation of charge carrier heating in 2DEG and Ohmic contact layers at high currents [P4] is covered in chapter 2.2.1.

Shortage of THz detectors operating with high-sensitivity at the room-temperature is often solved by semiconductor-based technologies [55], [170]. As discussed in the introduction, quite a few types of THz detectors are made using AlGa<sub>N</sub>/Ga<sub>N</sub> HEMT structures. While the best responsivity, NEP are achieved for TeraFETs, their fabrication requires advanced fab. On other hand, the THz detectors based on hot-electron effects are attractive due to their high sensitivity in broadband spectrum range and fast response time [171]–[173]. Another type of THz detectors is based on electron heating in the vicinity of apex area of bow-tie (BT) diodes. They exhibit fast response time in sub-nanosecond range, also are robust, resistant to ESD and don't require high resolution lithography. Historically, one of the drawbacks is comparatively low responsivity, when compared to TeraFETs or THz antenna coupled microbolometers. In chapters 2.2.2 and 2.2.3 the THz BT diodes and BT bolometers were developed of AlGa<sub>N</sub>/Ga<sub>N</sub> HEMT structure observing electron heating effects in Ohmic contact layer and in 2DEG layer, respectively. On the other hand, electron heating effects were also observed in Ohmic contact and *n*-Ga<sub>N</sub> layers under high current density, reporting findings elsewhere [P10] but not in the thesis.

### 2.2.1. Self-heating of electric contact resistance and 2DEG layer resistance

The self-heating effects of annealed Ti/Al/Ni/Au Ohmic contact resistance and 2DEG resistance in AlGa<sub>N</sub>/Ga<sub>N</sub> HEMT structures were investigated under strong electric fields [P4]. The experimental results revealed that the electron heating in ohmic contact layers dominate over the electrical conductivity (mobility) change of 2DEG with the increase of current density and electric field. The effects were studied measuring the resistance of rectangular shape TLM resistor samples fabricated of AlGa<sub>N</sub>/Ga<sub>N</sub> HEMT structures with annealed Ohmic contacts.

The HEMT, operating as a power amplifier or as a switch, dissipates the electric power in the conductive channel [174] and contacts [175] and at high

current densities, demonstrating the research importance of electric contact properties for example for transistor reliability tests [176], [177]. Ohmic contact resistance  $R_c$  and channel resistance  $R_{ch}$  for AlGaIn/GaN HEMT structures (HEMT C and HEMT E) were measured using 100 ns pulses in low-repetition rate ( $\sim 10^{-5}$ ) setup (Dr. Emilis Šermukšnis, FTMC, Vilnius, Lithuania). Due to geometry of TLM used, the spatial distribution of the electric fields is not trivial, therefore data was analyzed in respect to current density. The measured total resistance dependence on the current for different channel lengths for the heterostructure HEMT E is shown in Figure 16a. At higher fields I-V nonlinearity was observed and this increase of total resistance. Usually, such changes were explained in the literature as the increase of  $R_{ch}$ , due to electron mobility decrease via efficient electron-phonon scattering in GaN, while assuming that  $R_c$  is a constant and independent on current density. This should work for selected cases  $R_c \ll R_{ch}$  which should allow to neglect the impact of  $R_c$  [178], [179]. While  $R_c$  dependence on temperature has been investigated previously [178], [180], [181], however the investigation of the Ohmic contact self-heating and dependence on the current density or electric field were investigated first time in the work [P4].

Figure 16a shows that  $R_T$  weakly depends on the current and obey Ohm's law, up to values of 50-100 mA (the electric field - up to 1-2 kV/cm). Above  $\sim 100$  mA (2 kV/cm) a deviation from Ohm's law starts to be visible. Furthermore, the resistance ratio between shortest and longest channel (6  $\mu\text{m}$  and 65  $\mu\text{m}$ ) at low currents was approximately 6.5, while at current of 270 mA, this ratio was found to drop to  $\sim 4.8$ , indicating a steeper increase of total resistance for short channel sample. Figure 16b demonstrates the increase

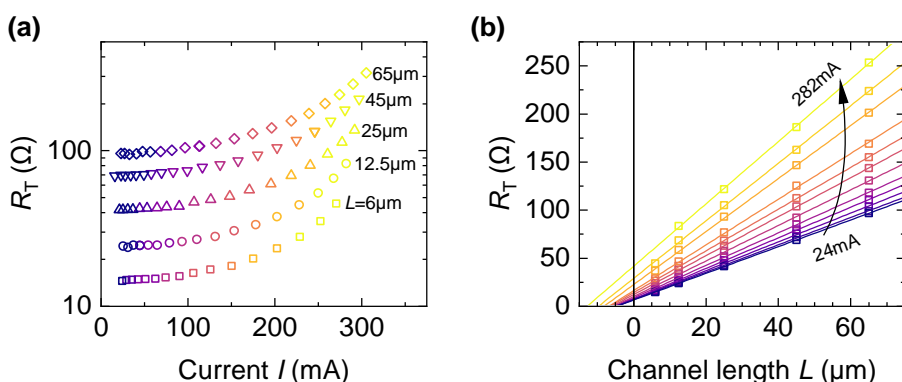


Figure 16. TLM measurements in a wide current range for one of the studied HEMT structures – HEMT E. (a) Dependence of the total resistance  $R_T$  on the current  $I$  for the different channel lengths  $L$  from 6  $\mu\text{m}$  to 65  $\mu\text{m}$ . (b) TLM graph from the data in panel (a).

Table 2.2 Low-field contact resistance  $R_{c0}$  and 2DEG sheet resistance  $R_{sh0}$  extracted from TLM measurements

Heterostructure sample	$R_{c0}$ ( $\Omega$ mm)	$R_{sh0}$ ( $\Omega$ /sq.)
HEMT E	0.8	350
HEMT C-1	1.1	510
HEMT C-2	2.5	520

in both  $R_c$  and  $R_{sh}$  values with the current increase, which is seen as the rise of the  $L=0$  intercept point and the increase in slope angle of  $R_T(I)$  lines. Current-dependent contact resistance was defined as  $R_c(I) = R_{c0} + \Delta R_c(I)$ , where  $R_{c0}$  is the standard low-field contact resistance extracted from TLM measurements and the  $\Delta R_c(I)$  is the current dependent contact resistance. Using analogous data to the HEMT E one in Figure 16, more AlGaIn/GaN HEMT structure samples (HEMT C-1 and HEMT C-2) with different 2DEG sheet and Ohmic contact resistances were investigated. The absolute values of  $R_{c0}$  and  $R_{sh0}$  for investigated samples are summarized in Table 2.2. The results of the contact resistance  $R_c$  and its current dependent resistance  $\Delta R_c$  are shown in Figure 17. The results were normalized to the conductive channel width  $W=250 \mu\text{m}$ . As seen in Figure 17a at low current densities Ohm's law holds and  $R_c$  weakly depends on the current. For the sample with smallest  $R_{c0}$  (black

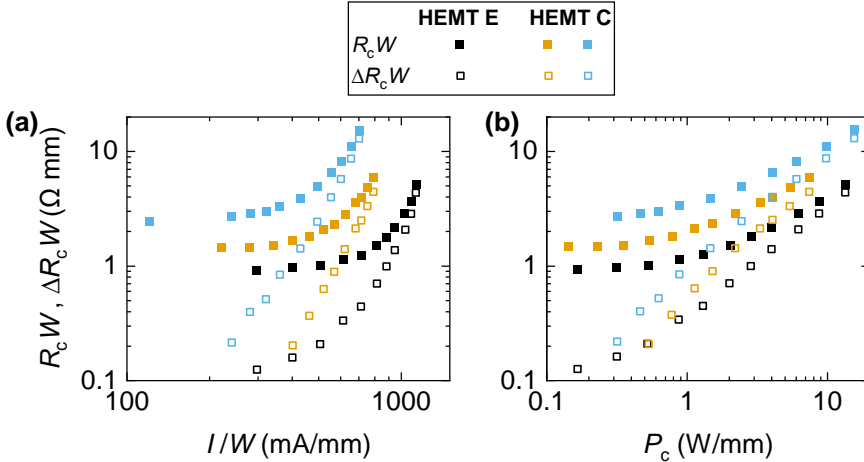


Figure 17. The dependence of the normalized contact resistance  $R_c W$  (solid symbols) and normalized contact resistance change  $\Delta R_c W$  (empty symbols) on: (a) current density  $I/W$  and (b) dissipated electric power density in contacts  $P_c$ . Three TLM samples from two different heterostructures HEMT E and HEMT C.

rectangles – heterostructure HEMT E), the increase of  $R_c$  is slower. In the range of currents used,  $R_c$  increases more than six times at current densities above 1 A/mm for sample with lowest  $R_{c0}$ , while for the two samples with higher  $R_{c0}$  same increase is observed at lower current density of  $\sim 0.6$  A/mm. Overall, nonlinear  $R_c(I)$  dependence was found with a slope of  $\Delta R_c \propto I^5$  or even steeper in the range of highest currents applied. This result means that even for very small  $R_{c0}$  contacts at high currents noticeable increase of  $R_c$  was found. The dependence of  $R_c$  and  $\Delta R_c$  on electric power density  $P_c = 2R_c I^2/W$  dissipated in the contacts was investigated. The results are shown in Figure 17b. The slopes of  $\Delta R_c \propto P_c$  are seen in a wide range of power values.

The dependence of  $R_c$  and  $R_{sh}$  at different currents was investigated to estimate how self-heating affects each  $R_c$  and  $R_{sh}$ . The results are shown in Figure 18a. The normalized characteristics of  $R_c/R_{c0}$  vs  $R_{ch}/R_{ch0}$  were also found. The results are shown in Figure 18b. At lower currents  $R_c$  is proportional to  $R_{sh}$ , however when electron mobility in 2DEG layer drops with the increase of electric field to level that is seen as the increase  $R_{sh} \approx 600 \Omega/\text{sq.}$ , the electron heating in contact layers becomes significant resulting in much faster change of the  $R_c$  resistance with further current increase. The same was observed for all three samples fabricated of various AlGaIn/GaN HEMT structures.

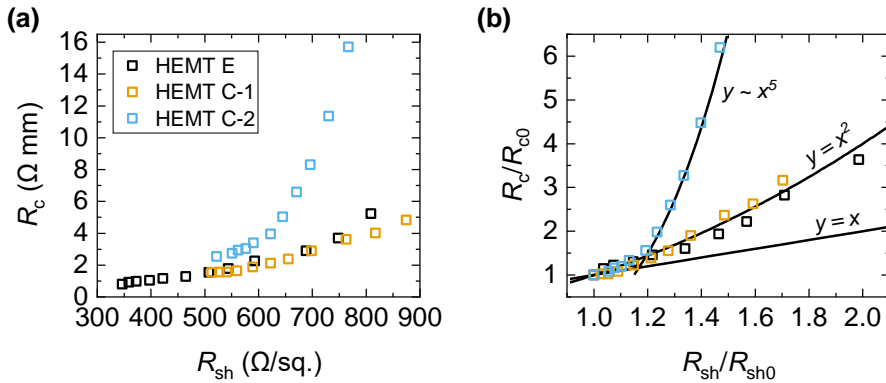


Figure 18. Contact resistance  $R_c$  and 2DEG sheet resistance  $R_{sh}$  values measured at different current densities for three AlGaIn/GaN HEMT structure samples (see Table 2.2). (a) Absolute and (b) normalized contact resistance  $R_c$  vs. 2DEG sheet resistance  $R_{sh}$  values for the respective current densities. Lines illustrate  $y=x$ ,  $y=x^2$  and  $y \sim x^5$  slopes as a guide to eye.

### 2.2.2. Bow-tie diode THz sensor

In this chapter research and development of the bow-tie (BT) diode THz sensors based on electron heating effects in shaped Ohmic contact layer with the effective THz detection in zero-bias mode [P5] are presented.

BT diodes were suggested as planar structures of  $n-n^+$ -GaAs shaped asymmetrically in a bow-tie antenna for the detection of electromagnetic waves in the GHz and lower part of THz frequency bands [182]. One of studied approaches to improve the BT diode sensitivity was to use heterostructures with 2DEG, offering significantly higher electron mobility than that achieved in epitaxial GaAs layers [183], [184]. Compared to previously studied GaAs-material, GaN-based system has an advantage of a higher electron densities in the 2DEG channel (up to  $\sim 2 \times 10^{13} \text{ cm}^{-2}$ ) and stable ohmic contact with specific resistance of  $\sim 10^{-5}$ - $10^{-7} \Omega \text{ cm}^2$ . Additionally, 2DEG in AlGaIn/GaN heterostructures and good ohmic contacts to 2DEG layer are obtained without heavy doping of semiconductor layers. All these features allow simplify the result interpretation of THz signals caused by carrier heating in the asymmetrically shaped ohmic contact and semiconductor material layers.

The BT diodes were developed of AlGaIn/GaN HEMT structure HEMT C with high electron mobility being at the room temperature of

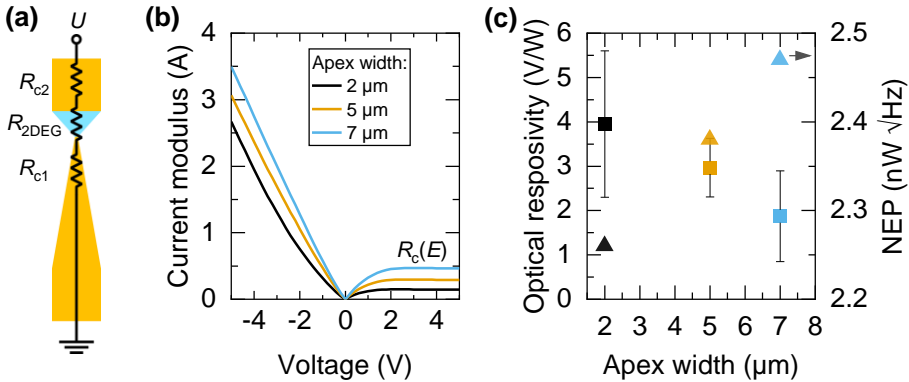


Figure 19. (a) Schematic view of BT diode with equivalent scheme. Gold parts  $R_{c1}$  and  $R_{c2}$  show the two Ohmic electrodes with their resistances, while blue trapezoid is the shaped 2DEG area with resistance  $R_{2DEG}$ . (b) Current–voltage characteristics of the fabricated BT diodes with different width of the apex demonstrating the resistance of metallized leaf’s strong dependence ( $R_c(E)$ ) on applied electric field. (c) Measured 150 GHz optical responsivity (squares) and calculated NEP values (triangles) dependence on the apex width.

$(1.9 \pm 0.2) \times 10^3 \text{ cm}^2 \text{ V}^{-1} \text{ s}^{-1}$ . The processed Ohmic contact exhibited resistance of  $1 \ \Omega \ \text{mm}$ . The design of BT diode and its equivalent scheme is shown in Figure 19a. This is a two-terminal (Ohmic) device with one of the contacts shaped as trapezoid and 2DEG layer in between. Coupled electric field of the incoming THz radiation is concentrated in the vicinity of the trapezoid base called apex by metallized BT antenna leaf. In general case, the detected THz signal by BT antenna originates from electron heating in the metallized leaf (BT diode) and from electron heating in the 2DEG layer (bolometric BT sensor).

The DC-IV characteristics for AlGaIn/GaN HEMT structure-based BT diodes were measured at room temperature. The results are shown in Figure 19b. The resistance of the BT diode was found to be sensitive to the polarity and absolute value of applied electric field, demonstrating an obvious asymmetry of IV characteristics. The  $R_c(E)$  was more pronounced with the decrease of apex width. The responsivity at 150 GHz frequency was obtained for BT diodes with various apex sizes. The results are shown in Figure 19c. The optical responsivity was calculated by dividing the induced voltage over the whole power of THz beam. The spectral characteristics of BT antenna were investigated in THz frequency domain system (Dr. Dalius Seliuta, FTMC, Vilnius, Lithuania). The results are shown in Figure 20. The results indicate that the resonance frequency of BT antenna to be at 150 GHz. The response speed of BT diodes was measured to be in sub-nanosecond range, and it was similar to the commercial Schottky barrier diodes.

Several sets of BT diodes with different apex widths from  $17 \ \mu\text{m}$  down to  $0.4 \ \mu\text{m}$  were developed and investigated at the close to resonance frequency of BT antenna in order to obtain more data for statistical analysis. The optical responsivity dependence on the resistance and on the apex width of BT diode

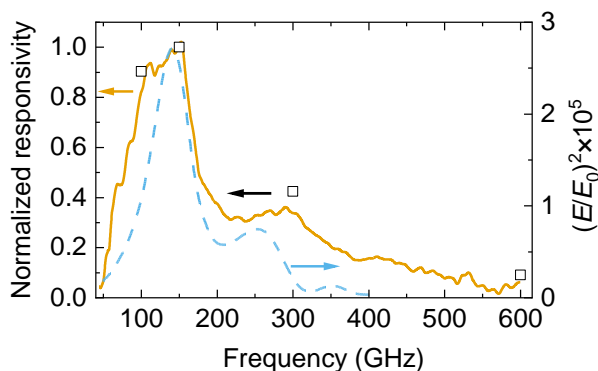


Figure 20. Responsivity of BT diode with  $d = 2 \ \mu\text{m}$ . THz frequency domain spectroscopy data (solid line), optical responsivity at specific frequencies (squares), and calculated electric field enhancement (dashed line).

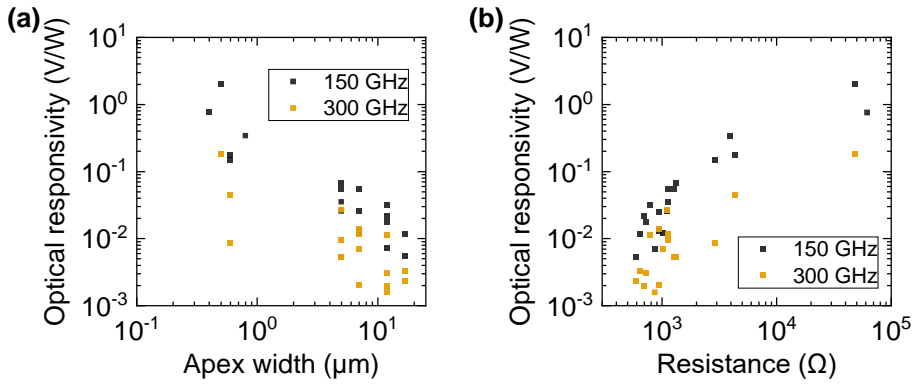


Figure 21. Dependence of optical responsivity at 150 GHz and 300 GHz frequencies on: (a) BT apex width, (b) BT resistance.

were found. The results are shown in Figure 21. It demonstrates a strong correlation between the resistance and the responsivity values of the BT diode. The responsivity of the BT diode scales nonlinearly with its resistance at values larger than approximately 1000  $\Omega$ . Thus, in applications which require low NEP values, tapering the diode apex below a few microns is ineffective.

### 2.2.3. Bow-tie bolometric THz sensor

In this chapter research and development of the bolometric BT sensors based on electron heating effects in 2DEG layer [K11] is presented.

The same AlGaIn/GaN HEMT structure HEMT C was also used to develop bolometric BT sensors based on electron heating effects in 2DEG layer. The Ohmic contact resistance of processed samples was characterized to be of 0.4  $\Omega$  mm, value of which was the lowest compared to all GaN-based HEMT structure samples discussed in the thesis. The design of bolometric sensor shape was kept the same as for BT diode (see Figure 19a). DC I-Vs of the fabricated detectors with different apex widths  $d$  were measured at the 300 K and 80 K temperatures. The results at room temperature are shown in Figure 22. Overall, these detectors exhibited almost symmetric IV characteristics with asymmetry factor below 2% (see Figure 22a). Narrowing of the apex width from 12  $\mu\text{m}$  to 5  $\mu\text{m}$  increased detector resistance from 1.1 to 2.4 k $\Omega$  (see Figure 22b). Furthermore, symmetric IVs indicate that the carrier heating in metallized BT antenna leaf with applied electric field was mitigated. This allows to directly see the heating of resistance of active 2DEG area. Highest resistance modulation was obtained for the devices with narrowest apexes width, value of which was 5  $\mu\text{m}$ . (see Figure 22b).

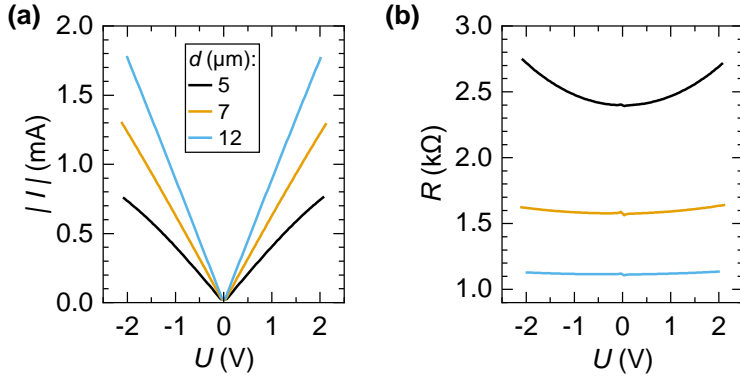


Figure 22. DC current-voltage characterization of the detectors with different apex widths  $d$  at the room temperature. (a) Current modulus vs applied voltage. (b) Resistance vs applied voltage.

The electron heating in 2DEG layers was experimentally investigated, using 20 ns pulsed low repetition rate measurement setup at the temperature of 300 K (Dr. Liudvikas Subačius, FTMC, Vilnius, Lithuania). Two types of devices (shown in Figure 23a) were selected on the same die: 50  $\mu\text{m}$  long and 100  $\mu\text{m}$  wide rectangular shape resistor and trapezoidal (BT) shape resistor with narrowest apex width of 5  $\mu\text{m}$  and length of 50  $\mu\text{m}$ . The resistance increase over low-field resistance value  $R(E)/R(0)$  was investigated. The results are shown in Figure 23b. The use of short 20 ns duration and low repetition rate pulses allowed probing of electron conductivity under high electric fields without significant lattice heating. The electric field was assumed to be uniformly distributed in the rectangular shape 2DEG resistor and its value was calculated dividing applied voltage by the contact spacing of 50  $\mu\text{m}$ . The resistance increase with electric field for this sample is shown in Figure 23b by red squares. The similar measurements were performed on BT resistor (sensor) with 5  $\mu\text{m}$  apex width. The results as a function of voltage  $R(U)/R(0)$  are shown in Figure 23b by black triangles. The voltage-electric field matching coefficient  $k=(1.1\pm 0.1)\times 10^3$  was obtained by matching the BT resistance  $R(U)/R(0)$  characteristic to the rectangular 2DEG sample  $R(E)/R(0)$  data. Performing the same matching of the BT resistance  $R(U)/R(0)$  characteristic for other apex width designs, voltage-to-field matching ratios of  $k_{7\mu\text{m}}=(7.9\pm 0.1)\times 10^2$  and  $k_{12\mu\text{m}}=(5.2\pm 0.1)\times 10^2$  were obtained.



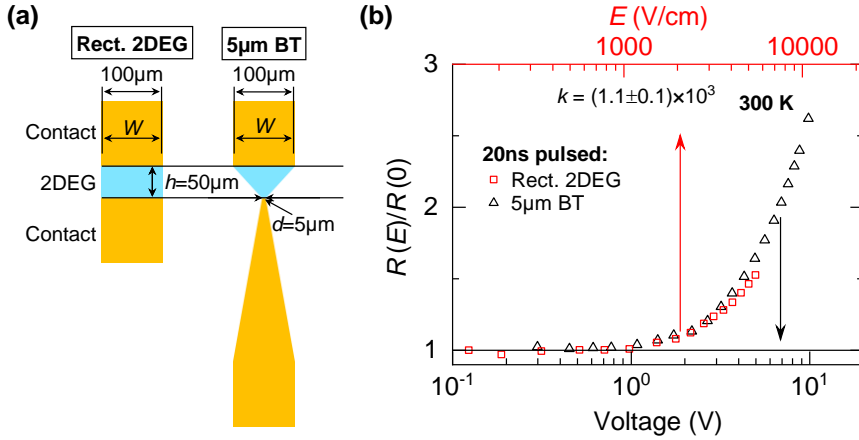


Figure 23. Resistance increase  $R(E)/R(0)$  dependence on electric field (red data)/voltage (black data) at the temperature of 300 K. (a) Schematic of investigated samples: rectangular  $50 \times 100 \mu\text{m}$  2DEG sample (red squares) and BT detector with apex width of  $5 \mu\text{m}$  (black triangles). (b) The 20 ns pulsed low repetition rate for rectangular 2DEG (red squares) is plotted as a function on electric field, while BT data (black triangles) as a function of voltage. Electric field was calculated for rectangular 2DEG data dividing applied voltage by contact spacing of  $50 \mu\text{m}$ . Coefficient  $k = (1.1 \pm 0.1) \times 10^3$  was used to match the rectangular 2DEG  $E$ -field dependent data to BT resistance voltage dependent data.

The total resistance of the BT device is assumed to be a sum of the contact  $R_c$  and the trapezoid 2DEG layer  $R_{2\text{DEG}}$  resistances:

$$R = R_c + R_{2\text{DEG}}, \quad (19)$$

$$R_{2\text{DEG}} = R_{\text{sh}} \frac{h}{W-d} \ln \frac{W}{d}, \quad (20)$$

where  $h$  is the height of the trapezoid (separation between two antenna contacts,  $50 \mu\text{m}$ ),  $d$  is the apex width and  $W$  is the other trapezoid base ( $100 \mu\text{m}$ ). In the case of BT bolometers using experimental low-field resistance data  $< 0.1 \text{ V}$  and device geometry parameters revealed that the influence of the contact resistance is insignificant. It is worth nothing that Eq.(20) is used only for relatively large shaping angles of the apex,  $d$  is a few microns and larger. Data further is presented as a function of voltage drop on the 2DEG resistance  $R_{2\text{DEG}}(U_{2\text{DEG}})$ .

The optical responsivity of the bolometric detectors in zero-bias and biased regimes at fixed frequencies of 150, 307 and 600 GHz was measured at room temperature. The results are shown in Figure 24. The optical responsivity shown in Figure 24a is higher for detectors with a narrow apex width. This is expected due to THz electric field being concentrated into smaller area.

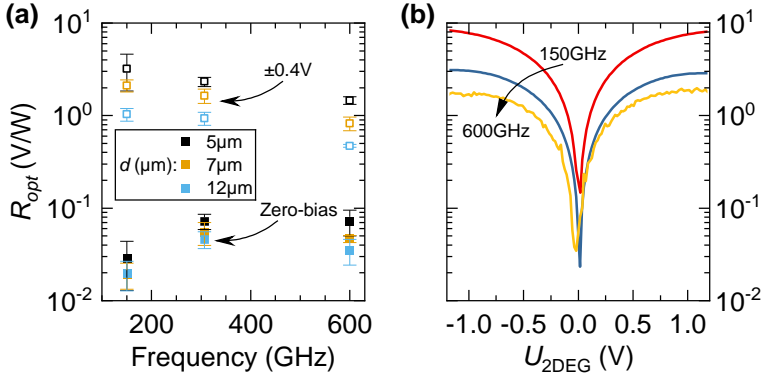


Figure 24. Room temperature optical responsivity ( $R_{opt}$ ) for BT bolometers at the room temperature. (a) Zero-bias and biased optical responsivity at 150 GHz for apex widths  $d$ : black squares – 5  $\mu\text{m}$ , brown squares – 7  $\mu\text{m}$ , blue squares – 12  $\mu\text{m}$ . (b) Bias dependent optical responsivity for detector with  $d = 5 \mu\text{m}$  at frequencies of 150 (red line), 307 (blue line) and 600 GHz (yellow line).

Compared to BT detectors which have obvious IV asymmetry (Figure 19b,c), here zero-bias responsivity is overall two orders of magnitude lower. The dependence of responsivity on bias voltage shown for one BT detector with apex width  $d = 5 \mu\text{m}$  is shown in Figure 24b. Applying external bias allowed to increase the responsivity by 13 dB or more for all apex designs and detection frequencies to a comparable level of detectors with obvious IV asymmetry (Figure 19b,c). Furthermore, monotonic and symmetric growth of the  $R_{opt}$  with applied bias was also observed having trend similar to current-voltage data shown in Figure 22a.

The BT bolometers were mounted in liquid nitrogen cryostat and illuminated from the substrate side through high-density polyethylene optical window to investigate properties at 80 K and 300 K. At 80 K current-voltage characteristics exhibit much stronger non-linearity (see [K11]). The IV demonstrates saturation behavior of charge current at voltages applied to the bolometer above  $\pm 1\text{ V}$ . This is a result of a much steeper change in the resistivity of the detector at 80 K. Placing the cryostat with the bolometers in the quasi-optical setup, optical responsivity was investigated at temperatures of 300 K and 80 K. Upon cooling the devices from 300 K to 80 K, the zero-bias responsivity increased by 9.2 times. The normalized results of biased responsivity at 300 K and 80 K are shown in Figure 25. At the temperature of 300 K (Figure 24b) the responsivity grows monotonically in the biasing range, but at 80 K different behavior is observed: much steeper growth is initially in the region approximately below  $U_{2DEG} = \pm 0.4\text{ V}$ , and afterwards responsivity

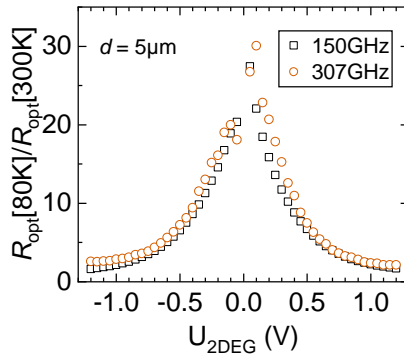


Figure 25. Normalized biased responsivity  $R_{\text{opt}}$  of the BT diode ( $d = 5 \mu\text{m}$ ) at 80 K versus 295 K temperatures measured at 150 GHz (solid line) and 307 GHz (dashed line).

decreases (see Figure 25), due to sensitive dependence of electron mobility on electric field applied.

## SUMMARY

1. Self-heating of annealed Ti/Al/Ni/Au contact resistance together with 2DEG channel resistance was observed for AlGaIn/GaN and AlGaIn/AlN/GaN HEMT structures possessing specific resistance and 2DEG sheet resistance in the range of 0.8-2.5  $\Omega$  mm and 350-520  $\Omega$ /sq., respectively. The increase of up to six times in contact resistance was found as the current density approached  $\sim 0.6$  A/mm. It was found that the change in contact resistance from its low-field value is proportional to the electric power dissipated in the contacts. The increase of contact resistance with charge current density was interpreted as electron heating in layers of the ohmic contact to 2DEG in AlGaIn/GaN HEMT structures.
2. The AlGaIn/GaN based BT diodes were developed for sensitive THz detection without biasing at 295 K, identifying the electron heating effects in contact layers as main mechanism for asymmetric IV characteristics and THz detection. The performance of BT diodes was investigated at several frequencies, demonstrating optimal operation at 150 GHz fundamental frequency of BT antenna with the responsivity and NEP values to be up to 4 V/W and down to 2 nW/ $\sqrt{\text{Hz}}$ , respectively. The responsivity of the BT diodes scaled nonlinearly with its resistance, demonstrating that the tapering of the diode apex below the range of a few micrometers is ineffective in applications which require low NEP values.
3. BT antenna coupled bolometer of 2DEG in AlGaIn/GaN heterostructure were developed for fast THz detection in wide spectrum range. Such sensors possessed symmetric IV characteristics resulting in significantly lower zero-bias responsivity values of THz detection even at resonance frequency of the BT antenna. The sensitivity was increased by 13 dB or more applying external voltage. The symmetric increase of responsivity with the applied external voltage was observed for all apex widths and detection frequencies. Cooling the detectors down to 80 K allowed to increase the zero-bias responsivity by 9.2 times and increased non-linearity of the I-V characteristics. This resulted in an increased biased responsivity in the region up to  $\pm 0.4$  V.

### 2.3. GRAPHENE

In this chapter, graphene transfer, cleaning, and patterning techniques for the CVD graphene on Si- and GaN-based semiconductors were proposed aiming minimize chemical doping and maintain high carrier mobility. The new method for PMMA cleaning off wet-transferred CVD graphene was developed [P6]. Furthermore, a method to fabricate graphene devices without exposure of the graphene to chemical dopants was developed, registering European patent application [P7]. The first results of processing and performance of graphene on AlGaIn/GaN HEMT structures are also discussed in the thesis.

CVD is among the most utilized synthesis techniques for the manufacture of single-layer graphene on a large substrate. However, to fabricate graphene-based electronic or optoelectronic devices usually require substrates other than the transition metals used for growth. Additional processing is needed to transfer CVD graphene to the application-compatible substrate, which includes dissolving the metal substrate via a wet etching process to release graphene. As free-standing graphene is fragile, typically, a supporting layer such as polymethyl methacrylate (PMMA) is used, which requires removal after successful transfer process. However, because PMMA interacts strongly with graphene, its complete removal from graphene is a very demanding task [185]–[189]. Since graphene is extremely sensitive to adsorbates and molecules in contact with its surface, the removal of the PMMA residues is crucial for improving the electric, optic, and optoelectronic characteristics of graphene devices.

The DUV exposure (254 nm) modifies PMMA: long polymer chains break and aldehyde/ketone type compounds are formed, making exposed PMMA more soluble. We propose to use mixture of water and alcohol, in particular isopropyl alcohol, in molar ratio of 1:1. A detailed discussion of changes in the PMMA during DUV exposure and mechanism of DUV-exposed PMMA removal was presented elsewhere [P6]. This method was used for graphene wet transfer onto high resistivity Si and AlGaIn/GaN HEMT structure HEMT E substrates. Method schematically is shown in Figure 3. The test samples were processed to compare the graphene performance after PMMA removal by new method and using standard approaches. The PMMA was also removed with common solvents in literature: acetone and chloroform. A total of five samples of graphene on Si were prepared: three samples with DUV exposure and removal in aqueous IPA, plus one sample each from PMMA removal in acetone and chloroform. Initial check of PMMA removal with SEM for all of

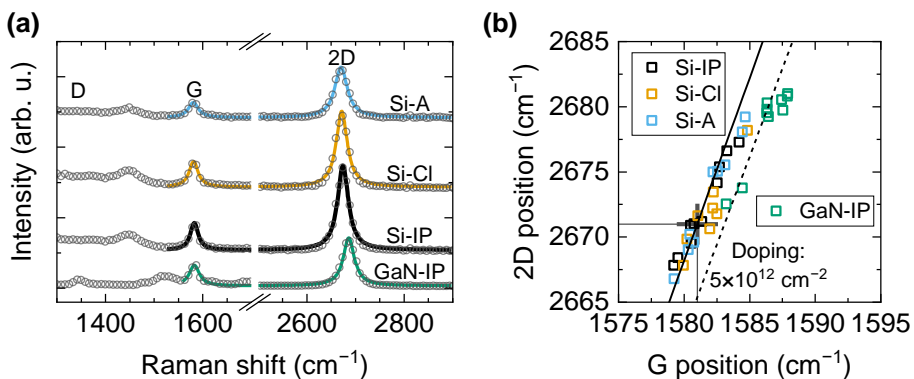


Figure 26. Raman measurements of wet-transferred CVD graphene after PMMA removal: (a) Experimental Raman spectra (circles) and Lorentz fits (lines) of G and 2D peaks for samples with graphene transferred to Si and AlGaN/GaN heterostructure. (b) Correlation analysis of G and 2D peak positions for graphene samples under study: 3 DUV method samples (black squares), chloroform sample (yellow squares), acetone sample (blue squares) and DUV method graphene on AlGaN/GaN HEMT structure HEMT E (green squares). Solid line demonstrates the G and 2D line frequencies correlation dependence for undoped graphene under biaxial strain. Dashed line shows correlation dependency for  $5 \times 10^{12} \text{ cm}^{-2}$  *p*-doped graphene under biaxial strain.

samples, revealed that samples processed with chloroform had highest number of PMMA residuals, while DUV and acetone processed samples showed similarly clean surfaces.

To verify quality of the transferred graphene using different PMMA removal methods Raman spectra were investigated. The spectra for selected samples processed using DUV (IP), acetone (A) and chloroform (Cl) methods are shown in Figure 26a. Raman spectroscopy statistics are given in Table 1.3. Overall, the samples on Si substrate with PMMA removed new method (Si-IP) demonstrated high 2D/G intensity ratio of  $2.9 \pm 0.2$  and had low FWHM of 2D line which was below  $30 \text{ cm}^{-1}$ . Both parameter values indicate good quality of the graphene. The samples prepared using chloroform (Si-Cl) and acetone (Si-A) also exhibited quite high 2D/G intensity ratio ( $>2.4$ ) and slightly bigger FWHM of 2D line ( $\geq 30 \text{ cm}^{-1}$ ). The Raman spectra of graphene on AlGaN/GaN HEMT structures with PMMA removed using new method (GaN-IP) were also investigated. The results are shown in Figure 26 as “GaN-IP”. The FWHM of 2D line was found to be  $32 \pm 2 \text{ cm}^{-1}$  with 2D/G ratio of  $2.6 \pm 0.2$ . Overall, all graphene samples exhibited good quality with no significant defect (D) peak around  $1350 \text{ cm}^{-1}$ , high 2D/G ratio ( $>2.4$ ) and narrow 2D peaks ( $\leq 32 \text{ cm}^{-1}$ ).

The correlational position analysis between 2D and G peaks allows to investigate strain and doping in the graphene films [190], [191]. It was performed using precise positions of G and 2D lines from the measured Raman spectra, by performing Lorentz fitting for all graphene samples. This analysis method is based on the fact that theoretically free-standing undoped graphene has  $G_0$  and  $2D_0$  lines at 1581 and 2671  $\text{cm}^{-1}$  exactly. Under strain G and 2D points are dispersed along a line crossing the  $(G_0; 2D_0)$  point, while  $p$ -doping shifts the whole dispersion line to higher G line frequencies parallel to the undoped strain line. Experimental data points and the theoretical biaxial strain dispersion lines for undoped and doped cases are shown in Figure 26b. Comparing the experimental data point locations with respect to the theoretical doped dispersion lines, we see that all graphene samples are relatively low doped with free charge carrier density being below  $5 \times 10^{12} \text{ cm}^{-2}$  level.

The experimental transmission spectroscopy (THz-TDS and FTIR) was used to investigate charge carrier properties in graphene samples. Data for the acetone processed sample (Si-A) are shown in Figure 27a. The fitting of both THz-TDS and FTIR spectral regions allowed us to obtain reliable results. All data fit is shown in Figure 27a by thick black line. Figure 27b shows the effect on transmission signal by presence of graphene on the AlGaIn/GaN heterostructure sample. Transmission decreases in the frequency region up to 8 THz. To obtain charge carrier properties in the graphene, the transmission spectrum is fitted in the frequency range above 1 THz – outside region of 2DEG features. The absorption peak of zone folded transverse acoustical (TA) phonons in the 4H-SiC substrate which was used to grow AlGaIn/GaN HEMT structure, is observed at 7.9 THz frequency, as previously reported in Ref. [192].

The results for the different PMMA removal method samples processed during the same processing run are summarized in Table 1.4. Generally, relatively low doping ( $\leq 3 \times 10^{12} \text{ cm}^{-2}$ ) and moderate ( $\geq 2400 \text{ cm}^2 \text{ V}^{-1} \text{ s}^{-1}$ ) to high ( $> 5800 \text{ cm}^2 \text{ V}^{-1} \text{ s}^{-1}$ ) mobilities were achieved for free charge carriers in the wet-transferred CVD graphene. More precisely, the DUV samples (Si-IP) demonstrated the lowest unintentional doping of  $8 \times 10^{11} \text{ cm}^{-2}$  and high electron mobility of  $6910 \text{ cm}^2 \text{ V}^{-1} \text{ s}^{-1}$ . The graphene processed in the same way but on the AlGaIn/GaN HEMT structure (GaN-IP) exhibited the lowest sheet resistance of  $670 \text{ } \Omega/\text{sq.}$ , which is a result of free charge carrier density  $3.2 \times 10^{12} \text{ cm}^{-2}$  and mobility of  $2960 \text{ cm}^2 \text{ V}^{-1} \text{ s}^{-1}$ .

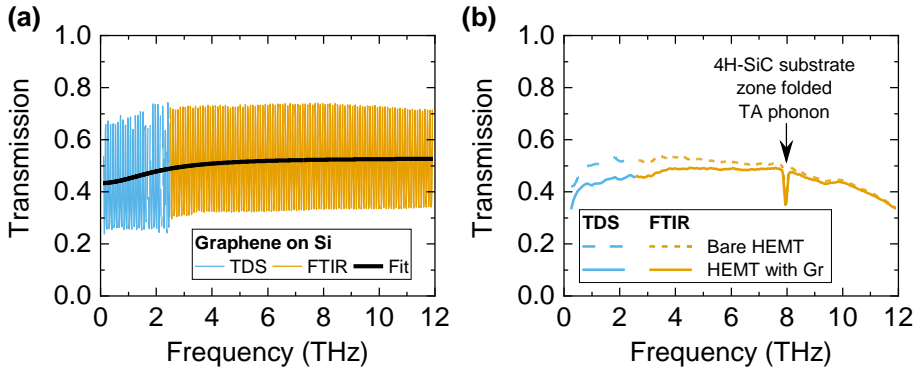


Figure 27. THz-TDS and FTIR transmission spectra for graphene samples. (a) Experimental spectra of graphene on high resistivity silicon substrate and the fit obtained using Drude conductivity. (b) Bare AlGaIn/GaN HEMT and graphene/AlGaIn/GaN HEMT spectra.

This achievement was interpreted by analysis of data in the literature for the case of graphene on AlGaIn/GaN HEMT structure. The donor surface states of the AlGaIn in close proximity to graphene [72] drastically affect the charge carrier mobility in the graphene via charged impurity scattering effect [193]. While there have been a lot of articles about graphene on GaN for device applications, such as Schottky contact [71]–[75], various sensors [76], [194], however the experimental charge carrier mobility characteristics have not been found in literature search by the author. Furthermore, charge carrier mobility extracted from THz spectroscopy can't be directly compared to mobility obtained by electrical measurements (field effect mobility, van der Pauw, micro four point probe). In these methods conductivity is affected by large scale surface defects such as grain, boundaries, wrinkles and bubbles [116], [195]. The parameters extracted from THz transmission spectroscopy represent statistical averages of any microscale properties over the THz beam [116], which in this case was 2-3 mm. So, the achieved value of  $\sim 3000 \text{ cm}^2 \text{ V}^{-1} \text{ s}^{-1}$  can be considered as high charge mobility for graphene on AlGaIn/GaN HEMT structures.

In principle any patterning method can be used for graphene, but it is important to note that any material in contact introduces doping to the graphene. Since substrate doping cannot be avoided in most graphene devices [196], [197], at least doping from other materials in contact (molecular doping) needs to be controlled or even avoided. Over the years, various patterning methods for graphene have been suggested, which allow to mitigate and avoid chemical doping. One of the most obvious solutions is to utilize the same PMMA layer used for wet transfer and for patterning in e-beam



lithography process [198]–[201]. The pattern writing with e-beam can be very precise, but it limits the speed of the lithographic process. Another approach to avoid any patterning media at all is patterning by the direct laser ablation (DLA) techniques [202]–[204]. Especially usage of fs-laser for DLA where pulse duration is shorter than the thermal relaxation time allows to minimize spatial heat diffusion effects and to prepare finer graphene structures [203], [205].

A method to use standard UV lithography for wet-transferred CVD graphene patterning without photoresist and graphene interaction was developed [P7]. The main idea relies on using specific patterned UV photoresist, as an intermediary DUV (254 nm) exposure mask to form etching mask for graphene out of PMMA. The whole processing procedure for already wet-transferred CVD graphene is shown in Figure 28. Utilizing the protective

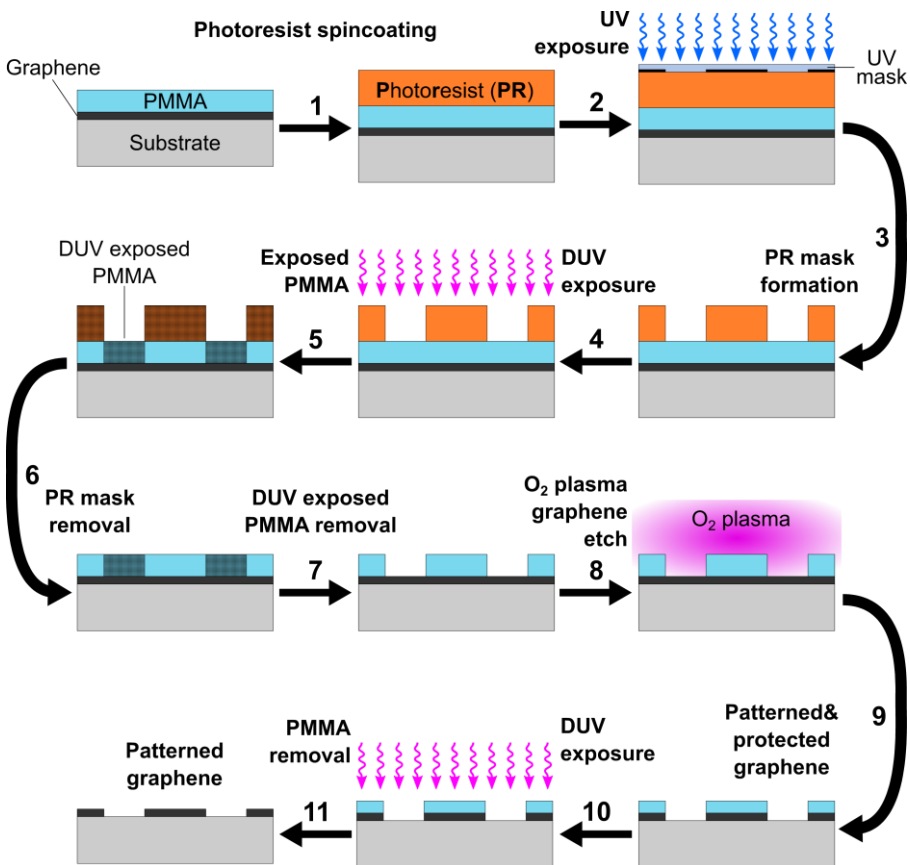


Figure 28. Processing steps for the proposed graphene patterning method using UV photolithography to avoid additional chemical doping.

PMMA layer, in the first step photoresist (PR) is spin coated and prepared for standard UV exposure. The PR needs to be specifically selected such that it also absorbs the 254 nm radiation and thus works as an intermediary DUV exposure mask for PMMA patterning (e.g. AZ MiR 701). Steps 2-3 cover the standard processing of the PR, namely UV exposure through mask aligner and development of PR to form the intermediary mask for PMMA. In step 4 the PMMA is exposed to 254 nm DUV irradiation using patterned PR mask to form soluble PMMA areas shown in darker color in step 5. Next, in step 6, the PR mask is removed by developing it, allowing to proceed with DUV exposed PMMA development in the aqueous IPA in step 7, as described in [P6]. The exposed areas of the graphene are etched using O<sub>2</sub> plasma (100 W RF power, 15 sccm O<sub>2</sub> flow at 0.5 mTorr chamber pressure) in step 8 and patterned PMMA protected graphene is obtained in step 9. Following steps 10-11 repeat the DUV exposure of PMMA and its removal using aqueous IPA [P6] to finally obtain patterned uncovered graphene. During the whole UV photolithography process the resultant graphene areas were protected by PMMA and were not in contact with the photoresist, its residuals and photoresist developer.

A fabricated THz bow-tie antenna of wet-transferred graphene on silicon oxide covered p-Si structured using this method is shown in Figure 29. Furthermore, this graphene patterning method was used for the fabrication of GR optics in the THz range which data were published in article [206] and PhD thesis [207]. In such a way applicability of the patterning method was also validated by other groups.

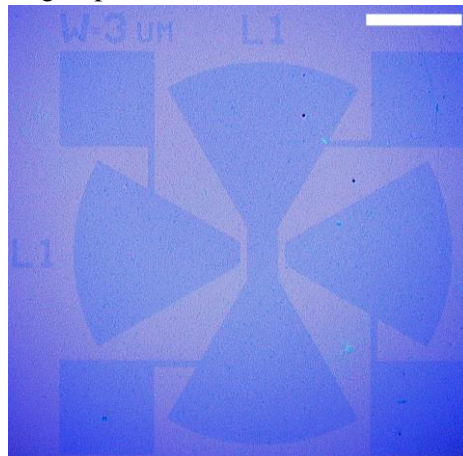


Figure 29. THz antenna coupled graphene, fabricated of wet-transferred CVD graphene on SiO<sub>2</sub>/Si wafer using new structuring method. Scale bar – 100  $\mu$ m.

## SUMMARY

1. A method was developed for the removal of PMMA supportive layer from the surface of CVD graphene wet transferred onto an application-compatible semiconductor substrates such as Si and AlGaIn/GaN HEMT structures. The high quality of graphene after the removal of PMMA by the new method confirmed by comprehensive research using SEM, AFM, and Raman spectroscopy. The mobility and density of charge carriers in DUV processed graphene samples were better than in graphene processed by typical solvents, demonstrating values up to  $6900 \text{ cm}^2/(\text{V}\cdot\text{s})$  and  $8 \times 10^{11} \text{ cm}^{-2}$ , respectively.
2. A method was developed to pattern CVD graphene using double purpose photoresist and standard UV lithography processes without contacting graphene by the photoresist and its residuals during all processing steps.

## 2.4. PYROLYTIC CARBON THIN-FILMS

Graphene has received wide attention due to its remarkable properties but as seen in Chapter 2.3, it remains a quite challenging material to work with. If end application does not require high charge carrier mobility values or active control of thin film properties, then graphitic films can be used. Pyrolytic carbon films are robust and have similar conductivity to graphene in a wide spectrum range [208], [209]. In this chapter alternative carbon-based conductive films – pyrolytic carbon thin-films, suitable for integration with GaN semiconductors are covered. The results of PPF [P8] and PyC [P9] and their possible applications in the THz range are discussed.

The characterization of PPFs made via pyrolysis of the negative e-beam resist AZ nLOF 2070, with the influence of cross-linking of the photoresist before pyrolyzation to the resultant electrical properties is investigated [P8].

The Raman spectra measured for PPF samples did not differ and consist of two broad bands at 1360 and 1600  $\text{cm}^{-1}$ , corresponding to D and G peaks of  $\text{sp}^2$  carbon. The ratio of intensities for G to D bands for films was the same at 1.1. Unlike graphene, graphitic films have very large width of these peaks ( $\sim 100 \text{ cm}^{-1}$ ) and indicate that the PPF is composed of small nanocrystalline graphene flakes with a size of  $\sim 4\text{-}5 \text{ nm}$ .

Using van der Pauw method, the sheet resistance of the films was found to be inversely proportional to film thickness, indicating that carrier scattering at the film surface does not affect the transport characteristics of the film. The results of sheet resistance measurements, film thicknesses, ratios of shrinkage from original thickness are given in Table 1.5.

Optical conductivity and carrier mobility in PPF films were investigated in the range of 0.2-1.5 THz. Measured and simulated THz transmission spectra are shown in Figure 30. Experimental spectra were fitted using transfer matrix method using:

$$\varepsilon(\omega) = \varepsilon_{\infty} + \frac{\sigma(\omega)}{i\omega\varepsilon_0}, \quad (21)$$

$$\sigma(\omega) = \frac{\sigma_{DC}}{1 - i\omega\tau}, \quad (22)$$

where  $\tau$  is the carrier momentum relaxation time,  $\omega$  is the angular frequency,  $\varepsilon(\omega)$  and  $\sigma(\omega)$  are the frequency dependent dielectric permittivity and conductivity,  $\varepsilon_0$  vacuum permittivity,  $\varepsilon_{\infty}$  silicon high frequency dielectric constant, and  $\sigma_{DC}$  is the DC conductivity of the material.

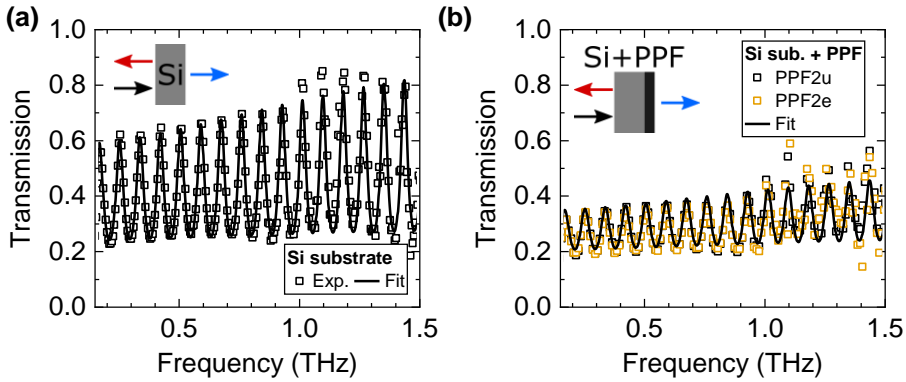


Figure 30. THz TDS results of PPF2e and PPF2u samples. (a) Experimental transmission spectrum of the Si wafer (squares) used and transfer matrix transmission fit (solid line). (b) Experimental transmission spectra of the PPF2u (black squares) and PPF2e (yellow squares) on Si wafer. Solid line shows fitted transmission using parameters described in the text.

First, the scattering time  $\tau$  for the Si substrate is obtained, by fitting the transmission spectrum of the bare Si substrate (Figure 30a) with  $\sigma_{DC} = 5 \text{ S/m}$ , as measured by the standard 4-probe van der Pauw method, and  $\epsilon_{\infty} = 11.6$ . The best fit was found at  $\tau = 0.15 \text{ ps}$ . The transmission of either PPFu or PPF<sub>e</sub> samples on Si substrate (Figure 30b) were found to be significantly lower than that of the bare silicon substrate. The best fit of PPF-covered wafer transmission spectra was obtained with the scattering time less than 10 fs and DC conductivity of  $1.3 \times 10^4 \text{ S/m}$ , which results in frequency independent conductivity in the frequency range of THz TDS system used. Data allows to

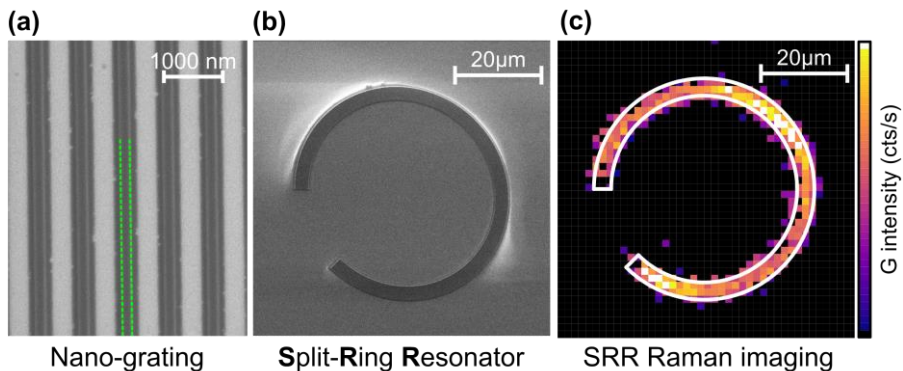


Figure 31. Some nano- and micro-structures for applications in THz range. (a) SEM image of periodic nano-grating. Green dashed lines mark 250 nm width PPF stripe. (b) SEM image of split-ring resonator (SRR) and its (c) Raman image of G peak intensity.

use  $\sigma_{DC}$  for designing circuits with PPF nano- or microelectrodes in the lower THz frequency range up to at least 1.5 THz.

To showcase some of the possible applications for PPFs, periodic structures were developed that are applicable in the THz range. The results are shown in Figure 31. The periodic nano-gratings and split-ring resonators (SRR) demonstrate the wide range of features easily achievable using PPF technology. The Raman mapping of the SRR demonstrates that structures made of PPF films have uniform signal and follow the fine features of SRR.

The conductive PyC films of even smaller 20 nm thickness were developed as an ultra-broadband absorber for various applications in THz-NIR range [P9]. Frequency independent absorption of 50% in thin film can be reached when sheet resistance is equal to half of the vacuum impedance at 377  $\Omega$ . Thin

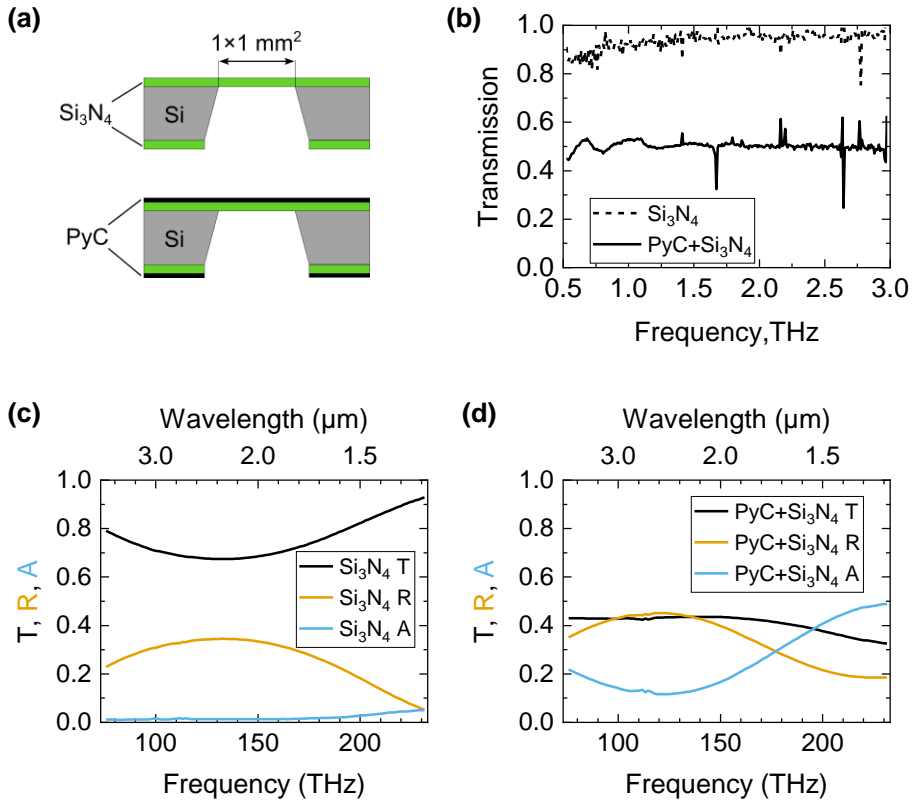


Figure 32. (a) Schematic cross-section view of the suspended Si<sub>3</sub>N<sub>4</sub> membrane without (bare) and with the PyC film (PyC/Si<sub>3</sub>N<sub>4</sub>) samples. (b) The THz transmission spectra of the bare 300 nm thick Si<sub>3</sub>N<sub>4</sub> membrane (blue dashed line) and with the 20 nm thick PyC film on it (blue solid line). Transmission, reflection, and absorption spectra of the same Si<sub>3</sub>N<sub>4</sub> membrane without (c) and with PyC film (d) measured in the NIR range.

metal films on dielectric membrane were historically used for this purpose, however, the thickness at which  $0.5 \times Z_0$  sheet resistance can be realized is small, just a tens of nanometers, due to high electrical conductivity [210]. Compared to metals, the conductivity of PyC is about two or three orders of magnitude smaller [78] and their use as absorber layers is not explored widely.

However, the conductivity is sufficient to make PyC film suitable as an absorber material for bolometers [211] with attractive ability to fabricate 3D structures [212].

The 20 nm PyC film was grown on both sides of a 250  $\mu\text{m}$  thick silicon wafer coated with 300 nm of high stress  $\text{Si}_3\text{N}_4$ . The as-grown PyC film exhibited sheet resistance of 600  $\Omega/\text{sq}$ . ( $\sigma_{\text{DC}}=8 \times 10^4 \text{ S/m}$ ). A  $1 \times 1 \text{ mm}^2$  PyC/ $\text{Si}_3\text{N}_4$  freestanding membrane was realized (NEST, CNR – Istituto Nanoscienze, Pisa Italy) with schematic view of the sample shown in Figure 32a. Raman spectra measured for as-grown PyC film and after whole processing did not change and were similar to PPF spectra with two broad peaks at the positions of  $1350 \text{ cm}^{-1}$  and  $1600 \text{ cm}^{-1}$  for D and G peaks, respectively. More details of Raman spectra analysis can be found elsewhere [P8].

Transmission, reflection, and absorption properties of the bare membrane of  $\text{Si}_3\text{N}_4$  without and with the PyC film (PyC/ $\text{Si}_3\text{N}_4$ ) were investigated in THz and NIR-MIR ranges. The THz transmission spectra are shown in Figure 32b. The bare  $\text{Si}_3\text{N}_4$  membrane exhibited higher than 90% transmission, while deposition of PyC layer reduced the transmission to a constant  $\sim 50\%$  in the whole spectrum range of measurement.

The transmission and reflection spectra of the same membrane without and with PyC film were investigated in the NIR range by micro-FTIR spectroscopy technique (NEST, CNR – Istituto Nanoscienze, Pisa Italy). The results are shown in Figure 32c and d. The absorption (blue lines) of the bare  $\text{Si}_3\text{N}_4$  membrane is almost 0 (Figure 32c), while for the PyC/ $\text{Si}_3\text{N}_4$  sample it varies from 0.1 to 0.5 in the spectrum range of measurement (Figure 32d).

The transfer matrix method was used to fit experimental data with the Drude-Lorentz model for PyC/ $\text{Si}_3\text{N}_4$  [213] and Lorentz model for the  $\text{Si}_3\text{N}_4$  membranes by using respective dielectric functions:

$$\varepsilon_{\text{PyC}}(\omega) = \varepsilon_{\infty} + A_T \frac{\omega_T}{\omega_T^2 - \omega^2 - i\omega\gamma_T} - \varepsilon_{\infty} \frac{4\pi\sigma_{\text{DC}}}{i\omega(1 - i\omega\tau)}, \quad (23)$$

$$\varepsilon_{\text{Si}_3\text{N}_4}(\omega) = \varepsilon_{\infty} + A_T \frac{\omega_T}{\omega_T^2 - \omega^2 - i\omega\gamma_T}. \quad (24)$$

In the PyC/ $\text{Si}_3\text{N}_4$  dielectric function eq.(23), the second term describes the contribution of the  $\pi$ - $\pi^*$  electron transitions (4.6 eV) to the dielectric function.

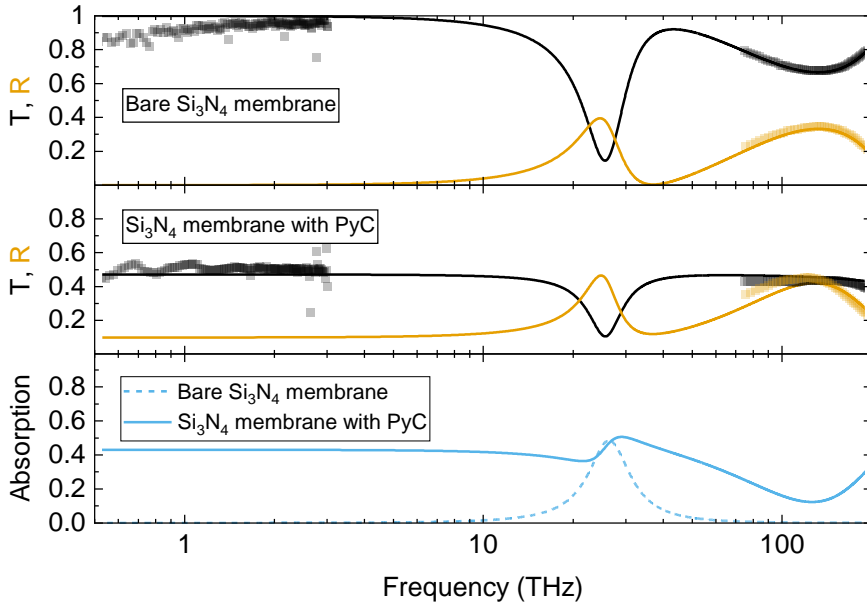


Figure 33. Optical properties of the PyC film deposited on the  $\text{Si}_3\text{N}_4$  membrane. (a) Calculated (thin lines) and measured (rectangles) transmission T (black) and reflection R (yellow) spectra of bare  $\text{Si}_3\text{N}_4$  membrane. (b) The same but for  $\text{Si}_3\text{N}_4$  membrane with a 20 nm thick PyC film on top. (c) Calculated absorption of bare  $\text{Si}_3\text{N}_4$  membrane (dashed line) and with a 20 nm thick PyC coating (solid line).

The values for transition strength  $A_T$  and the full width at half maximum (FWHM) for relaxation time  $\gamma_T$ , were taken from [214]. The third term is used to describe Drude conductivity of free charge carriers. In a dielectric function for bare  $\text{Si}_3\text{N}_4$  membrane eq.(24), the second term describes the resonant absorption around at around 26 THz due to the optical phonon excitation [215], [216]. The spectra calculated using equations (23) and (24) and experimental data are shown in Figure 33. A good agreement between the calculated and experimental spectra is obtained in both THz and MIR-NIR ranges.

Overall, while the resistivity of the PPF and PyC film samples remains still relatively large in comparison to metals, in both cases the sheet resistance of about  $500 \Omega/\text{sq.}$  was achieved, like that of the CVD graphene. In the case of PPF, these experimental findings show a way to employ EBL or UV photolithography to fabricate nanostructured graphitic electrodes in a few technological steps, offering a viable alternative to the CVD graphene. In the case of the PyC films, near to 50 % absorption of the PyC/ $\text{Si}_3\text{N}_4$  samples in the ultra-broadband range of 0.5 – 200 THz range were achieved revealing the



potential for a 20 nm PyC film technology. Such PyC film could be included in micromechanical bolometers operating in the THz range, where the thin graphitic film can be safely embedded enhancing responsivity without degrading the resonator quality [217], [218].

## SUMMARY

1. The sheet conductivity and morphology of the PPF made by annealing of the AZ nLOF 2070 resist used in the EBL do not depend on whether the resist was or was not cross-linked before pyrolyzation. PPF samples exhibited frequency independent conductivity of up to  $1.3 \times 10^4$  S/m in the frequency range up to 1.5 THz.
2. Thin PyC film on suspended Si<sub>3</sub>N<sub>4</sub> membrane fabrication technologies were developed. The 20 nm thick PyC film on a 300 nm thick Si<sub>3</sub>N<sub>4</sub> membrane was fabricated to absorb up to 40% of the incident THz radiation and 10-40% of NIR radiation in the ultrabroadband frequency range of 0.5-200 THz.

## MAIN RESULTS AND CONCLUSIONS

1. Thin AlGaIn/GaN HEMT structure on SiC substrate without GaN buffer layers was found to exhibit high 2DEG density (up to  $10^{13} \text{ cm}^{-2}$ ) and breakdown field (up to 0.8 MV/cm) with improved thermal dissipation of excess heat.

2. Quaternary InAlGaIn lattice-matched barrier layer of 9 nm thickness only was developed for GaN-based HEMT structures. Detailed analysis of the structural, optical, and electrical properties allowed to determine the composition of the barrier layer. Even at only 9 nm barrier thickness the 2DEG density was experimentally confirmed to be of  $1.2 \times 10^{13} \text{ cm}^{-2}$  with significantly smaller pinch-off voltage of  $-1.74 \text{ V}$ .

3. Effective trap density extracted using McWhorter model from low frequency noise measurements of the AlGaIn/GaN HEMTs was found to correlate to the results of secondary ion mass and terahertz electroluminescence spectroscopies, demonstrating that noise measurements are a sensitive method to estimate material quality. The effective trap density in a typical AlGaIn/GaN and in a thin AlGaIn/GaN HEMT structures was found to be as low  $10^{19} \text{ eV}^{-1} \text{ cm}^{-3}$ .

4. Self-heating of contact and 2DEG channel resistances in GaN-based HEMT structures was investigated under high electric fields and large current densities. Increase of contact resistance due to self-heating was observed in all studied heterostructure samples and it was larger than the self-heating of 2DEG channel resistance. The contact resistance increase was found to be proportional to electric power dissipated in the contacts.

5. Sensitive THz detection at zero-bias was demonstrated by the AlGaIn/GaN BT diodes with asymmetric IV characteristics. It was found that the responsivity of the BT diode varies nonlinearly with its resistance, demonstrating that the tapering of the diode apex below the range of a few micrometers could be ineffective in applications which require low NEP values.

6. Significantly lower THz responsivity at zero-bias was demonstrated by the AlGaIn/GaN BT bolometers with symmetric IV characteristics, in contrast to BT diodes. However, the responsivity was increased to a comparable level by applied external either positive or negative voltage in the range of  $+0.4 \text{ V}$  or  $-0.4 \text{ V}$ , respectively. Cooling the detectors from 300 K

down to 80 K increased non-linearity of the I-V characteristic, which resulted in larger THz responsivity values under external bias in the region of  $\pm 0.4$  V.

7. A method based on PMMA degradation at 254 nm wavelength and exposed PMMA removal in solvent mixture of isopropyl alcohol and water was developed and used to remove PMMA supportive layer from the surface of wet transferred CVD graphene on various semiconductor substrates. The high quality of graphene after PMMA removal was confirmed with SEM, AFM, and Raman spectroscopy. Small density of free charge carriers in the released graphene was found from THz-TDS results, demonstrating also the mobility values up to  $6900 \text{ cm}^2\text{V}^{-1}\text{s}^{-1}$ .

8. A method based on standard UV lithography means was developed for the patterning of wet-transferred CVD graphene. There is no contact between the graphene and the photoresist and its residuals during all processing steps using intermediary mask of specific photoresist formed on the PMMA supportive layer serving as the second mask.

9. The PPFs made by pyrolyzing AZ nLOF 2070 resist and the PyC layers deposited using CVD methods exhibited frequency independent conductivity in the THz range allowing to achieve sheet resistance values similar to that of wet-transferred CVD graphene. These conductive pyrolytic carbon films can be used as robust alternative to the CVD graphene for applications in the THz range.

# SANTRAUKA

## SANTRUMPOS

2DEG	Dvimatės elektronų dujos
BT	Peteliškės tipo
CVD	Cheminio nusodinimo metodas
DC	Nuostoviosios srovės
FET	Lauko efekto tranzistorius
GaN	Galio nitridas
HEMT	Didelio elektronų judrio tranzistorius
IV	Voltamperinė
MOCVD	Metalorganinis cheminio nusodinimo metodas
NEP	Triukšmo ekvivalentinė galia
PPF	Pirolizuoto fotorezisto plėvelė
PMMA	Polimetilmetaakrilatas
PyC	Pirolitinė anglis
RF	Aukšti dažniai
SBD	Šotkio barjero diodas
Si	Silicis
SiC	Silicio karbidas
SIMS	Antrinių jonų masių spektroskopija
TDS	Spektroskopija su laikine skyra
THz	Terahercinis

## ĮVADAS

Elektroniniai prietaisai patiria didžiulius pokyčius dėl siekio pagerinti jų efektyvumą ir sumažinti matmenis. Pastaruoju metu GaN išpopuliarėjo dėl galimybių gerokai išplėsti elektroninių prietaisų taikymo ribas, nes, kaip tiesiatarpis III–V grupės puslaidininkis, GaN pasižymi išskirtinėmis fizikinėmis savybėmis, pagrindinės iš jų išvardytos 1 lentelėje. Lyginant su pramonės standartu Si, GaN turi 3,1 karto didesnę draustinę juostos tarpą (3,4 eV), daugiau nei du kartus didesnę elektronų soties greitį ir iki 12 kartų didesnę kritinį elektrinį lauką, todėl jis naudojamas šviesos dioduose (LED) [1]–[3], aukštų dažnių (RF) elektronikoje, galios keitikliuose [4], taip pat aukštos įtampos blokavimo ir didelės galios perjungimo prietaisuose [5], [6]. Dėl savo savybių GaN leidžia pasiekti didelį efektyvumą (>99 %), greitą perjungimą (>1 MHz) prietaisuose, kurie gali saugiai veikti aukštoje temperatūroje (>400 °C). Dėl didelio pramušimo lauko vertikalios konstrukcijos GaN prietaisai gali būti gerokai plonesni nei Si atitinkamos klasės prietaisai, o tai leidžia sukurti našesnius ir kompaktiškesnius komponentus. Kaip GaN alternatyva, SiC turi panašų draustinę juostos tarpą (3,3 eV) ir aukštesnį šiluminį laidumą, kuris jam suteikia pranašumą aukštos galios, bet mažesnio dažnio įtampos blokavimo prietaisuose. Naudojant Baliga aukšto dažnio parametą (BHFFoM), kuris aprašo perjungimo nuostolius medžiagoje [7], GaN išsiskiria iš kitų puslaidininkių, naudojamų aukštų dažnių srityje.

GaN pagrindu sudarytos heterostrukūros, kuriose yra didelio tankio ir judrio 2D elektronų dujų (2DEG) laidus kanalas, tinkamos, kur reikia didesnio krūvininkų judrio nei pasiekiamas GaN sluoksniuose (didžiausias apie  $1250 \text{ cm}^2 \text{ V}^{-1} \text{ s}^{-1}$ ). Heterostrukūrą suformuoti ant GaN kanalo sluoksnio užauginamas plonas barjero sluoksnis su didesniu draustiniu juostos tarpu (AlGa<sub>N</sub>, AlIn<sub>N</sub> arba InAlGa<sub>N</sub>) dažniausiai kristalografine [0001] kryptimi. AlGa<sub>N</sub> ir Ga<sub>N</sub> sluoksnių sandūroje atsiranda energijos trūkis dėl draustinių juostų tarpų neatitikties. Gardelės konstantos neatitiktis tarp Ga<sub>N</sub> ir barjero sluoksnio sukuria tempiamąją arba spaudimo deformaciją barjero sluoksnyje, kuri kompensuoja gardelės neatitiktį plokštumoje. Al<sub>x</sub>Ga<sub>1-x</sub>N barjero atveju spontaninė ir piezoelektrinė poliarizacijos susideda sluoksnyje ir poliarizacijos dipolis tarp AlGa<sub>N</sub> paviršiaus ir AlGa<sub>N</sub>/Ga<sub>N</sub> sandūros kompensuojamas 2DEG susidarymu. Tipinė energetinė diagrama ir elektronų pasiskirstymas HEMT struktūroje, sudarytoje iš 25 nm storio Al<sub>0,25</sub>Ga<sub>0,75</sub>N barjero ant Ga<sub>N</sub> sluoksnio, parodyti 1b pav. Tokiame darinyje susidariusiame 2DEG kanale elektronai pasižymi didelėmis judrio vertėmis (siekia  $\sim 2400 \text{ cm}^2 \text{ V}^{-1} \text{ s}^{-1}$ ), kai jų tankis yra  $\sim 1 \times 10^{13} \text{ cm}^{-2}$  [11]. Alternatyva

$\text{Al}_{0.25}\text{Ga}_{0.75}\text{N}$  gali būti  $\text{Al}_x\text{In}_{1-x}\text{N}$  barjeras [12], [13], kurio kristalinė gardelė, esant  $x \approx 0,82$  sudėčiai, yra suderinta su GaN (žr. 1 pav.), o tai lemia dideles judrio vertes dėl sumažėjusios elektronų sklaidos. Be to, plonas AlInN barjeras leidžia pasiekti didelį elektronų tankį 2DEG kanale, pavyzdžiui,  $\sim 2,5 \times 10^{13} \text{ cm}^{-2}$  gaunamas suformavus tokį patį ( $\sim 20\text{--}25 \text{ nm}$ ) barjero sluoksnio storį arba pasiekiamas tas pats  $\sim 1 \times 10^{13} \text{ cm}^{-2}$  tankis, kai barjero storis yra diapazone nuo 7 nm iki 12 nm [12], [14].

Per pastarąjį dešimtmetį AlGaIn/GaN medžiagų platforma pradėta intensyviau tyrinėti už tipinių sričių, kaip antai GaN kietakūnis apšvietimas ir galios elektronika. Tai leido atsirasti naujų jų pritaikymo galimybių fotonikoje [18], [19], netiesinėje fotonikoje [20], gilaus UV LED/lazerių dioduose [21]–[23], THz plazmonikoje [24]–[26],[P12]–[P13],[P15], THz jutikliuose [27].

Lauko efekto tranzistoriai (FETai) sujungti su THz antena, vadinami TeraFETai, plačiausiai paplito kaip THz dažnio bangų jutikliai, kurie gali būti gaminami ir iš AlGaIn/GaN HEMT struktūrų [27]–[32]. TeraFET veikimas yra pagrįstas varžos moduliacija krįntančia THz dažnio banga (angl. *resistive self-mixing*), realizavus užslopintų plazminių bangų režimą tranzistoriaus kanale [27]. Rekordinio jautrumo TeraFETams gaminti naudojamos santykinai pažangios aukštadažnės integrinių GaN grandynų gamybos technologijos, kurios leidžia pagaminti tranzistorius, kurių užtūros ilgis  $\leq 100 \text{ nm}$ . Neseniai buvo pasiūlyti naujo tipo AlGaIn/GaN HEMT THz jutikliai (EdgeFETai), kuriuose elektrodų geometrija yra panaši kaip „Fin“ formos tranzistoriuose (FinFET), tačiau nauja, kad du Šotkio užtūros elektrodai suformuoti iš abiejų tranzistoriaus kanalo pusių, kurio viršus paliekamas neuždengtas [34], [35]. EdgeFET topologija leidžia elektriškai kontroliuoti 2DEG tranzistoriaus kanalo plotį, taip sustiprinant rezonansinį plazmoninį detekcijos mechanizmą. Istoriskai vieni sėkmingiausių kietakūnių THz detektorių yra Šotkio barjeriniai diodai (SBD), naudojami maišymui ir tiesioginiam elektromagnetinės spinduliuotės lyginimui dėl jų stipriai netiesinės voltamperinės charakteristikos. Pažymėtina, kad SBD kaip THz detektoriai buvo sukurti ir iš AlGaIn/GaN heterostruktūrų [36], [37]. Karštų elektronų mikrobolometrai THz detekcijai buvo pademonstruoti panaudojant ir 2DEG AlGaIn/GaN heterostruktūrose [38], [39]. Siekis padidinti efektyvumą / dažnį elektronikoje ir geresnį THz jautrį galimas tobulinant AlGaIn/GaN HEMT platformą [5] arba kuriant naujas heterostruktūras, tokias kaip InAlIn/GaN [40]–[42], InAlGaIn/GaN [43]–[45]. Iš tiesų InAlIn ar InAlGaIn barjerai leidžia pasiekti panašias 2DEG charakteristikas esant mažesniai barjero storiui, o tai yra svarbu kuriant trumpo kanalo aukštadažnius HEMTus, naudojamus RF elektronikoje ir THz detektuoti.

Grafenas yra dvimatis anglies alotropas su atomais, išdėstytais heksagoninėje gardelėje, kuriam būdinga betarpė juostinė diagrama. Jo atradimas 2004 m. vis dar domina mokslinę bendruomenę [46], [47]. Grafeno išskirtinės savybės, tokios kaip didžiulis šiluminis laidumas (38 kartus didesnis nei GaN) ir didžiulis elektrinis laidumas [48], [49] (žr.1 lentelę), padaro jį itin patrauklų plačiam pritaikymo spektrui, pavyzdžiui, RF tranzistoriai su ribiniu dažniu  $f_T$ , siekančiu THz diapazoną [50], magnetiniai ar mechaniniai jutikliai [51], aplinkos dujų jutikliai [52] ir kt. Palyginti su GaN grafenas nėra tinkamas galios elektronikai dėl savo betarpės juostinės struktūros, dėl ko iš jo pagaminti tranzistoriai turi mažą įjungimo / išjungimo srovės santykį [53]. Kita vertus, ~97,7 % grafeno skaidrumas matomame diapazone [54] suteikia unikalią galimybę kurti iš jo optoelektroninius prietaisus, tokius kaip fototranzistoriai vaizdo jutikliams [55] ir kt. Ilgesnių bangų ruože, pavyzdžiui, THz diapazone, vienasluoksniu grafenu sugertis kur kas didesnė dėl bangų sugerties laisvaisiais krūvininkais [56], [57]. Dažniausiai grafenu FET (GFET) su integruota THz antena naudojami kaip detektoriai [58]–[62]. Tokiu atveju GFET atsakas į THz susideda iš dviejų komponentų: savaiminio varžinio maišymo (angl. *resistive self-mixing*) ir fototermoelektrinio efekto [63]. GFET savaiminis varžos maišymas gaunamas dėl krūvininkų tankio ir greičio moduliacijos, o fototermoelektrinis efektas priskiriamas krūvininkų kaitimui grafenu. Nors vienasluoksniu grafenu kaip bolometriniu jutikliu THz diapazone tyrimų rezultatai jau publikuoti [64], [65], tačiau grafenu šiluminis varžos koeficientas yra mažesnis nei standartinių metalo ar puslaidininkų pagrindu pagamintų bolometrų atvejais [66], [67], todėl gaunamas mažesnis jautris.

Integravus grafenu su GaN puslaidininkiais tikimasi pagerinti prietaisų veikimą ir rasti naujų pritaikymo galimybių. Vienas iš unikalesnių grafenu ir GaN integracijos atvejų yra panaudoti grafenu padengtą GaN padėklą epitaksiniam plonų sluoksnių auginimui, toks būdas literatūroje yra vadinamas nuotoline epitaksija [68]–[70]. Naudojant šį metodą auginami GaN sluoksniai ar heterostruktūros gali būti atskirti nuo padėklo, o grafenu padengtas padėklas naudojamas pakartotinai. Iki šiol dažniausiai grafenu su GaN buvo integruoti tik prietaisų lygyje. Grafenu su GaN sudaro elektrinį Šotkio kontaktą [71], [72], tačiau, skirtingai nuo metalų, kurie naudojami Šotkio kontaktams, jis yra skaidrus [57]. Literatūroje yra aprašyti įvairūs prietaisai, tokie kaip grafenu ir GaN diodai [73], tranzistoriai [71] ir UV diapazono fotodiodai [74], [75], fototranzistoriai [76]. Žvelgiant į ateitį, reikia tyrimų siekiant išspręsti pagrindinius uždavinius, kurie susiję su grafenu ir GaN puslaidininkų integracija. Galimi uždaviniai – tobulinti gamybos metodus ir apdorojimo sprendimus, kad būtų sumažintas defektų kiekis ir



pagerintas prietaisų veikimas. Be to, būtina standartizuoti grafeno charakterizavimo metodus [77] ir kurti modelius, tinkamus prietaisų charakteristikoms skaičiuoti, siekiant komercializuoti grafeno prietaisus.

Jei nereikia aktyvaus elektroninio parametrų valdymo, gali būti pritaikyti ir alternatyvūs anglies pagrindu pagaminti laidūs sluoksniai, pavyzdžiui, pirolitinė anglis. Yra du pagrindiniai pirolitinės anglies sluoksnių tipai: pirolitinė anglis (PyC), gaunama iš angliavandenilių dujų skilimo pirolizės metu [78], [79], ir pirolizuoto fotoresisto sluoksniai (PPF), gaunami dėl fotoresisto pirolizacijos [80]–[82]. Abiem atvejais sluoksnis sudarytas iš netvarkingai išdėstytų grafeno nanokristalų [83], kuriam yra būdingas aukštas elektrinis laidumas ir cheminis atsparumas. Šios savybės tinkamos įvairiems taikymams, vienas iš kurių gali būti sugeriantysis sluoksnis bolometriniuose MIR ar THz diapazonų jutikliuose [84]–[86].

Apibendrinant reikia pažymėti, kad GaN ir grafeno integracija yra perspektyvi kryptis, leisianti peržengti tam tikras šiuolaikinės puslaidininkių technologijos ribas. Sinergija tarp GaN aukštos galios, aukšto dažnio galimybių ir išskirtinių grafeno savybių gali lemti naujų prietaisų atsiradimą. Šis darbas skirtas dviejų skirtingų puslaidininkių – GaN heterostruktūrų ir grafeno – THz diapazono optinių ir elektrinių savybių tyrimui, siekiant integracijos THz jutiklių taikymams.

## DARBO TIKSLAS

Tirti naujus GaN pagrindo puslaidininkius ir integruotus su grafeno ir pirolitinės anglies sluoksniais prietaisus, tinkamus THz detektavimui.

## DARBO UŽDAVINIAI

1. Sukurti ir ištirti plonus GaN pagrindo heterosandūrinius darinius, kuriuose gaunamas didelis elektronų judris ir tankis 2DEG kanale, kuris naudojamas tranzistoriams (HEMTams) ir jautriems THz detektoriams kurti.
2. Ištirti elektronų kaitimą kontaktiniame sluoksnyje ir 2DEG kanale GaN pagrindo HEMT struktūrose bei efektus, naudingus kuriant THz detektorius.
3. Kurti grafeno apdorojimo technologijas, siekiant panaudoti didelį krūvininkų judrį su grafenu susijusiose medžiagose, siekiant tobulinti GaN pagrindu pagamintus THz jutiklius.

## DARBO NAUJUMAS

1. Sukurta plona AlGaIn/GaN HEMT struktūra, neturinti storo GaN buferinio sluoksnio, pasižyminti dideliu, termiškai stabiliu 2DEG sluoksniu, kuriame elektronų tankis siekė  $1,0 \times 10^{13} \text{ cm}^{-2}$ , o judris –  $1,7 \times 10^3 \text{ cm}^2 \text{ V}^{-1} \text{ s}^{-1}$  vertes 300 K laipsnių temperatūroje. Pagamintų SBD'ų pramušimo laukas siekė iki 0,8 MV/cm, išėjimo DC charakteristikos parodė, kad HEMT'ų santakos srovė praktiškai nesumažėja perjungiant didelius galingumus  $\geq 2,5 \text{ W/mm}$  dėl pagerinto heterostruktūros šiluminio dizaino. HEMT'ų RF charakteristikos siekė dažnius  $f_T = 1,33 \text{ GHz}$  ir  $f_{\max} = 6,7 \text{ GHz}$ , kas atitiko lyginamojo rodiklio vertę  $f_T \times L_G = 6,7 \text{ GHz} \times \mu\text{m}$ .
2. Sukurtas keturnaris InAlGaIn suderintos gardelės 9 nm storio barjero sluoksnis GaN pagrindo HEMT struktūrai, kuris leidžia pasiekti panašius 2DEG parametrus – tankis apie  $1,2 \times 10^{13} \text{ cm}^{-2}$  ir judris apie  $1,6 \times 10^3 \text{ cm}^2 \text{ V}^{-1} \text{ s}^{-1}$  300 K temperatūroje, kaip ir standartinėse AlGaIn/GaN HEMT struktūrose, kuriose naudojamas 20 nm ar storesnis barjero sluoksnis.
3. Atlikus žemo dažnio triukšmo matavimus ir pritaikius McWhorter modelį, nustatytas mažas efektyvių krūvio gaudyklių tankis AlGaIn/GaN HEMT'uose, ne daugiau kaip  $10^{19} \text{ eVcm}^{-3}$ . Šis skaičius koreliavo su nekompensuotų donorų tankiu, kuris nustatytas panaudojant antrinių jonų masės spektroskopijos bei THz elektroliuminescencijos spektroskopijos matavimus, taip įrodyta, kad žemo dažnio triukšmas yra tinkamas būdas AlGaIn/GaN heterostruktūros kokybei įvertinti.
4. Nustatytas savaiminis kaitimas ominių kontakto ir 2DEG kanalo varžoms, kai praleidžiami dideli impulsinės srovės tankiai per AlGaIn/GaN ir AlGaIn/AlN/GaN HEMT struktūras. Kontaktinės varžos padidėjimas iki 6 kartų nuo pradinės vertės buvo nustatytas visuose iširtuose bandiniuose ir šis efektas buvo didesnis nei 2DEG kanalo varžos savaiminis pakaitimas, kai srovės vertė buvo didesnė kaip 0,6 A/mm.
5. Iširti peteliškės tipo diodiniai ir peteliškės tipo bolometriniai THz jutikliai, pagrįsti asimetriškai susiaurintomis AlGaIn/GaN HEMT struktūromis ir ominiais kontaktais dviejose pasirinktose 300 K ir 80 K temperatūrose. Peteliškės tipo diodų THz jautrio vertės siekė iki 4 V/W, o triukšmo ekvivalentinė galia –  $2 \text{ nW}/\sqrt{\text{Hz}}$  matuojant ties pagrindiniu THz antenos dažniu, kuris nustatytas ties 150 GHz. Didėjant peteliškės tipo diodo varžai, jos jautris didėjo netiesiškai, taigi atskleista, kad diodo kakliuko siaurinimas mažiau nei keli mikrometrai yra nevertingas dėl didėjančios triukšmo ekvivalentinės galios vertės.

6. Sukurtas metodas PMMA pašalinti nuo CVD grafeno paviršiaus, kuriame panaudojami PMMA fotoardymas apšviečiant iš UV-C (254 nm bangos ilgis) šaltiniu ir jos pašalinimas izopropanolio ir vandens tirpale. Aukšta grafeno kokybė po PMMA pašalinimo buvo patvirtinta SEM, AFM ir Ramano spektroskopijos metodais. Švaraus grafeno tyrimai THz-TDS metodais parodė, kad krūvininkų judris siekė iki  $6900 \text{ cm}^2\text{V}^{-1}\text{s}^{-1}$ .
7. Sukurta metodika PMMA apsaugoto grafeno struktūravimui panaudojant UV fotolitografiją. Naudojant fotorezistą ir apsauginį PMMA sluoksnį, galima išvengti tiesioginio grafeno kontakto su fotorezistu ar jo liekanomis, taip pat cheminio grafeno legiravimo.
8. Piroлізуojant AZ nLOF 2070 rezistą buvo sukurtas PPF, kurio laidumas siekė iki  $1,3 \times 10^4 \text{ S/m}$  vertės, nepriklausančios nuo dažnio diapazone nuo DC iki 1,5 THz.
9. Sukurta plona, dešimčių nanometrų storio, laidų grafitinė plėvelė ant dielektrinės  $\text{Si}_3\text{N}_4$  membranos. Tokia 20 nm storio grafitinė plėvelė ant  $\text{Si}_3\text{N}_4$  sugėrė apie 40 % krintančio intensyvumo THz diapazone ir nuo 10 iki 40 % – NIR diapazone, bendrai apimant spektrą nuo 0,5 iki 200 THz.

#### GINAMIEJI TEIGINIAI

1. Plonasluoksnės AlGaIn/GaN ir suderintos kristalinės gardelės InAlGaIn/GaN HEMT struktūros yra tinkamos pasiekti kambario temperatūroje didelį 2D elektronų tankį (apie  $10^{13} \text{ cm}^{-2}$ ) ir judrį daugiau nei  $1700 \text{ cm}^2\text{V}^{-1}\text{s}^{-1}$ .
2. Elektronų kaitimas omino kontakto sluoksnyje ir 2DEG kanale gali būti identifiktuotas AlGaIn/GaN HEMT struktūrose ir pritaikytas atitinkamai peteliškės tipo diodinams bei peteliškės tipo bolometriniams THz jutikliams kurti.
3. Grafenas, pasižymintis dideliu krūvininkų judriu ( $>2900 \text{ cm}^{-2}$ ) ir mažu legiravimu ( $\leq 3 \times 10^{12} \text{ cm}^{-2}$ ) bei tinkamumu integracijai su GaIn struktūromis, yra gaunamas, kai naudojamas dviejų žingsnių procesas polimetilmetakrilatui nuvalyti bei struktūroms suformuoti, panaudojant UV-C apšvietimą ir pašalinimą izopropanolio ir vandens (3:1) tirpale.
4. Ploni (20–160 nm) pirolitinės anglies ant  $\text{Si}_3\text{N}_4$  sluoksniai, kurių sluoksnio varža  $500 \text{ } \Omega/\text{kv.}$ , gali būti sukurti THz ruožui (iki 10 THz) ir panaudoti kaip CVD grafeno alternatyva.

## AUTORIAUS INDĒLIS

Dauguma bandinių gamybos ir eksperimentinių tyrimų buvo atlikta Fizinių ir technologijos mokslų centre (FTMC) (Vilnius, Lietuva). Dalis straipsniuose paminėtų GaN puslaidininkinių bandinių buvo gaminama Didelių slėgių fizikos institute PAS (UNIPRESS, Varšuva, Lenkija, vadovaujant Dr. Pawel Prystawko). Autorius kūrė UV fotolitografijos kaukes ir atliko GaN pagrindu pagamintų heterostruktūrų apdorojimą, siekiant sukurti įrenginius ir testavimo struktūras [P1–P5, P12–P13, P15–P16]. Autorius padėjo R. M. Balagulai kuriant UV fotolitografijos kaukes *n*-GaN mėginiams, tai aprašyta straipsniuose [P10–P11]. Autorius nuodugniai atliko DC elektrinių charakterizavimą naudojant pagamintas van der Pauw, TLM/CTLM testavimo struktūras, SBD ir HEMT [P1–P5, P12–P13, P15–P16], ir iš dalies straipsniuose [P10–P11, P14]. Autorius atliko dalinį DC elektrinių ir THz jautrio charakterizavimą AlGaIn/GaN BT diodams straipsnyje [P5].

Autorius atliko visą bandinių gamybą (CVD grafeno ir PMMA mėginiai), vandens kontaktinio kampo matavimus, detalią Ramano spektroskopijos duomenų analizę ir elektrinius Van der Pauw bandinių tyrimus, rezultatai kurių aprašyti straipsnyje [P6] ir patentinėje paraiškoje [P7]. Pirolitinės anglies mėginiai, aprašyti straipsniuose [P8–P9], buvo pagaminti ir elektriškai charakterizuoti autoriaus Rytų Suomijos universitete (Joensu, Suomija), kartu su bendrautoriais atlikti PPF THz spektroskopijos tyrimai FTMC, aprašyti straipsnyje [P8].

## DALYVAVIMAS PROJEKTUOSE

Moksliniai tyrimai, atlikti vykdant projektus:

1. TERAGANWIRE projektą, kurį finansavo Lietuvos mokslo taryba (Nr. S-LL-19-1) ir Lenkijos nacionalinis mokslo centras (Nr. 2017/27/L/ST7/03283)
2. Lietuvos mokslo tarybos finansuotą projektą „Kompaktiški terahercinės spinduliuotės plazmoniniai emiteriai (KOTERA-PLAZA)“ (Nr. 01.2.2-LMT-K-718-01-0047)
3. Vykdant Flagmano programą PREIN, finansuotą Suomijos mokslų akademijos (sprendimas 320166)
4. „Micromechanical Bolometers arrays for THz hyperspectral imaging (h-cube)“ H2020 projekto subprojektą EU ATTRACT Phase 2 (Nr. 101004462)

5. Lietuvos mokslo tarybos finansuotą projektą „Hibridiniai plazmonikos komponentai THz dažnių ruožui (T-HP)“ (Nr. 01.2.2-LMT-K-718-01-0096).

## STAŽUOTĖS

Doktorantūros studijų metu išvykta į stažuotes:

1. 2020 m. sausio 13–26 d. prietaisų gamyba iš AlGaIn/GaN ir InAlGaIn/GaN HEMT struktūrų Didelių slėgių fizikos institute (UNIPRESS), Varšuva, Lenkija.
2. 2020 m. liepos 31 d. – rugpjūčio 7 d. AlGaIn/GaN HEMT žemadažnio triukšmo matavimai bei peteliškės tipo diodinių THz jutiklių charakterizavimas CENTERA laboratorijose Didelių slėgių fizikos institute (UNIPRESS), Varšuva, Lenkija.
3. 2022 m. rugpjūčio 1 d. – gruodžio 31 d. pirolitinės anglies (PPF ir PyC) technologijos perėmimas. Suformuotų laidžių dangų DC elektriniai matavimai ir optinis charakterizavimas THz dažnių ruože. Mokymasis dirbti su Raith elektronų pluošto litografijos įranga submikroninėms plazmoninėms struktūroms formuoti ant AlGaIn/GaN HEMT struktūrų Rytų Suomijos universitete (UEF), Joensuu, Suomija.
4. 2023 m. liepos 17 d. – rugpjūčio 18 d. submikroninių plazmoninių struktūrų formavimas naudojant elektronų pluošto litografiją ant AlGaIn/GaN HEMT struktūrų THz dažnių diapazonui Rytų Suomijos universitete (UEF), Joensuu, Suomija.

## REZULTATŲ APŽVALGA

### 1. GaN pagrindu sukurtų HEMT struktūrų vystymas

Siekiant didinti THz jutiklių jautrį, gerinti DC ir RF elektronikos našumą bei vystyti THz dvimačių elektronų plazmoniką iširtos dvi perspektyvios GaN pagrindu sukurtos HEMT struktūros: plona AlGaIn/GaN HEMT struktūra užauginta be storo akceptorinėmis priemaišomis kompensuoto GaN buferinio sluoksnio (pavadinta HEMT D) ir plona suderintos gardelės  $\text{In}_{0.165}\text{Al}_{0.775}\text{Ga}_{0.06}\text{N}$  barjerinio sluoksnio HEMT struktūra (pavadinta HEMT F). Šių ir kitų tipinių AlGaIn/GaN HEMT struktūrų sluoksnių sandara ir nustatyti 2DEG elektriniai parametrai pateikiami 1.1 ir 1.2 lentelėse

Plonosios AlGaIn/GaN HEMT struktūros (HEMT D) bendras storis buvo tik 340 nm ir ji panaudota SBD, tranzistorių ir testinių prietaisų gamybai [P1]. Išmatuotos 2DEG elektrinės savybės buvo analogiškos tipiniams storų AlGaIn/GaN HEMT struktūrų 2DEG parametrams (žr .1.2 lentelę). Tiriant SBD DC režimu nustatyta, kad prietaisai pasižymėjo pramušimo įtampomis iki  $-780$  V (40  $\mu\text{m}$  kontaktų atskyrimas) ir pramušimo laukas siekė iki 0,8 MV/cm (5  $\mu\text{m}$  kontaktų atskyrimas). Tai pirmieji išmatuoti realaus srovę blokuojančio prietaiso, pagaminto ant plonos AlGaIn/GaN HEMT struktūros, pramušimo lauko rezultatai. Tiriant plonųjų tranzistorių (T-HEMT) DC charakteristikas nustatyta, kad nebuvo kanalo srovės sumažėjimo esant didelei elektrinei galiai tranzistoriuje ( $>2,5$  W/mm), dėl HEMT D struktūros sumažintų šiluminių barjerų tarp 2DEG ir SiC padėklo, kurio šiluminis laidumas yra didelis. T-HEMT ( $L_G = 5$   $\mu\text{m}$ ;  $L_{SD} = 14$   $\mu\text{m}$ ;  $W = 2 \times 200$   $\mu\text{m}$ ) RF charakterizavimo metu nustatyti maksimalūs srovės stiprinimo ( $f_T$ ) ir galios stiprinimo ( $f_{max}$ ) dažniai siekė iki 1,3 GHz ir 6,7 GHz atitinkamai. Didesnių dažnių pasiekti nepavyko dėl FTMC naudojamos litografijos įrangos 2–3  $\mu\text{m}$  rezoliucijos apribojimų. Autoriaus žiniomis, tai pirmieji FTMC sukurti ir pagaminti aukštadažniai AlGaIn/GaN HEMT'ai su  $f_T$  ir  $f_{max}$  vertėmis daugiau kaip 1 GHz.

Plonas 9 nm storio suderintos gardelės  $\text{In}_{0.165}\text{Al}_{0.775}\text{Ga}_{0.06}\text{N}$  barjeras buvo sukurtas GaN pagrindu sukurtai HEMT struktūrai ant safyro padėklo (HEMT F) [P2]. Atliekant detalią XRD, SIMS, fotoluminescencijos ir eksperimentinio 2DEG tankio duomenų analizę, kartu juostinių diagramų ir krūvininkų jose modeliavimą buvo tiksliai nustatyta keturnario suderintos gardelės  $\text{In}_{0.165}\text{Al}_{0.775}\text{Ga}_{0.06}\text{N}$  barjero sudėtis ir 8,6 nm storis. Nors heterostruktūroje buvo panaudotas plonas barjerinis InAlGaIn sluoksnis, tačiau HEMT F struktūroje pasiektas didelis  $1,2 \times 10^{12} \text{ cm}^{-2}$  2DEG krūvininkų tankis dėl didelės AlN frakcijos kietajame lydinyje. Kambario temperatūroje elektronų judris palyginamas su tipinėmis AlGaIn/GaN HEMT struktūromis ir siekia  $1,6 \times 10^3 \text{ cm}^2 \text{ V}^{-1} \text{ s}^{-1}$ . Atšaldžius iki 77 K elektronų judris padidėjo tik iki  $8,8 \times 10^3 \text{ cm}^2 \text{ V}^{-1} \text{ s}^{-1}$  dėl gaunamos sąlygiškai prastesnės sluoksnių kokybės auginant ant safyro padėklo. Mažo barjero storio HEMT struktūros yra naudingos siekiant sumažinti trumpo kanalo efektų (angl. *short channel effects*) įtaką aukštadažniams tranzistoriams. Taip pat, priartinus dvimates dujas arčiau paviršiaus, padidinama jų sąveika su paviršiumi, o tai yra naudinga įvairių jutiklių taikymams bei THz ruožo plazmoninių struktūrų rezonansinio dažnio pozicijai keisti. Iš šios HEMT struktūros (HEMT F) pagaminti SBD ir HEMT dėl plono barjero storio pasižymi maža 2DEG DC  $-1,75$  V atkirtos įtampa, lyginant su  $-3$  V verte tipinėms AlGaIn/GaN HEMT struktūroms. Matuojant SBD DC režime iki pramušimo, gautas didžiausias

kritinis elektrinis laukas buvo 0,4 MV/cm. Gana maža kritinio elektrinio lauko vertė gauta dėl didelio siūlinių dislokacijų tankio šioje HEMT struktūroje, užaugintoje ant safyro padėklo. HEMT ( $L_G = 5 \mu\text{m}$ ;  $L_{SD} = 12 \mu\text{m}$ ;  $W = 2 \times 200 \mu\text{m}$ ) RF charakterizavimo metu nustatyti  $f_T$  ir  $f_{\text{max}}$  dažniai siekė iki 1,0 GHz ir 4,5 GHz atitinkamai. Šios vertės yra palygintos su vertėmis, gautomis tranzistoriuose, pagamintuose iš tipinių AlGaIn/HEMT struktūrų bei plonosios AlGaIn/GaN HEMT struktūros (HEMT D).

Efektinis elektriškai aktyvių gaudyklių tankis buvo tiriamas keliose tipinėse AlGaIn/GaN HEMT struktūrose (HEMT A, HEMT B, HEMT C) ir plonojoje AlGaIn/GaN HEMT struktūroje (HEMT D) atliekant  $1/f$  žemadažnių triukšmų ir DC IV matavimus bei pritaikant McWhorter modelį. Nors tirtos tipinės HEMT struktūros (HEMT A-C) turėjo gana panašią sluoksnių struktūrą (žr. 1.1 lentelę) ir artimas 2DEG sluoksnio varžos vertės (žr. 1.2 lentelę), tačiau gautos efektyvių elektriškai aktyvių gaudyklių tankių vertės skyrėsi iki dviejų eilių. Papildomai atlikti SIMS tyrimai, kurių matavimų rezultatai, įvertinus įprastų sekliųjų donorų priemaišų (silicis ir deguonis) ir akceptorinės anglies priemaišų kiekius, pateikiami 2.1 lentelėje. Nustatyta, kad nekompensuotų donorų tankio ( $N_D - N_A$ ) vertės koreliuoja su gautomis efektyvių gaudyklių tankio vertėmis. Tranzistoriams pagamintiems iš HEMT B struktūros su didžiausiu nekompensuotų donorų kiekiu ( $2,4 \times 10^{16} \text{cm}^{-3}$ ) gauti didžiausi gaudyklių tankiai  $> 10^{20} \text{eV}^{-1} \text{cm}^{-3}$ . Tranzistoriams pagamintiems iš kitų dviejų tipinių HEMT struktūrų (HEMT A ir HEMT C) bei plonosios HEMT struktūros (HEMT D) gauti mažesni efektyviai gaudyklių tankiai apie  $\leq 10^{19} \text{eV}^{-1} \text{cm}^{-3}$ , kurie yra palyginami su vertėmis, publikuotomis Si MOSFET [165–167] bei AlGaIn/GaN HEMT [168].

## 2. AlGaIn/GaN HEMT struktūros dideliuose elektriniuose laukuose ir srovės tankiuose

Ištirti atkaitintų Ti/Al/Ni/Au ominių kontaktų varžos ir 2DEG kanalo varžos savaiminio kaitimo reiškiniai tipinėse AlGaIn/GaN HEMT struktūrose (HEMT C ir HEMT E) didelių elektrinių laukų ir srovės tankių režime [P4]. Nors kontaktinės varžos priklausomybė keičiant bandinio temperatūrą buvo aprašyta darbuose [177], [179–180], tačiau kontaktinės varžos savaiminio kaitimo priklausomybė nuo srovės tankio stipriuose elektriniuose laukuose anksčiau nebuvo tirta. Tyrime buvo naudojamas perdavimo linijos metodas (angl. *transition line method* – TLM) ir 100 ns trukmės itin mažos užpildos ( $\sim 10^{-5}$ ) impulsinis standas, siekiant išvengti gardelės kaitimo reiškinį ir tirti

tik elektronų posistemės nulemtus varžos savaiminio kaitimo efektus. Viso prietaiso varža  $R_T = 2R_c + R_{ch}$  ( $R_c$  – kontaktinė varža,  $R_{ch}$  – 2DEG kanalo varža). Nustatyta, kad viso prietaiso varža elektrinių laukų ruože iki 1–2 kV/cm atitinka Omo dėsnį. Kai laukas didesnis kaip 2 kV/cm, stebimas nuokrypis nuo tiesinės Omo dėsnio priklausomybės. Naudojant TLM metodą nustatyta, kad, didėjant srovės tankiui, auga tiek 2DEG sluoksnio varža  $R_{sh}$ , tiek kontaktinė varža  $R_c$ . Apibrėžiant nuo srovės priklausomas varžas, kaip  $R_c(I) = R_{c0} + \Delta R_c(I)$  ir  $R_{sh}(I) = R_{sh0} + \Delta R_{sh}(I)$ , čia  $R_{c0}$  ir  $R_{sh0}$  vertės, gautos iš TLM matavimų mažiausių matavimo srovių tankių / elektrinių laukų atveju. Nustatyta, kad nuo srovės priklausomi  $\Delta R_c(I)$  ir  $\Delta R_{sh}(I)$  proporcingai auga nuo elektrinės galios išsklaidytose kontaktinėse srityse  $P_c(I)$  ir 2DEG kanale  $P_{2D}(I)$  atitinkamai. Tirtuose trijuose dviejų HEMT struktūrų (HEMT C ir HEMT E) bandiniuose, kai srovės tankis didesnis kaip 0,6 A/mm, nustatytas didesnis nei 6 kartų kontaktinės varžos  $R_c$  padidėjimas (nuo  $R_{c0}$  vertės), o kontaktinės varžos prieaugis  $\Delta R_c(I)$  nuo srovės priklauso  $\bar{F}$  arba stipresne priklausomybe. Tuo pačiu tirtų bandinių  $R_{sh}$  padidėjo tik iki dviejų kartų nuo  $R_{sh0}$  vertės. Apibendrinant reikia pažymėti, kad elektronų kaitimas kontaktiniuose sluoksniuose pradeda augti virš  $R_{sh} \approx 600 \Omega/kv$ . ir  $R_c$  savaiminis kaitimas greičiau auga nei  $R_{sh}$  atveju, kai didėja srovės tankis.

Elektronų kaitimas asimetrinės formos ominių kontaktų sluoksniuose ir asimetrinės formos 2DEG sluoksniuose buvo panaudotas peteliškės tipo diodiniais ir peteliškės tipo bolometriniais THz jutikliams kurti. Abiejų tipų THz jutikliai buvo pagaminti iš tipinės AlGaIn/GaN HEMT struktūros HEMT C, pasižyminties dideliu elektronų judriu tiek kambario, tiek skysto azoto temperatūrose (žr. 1.2 lentelę). Peteliškės tipo jutiklio schema parodyta 19a pav. Peteliškės tipo diodiniais THz jutikliai išsiskyrė asimetrinėmis IV charakteristikomis (žr. 19b pav.), nulemtomis krūvininkų kaitimo susiaurintame ominiame elektrode. Šie peteliškės tipo diodiniais jutikliai pasižymėjo iki 4 V/W optiniu jautriu ir 2 nW/ $\sqrt{Hz}$  triukšmo ekvivalentine galia, detekuojuotą 150 GHz spinduliuotę be išorinės postūmio įtampos (žr. 19c pav.). Didelis šių jutiklių jautris leido išmatuoti peteliškės tipo antenos dažninę charakteristiką, kuri patvirtino, jog pagrindinis antenos rezonansas yra apie 150 GHz (žr. 20 pav.). Jutiklių atsakas į trumpą impulsinę spinduliuotę buvo kiek trumpesnis nei nanosekundė ir buvo palyginamas su komercinių Šotkio diodų atsako sparta. Tiriant peteliškės tipo diodus statistiškai, nustatyta, kad sumažinti kakliuko plotį mažiau nei mikroną nėra naudinga. Nors ir gaunamas didelis jautris, tačiau netiesiškai padidėja ir jutiklio varža. Tai reiškia, kad, siekiant mažų triukšmo ekvivalentinių galių, peteliškės kakliuko siaurinti mažiau nei keletą mikronų yra neefektyvu.



Naudojant tą pačią peteliškės tipo geometriją buvo sukurti ir peteliškės tipo bolometriniai THz jutikliai. Bandinys, ant kurio pagaminti peteliškės tipo bolometriniai jutikliai, pasižymėjo mažiausia ominių kontaktų varža ( $0,4 \Omega \text{ mm}$ ) iš visų disertacijoje pristatytų bandinių. Kitaip nei peteliškės tipo diodai, šie pasižymėjo simetrinėmis IV charakteristikomis (žr. 22 pav.). Simetrinės IV charakteristikos indikuoja, kad stipraus krūvininkų savaiminio kaitimo efektas susiaurintame ominiame elektrode buvo labai sumažintas, ir tai, kad dominuoja kaitimas asimetrinės formos 2DEG sluoksnio varžos. Charakterizuojant bolometrinius jutiklius 150–600 GHz ruože kambario temperatūroje nustatyta, kad bolometrinių tipo jutikliai pasižymėjo 1–2 eilėmis mažesniu optiniu jautriu, palyginti su diodiniais jutikliais. Tačiau pridėjus nedidelę  $\pm 0,4 \text{ V}$  įtampą ant dvimačių dujų aktyviosios srities gautas tokio pat dydžio optinis jautris (žr. 24a pav.). Bolometrinių jutiklių jautrio priklausomybės nuo pridėtos išorinės įtampos charakteristika taip pat buvo simetrinė 0 V atžvilgiu visų tirtų jutiklių ir detekcijos dažnių (žr. 24b pav.). Peteliškės tipo bolometriniai jutikliai buvo tirti ir 80 K temperatūroje, gautos labiau netiesinės, tačiau taip pat simetrinės IV charakteristikos. Atšaldžius jutiklių optinis jautris be išorinės postūmio įtampos paaugo 9,2 karto. Jutiklių optinio jautrio charakteristikos pokyčiai esant 80 K temperatūrai išmatuoti ir pridėjus išorinę postūmio įtampą (žr. 25 pav.). Nustatyta, kad srityje tarp  $\pm 0,4 \text{ V}$  gaunamas daug didesnis optinis jautris nei 300 K temperatūroje, o didėjant pridėtai įtampai optinio jautrio padidėjimas 80 K temperatūroje silpnėja. Tiek didesnę IV charakteristikų netiesiškumą 80 K temperatūroje, tiek optinio jautrio santykio (80 K/300 K) charakteristikų sumažėjimą galima paaiškinti stipriai jautresne elektronų judrio priklausomybe nuo elektrinio lauko esant 80 K temperatūrai.

### 3. Grafenas

Šis skyrius skirtas CVD grafeno pernašos, valymo ir struktūravimo technologijoms, siekiant sumažinti cheminį grafeno legiravimą ir išlaikyti didelį krūvininkų judrį, kai CVD grafenas pernešamas ant GaN pagrindu sukurtų HEMT struktūrų ir silicio.

CVD grafenas yra plačiausiai naudojama grafeno forma moksliniuose tyrimuose bei taikymuose. Šiuo būdu pagamintas vienasluoksnis grafenas pernešamas ant galutiniam taikymui reikalingo padėklo, o trapiam grafenui pernešti įprastai naudojamas atraminis (angl. *supporting*) polimetilmetakrilato (PMMA) sluoksnis, kurį būtina visiškai pašalinti po pernešimo procedūros. Efektyviai PMMA pašalinti nuo pernešto CVD grafeno paviršiaus sukurtas

metodas, naudojantis gilaus UV (254 nm) fotocheminį PMMA ardymą ir mažai toksišką izopropilo ir vandens (3:1) tirpiklį [P6]. Šis PMMA pašalinimo metodas buvo pritaikytas grafenui, perneštam ant AlGaIn/GaN HEMT struktūros ir silicio padėklų, tiriant grafeno kokybę ir elektrinės pernašos savybes. Grafeno kokybė po valymo procedūros buvo tikrinama naudojantis Ramano spektroskopija. Gauta, kad naudojant šį PMMA šalinimo metodą grafenas ant abiejų tipų padėklų pasižymėjo aukšta kokybe: mažu 2D linijos plociu ( $\leq 32 \text{ cm}^{-1}$ ), dideliu 2D/G smailių intensyvumo santykiu ( $> 2,6$ ) ir nebuvo su defektais susijusios (D) smailės apie  $1350 \text{ cm}^{-1}$  (žr. 26 pav. ir 1.3 lentelę). Koreliacinė 2D ir G smailių pozicijų analizė (žr. 26b pav.) leido nustatyti, kad grafenas ant abiejų tipų padėklų turi  $\leq 5 \times 10^{12} \text{ cm}^{-2}$  krūvininkų tankį. Detalesnis grafeno elektrinių savybių tyrimas atliktas naudojant bekontaktę THz spektroskopiją (THz-TDS ir FTIR), kurios eksperimentiniai rezultatai buvo suderinti su analitine pralaidumo formule, įskaitančia krūvininkų įtaką pagal Drude modelį. Nustatytos standartinės puslaidininkų elektrinės savybės (krūvininkų judris  $\mu$ , dvimatis krūvininkų tankis  $N_s$ , sluoksnio varža  $R_{sh}$ ) pateikiamos 1.4 lentelėje. Grafenas ant silicio padėklo, nuvalytas sukurtu metodu, pasižymėjo itin mažu krūvininkų tankiu ( $0,8 \times 10^{12} \text{ cm}^{-2}$ ) ir dideliu krūvininkų judriu, kuris siekė net  $6910 \text{ cm}^2 \text{ V}^{-1} \text{ s}^{-1}$ . Grafenas ant AlGaIn/GaN HEMT struktūros pasižymėjo kiek didesniu krūvininkų tankiu ( $3,2 \times 10^{12} \text{ cm}^{-2}$ ), tačiau taip pat dideliu krūvininkų judriu  $\sim 3000 \text{ cm}^2 \text{ V}^{-1} \text{ s}^{-1}$  ir, autorių žiniomis, tai pirmieji grafeno krūvininkų judrio ant GaN paviršiaus rezultatai.

Taip pat sukurtas metodas naudojant standartinę UV litografijos technologiją CVD grafenui struktūrizuoti išvengiant sąlyčio tarp fotorezisto ir grafeno [P7]. Šiuo metodu specifinio UV fotorezisto suformuota kaukė naudojama kaip tarpinė kaukė PMMA eksponavimui naudojant gilaus UV (254 nm) spinduliuotę, kuri vėliau naudojama grafenui struktūrizuoti plazminio išdininimo būdu. Viso proceso seka pateikiama 28 pav. Panaudojant atraminę PMMA sluoksnį, naudojamą CVD grafenui pernešti, standartiniais metodais papildomas fotorezisto sluoksnis. Šis fotorezistas turi būti specialiai parinktas, kad sugertų ne tik UV, bet ir 254 nm spinduliuotę – kad galėtų veikti kaip neprašviečiama kaukė 254 nm spinduliuotei, eksponuojant atidengtą PMMA sluoksnį. Panaudota fotorezisto kaukė PMMA eksponuoti pašalinama, kad būtų galima atlikti PMMA ryškinimą, naudojant izopropanolio ir vandens (3:1) ryškalą remiantis idėja iš [P6]. Suformavus norimą struktūrą iš PMMA, atliekamas atidengto grafeno pašalinimas naudojant deguonies plazmą. Gaunamos elektriškai izoliuotos norimos grafeno struktūros, apsaugotos PMMA. Toliau atliekama PMMA šalinimo procedūra pagal straipsnį [P6] – 254 nm eksponavimas ir fotochemiškai

suardyto PMMA šalinimas naudojant izopropanolio ir vandens (3:1) tirpalą. Viso šio proceso metu norimos grafeno struktūros yra apsaugotos PMMA ir išvengia papildomo cheminio legiravimo iš UV fotorezisto ar dėl jo ryškų kontakto.

#### 4. Ploni pirolitinės anglies sluoksniai

Kaip matyti iš ankstesnio skyriaus, norint išnaudoti grafeno elektrinių savybių potencialą, reikia skirti daug dėmesio jam pernešti, valyti ir struktūruoti. Jei galutiniam taikymui DC režimu ar THz dažnių ruože nėra reikalinga laidumo savybių moduliacija (elektrinė ar optinė), galima naudoti alternatyvius plonus plėveles anglies pagrindu – plonus pirolitinės anglies sluoksnius. Ploni pirolitinės anglies sluoksniai, tiksliau CVD nusodintos pirolitinės anglies (PyC) ir pirolizuoto fotorezisto (PPF) sluoksniai, pasižymi palyginamu laidumu plačiame dažnių diapazone ir svarbiausia yra lengvai pagaminami ir chemiškai atsparūs bei mechaniškai tvirti [207, 208]. Šiame skyriuje aptariami PPF [P8] ir PyC [P9] rezultatai bei taikymo THz dažnių ruože pavyzdžiai.

PPF sluoksnių, pagamintų pirolizuojant neigiamą elektronų pluošto litografijos rezistą AZ nLOF 2070 charakterizavimas DC režime ir THz dažnių ruože, publikuotas [P8]. Iš DC režimo van der Pauw sluoksnio varžos matavimų kambario temperatūroje nustatyta, kad sluoksnio varža yra atvirkščiai proporcinga sluoksnio storiui, o tai rodo, jog krūvininkų sklaida sluoksnio paviršiuje neturi reikšmingos įtakos krūvio pernašai sluoksnyje. Visi sluoksnio varžos, sluoksnių storių ir sluoksnio storio sumažėjimo po pirolizės faktoriai pateikiami 1.5 lentelėje. Mažiausios PPF sluoksnių varžos apie 470–570  $\Omega/\text{kv.}$  gautos pirolizuojant 900 °C temperatūroje su galutiniu storiu apie 150–160 nm (savitoji varža apie 7–9  $\text{m}\Omega\text{ cm}$ ). Tiriant PPF sluoksnių laidumą (padėklas – silicio nitridu  $\text{Si}_3\text{N}_4$  padengtas silicis) naudojantis THz-TDS dažnių ruože iki 1,5 THz nustatyta, kad sluoksniai pasižymi tuo pačia  $\sim 8\text{ m}\Omega\text{ cm}$  savitąja varža (savitasis laidumas apie  $1,3 \times 10^4\text{ S/m}$ ) su krūvininkų sklaidos laiko verte, mažesne nei 10 fs. Esant tokiam trumpam krūvininkų sklaidos laikui, šių sluoksnių laidumą galima laikyti nepriklausomą nuo dažnio bent iki 1,5 THz ribos ir tinkamą taikymams visame dažnių ruože. Darbo metu pavyko sukurti keletą optinių elementų iš PPF pavyzdžių (250 nm pločio nanogardelė ir metapaviršiaus  $\sim 40\text{ }\mu\text{m}$  dydžio C-formos metatomas) (žr. 31 pav.).

Jei reikia itin plono laidaus sluoksnio, tada CVD nusodinti PyC sluoksniai yra tinkamesni nei PPF. Pavyko sukurti 20 nm storio PyC danga 300 nm storio

$\text{Si}_3\text{N}_4$  membranai su itin plačiąjuoste sugertimi THz-NIR dažnių ruožuose bolometriniam spinduliuotės sugėrikliui [P9]. Nusodinus PyC ant 300 nm storio  $\text{Si}_3\text{N}_4$  padengto silicio padėklo buvo suformuota  $1 \times 1 \text{ mm}^2$  ploto membrana (PyC/ $\text{Si}_3\text{N}_4$ ). Užauginto 20 nm storio PyC sluoksnio varža siekė  $600 \Omega/\text{kv.}$ , tai reiškia, kad nusodinto PyC savitoji varža yra >6 kartus mažesnė. Atliekant THz ruožo pralaidumo (THz-TDS) bei NIR ruožo pralaidumo, atspindžio (FTIR) spektroskopijas buvo apskaičiuota PyC/ $\text{Si}_3\text{N}_4$  membranos sugertis dažnių juostoje tarp 0,5–200 THz (žr. 33c pav.). Dažnių ruože iki apie 20 THz gauta pastovioji sugertis virš 40 %, o dažnių ruože nuo 20–200 THz sugertis nuo 10 iki 40 %.

Reikia pažymėti, kad tiek PPF, tiek PyC savitoji varža yra daug didesnė nei metalų, tačiau su abiem pirolitinės anglies sluoksnių tipais pasiektos sluoksnio varžos apie  $500 \Omega/\text{kv.}$ , o tai yra tipinė CVD grafeno sluoksnio varžos vertė.

## IŠVADOS

1. Plonoji AlGa<sub>N</sub>/Ga<sub>N</sub> HEMT struktūra, užauginta ant SiC padėklo be storo akceptorinėmis priemaišomis kompensuoto Ga<sub>N</sub> buferinio sluoksnio, pasižymi dideliu 2DEG tankiu ir pramušimo lauku iki 0,8 MV/cm bei didesniu šiluminiu laidumu dėl mažo storio heterostruktūros dizaino.

2. Keturnaris 9 nm storio suderintos su Ga<sub>N</sub> gardelės InAlGa<sub>N</sub> barjerinis sluoksnis buvo sukurtas HEMT struktūrai. Detalus struktūrinių, optinių ir elektrinių savybių tyrimas leido nustatyti barjero sudėtį. Nors naudojamas tik 9 nm storio barjeras, gautos didelio  $1,2 \times 10^{13} \text{ cm}^{-2}$  tankio 2DEG su gerokai sumažinta atkirtos įtampa  $-1,74 \text{ V}$ .

3. Efektinis gaudyklių tankis, nustatytas naudojant McWhorter modelį ir žemadažnių AlGa<sub>N</sub>/Ga<sub>N</sub> HEMT triukšmų rezultatus, koreliavo su SIMS ir terahercinės elektroliuminescencijos spektroskopijų rezultatais. Tai rodo, kad triukšmo matavimas yra jautrus metodas siekiant įvertinti medžiagos kokybę.

4. Visuose tirtose AlGa<sub>N</sub>/Ga<sub>N</sub> ir AlGa<sub>N</sub>/AlN/Ga<sub>N</sub> HEMT struktūrose buvo nustatytas didesnis savaiminis kontaktinės varžos nei 2DEG sluoksnio varžos kaitimas nuo srovės. Nustatyta, kad savaiminis kontaktinės varžos kaitimas proporcingas galiai, išsklaidytai kontaktuose.

5. Jautri THz detekcija be postūmio įtampos nustatyta AlGa<sub>N</sub>/Ga<sub>N</sub> BT diodinių jutiklių, pasižyminčių aiškia IV asimetrija 295 K temperatūroje. BT diodinių jutiklių varža didėjo netiesiškai greičiau nei jų jautris. Tai indikuoja, kad BT jutiklių kakliuko siaurinimas mažiau nei iki keleto mikronų pločio yra neefektyvus kuriant jutiklius, pasižyminčius mažomis NEP vertėmis.

6. Mažesnis jautris be postūmio įtampos gautas AlGa<sub>N</sub>/Ga<sub>N</sub> BT bolometrinių jutiklių, kurių IV yra simetrinė, tačiau jautris gali būti padidintas iki panašaus lygio pridendant  $\pm 0,4 \text{ V}$  išorinio postūmio įtampą. Atšaldžius jutiklius iki 80 K temperatūros, padidėjo IV charakteristikos netiesiškumas, kuris nulėmė didesnę jautrį įtampų regione iki  $\pm 0,4 \text{ V}$ .

7. Sukurtas metodas PMMA atraminiam sluoksniui šalinti nuo pernešto CVD grafeno naudojant 254 nm fotocheminį ardymą ir pašalinimą izopropanolio ir vandens tirpale. Naudojant šį metodą PMMA valyti iš THz-TDS pralaidumo spektrų nustatyta, kad krūvininkų judris siekė iki  $6900 \text{ cm}^2 \text{ V}^{-1} \text{ s}^{-1}$ .

8. Sukurtas pernešto CVD grafeno struktūravimo metodas grindžiamas standartine UV litografija ant atraminio PMMA ir sukurtu PMMA šalinimo metodu. Naudojant šį metodą, suformuota tarpinė fotorezisto kaukė yra naudojama formuoti galutinei kaukei iš PMMA grafenui struktūruoti. Viso proceso metu yra užtikrinama, kad grafeno struktūros nesiliestų su fotorezistu ar jo liekanomis, o tai leidžia išvengti papildomo cheminio legiravimo grafene.
9. PPF sluoksniai pagaminti pirolizuojant AZ nLOF 2070 rezistą, o PyC sluoksniai, pagaminti CVD, pasižymi nuo dažnio nepriklausomu laidumu THz dažnių ruože ir leidžia pasiekti sluoksnio varžas, artimas grafeno sluoksnio varžai. Šie laidūs pirolitinės anglies sluoksniai gali būti naudojami kaip grafeno alternatyva THz dažnių ruožo taikymams.

## REFERENCES

- [1] M. Buffolo *et al.*, “Defects and Reliability of GaN-Based LEDs: Review and Perspectives,” *Phys. status solidi*, vol. 219, no. 8, Apr. 2022, doi: 10.1002/pssa.202100727.
- [2] P. Tian *et al.*, “High-speed underwater optical wireless communication using a blue GaN-based micro-LED,” *Opt. Express*, vol. 25, no. 2, p. 1193, Jan. 2017, doi: 10.1364/OE.25.001193.
- [3] H. S. Wasisto, J. D. Prades, J. Gülink, and A. Waag, “Beyond solid-state lighting: Miniaturization, hybrid integration, and applications of GaN nano- and micro-LEDs,” *Appl. Phys. Rev.*, vol. 6, no. 4, Dec. 2019, doi: 10.1063/1.5096322.
- [4] R. Sun, J. Lai, W. Chen, and B. Zhang, “GaN Power Integration for High Frequency and High Efficiency Power Applications: A Review,” *IEEE Access*, vol. 8, pp. 15529–15542, 2020, doi: 10.1109/ACCESS.2020.2967027.
- [5] M. Meneghini *et al.*, “GaN-based power devices: Physics, reliability, and perspectives,” *J. Appl. Phys.*, vol. 130, no. 18, Nov. 2021, doi: 10.1063/5.0061354.
- [6] H. Amano *et al.*, “The 2018 GaN power electronics roadmap,” *J. Phys. D. Appl. Phys.*, vol. 51, no. 16, p. 163001, Apr. 2018, doi: 10.1088/1361-6463/aaaf9d.
- [7] B. J. Baliga, “Power semiconductor device figure of merit for high-frequency applications,” *IEEE Electron Device Lett.*, vol. 10, no. 10, pp. 455–457, Oct. 1989, doi: 10.1109/55.43098.
- [8] Q. Yu *et al.*, “A Fully Integrated 3.2-4.7GHz Doherty Power Amplifier in 300nm GaN-on-Si Technology,” in *2022 IEEE BiCMOS and Compound Semiconductor Integrated Circuits and Technology Symposium (BCICTS)*, IEEE, Oct. 2022, pp. 144–147. doi: 10.1109/BCICTS53451.2022.10051762.
- [9] H. W. Then *et al.*, “Enhancement-Mode 300-mm GaN-on-Si(111) With Integrated Si CMOS for Future mm-Wave RF Applications,” *IEEE Microw. Wirel. Technol. Lett.*, vol. 33, no. 6, pp. 835–838, Jun. 2023, doi: 10.1109/LMWT.2023.3268184.
- [10] Q. Yu *et al.*, “Advancements in 300 mm GaN-on-Si Technology With Industry’s First Circuit Demonstration of Monolithically Integrated GaN and Si Transistors,” *IEEE Microw. Wirel. Technol. Lett.*, pp. 1–4, 2024, doi: 10.1109/LMWT.2024.3383390.
- [11] E. Frayssinet *et al.*, “High electron mobility in AlGaIn/GaN heterostructures grown on bulk GaN substrates,” *Appl. Phys. Lett.*, vol. 77, no. 16, pp. 2551–2553, Oct. 2000, doi: 10.1063/1.1318236.
- [12] J. Kuzmík, “Power electronics on InAlN/(In)GaN: Prospect for a record performance,” *IEEE Electron Device Lett.*, vol. 22, no. 11, pp. 510–512, 2001, doi: 10.1109/55.962646.
- [13] J. Kuzmík, “InAlN/(In)GaN high electron mobility transistors: Some aspects

- of the quantum well heterostructure proposal,” *Semicond. Sci. Technol.*, vol. 17, no. 6, pp. 540–544, 2002, doi: 10.1088/0268-1242/17/6/307.
- [14] F. Medjdoub *et al.*, “Barrier-Layer Scaling of InAlN/GaN HEMTs,” *IEEE Electron Device Lett.*, vol. 29, no. 5, pp. 422–425, May 2008, doi: 10.1109/LED.2008.919377.
- [15] V. Jakštas, “Kompatiški AlGaIn/GaN heterosandūriniai terahercinės spinduliuotės šaltiniai,” Vilnius University, 2018.
- [16] M. A. Yamoah, W. Yang, E. Pop, and D. Goldhaber-Gordon, “High-Velocity Saturation in Graphene Encapsulated by Hexagonal Boron Nitride,” *ACS Nano*, vol. 11, no. 10, pp. 9914–9919, Oct. 2017, doi: 10.1021/acsnano.7b03878.
- [17] S. Ghosh *et al.*, “Extremely high thermal conductivity of graphene: Prospects for thermal management applications in nanoelectronic circuits,” *Appl. Phys. Lett.*, vol. 92, no. 15, Apr. 2008, doi: 10.1063/1.2907977.
- [18] M. Gromovyi *et al.*, “Low-loss GaN-on-insulator platform for integrated photonics,” *Opt. Express*, vol. 30, no. 12, p. 20737, Jun. 2022, doi: 10.1364/OE.461138.
- [19] D. Li, K. Jiang, X. Sun, and C. Guo, “AlGaIn photonics: recent advances in materials and ultraviolet devices,” *Adv. Opt. Photonics*, vol. 10, no. 1, p. 43, Mar. 2018, doi: 10.1364/AOP.10.000043.
- [20] Y. Zheng *et al.*, “Integrated Gallium Nitride Nonlinear Photonics,” *Laser Photon. Rev.*, vol. 16, no. 1, Jan. 2022, doi: 10.1002/lpor.202100071.
- [21] Y. Zhao *et al.*, “Low-threshold AlGaIn-based deep ultraviolet laser enabled by a nanoporous cladding layer,” *Opt. Lett.*, vol. 49, no. 4, p. 1061, Feb. 2024, doi: 10.1364/OL.511224.
- [22] Z. Zhang *et al.*, “Key temperature-dependent characteristics of AlGaIn-based UV-C laser diode and demonstration of room-temperature continuous-wave lasing,” *Appl. Phys. Lett.*, vol. 121, no. 22, Nov. 2022, doi: 10.1063/5.0124480.
- [23] M. Usman, S. Malik, and M. Munsif, “AlGaIn-based ultraviolet light-emitting diodes: challenges and opportunities,” *Luminescence*, vol. 36, no. 2, pp. 294–305, Mar. 2021, doi: 10.1002/bio.3965.
- [24] P. Sai *et al.*, “Electrical Tuning of Terahertz Plasmonic Crystal Phases,” Apr. 2023, [Online]. Available: <http://arxiv.org/abs/2305.00211>
- [25] V. V. Popov, “Plasmon excitation and plasmonic detection of terahertz radiation in the grating-gate field-effect-transistor structures,” *J. Infrared, Millimeter, Terahertz Waves*, vol. 32, no. 10, pp. 1178–1191, 2011, doi: 10.1007/s10762-011-9813-6.
- [26] M. Shur, G. Aizin, T. Otsuji, and V. Ryzhii, “Plasmonic Field-Effect Transistors (TeraFETs) for 6G Communications,” *Sensors*, vol. 21, no. 23, p. 7907, Nov. 2021, doi: 10.3390/s21237907.
- [27] M. Bauer *et al.*, “A High-Sensitivity AlGaIn/GaN HEMT Terahertz Detector With Integrated Broadband Bow-Tie Antenna,” *IEEE Trans. Terahertz Sci. Technol.*, vol. 9, no. 4, pp. 430–444, Jul. 2019, doi:



- 10.1109/TTHZ.2019.2917782.
- [28] J. Sun *et al.*, “Smaller antenna-gate gap for higher sensitivity of GaN/AlGa<sub>N</sub> HEMT terahertz detectors,” *Appl. Phys. Lett.*, vol. 116, no. 16, p. 161109, Apr. 2020, doi: 10.1063/1.5142436.
- [29] D. Voß *et al.*, “Imaging and Spectroscopic Sensing with Low-Repetition-Rate Terahertz Pulses and GaN TeraFET Detectors,” *J. Infrared, Millimeter, Terahertz Waves*, vol. 39, no. 3, pp. 262–272, 2018, doi: 10.1007/s10762-017-0447-1.
- [30] M. Bauer *et al.*, “Optimization of the Design of Terahertz Detectors Based on Si CMOS and AlGa<sub>N</sub>/Ga<sub>N</sub> Field-Effect Transistors,” *Int. J. High Speed Electron. Syst.*, vol. 25, no. 03n04, p. 1640013, 2016, doi: 10.1142/S0129156416400139.
- [31] J. Sun *et al.*, “Two-terminal terahertz detectors based on AlGa<sub>N</sub>/Ga<sub>N</sub> high-electron-mobility transistors,” *Appl. Phys. Lett.*, vol. 115, no. 11, p. 111101, Sep. 2019, doi: 10.1063/1.5114682.
- [32] J. Vyšniauskas, K. Ikamas, D. Vizbaras, and A. Lisauskas, “Two-dimensional hydrodynamic modelling of AlGa<sub>N</sub>/Ga<sub>N</sub> transistor-based THz detectors,” *Lith. J. Phys.*, vol. 63, no. 4, Dec. 2023, doi: 10.3952/physics.2023.63.4.4.
- [33] J. Holstein *et al.*, “8x8 Patch-Antenna-Coupled TeraFET Detector Array for Terahertz Quantum-Cascade-Laser Applications,” Apr. 2024, [Online]. Available: <http://arxiv.org/abs/2404.07309>
- [34] P. Sai *et al.*, “AlGa<sub>N</sub>/Ga<sub>N</sub> field effect transistor with two lateral Schottky barrier gates towards resonant detection in sub-mm range,” *Semicond. Sci. Technol.*, vol. 34, no. 2, p. 24002, 2019, doi: 10.1088/1361-6641/aaf4a7.
- [35] G. Cywiński *et al.*, “Electrically controlled wire-channel Ga<sub>N</sub>/AlGa<sub>N</sub> transistor for terahertz plasma applications,” *Appl. Phys. Lett.*, vol. 112, no. 13, p. 133502, 2018, doi: 10.1063/1.5023391.
- [36] H. Sánchez-Martín *et al.*, “Ga<sub>N</sub> nanodiode arrays with improved design for zero-bias sub-THz detection,” *Semicond. Sci. Technol.*, vol. 33, no. 9, p. 095016, Sep. 2018, doi: 10.1088/1361-6641/aad766.
- [37] I. Íñiguez-de-la-Torre *et al.*, “Current and voltage responsivity up to 110 GHz in Ga<sub>N</sub> asymmetric nano-diodes,” *Appl. Phys. Lett.*, vol. 123, no. 12, Sep. 2023, doi: 10.1063/5.0167277.
- [38] V. Mitin, V. Pogrebnyyak, M. Shur, R. Gaska, B. Karasik, and A. Sergeev, “Hot-electron micro & nanobolometers based on low-mobility 2DEG for high resolution THz spectroscopy,” *J. Phys. Conf. Ser.*, vol. 486, p. 012028, Mar. 2014, doi: 10.1088/1742-6596/486/1/012028.
- [39] J. K. Choi *et al.*, “THz Hot-Electron Micro-Bolometer Based on Low-Mobility 2-DEG in Ga<sub>N</sub> Heterostructure,” *IEEE Sens. J.*, vol. 13, no. 1, pp. 80–88, Jan. 2013, doi: 10.1109/JSEN.2012.2224334.
- [40] D. Maier *et al.*, “InAl<sub>N</sub>/Ga<sub>N</sub> HEMTs for Operation in the 1000 C Degrees Regime: A First Experiment,” *IEEE Electron Device Lett.*, vol. 33, no. 7, pp. 985–987, 2012, doi: 10.1109/LED.2012.2196972.

- [41] J. Lu *et al.*, “Very high channel conductivity in ultra-thin channel N-polar GaN/(AlN, InAlN, AlGaIn) high electron mobility hetero-junctions grown by metalorganic chemical vapor deposition,” *Appl. Phys. Lett.*, vol. 102, no. 23, p. 232104, 2013, doi: 10.1063/1.4809997.
- [42] H. S. Lee, D. Piedra, M. Sun, X. Gao, S. Guo, and T. Palacios, “3000-V 4.3-m $\Omega$   $\times$  cm<sup>2</sup> InAlN/GaN MOSHEMTs with AlGaIn back barrier,” *IEEE Electron Device Lett.*, vol. 33, no. 7, pp. 982–984, 2012, doi: 10.1109/LED.2012.2196673.
- [43] A. Yamada *et al.*, “31 W/mm at 8 GHz in InAlGaIn/GaN HEMT with thermal CVD SiN<sub>x</sub> passivation,” *IEEE Electron Device Lett.*, pp. 1–1, 2024, doi: 10.1109/LED.2024.3355051.
- [44] I. Sanyal *et al.*, “AlInGaIn/GaN HEMTs With High Johnson’s Figure-of-Merit on Low Resistivity Silicon Substrate,” *IEEE J. Electron Devices Soc.*, vol. 9, pp. 130–136, 2021, doi: 10.1109/JEDS.2020.3043279.
- [45] W. Wang *et al.*, “Improvement of Power Performance of GaN HEMT by Using Quaternary InAlGaIn Barrier,” *IEEE J. Electron Devices Soc.*, vol. 6, pp. 360–364, 2018, doi: 10.1109/JEDS.2018.2807185.
- [46] K. S. Novoselov *et al.*, “Electric Field Effect in Atomically Thin Carbon Films,” *Science (80-. )*, vol. 306, no. 5696, pp. 666–669, Oct. 2004, doi: 10.1126/science.1102896.
- [47] A. K. Geim and K. S. Novoselov, “The rise of graphene,” *Nat. Mater.*, vol. 6, no. 3, pp. 183–191, Mar. 2007, doi: 10.1038/nmat1849.
- [48] K. I. Bolotin, “Electronic transport in graphene: towards high mobility,” in *Graphene*, Elsevier, 2014, pp. 199–227. doi: 10.1533/9780857099334.3.199.
- [49] M. J. Allen, V. C. Tung, and R. B. Kaner, “Honeycomb Carbon: A Review of Graphene,” *Chem. Rev.*, vol. 110, no. 1, pp. 132–145, Jan. 2010, doi: 10.1021/cr900070d.
- [50] N. Norhakim, H. F. Hawari, and Z. A. Burhanudin, “Assessing the Figures of Merit of Graphene-Based Radio Frequency Electronics: A Review of GFET in RF Technology,” *IEEE Access*, vol. 10, pp. 17030–17042, 2022, doi: 10.1109/ACCESS.2022.3147832.
- [51] S. Wittmann, C. Glacier, S. Wagner, S. Pindl, and M. C. Lemme, “Graphene Membranes for Hall Sensors and Microphones Integrated with CMOS-Compatible Processes,” *ACS Appl. Nano Mater.*, vol. 2, no. 8, pp. 5079–5085, Aug. 2019, doi: 10.1021/acsanm.9b00998.
- [52] D. J. Buckley, N. C. G. Black, E. G. Castanon, C. Melios, M. Hardman, and O. Kazakova, “Frontiers of graphene and 2D material-based gas sensors for environmental monitoring,” *2D Mater.*, vol. 7, no. 3, p. 032002, Jul. 2020, doi: 10.1088/2053-1583/ab7bc5.
- [53] F. Giannazzo *et al.*, “Graphene integration with nitride semiconductors for high power and high frequency electronics,” *Phys. status solidi*, vol. 214, no. 4, p. 1600460, Apr. 2017, doi: 10.1002/pssa.201600460.
- [54] R. R. Nair *et al.*, “Fine Structure Constant Defines Visual Transparency of

- Graphene,” *Science* (80-. ), vol. 320, no. 5881, pp. 1308–1308, Jun. 2008, doi: 10.1126/science.1156965.
- [55] S. Goossens *et al.*, “Broadband image sensor array based on graphene–CMOS integration,” *Nat. Photonics*, vol. 11, no. 6, pp. 366–371, Jun. 2017, doi: 10.1038/nphoton.2017.75.
- [56] K. Arts, R. Vervuurt, A. Bhattacharya, J. Gómez Rivas, J. W. Oosterbeek, and A. A. Bol, “Broadband optical response of graphene measured by terahertz time-domain spectroscopy and FTIR spectroscopy,” *J. Appl. Phys.*, vol. 124, no. 7, Aug. 2018, doi: 10.1063/1.5044265.
- [57] J. M. Dawlaty *et al.*, “Measurement of the optical absorption spectra of epitaxial graphene from terahertz to visible,” *Appl. Phys. Lett.*, vol. 93, no. 13, Sep. 2008, doi: 10.1063/1.2990753.
- [58] L. Vicarelli *et al.*, “Graphene field-effect transistors as room-temperature terahertz detectors,” *Nat. Mater.*, vol. 11, no. 10, pp. 865–871, Oct. 2012, doi: 10.1038/nmat3417.
- [59] R. M. G K, P. Deshmukh, S. S. Prabhu, and P. K. Basu, “Antenna coupled graphene-FET as ultra-sensitive room temperature broadband THz detector,” *AIP Adv.*, vol. 8, no. 12, Dec. 2018, doi: 10.1063/1.5063399.
- [60] H. Qin *et al.*, “Room-temperature, low-impedance and high-sensitivity terahertz direct detector based on bilayer graphene field-effect transistor,” *Carbon N. Y.*, vol. 116, pp. 760–765, May 2017, doi: 10.1016/j.carbon.2017.02.037.
- [61] A. A. Generalov, M. A. Andersson, X. Yang, A. Vorobiev, and J. Stake, “A 400-GHz Graphene FET Detector,” *IEEE Trans. Terahertz Sci. Technol.*, vol. 7, no. 5, pp. 614–616, Sep. 2017, doi: 10.1109/TTHZ.2017.2722360.
- [62] D. Vizbaras, K. Ikamas, S. Pralgauskaitė, J. Matukas, A. A. Generalov, and A. Lisauskas, “Optimization of terahertz detectors based on graphene field effect transistors by high impedance antennae,” *Lith. J. Phys.*, vol. 62, no. 4, Dec. 2022, doi: 10.3952/physics.v62i4.4822.
- [63] F. Ludwig *et al.*, “Terahertz Detection with Graphene FETs: Photothermoelectric and Resistive Self-Mixing Contributions to the Detector Response,” *ACS Appl. Electron. Mater.*, vol. 6, no. 4, pp. 2197–2212, Apr. 2024, doi: 10.1021/acsaelm.3c01511.
- [64] J. Yan *et al.*, “Dual-gated bilayer graphene hot-electron bolometer,” *Nat. Nanotechnol.*, vol. 7, no. 7, pp. 472–478, Jul. 2012, doi: 10.1038/nnano.2012.88.
- [65] A. Zoghi and H. Rasooli Saghai, “Enhancing performance of graphene-based bolometers at 1 THz,” *Phys. C Supercond. its Appl.*, vol. 557, pp. 44–48, Feb. 2019, doi: 10.1016/j.physc.2018.10.008.
- [66] A. Rogalski, “Graphene-based materials in the infrared and terahertz detector families: a tutorial,” *Adv. Opt. Photonics*, vol. 11, no. 2, p. 314, Jun. 2019, doi: 10.1364/AOP.11.000314.
- [67] J. Liu *et al.*, “Recent Progress in the Development of Graphene Detector for

- Terahertz Detection,” *Sensors*, vol. 21, no. 15, p. 4987, Jul. 2021, doi: 10.3390/s21154987.
- [68] W. Kong *et al.*, “Polarity governs atomic interaction through two-dimensional materials,” *Nat. Mater.*, vol. 17, no. 11, pp. 999–1004, Nov. 2018, doi: 10.1038/s41563-018-0176-4.
- [69] J. Jeong *et al.*, “Transferable, flexible white light-emitting diodes of GaN p–n junction microcrystals fabricated by remote epitaxy,” *Nano Energy*, vol. 86, p. 106075, Aug. 2021, doi: 10.1016/j.nanoen.2021.106075.
- [70] K. Qiao *et al.*, “Graphene Buffer Layer on SiC as a Release Layer for High-Quality Freestanding Semiconductor Membranes,” *Nano Lett.*, vol. 21, no. 9, pp. 4013–4020, May 2021, doi: 10.1021/acs.nanolett.1c00673.
- [71] M. Dub *et al.*, “Graphene as a Schottky Barrier Contact to AlGaIn/GaN Heterostructures,” *Materials (Basel)*, vol. 13, no. 18, p. 4140, Sep. 2020, doi: 10.3390/ma13184140.
- [72] G. Fisichella, G. Greco, F. Roccaforte, and F. Giannazzo, “Current transport in graphene/AlGaIn/GaN vertical heterostructures probed at nanoscale,” *Nanoscale*, vol. 6, no. 15, pp. 8671–8680, 2014, doi: 10.1039/C4NR01150C.
- [73] J. Kierdaszuk *et al.*, “Highly effective gating of graphene on GaN,” *Appl. Surf. Sci.*, vol. 560, p. 149939, Sep. 2021, doi: 10.1016/j.apsusc.2021.149939.
- [74] F. Lin *et al.*, “Graphene/GaN diodes for ultraviolet and visible photodetectors,” *Appl. Phys. Lett.*, vol. 105, no. 7, Aug. 2014, doi: 10.1063/1.4893609.
- [75] S. Wang *et al.*, “Highly-Rectifying Graphene/GaN Schottky Contact for Self-Powered UV Photodetector,” *IEEE Photonics Technol. Lett.*, vol. 33, no. 4, pp. 213–216, Feb. 2021, doi: 10.1109/LPT.2021.3052171.
- [76] H. Tian, Q. Liu, A. Hu, X. He, Z. Hu, and X. Guo, “Hybrid graphene/GaN ultraviolet photo-transistors with high responsivity and speed,” *Opt. Express*, vol. 26, no. 5, p. 5408, Mar. 2018, doi: 10.1364/OE.26.005408.
- [77] C. Melios *et al.*, “Towards standardisation of contact and contactless electrical measurements of CVD graphene at the macro-, micro- and nano-scale,” *Sci. Rep.*, vol. 10, no. 1, p. 3223, Dec. 2020, doi: 10.1038/s41598-020-59851-1.
- [78] N. McEvoy *et al.*, “Synthesis and analysis of thin conducting pyrolytic carbon films,” *Carbon N. Y.*, vol. 50, no. 3, pp. 1216–1226, Mar. 2012, doi: 10.1016/j.carbon.2011.10.036.
- [79] T. Kaplas and Y. Svirko, “Direct deposition of semitransparent conducting pyrolytic carbon films,” *J. Nanophotonics*, vol. 6, no. 1, p. 061703, Oct. 2012, doi: 10.1117/1.JNP.6.061703.
- [80] J. A. Lee, K.-C. Lee, S. Il Park, and S. S. Lee, “The fabrication of carbon nanostructures using electron beam resist pyrolysis and nanomachining processes for biosensing applications,” *Nanotechnology*, vol. 19, no. 21, p. 215302, May 2008, doi: 10.1088/0957-4484/19/21/215302.
- [81] R. Kostecki, B. Schnyder, D. Alliata, X. Song, K. Kinoshita, and R. Kötz, “Surface studies of carbon films from pyrolyzed photoresist,” *Thin Solid Films*, vol. 396, no. 1–2, pp. 36–43, Sep. 2001, doi: 10.1016/S0040-

6090(01)01185-3.

- [82] J. Kim, X. Song, K. Kinoshita, M. Madou, and R. White, “Electrochemical Studies of Carbon Films from Pyrolyzed Photoresist,” *J. Electrochem. Soc.*, vol. 145, no. 7, pp. 2314–2319, Jul. 1998, doi: 10.1149/1.1838636.
- [83] M. J. Matthews, M. A. Pimenta, G. Dresselhaus, M. S. Dresselhaus, and M. Endo, “Origin of dispersive effects of the Raman D band in carbon materials,” *Phys. Rev. B*, vol. 59, no. 10, pp. R6585–R6588, Mar. 1999, doi: 10.1103/PhysRevB.59.R6585.
- [84] U. Sassi *et al.*, “Graphene-based mid-infrared room-temperature pyroelectric bolometers with ultrahigh temperature coefficient of resistance,” *Nat. Commun.*, vol. 8, no. 1, p. 14311, Jan. 2017, doi: 10.1038/ncomms14311.
- [85] G.-H. Lee *et al.*, “Graphene-based Josephson junction microwave bolometer,” *Nature*, vol. 586, no. 7827, pp. 42–46, Oct. 2020, doi: 10.1038/s41586-020-2752-4.
- [86] Z. Liu, Z. Liang, W. Tang, and X. Xu, “Design and fabrication of low-deformation micro-bolometers for THz detectors,” *Infrared Phys. Technol.*, vol. 105, p. 103241, Mar. 2020, doi: 10.1016/j.infrared.2020.103241.
- [87] S. Keller, “Substrates and Materials,” in *Power GaN Devices: Materials, Applications and Reliability*, M. Meneghini, G. Meneghesso, and E. Zanoni, Eds., Springer Cham, 2017, pp. 27–52. doi: 10.1007/978-3-319-43199-4\_2.
- [88] L. Liu and J. H. Edgar, “Substrates for gallium nitride epitaxy,” *Mater. Sci. Eng. R Reports*, vol. 37, no. 3, pp. 61–127, Apr. 2002, doi: 10.1016/S0927-796X(02)00008-6.
- [89] L. Shen *et al.*, “AlGaN/AlN/GaN high-power microwave HEMT,” *IEEE Electron Device Lett.*, vol. 22, no. 10, pp. 457–459, Oct. 2001, doi: 10.1109/55.954910.
- [90] I. P. Smorchkova *et al.*, “AlN/GaN and (Al,Ga)N/AlN/GaN two-dimensional electron gas structures grown by plasma-assisted molecular-beam epitaxy,” *J. Appl. Phys.*, vol. 90, no. 10, pp. 5196–5201, Nov. 2001, doi: 10.1063/1.1412273.
- [91] L. Hsu and W. Walukiewicz, “Effect of polarization fields on transport properties in AlGa<sub>x</sub>N/GaN heterostructures,” *J. Appl. Phys.*, vol. 89, no. 3, pp. 1783–1789, Feb. 2001, doi: 10.1063/1.1339858.
- [92] J.-T. Chen *et al.*, “Room-temperature mobility above 2200 cm<sup>2</sup>/V·s of two-dimensional electron gas in a sharp-interface AlGa<sub>x</sub>N/GaN heterostructure,” *Appl. Phys. Lett.*, vol. 106, no. 25, Jun. 2015, doi: 10.1063/1.4922877.
- [93] J. Lu *et al.*, “Transmorphic epitaxial growth of AlN nucleation layers on SiC substrates for high-breakdown thin GaN transistors,” *Appl. Phys. Lett.*, vol. 115, no. 22, p. 221601, Nov. 2019, doi: 10.1063/1.5123374.
- [94] H. K. Cho, J. Y. Lee, K. S. Kim, G. M. Yang, J. H. Song, and P. W. Yu, “Effect of buffer layers and stacking faults on the reduction of threading dislocation density in GaN overlayers grown by metalorganic chemical vapor deposition,” *J. Appl. Phys.*, vol. 89, no. 5, pp. 2617–2621, Mar. 2001, doi:

10.1063/1.1344213.

- [95] J. S. Speck, M. A. Brewer, G. Beltz, A. E. Romanov, and W. Pompe, "Scaling laws for the reduction of threading dislocation densities in homogeneous buffer layers," *J. Appl. Phys.*, vol. 80, no. 7, pp. 3808–3816, Oct. 1996, doi: 10.1063/1.363334.
- [96] D. Bisi *et al.*, "Effects of buffer compensation strategies on the electrical performance and RF reliability of AlGaIn/GaN HEMTs," *Microelectron. Reliab.*, vol. 55, no. 9–10, pp. 1662–1666, Aug. 2015, doi: 10.1016/j.microrel.2015.06.038.
- [97] P. Gamarra, C. Lacam, M. Tordjman, J. Spletstösser, B. Schauwecker, and M.-A. di Forte-Poisson, "Optimisation of a carbon doped buffer layer for AlGaIn/GaN HEMT devices," *J. Cryst. Growth*, vol. 414, pp. 232–236, Mar. 2015, doi: 10.1016/j.jcrysgro.2014.10.025.
- [98] D.-Y. Chen *et al.*, "Microwave Performance of 'Buffer-Free' GaN-on-SiC High Electron Mobility Transistors," *IEEE Electron Device Lett.*, vol. 41, no. 6, pp. 828–831, Jun. 2020, doi: 10.1109/LED.2020.2988074.
- [99] J.-T. Chen *et al.*, "A GaN–SiC hybrid material for high-frequency and power electronics," *Appl. Phys. Lett.*, vol. 113, no. 4, p. 041605, Jul. 2018, doi: 10.1063/1.5042049.
- [100] A. Yamada, T. Ishiguro, J. Kotani, and N. Nakamura, "Electron mobility enhancement in metalorganic-vapor-phase-epitaxy-grown InAlN high-electron-mobility transistors by control of surface morphology of spacer layer," *Jpn. J. Appl. Phys.*, vol. 57, no. 1S, p. 01AD01, 2018, doi: 10.7567/JJAP.57.01AD01.
- [101] S. W. Kaun *et al.*, "GaN-based high-electron-mobility transistor structures with homogeneous lattice-matched InAlN barriers grown by plasma-assisted molecular beam epitaxy," *Semicond. Sci. Technol.*, vol. 29, no. 4, 2014, doi: 10.1088/0268-1242/29/4/045011.
- [102] Y. Niida *et al.*, "3.6 W/mm high power density W-band InAlGaIn/GaN HEMT MMIC power amplifier," in *2016 IEEE Topical Conference on Power Amplifiers for Wireless and Radio Applications (PAWR)*, IEEE, Jan. 2016, pp. 24–26. doi: 10.1109/PAWR.2016.7440153.
- [103] F. Medjdoub *et al.*, "High electron mobility in high-polarization sub-10 nm barrier thickness InAlGaIn/GaN heterostructure," *Appl. Phys. Express*, vol. 8, no. 10, p. 101001, 2015, doi: 10.7567/APEX.8.101001.
- [104] D. S. Lee *et al.*, "317 GHz InAlGaIn/GaN HEMTs with extremely low on-resistance," *Phys. status solidi*, vol. 10, no. 5, pp. 827–830, 2013, doi: 10.1002/pssc.201200541.
- [105] R. Wang *et al.*, "Quaternary Barrier InAlGaIn HEMTs With ft/fmax of 230/300 GHz," *IEEE Electron Device Lett.*, vol. 34, no. 3, pp. 378–380, Mar. 2013, doi: 10.1109/LED.2013.2238503.
- [106] H. Sun, K. B. Lee, L. Yuan, W. Wang, S. L. Selvaraj, and G.-Q. Lo, "Theoretical study of short channel effect in highly scaled GaN HEMTs," in *2012 IEEE International Symposium on Radio-Frequency Integration*

- Technology (RFIT)*, IEEE, Nov. 2012, pp. 204–206. doi: 10.1109/RFIT.2012.6401661.
- [107] X. Liang *et al.*, “Toward Clean and Crackless Transfer of Graphene,” *ACS Nano*, vol. 5, no. 11, pp. 9144–9153, Nov. 2011, doi: 10.1021/nn203377t.
- [108] J. W. Suk *et al.*, “Transfer of CVD-Grown Monolayer Graphene onto Arbitrary Substrates,” *ACS Nano*, vol. 5, no. 9, pp. 6916–6924, Sep. 2011, doi: 10.1021/nn201207c.
- [109] A. M. Lyons, “Photodefinable carbon films: Control of image quality,” *J. Vac. Sci. Technol. B Microelectron. Nanom. Struct.*, vol. 3, no. 1, p. 447, Jan. 1985, doi: 10.1116/1.583284.
- [110] M. Schreiber *et al.*, “Transparent ultrathin conducting carbon films,” *Appl. Surf. Sci.*, vol. 256, no. 21, pp. 6186–6190, Aug. 2010, doi: 10.1016/j.apsusc.2010.03.138.
- [111] W. Benzinger, A. Becker, and K. J. Hüttinger, “Chemistry and kinetics of chemical vapour deposition of pyrocarbon: I. Fundamentals of kinetics and chemical reaction engineering,” *Carbon N. Y.*, vol. 34, no. 8, pp. 957–966, 1996, doi: 10.1016/0008-6223(96)00010-3.
- [112] R. Peretti *et al.*, “THz-TDS Time-Trace Analysis for the Extraction of Material and Metamaterial Parameters,” *IEEE Trans. Terahertz Sci. Technol.*, vol. 9, no. 2, pp. 136–149, Mar. 2019, doi: 10.1109/TTHZ.2018.2889227.
- [113] J. Lloyd-Hughes and T.-I. Jeon, “A Review of the Terahertz Conductivity of Bulk and Nano-Materials,” *J. Infrared, Millimeter, Terahertz Waves*, vol. 33, no. 9, pp. 871–925, Sep. 2012, doi: 10.1007/s10762-012-9905-y.
- [114] W. Ma, C. Li, Z. Wang, L. Li, S. Wang, and C. Sun, “Application of Terahertz Time-Domain Spectroscopy in Characterizing Thin Metal Film–Substrate Structures,” *IEEE Trans. Terahertz Sci. Technol.*, vol. 10, no. 6, pp. 593–598, Nov. 2020, doi: 10.1109/TTHZ.2020.3013805.
- [115] P. R. Whelan *et al.*, “Reference-free THz-TDS conductivity analysis of thin conducting films,” *Opt. Express*, vol. 28, no. 20, p. 28819, Sep. 2020, doi: 10.1364/OE.402447.
- [116] J. D. Buron *et al.*, “Electrically Continuous Graphene from Single Crystal Copper Verified by Terahertz Conductance Spectroscopy and Micro Four-Point Probe,” *Nano Lett.*, vol. 14, no. 11, pp. 6348–6355, Nov. 2014, doi: 10.1021/nl5028167.
- [117] P. Bøggild *et al.*, “Mapping the electrical properties of large-area graphene,” *2D Mater.*, vol. 4, no. 4, p. 042003, Sep. 2017, doi: 10.1088/2053-1583/aa8683.
- [118] P. R. Whelan, K. Iwaszczuk, R. Wang, S. Hofmann, P. Bøggild, and P. U. Jepsen, “Robust mapping of electrical properties of graphene from terahertz time-domain spectroscopy with timing jitter correction,” *Opt. Express*, vol. 25, no. 3, p. 2725, Feb. 2017, doi: 10.1364/OE.25.002725.
- [119] P. Gopalan, Y. Wang, and B. Sensale-Rodriguez, “Terahertz characterization of two-dimensional low-conductive layers enabled by metal gratings,” *Sci.*

- Rep.*, vol. 11, no. 1, p. 2833, Feb. 2021, doi: 10.1038/s41598-021-82560-2.
- [120] F. W. Smith *et al.*, “Picosecond GaAs-based photoconductive optoelectronic detectors,” *Appl. Phys. Lett.*, vol. 54, no. 10, pp. 890–892, 1989, doi: 10.1063/1.100800.
- [121] M. van Exter, C. Fattinger, and D. Grischkowsky, “High-brightness terahertz beams characterized with an ultrafast detector,” *Appl. Phys. Lett.*, vol. 55, no. 4, pp. 337–339, 1989, doi: 10.1063/1.101901.
- [122] J. Neu and C. A. Schmuttenmaer, “Tutorial: An introduction to terahertz time domain spectroscopy (THz-TDS),” *J. Appl. Phys.*, vol. 124, no. 23, Dec. 2018, doi: 10.1063/1.5047659.
- [123] V. A. Bershtein and V. A. Ryzhov, “Far infrared spectroscopy of polymers,” in *Polymer Analysis and Characterization*, Berlin/Heidelberg: Springer-Verlag, pp. 43–121. doi: 10.1007/BFb0008694.
- [124] R. Ullah, H. Li, and Y. Zhu, “Terahertz and FTIR spectroscopy of ‘Bisphenol A,’” *J. Mol. Struct.*, vol. 1059, pp. 255–259, Feb. 2014, doi: 10.1016/j.molstruc.2013.11.055.
- [125] Q. Yang *et al.*, “Qualitative and Quantitative Analysis of Caffeine in Medicines by Terahertz Spectroscopy Using Machine Learning Method,” *IEEE Access*, vol. 9, pp. 140008–140021, 2021, doi: 10.1109/ACCESS.2021.3116980.
- [126] T. Azuhata *et al.*, “Optical phonons in GaN,” *Phys. B Condens. Matter*, vol. 219–220, pp. 493–495, Apr. 1996, doi: 10.1016/0921-4526(95)00789-X.
- [127] J. S. Blakemore, “Semiconducting and other major properties of gallium arsenide,” *J. Appl. Phys.*, vol. 53, no. 10, pp. R123–R181, Oct. 1982, doi: 10.1063/1.331665.
- [128] C. B. Lim, “GaN/AlGaN heterostructures for infrared optoelectronics: polar vs nonpolar orientations,” Université Grenoble Alpes, 2017. [Online]. Available: <https://theses.hal.science/tel-01693891>
- [129] M. Naftaly *et al.*, “Sheet Resistance Measurements of Conductive Thin Films: A Comparison of Techniques,” *Electronics*, vol. 10, no. 8, p. 960, Apr. 2021, doi: 10.3390/electronics10080960.
- [130] G. I. Syngayivska and V. V. Korotyeyev, “Electrical and High-Frequency Properties of Compensated GaN under Electron Streaming Conditions,” *Ukr. J. Phys.*, vol. 58, no. 1, pp. 40–55, Jan. 2013, doi: 10.15407/ujpe58.01.0040.
- [131] L. J. van der PAUW, “A Method of Measuring Specific Resistivity and Hall Effect of Discs of Arbitrary Shape,” *Philips Res. Repts.*, vol. 13, pp. 1–9, 1958.
- [132] L. J. van der PAUW, “A Method of Measuring the Resistivity and Hall Coefficient on Lamellae of Arbitrary Shape,” *Philips Tech. Rev.*, vol. 20, pp. 220–224, 1958.
- [133] I. Tan, G. L. Snider, L. D. Chang, and E. L. Hu, “A self-consistent solution of Schrödinger–Poisson equations using a nonuniform mesh,” *J. Appl. Phys.*, vol. 68, no. 8, pp. 4071–4076, 1990, doi: 10.1063/1.346245.



- [134] G. L. Snider, I. -H. Tan, and E. L. Hu, "Electron states in mesa-etched one-dimensional quantum well wires," *J. Appl. Phys.*, vol. 68, no. 6, pp. 2849–2853, 1990, doi: 10.1063/1.346443.
- [135] W. Shockley, A. Goetzberger, and R. M. Scarlett, "Research and investigation of inverse epitaxial UHF power transistors. Appendix B: Theory and experiment on current transfer from alloyed contact to diffusid layer," 1964. [Online]. Available: <https://apps.dtic.mil/sti/citations/AD0605376>
- [136] H. H. Berger, "Models for contacts to planar devices," *Solid. State. Electron.*, vol. 15, no. 2, pp. 145–158, 1972, doi: 10.1016/0038-1101(72)90048-2.
- [137] D. K. Schroder, "Contact Resistance and Schottky Barriers," in *Semiconductor Material and Device Characterization*, 3rd ed. Hoboken, NJ, USA: John Wiley & Sons, Inc., 2005, pp. 127–184. doi: 10.1002/0471749095.ch3.
- [138] G. K. Reeves, "Specific contact resistance using a circular transmission line model," *Solid. State. Electron.*, vol. 23, no. 5, pp. 487–490, May 1980, doi: 10.1016/0038-1101(80)90086-6.
- [139] M. C. J. C. M. Krämer, "Fabrication and characterization of metal-semiconductor contacts for application in Al<sub>x</sub>Ga<sub>1-x</sub>N/GaN HEMTs," Eindhoven University of Technology, 2000. [Online]. Available: <https://research.tue.nl/en/studentTheses/fabrication-and-characterization-of-metal-semiconductor-contacts->
- [140] K.-H. Wen, "Study of ohmic contact formation on AlGaN/GaN heterostructures," KTH Royal Institute of Technology, 2019. [Online]. Available: <http://www.diva-portal.org/smash/record.jsf?pid=diva2%3A1353343&dsid=5438>
- [141] S. Grover, "Effect of Transmission Line Measurement (TLM) Geometry on Specific Contact Resistivity Determination," Rochester Institute of Technology, 2016. [Online]. Available: <https://repository.rit.edu/theses/9343/>
- [142] A. L. McWhorter, "1/f noise and germanium surface properties," in *Semiconductor Surface Physics*, R. H. Kingston, Ed., Philadelphia: University of Pennsylvania Press, 1957, pp. 207–228.
- [143] S. Christensson, I. Lundström, and C. Svensson, "Low frequency noise in MOS transistors—I Theory," *Solid. State. Electron.*, vol. 11, no. 9, pp. 797–812, Sep. 1968, doi: 10.1016/0038-1101(68)90100-7.
- [144] K. Takakura *et al.*, "Low-Frequency Noise Investigation of GaN/AlGaN Metal–Oxide–Semiconductor High-Electron-Mobility Field-Effect Transistor With Different Gate Length and Orientation," *IEEE Trans. Electron Devices*, vol. 67, no. 8, pp. 3062–3068, Aug. 2020, doi: 10.1109/TED.2020.3002732.
- [145] K.-S. Im *et al.*, "Low-Frequency Noise Characteristics of GaN Nanowire Gate-All-Around Transistors With/Without 2-DEG Channel," *IEEE Trans. Electron Devices*, vol. 66, no. 3, pp. 1243–1248, Mar. 2019, doi: 10.1109/TED.2019.2894806.
- [146] H.-C. Chiu, C.-W. Yang, C.-H. Chen, and C.-H. Wu, "Quality of the Oxidation Interface of AlGaN in Enhancement-Mode AlGaN/GaN High-Electron Mobility Transistors," *IEEE Trans. Electron Devices*, vol. 59, no. 12, pp.

3334–3338, Dec. 2012, doi: 10.1109/TED.2012.2215872.

- [147] F. Medjdoub *et al.*, “Can InAlN/GaN be an alternative to high power / high temperature AlGaIn/GaN devices?,” in *2006 International Electron Devices Meeting*, IEEE, 2006, pp. 1–4. doi: 10.1109/IEDM.2006.346935.
- [148] J. Kuzmík, A. Kostopoulos, G. Konstantinidis, J. F. Carlin, A. Georgakilas, and D. Pogany, “InAlN/GaN HEMTs: A first insight into technological optimization,” *IEEE Trans. Electron Devices*, vol. 53, no. 3, pp. 422–426, 2006, doi: 10.1109/TED.2005.864379.
- [149] M. Gonschorek *et al.*, “Two-dimensional electron gas density in Al<sub>1-x</sub>In<sub>x</sub>N/AlN/GaN heterostructures ( $0.03 \leq x \leq 0.23$ ),” *J. Appl. Phys.*, vol. 103, no. 9, p. 093714, May 2008, doi: 10.1063/1.2917290.
- [150] J. Kim *et al.*, “Origins of unintentional incorporation of gallium in InAlN layers during epitaxial growth, part II: Effects of underlying layers and growth chamber conditions,” *J. Cryst. Growth*, vol. 388, no. 1, pp. 143–149, 2014, doi: 10.1016/j.jcrysgro.2013.09.046.
- [151] G. Naresh-Kumar *et al.*, “Multicharacterization approach for studying InAl(Ga)N/Al(Ga)N/GaN heterostructures for high electron mobility transistors,” *AIP Adv.*, vol. 4, no. 12, 2014, doi: 10.1063/1.4903227.
- [152] M. Hiroki, Y. Oda, N. Watanabe, and N. Maeda, “Unintentional Ga incorporation in metalorganic vapor phase epitaxy of In-containing III-nitride semiconductors,” *J. Cryst. Growth*, vol. 382, pp. 36–40, 2013, doi: 10.1016/j.jcrysgro.2013.07.034.
- [153] R. Butté *et al.*, “Current status of AlInN layers lattice-matched to GaN for photonics and electronics,” *J. Phys. D: Appl. Phys.*, vol. 40, no. 20, pp. 6328–6344, Oct. 2007, doi: 10.1088/0022-3727/40/20/S16.
- [154] S. Marcinkevičius *et al.*, “Transient photoreflectance of AlInN/GaN heterostructures,” *AIP Adv.*, vol. 2, no. 4, p. 042148, Dec. 2012, doi: 10.1063/1.4768670.
- [155] V. Liuolia *et al.*, “Photoexcited carrier dynamics in AlInN/GaN heterostructures,” *Appl. Phys. Lett.*, vol. 100, no. 24, p. 242104, Jun. 2012, doi: 10.1063/1.4729033.
- [156] Y. J. Yoon *et al.*, “TMAH-based wet surface pre-treatment for reduction of leakage current in AlGaIn/GaN MIS-HEMTs,” *Solid. State. Electron.*, vol. 124, pp. 54–57, Oct. 2016, doi: 10.1016/j.sse.2016.06.009.
- [157] T. Inagaki, T. Hashizume, and H. Hasegawa, “Effects of surface processing on 2DEG current transport at AlGaIn/GaN interface studied by gateless HFET structure,” *Appl. Surf. Sci.*, vol. 216, no. 1–4, pp. 519–525, Jun. 2003, doi: 10.1016/S0169-4332(03)00482-3.
- [158] S. Linkohr *et al.*, “Influence of plasma treatments on the properties of GaN/AlGaIn/GaN HEMT structures,” *Phys. status solidi c*, vol. 9, no. 3–4, pp. 1096–1098, Mar. 2012, doi: 10.1002/pssc.201100210.
- [159] S. Marcinkevičius, A. Sztejn, S. Nakamura, and J. S. Speck, “Properties of sub-band edge states in AlInN studied by time-resolved photoluminescence of a

- AlInN/GaN heterostructure,” *Semicond. Sci. Technol.*, vol. 30, no. 11, p. 115017, Nov. 2015, doi: 10.1088/0268-1242/30/11/115017.
- [160] M. Gonschorek, D. Simeonov, J.-F. Carlin, E. Feltin, M. A. Py, and N. Grandjean, “Temperature mapping of Al<sub>0.85</sub>In<sub>0.15</sub>N/AlN/GaN high electron mobility transistors through micro-photoluminescence studies,” *Eur. Phys. J. Appl. Phys.*, vol. 47, no. 3, p. 30301, Sep. 2009, doi: 10.1051/epjap/2009091.
- [161] A. Mouti *et al.*, “Stress-modulated composition in the vicinity of dislocations in nearly lattice matched Al<sub>x</sub>In<sub>1-x</sub>N/GaN heterostructures: A possible explanation of defect insensitivity,” *Phys. Rev. B*, vol. 83, no. 19, p. 195309, May 2011, doi: 10.1103/PhysRevB.83.195309.
- [162] S. Schulz, M. A. Caro, L.-T. Tan, P. J. Parbrook, R. W. Martin, and E. P. O’Reilly, “Composition-Dependent Band Gap and Band-Edge Bowing in AlInN: A Combined Theoretical and Experimental Study,” *Appl. Phys. Express*, vol. 6, no. 12, p. 121001, Dec. 2013, doi: 10.7567/APEX.6.121001.
- [163] G. Ghibaudo, O. Roux, C. Nguyen-Duc, F. Balestra, and J. Brini, “Improved Analysis of Low Frequency Noise in Field-Effect MOS Transistors,” *Phys. Status Solidi*, vol. 124, no. 2, pp. 571–581, Apr. 1991, doi: 10.1002/pssa.2211240225.
- [164] I. Grigelionis *et al.*, “Terahertz Electroluminescence of Shallow Impurities in AlGaIn/GaN Heterostructures at Temperatures above 80 K,” *Phys. status solidi*, vol. 255, no. 5, p. 1700421, 2018, doi: 10.1002/pssb.201700421.
- [165] I. Grigelionis *et al.*, “Terahertz electroluminescence of shallow impurities in AlGaIn/GaN heterostructures at 20 K and 110 K temperature,” *Mater. Sci. Semicond. Process.*, vol. 93, pp. 280–283, 2019, doi: 10.1016/j.mssp.2019.01.005.
- [166] P. Magnone *et al.*, “1/f Noise in Drain and Gate Current of MOSFETs With High- $\kappa$  Gate Stacks,” *IEEE Trans. Device Mater. Reliab.*, vol. 9, no. 2, pp. 180–189, Jun. 2009, doi: 10.1109/TDMR.2009.2020406.
- [167] T. Nguyen, “Gate and drain low frequency noise in HfO<sub>2</sub> NMOSFETs,” in *AIP Conference Proceedings*, AIP, 2005, pp. 235–238. doi: 10.1063/1.2036739.
- [168] E. Simoen, A. Mercha, L. Pantisano, C. Claeys, and E. Young, “Low-frequency noise behavior of SiO<sub>2</sub>/HfO<sub>2</sub> dual-layer gate dielectric nMOSFETs with different interfacial oxide thickness,” *IEEE Trans. Electron Devices*, vol. 51, no. 5, pp. 780–784, May 2004, doi: 10.1109/TED.2004.826877.
- [169] H.-C. Chiu, C.-W. Yang, C.-H. Chen, and C.-H. Wu, “Quality of the Oxidation Interface of AlGaIn in Enhancement-Mode AlGaIn/GaN High-Electron Mobility Transistors,” *IEEE Trans. Electron Devices*, vol. 59, no. 12, pp. 3334–3338, Dec. 2012, doi: 10.1109/TED.2012.2215872.
- [170] R. Yadav *et al.*, “State-of-the-Art Room Temperature Operable Zero-Bias Schottky Diode-Based Terahertz Detector Up to 5.56 THz,” *Sensors*, vol. 23, no. 7, p. 3469, Mar. 2023, doi: 10.3390/s23073469.

- [171] A. M. Cowley and H. O. Sorensen, "Quantitative Comparison of Solid-State Microwave Detectors," *IEEE Trans. Microw. Theory Tech.*, vol. MTT-14, no. 12, pp. 588–602, Dec. 1966, doi: 10.1109/TMTT.1966.1126337.
- [172] C. Liu *et al.*, "Room-Temperature High-Gain Long-Wavelength Photodetector via Optical–Electrical Controlling of Hot Carriers in Graphene," *Adv. Opt. Mater.*, vol. 6, no. 24, p. 1800836, Dec. 2018, doi: 10.1002/adom.201800836.
- [173] D. Seliuta *et al.*, "Symmetric bow-tie diode for terahertz detection based on transverse hot-carrier transport," *J. Phys. D: Appl. Phys.*, vol. 53, no. 27, p. 275106, Jul. 2020, doi: 10.1088/1361-6463/ab831d.
- [174] M. Gonschorek, J.-F. Carlin, E. Feltin, M. A. Py, and N. Grandjean, "Self heating in AlInN/AlN/GaN high power devices: Origin and impact on contact breakdown and IV characteristics," *J. Appl. Phys.*, vol. 109, no. 6, Mar. 2011, doi: 10.1063/1.3552932.
- [175] J. Kuzmík, S. Bychikhin, D. Pogany, C. Gaquière, and E. Morvan, "Current conduction and saturation mechanism in AlGaIn/GaN ungated structures," *J. Appl. Phys.*, vol. 99, no. 12, Jun. 2006, doi: 10.1063/1.2207572.
- [176] P. Moens, A. Constant, and A. Banerjee, "Reliability Aspects of 650-V-Rated GaN Power Devices," 2017, pp. 319–344. doi: 10.1007/978-3-319-43199-4\_14.
- [177] D. J. Cheney *et al.*, "Reliability studies of AlGaIn/GaN high electron mobility transistors," *Semicond. Sci. Technol.*, vol. 28, no. 7, p. 074019, Jul. 2013, doi: 10.1088/0268-1242/28/7/074019.
- [178] G. Greco, F. Iucolano, and F. Roccaforte, "Ohmic contacts to Gallium Nitride materials," *Appl. Surf. Sci.*, vol. 383, pp. 324–345, Oct. 2016, doi: 10.1016/j.apsusc.2016.04.016.
- [179] M. Haziq, S. Falina, A. A. Manaf, H. Kawarada, and M. Syamsul, "Challenges and Opportunities for High-Power and High-Frequency AlGaIn/GaN High-Electron-Mobility Transistor (HEMT) Applications: A Review," *Micromachines*, vol. 13, no. 12, p. 2133, Dec. 2022, doi: 10.3390/mi13122133.
- [180] D. Zhou *et al.*, "Temperature dependent characteristics of Ti/Al/Ni/Au Ohmic contact on lattice-matched In<sub>0.17</sub>Al<sub>0.83</sub>N/GaN heterostructures," *Solid. State. Electron.*, vol. 183, p. 108108, Sep. 2021, doi: 10.1016/j.sse.2021.108108.
- [181] N. S. I. Guiney, C. J. Humphreys, P. Sen, R. Muralidharan, and D. N. Nath, "Au-free recessed Ohmic contacts to AlGaIn/GaN high electron mobility transistor: Study of etch chemistry and metal scheme," *J. Vac. Sci. Technol. B, Nanotechnol. Microelectron. Mater. Process. Meas. Phenom.*, vol. 38, no. 3, May 2020, doi: 10.1116/1.5144509.
- [182] A. Sužiedelis, J. Gradauskas, S. Ašmontas, G. Valušis, and H. G. Roskos, "Giga- and terahertz frequency band detector based on an asymmetrically necked n-n+-GaAs planar structure," *J. Appl. Phys.*, vol. 93, no. 5, pp. 3034–3038, Mar. 2003, doi: 10.1063/1.1536024.
- [183] D. Seliuta *et al.*, "Detection of terahertz/sub-terahertz radiation by asymmetrically-shaped 2DEG layers," *Electron. Lett.*, vol. 40, no. 10, p. 631, 2004, doi: 10.1049/el:20040412.

- [184] M. Lee, L. N. Pfeiffer, and K. W. West, “Ballistic cooling in a wideband two-dimensional electron gas bolometric mixer,” *Appl. Phys. Lett.*, vol. 81, no. 7, pp. 1243–1245, 2002, doi: 10.1063/1.1500429.
- [185] T. Nasir *et al.*, “Design of softened polystyrene for crack- and contamination-free large-area graphene transfer,” *Nanoscale*, vol. 10, no. 46, pp. 21865–21870, 2018, doi: 10.1039/C8NR05611K.
- [186] Y.-C. Lin, C.-C. Lu, C.-H. Yeh, C. Jin, K. Suenaga, and P.-W. Chiu, “Graphene Annealing: How Clean Can It Be?,” *Nano Lett.*, vol. 12, no. 1, pp. 414–419, Jan. 2012, doi: 10.1021/nl203733r.
- [187] Y. Ahn, J. Kim, S. Ganorkar, Y.-H. Kim, and S.-I. Kim, “Thermal annealing of graphene to remove polymer residues,” *Mater. Express*, vol. 6, no. 1, pp. 69–76, Feb. 2016, doi: 10.1166/mex.2016.1272.
- [188] B. Zhuang, S. Li, S. Li, and J. Yin, “Ways to eliminate PMMA residues on graphene — superclean graphene,” *Carbon N. Y.*, vol. 173, pp. 609–636, Mar. 2021, doi: 10.1016/j.carbon.2020.11.047.
- [189] A. Pirkle *et al.*, “The effect of chemical residues on the physical and electrical properties of chemical vapor deposited graphene transferred to SiO<sub>2</sub>,” *Appl. Phys. Lett.*, vol. 99, no. 12, p. 122108, Sep. 2011, doi: 10.1063/1.3643444.
- [190] J. E. Lee, G. Ahn, J. Shim, Y. S. Lee, and S. Ryu, “Optical separation of mechanical strain from charge doping in graphene,” *Nat. Commun.*, vol. 3, no. 1, p. 1024, Jan. 2012, doi: 10.1038/ncomms2022.
- [191] F. Ding *et al.*, “Stretchable Graphene: A Close Look at Fundamental Parameters through Biaxial Straining,” *Nano Lett.*, vol. 10, no. 9, pp. 3453–3458, Sep. 2010, doi: 10.1021/nl101533x.
- [192] A. T. Tarekegne, B. Zhou, K. Kaltenecker, K. Iwaszczuk, S. Clark, and P. U. Jepsen, “Terahertz time-domain spectroscopy of zone-folded acoustic phonons in 4H and 6H silicon carbide,” *Opt. Express*, vol. 27, no. 3, p. 3618, Feb. 2019, doi: 10.1364/OE.27.003618.
- [193] H. Hirai, H. Tsuchiya, Y. Kamakura, N. Mori, and M. Ogawa, “Electron mobility calculation for graphene on substrates,” *J. Appl. Phys.*, vol. 116, no. 8, Aug. 2014, doi: 10.1063/1.4893650.
- [194] J. Ahn, D. Kim, K.-H. Park, G. Yoo, and J. Heo, “Pt-Decorated Graphene Gate AlGaIn/GaN MIS-HEMT for Ultrahigh Sensitive Hydrogen Gas Detection,” *IEEE Trans. Electron Devices*, vol. 68, no. 3, pp. 1255–1261, Mar. 2021, doi: 10.1109/TED.2021.3053515.
- [195] S. Scarfe, W. Cui, A. Luican-Mayer, and J.-M. Ménard, “Systematic THz study of the substrate effect in limiting the mobility of graphene,” *Sci. Rep.*, vol. 11, no. 1, p. 8729, Apr. 2021, doi: 10.1038/s41598-021-87894-5.
- [196] A. K. Singh, R. S. Singh, and A. K. Singh, “Recent Developments in Chemical Doping of Graphene using Experimental Approaches and Its Applications,” *Adv. Eng. Mater.*, vol. 24, no. 11, Nov. 2022, doi: 10.1002/adem.202200259.
- [197] H. Liu, Y. Liu, and D. Zhu, “Chemical doping of graphene,” *J. Mater. Chem.*, vol. 21, no. 10, pp. 3335–3345, 2011, doi: 10.1039/C0JM02922J.

- [198] W. S. Hwang *et al.*, “Graphene nanoribbon field-effect transistors on wafer-scale epitaxial graphene on SiC substrates,” *APL Mater.*, vol. 3, no. 1, Jan. 2015, doi: 10.1063/1.4905155.
- [199] W. S. Hwang *et al.*, “Transport properties of graphene nanoribbon transistors on chemical-vapor-deposition grown wafer-scale graphene,” *Appl. Phys. Lett.*, vol. 100, no. 20, May 2012, doi: 10.1063/1.4716983.
- [200] Z. Fang *et al.*, “Active Tunable Absorption Enhancement with Graphene Nanodisk Arrays,” *Nano Lett.*, vol. 14, no. 1, pp. 299–304, Jan. 2014, doi: 10.1021/nl404042h.
- [201] A. D. Bobadilla, L. E. Ocola, A. V. Sumant, M. Kaminski, and J. M. Seminario, “PMMA-Assisted Plasma Patterning of Graphene,” *J. Nanotechnol.*, vol. 2018, pp. 1–8, Aug. 2018, doi: 10.1155/2018/8349626.
- [202] R. Wang, “Laser Ablation of Graphene: Fundamental Processes and Applications,” ETH Zürich, 2013. doi: 10.3929/ethz-a-010089121.
- [203] R. Sahin, E. Simsek, and S. Akturk, “Nanoscale patterning of graphene through femtosecond laser ablation,” *Appl. Phys. Lett.*, vol. 104, no. 5, Feb. 2014, doi: 10.1063/1.4864616.
- [204] R. You, Y. Liu, Y. Hao, D. Han, Y. Zhang, and Z. You, “Laser Fabrication of Graphene-Based Flexible Electronics,” *Adv. Mater.*, vol. 32, no. 15, Apr. 2020, doi: 10.1002/adma.201901981.
- [205] T. Wei, F. Hauke, and A. Hirsch, “Evolution of Graphene Patterning: From Dimension Regulation to Molecular Engineering,” *Adv. Mater.*, vol. 33, no. 45, Nov. 2021, doi: 10.1002/adma.202104060.
- [206] R. Ivaškevičiūtė-Povilauskienė *et al.*, “Advantages of optical modulation in terahertz imaging for study of graphene layers,” *J. Appl. Phys.*, vol. 131, no. 3, Jan. 2022, doi: 10.1063/5.0074772.
- [207] R. Ivaškevičiūtė-Povilauskienė, “Optical engineering in terahertz imaging and 2D materials inspection,” Vilnius University, Lithuania, 2023. doi: 10.15388/vu.thesis.518.
- [208] T. Kaplas and P. Kuzhir, “Ultra-Thin Pyrocarbon Films as a Versatile Coating Material,” *Nanoscale Res. Lett.*, vol. 12, no. 1, p. 121, Dec. 2017, doi: 10.1186/s11671-017-1896-0.
- [209] P. P. Kuzhir *et al.*, “Main principles of passive devices based on graphene and carbon films in microwave—THz frequency range,” *J. Nanophotonics*, vol. 11, no. 3, p. 032504, Feb. 2017, doi: 10.1117/1.JNP.11.032504.
- [210] G. D. Mahan and D. T. F. Marple, “Infrared absorption of thin metal films: Pt on Si,” *Appl. Phys. Lett.*, vol. 42, no. 3, pp. 219–221, Feb. 1983, doi: 10.1063/1.93898.
- [211] P. P. Kuzhir, A. G. Paddubskaya, S. A. Maksimenko, T. Kaplas, and Y. Svirko, “Microwave absorption properties of pyrolytic carbon nanofilm,” *Nanoscale Res. Lett.*, vol. 8, no. 1, p. 60, Dec. 2013, doi: 10.1186/1556-276X-8-60.
- [212] J. J. Heikkinen, J. Košir, V. Jokinen, and S. Franssila, “Fabrication and design rules of three dimensional pyrolytic carbon suspended microstructures,” *J.*

- Micromechanics Microengineering*, vol. 30, no. 11, p. 115003, Nov. 2020, doi: 10.1088/1361-6439/ab9f5b.
- [213] G. I. Dovbeshko *et al.*, “Optical Properties of Pyrolytic Carbon Films Versus Graphite and Graphene,” *Nanoscale Res. Lett.*, vol. 10, no. 1, p. 234, Dec. 2015, doi: 10.1186/s11671-015-0946-8.
- [214] G. I. Dovbeshko *et al.*, “Optical Properties of Pyrolytic Carbon Films Versus Graphite and Graphene,” *Nanoscale Res. Lett.*, vol. 10, no. 1, p. 234, Dec. 2015, doi: 10.1186/s11671-015-0946-8.
- [215] N. Wada, S. A. Solin, J. Wong, and S. Prochazka, “Raman and IR absorption spectroscopic studies on  $\alpha$ ,  $\beta$ , and amorphous Si<sub>3</sub>N<sub>4</sub>,” *J. Non. Cryst. Solids*, vol. 43, no. 1, pp. 7–15, Jan. 1981, doi: 10.1016/0022-3093(81)90169-1.
- [216] W. R. Knolle and D. L. Allara, “Infrared Spectroscopic Characterization of Silicon Nitride Films—Optical Dispersion Induced Frequency Shifts,” *Appl. Spectrosc.*, vol. 40, no. 7, pp. 1046–1049, Sep. 1986, doi: 10.1366/0003702864507855.
- [217] L. Vicarelli, A. Tredicucci, and A. Pitanti, “Micromechanical Bolometers for Subterahertz Detection at Room Temperature,” *ACS Photonics*, vol. 9, no. 2, pp. 360–367, Feb. 2022, doi: 10.1021/acsp Photonics.1c01273.
- [218] M. Piller, J. Hiesberger, E. Wistrela, P. Martini, N. Luhmann, and S. Schmid, “Thermal IR Detection With Nanoelectromechanical Silicon Nitride Trampoline Resonators,” *IEEE Sens. J.*, vol. 23, no. 2, pp. 1066–1071, Jan. 2023, doi: 10.1109/JSEN.2022.3223439.

## CURRICULUM VITAE

**Name** Justinas  
**Surname** Jorudas  
**Date of birth** 1994-05-15  
**Place of birth** Tauragė, Lithuania  
**Current town** Vilnius, Lithuania  
**E-mail** justinas.jorudas@ftmc.lt  
justasjorudas@gmail.com

### Education

2019-2024 Center for Physical Sciences and Technology (FTMC) & Vilnius university, Faculty of Physics, *joint Ph.D. studies*  
2017-2019 Vilnius university (VU), Faculty of Physics, *Master's degree in Technology*  
2013-2017 Kaunas University of Technology (KTU), Faculty of Physics and Mathematics, *Bachelor's degree in Technology*

### Work experience

2020-now Center for Physical Sciences and Technology (FTMC)  
*Junior Research Fellow*  
2022 August – December University of Eastern Finland (UEF), Department of Physics and Mathematics  
*Project Researcher*  
2017-2020 Center for Physical Sciences and Technology (FTMC)  
Engineer  
2017 Center for Physical Sciences and Technology (FTMC)  
Technician



## Secondments

- 2020 January 13<sup>th</sup>-  
26<sup>th</sup> High Pressure Physics Institute (UNIPRESS),  
Warsaw, Poland  
*AlGaN/GaN and InAlGaN/GaN HEMT structure  
processing*
- 2020 August July  
31<sup>st</sup> – August 7<sup>th</sup> CENTERA labs of High Pressure Physics Institute  
(UNIPRESS), Warsaw, Poland  
*AlGaN/GaN HEMT low-frequency noise  
measurements and bow-tie diode THz detector  
characterization*
- 2022 August 1<sup>st</sup> –  
December 31<sup>st</sup> University of Eastern Finland (UEF), Department  
of Physics and Mathematics  
*Deposition and studies of pyrolytic carbon (PPF  
and PyC) in DC and THz frequency ranges;  
Training to use Raith electron beam lithography  
equipment*
- 2023 July 17<sup>th</sup> –  
August 18<sup>th</sup> University of Eastern Finland (UEF), Department  
of Physics and Mathematics  
*Plasmonic structure fabrication using electron  
beam lithography on AlGaN/GaN HEMT structures  
for the THz range*

## REPRINTED PUBLICATIONS

**AlGaN/GaN on SiC Devices without a GaN Buffer Layer: Electrical and Noise Characteristics**

**J. Jorudas** A. Šimukovič, M. Dub, M. Sakowicz, S. Indirišiūnas, V. Kovalevskij,  
S. Rumyantsev, W. Knap, I. Kašalynas  
*Micromachines*, vol. 11, no. 12, 1131 (2020)  
DOI: 10.3390/mi11121131

This is an open access article distributed under the Creative Commons Attribution License (CC-BY).

The article may be accessed online at <https://doi.org/10.3390/mi11121131>



Article

# AlGa<sub>N</sub>/Ga<sub>N</sub> on SiC Devices without a GaN Buffer Layer: Electrical and Noise Characteristics

Justinas Jorudas<sup>1,\*</sup>, Artūr Šimukovič<sup>1</sup>, Maksym Dub<sup>2,3</sup>, Maciej Sakowicz<sup>2,3</sup>,  
Paweł Prystawko<sup>2</sup>, Simonas Indrišiūnas<sup>1</sup>, Vitalij Kovalevskij<sup>1</sup>, Sergey Rumyantsev<sup>2,3</sup>,  
Wojciech Knap<sup>2,3</sup> and Irmantas Kašalynas<sup>1,\*</sup>

<sup>1</sup> Center for Physical Sciences and Technology (FTMC), Saulėtekio 3, 10257 Vilnius, Lithuania; arturas.simukovic@ftmc.lt (A.Š.); simonas.indrisiunas@ftmc.lt (S.I.); vitalij@ftmc.lt (V.K.)

<sup>2</sup> Institute of High Pressure Physics PAS, ul. Sokołowska 29/37, 01-142 Warsaw, Poland; mdub@unipress.waw.pl (M.D.); sakowicz400@gmail.com (M.S.); pprysta@unipress.waw.pl (P.P.); roumis4@gmail.com (S.R.); knap.wojciech@gmail.com (W.K.)

<sup>3</sup> CENTERA Laboratories, Institute of High Pressure Physics PAS, ul. Sokołowska 29/37, 01-142 Warsaw, Poland

\* Correspondence: justinas.jorudas@ftmc.lt (J.J.); irmantas.kasalynas@ftmc.lt (I.K.); Tel.: +370-5-231-2418 (I.K.)

Received: 29 November 2020; Accepted: 16 December 2020; Published: 20 December 2020



**Abstract:** We report on the high-voltage, noise, and radio frequency (RF) performances of aluminium gallium nitride/gallium nitride (AlGa<sub>N</sub>/Ga<sub>N</sub>) on silicon carbide (SiC) devices without any GaN buffer. Such a GaN–SiC hybrid material was developed in order to improve thermal management and to reduce trapping effects. Fabricated Schottky barrier diodes (SBDs) demonstrated an ideality factor  $n$  at approximately 1.7 and breakdown voltages (fields) up to 780 V (approximately 0.8 MV/cm). Hall measurements revealed a thermally stable electron density at  $N_{2DEG} = 1 \times 10^{13} \text{ cm}^{-2}$  of two-dimensional electron gas in the range of 77–300 K, with mobilities  $\mu = 1.7 \times 10^3 \text{ cm}^2/\text{V}\cdot\text{s}$  and  $\mu = 1.0 \times 10^4 \text{ cm}^2/\text{V}\cdot\text{s}$  at 300 K and 77 K, respectively. The maximum drain current and the transconductance were demonstrated to be as high as 0.5 A/mm and 150 mS/mm, respectively, for the transistors with gate length  $L_G = 5 \text{ }\mu\text{m}$ . Low-frequency noise measurements demonstrated an effective trap density below  $10^{19} \text{ cm}^{-3} \text{ eV}^{-1}$ . RF analysis revealed  $f_T$  and  $f_{max}$  values up to 1.3 GHz and 6.7 GHz, respectively, demonstrating figures of merit  $f_T \times L_G$  up to  $6.7 \text{ GHz} \times \mu\text{m}$ . These data further confirm the high potential of a GaN–SiC hybrid material for the development of thin high electron mobility transistors (HEMTs) and SBDs with improved thermal stability for high-frequency and high-power applications.

**Keywords:** AlGa<sub>N</sub>/Ga<sub>N</sub>; SiC; high electron mobility transistor; Schottky barrier diode; breakdown field; noise; charge traps; radio frequency

## 1. Introduction

Aluminium gallium nitride/gallium nitride (AlGa<sub>N</sub>/Ga<sub>N</sub>) high electron mobility transistors (HEMTs) are widely used in high-power and high-frequency applications due to their superior characteristics based on the unique physical properties of III-nitride materials. The AlGa<sub>N</sub>/Ga<sub>N</sub> heterostructures can be grown on sapphire, silicon, silicon carbide, and native GaN substrates [1–7]. While sapphire and silicon substrates are the most cost-effective, the best characteristics are achieved on transistors fabricated on silicon carbide (SiC) and GaN substrates. Considerable improvements in electrical performance including the low-frequency noise were demonstrated on the AlGa<sub>N</sub>/Ga<sub>N</sub>/sapphire platform [8,9]. The advantage of the SiC over GaN substrates is higher SiC thermal conductivity and therefore potentially better thermal management of the transistors fabricated using AlGa<sub>N</sub>/Ga<sub>N</sub>/SiC structures. The common

approach to compensate for lattice mismatch and to reduce the dislocation density in these structures is to grow the aluminium gallium nitride (AlN) nucleation layer (NL) with reduced crystalline quality followed by a several-micrometres-thick GaN buffer doped with deep acceptors such as Fe or C which compensate for residual doping of an *n*-type GaN [10–12]. However, this approach deteriorates the overall thermal resistance of the structure and diminishes the advantage of a SiC substrate operating as a heatsink [13,14]. Also, the acceptor-type impurities in a thick GaN buffer introduce deep charge trapping centres, resulting in the increase of low-frequency noise, and facilitate the current collapse effects in HEMTs [9,15,16].

A new heteroepitaxy approach based on thin GaN–AlN–SiC heterostructures without a GaN buffer has been developed recently [17,18]. Although this approach has already been demonstrated to be promising, there are only a few studies on realistic devices such as transistors [17,19]. Thin GaN–AlN–SiC structures should provide better thermal management of the devices and could potentially reduce short channel effects. One expects also that this technology will reduce the effects of traps from a GaN:C buffer. However, the GaN:C buffer helps in reducing the number of threading dislocations. Therefore, GaN–AlN–SiC structures with the thin buffer may exhibit a higher concentration of threading dislocations, which may deteriorate the characteristics of devices. Indeed, it is well known that the dislocations may act as traps increasing low-frequency noise and current collapse effects and/or lowering maximum voltage breakdown of the devices.

In this work, the GaN–AlN–SiC hybrid material was used to develop thin Schottky barrier diodes (SBDs) and thin HEMTs (T-HEMTs) to study realistic devices under high DC voltages and in radio frequency (RF) regimes. We show that all the devices fabricated on this material have good thermal stability and demonstrate good DC as well as radio frequency (RF) characteristics. By systematic low-frequency noise measurements, we estimated the trap density, showing that avoiding a GaN:C buffer in the GaN–AlN–SiC material does not lead to an increase in active (dislocation related) trap density. We also show that deep trap-related current collapse phenomena are avoided and that all the fabricated devices demonstrate good DC, high voltage, as well as radio frequency (RF) characteristics. This way, we confirm the high potential of a GaN–SiC hybrid material in the development of improved thermal stability HEMTs and SBDs for high-frequency and high-power applications.

## 2. Materials and Methods (Experimental Details)

The heterostructures with the sequence of layers shown in Figure 1a were obtained commercially from the “SweGaN” company. They were grown on a 4” diameter, 500- $\mu\text{m}$ -thick semi-insulating SiC substrate. The layers consisted of a 2.4-nm GaN cap, a 20.5-nm  $\text{Al}_{0.25}\text{Ga}_{0.75}\text{N}$  barrier, and a 255-nm GaN channel grown directly on a 62-nm high-quality AlN NL on SiC. The sheet resistance ( $R_{Sh}$ ) of the as-grown T-HEMT structure determined from contactless eddy current measurements was  $380 \pm 10 \Omega/\square$ . The band diagram and electron distribution were calculated by a 1D Poisson simulator using the nominal thickness of all layers [20,21]. The results are shown in Figure 1b. The density of the two dimensional electron gas (2DEG) was calculated by integrating an electron distribution in the quantum well. Its value was found to be about  $1 \times 10^{13} \text{ cm}^{-2}$ .

The devices were fabricated using standard ultraviolet (UV) photolithography [8,22]. Mesas of 140 nm depth were formed by inductively coupled plasma reactive ion etching (ICP-RIE) (Oxford Instruments, Bristol, UK) using Cl plasma and chemical treatment in tetramethylammonium hydroxide (TMAH) solution (Microchemicals, Ulm, Germany). For ohmic contacts, Ti/Al/Ni/Au metal stacks of thicknesses 30/90/20/150 nm were deposited and annealed in nitrogen ambient for 30 s at 850 °C. The resistance ( $R_c$ ), and the specific resistivity ( $\rho_c$ ) of ohmic contacts were determined by transmission line method (TLM), demonstrating average values of about  $1 \Omega \times \text{mm}$  and  $2 \times 10^{-5} \Omega \times \text{cm}^2$ , respectively. Schottky contacts were formed from Ni/Au (25/150 nm).

The Schottky diodes (Figure 2) and HEMTs of two different designs (see Figures 3 and 4) were fabricated. Circular SBDs were used by depositing an inner Schottky contact with radius  $r = 40 \mu\text{m}$  and an outer ohmic contact of a variable radius in such a way that the distance between the electric contact,

$L$ , ranged from 5  $\mu\text{m}$  to 40  $\mu\text{m}$  (see Figure 2). The designs of the Schottky diodes and transistors shown in Figures 2 and 4, respectively, do not require mesa isolation. For testing at RF, the transistor design shown in Figure 3 was used (RF T-HEMT).

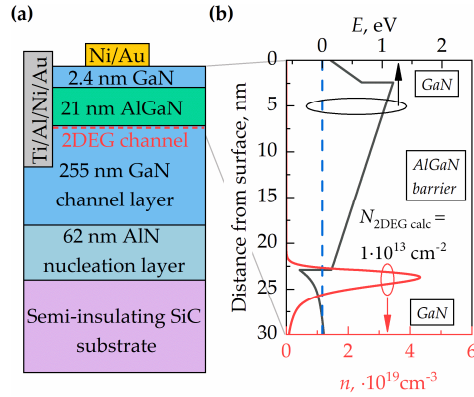


**Figure 1.** (a) Schematic of the thin high electron mobility transistor (T-HEMT) structure cross section with ohmic and Schottky contacts and (b) the calculated band diagram and electron density distribution in the upper layers of the heterostructure.

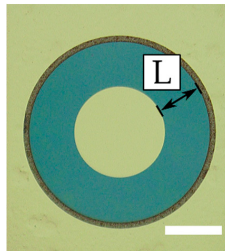


**Figure 2.** Microscope image of the fabricated Schottky barrier diode (SBD):  $L$  is the separation between the Ohmic and Schottky contacts. The scale bar is 50  $\mu\text{m}$ .

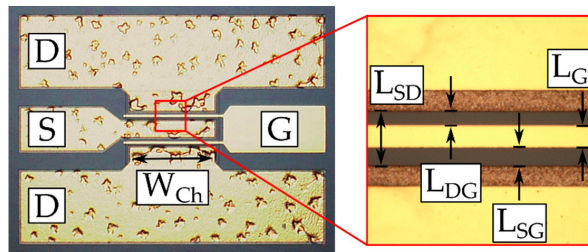


**Figure 3.** Microscope image of the radio frequency (RF) T-HEMT (left hand side) and details of the design parameters (right hand side) illustrating the Gate (G), Source (S), and Drain (D) electrodes in a 150- $\mu\text{m}$  pitch implementation.

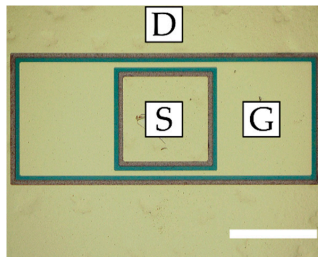


**Figure 4.** Microscope image of the fabricated DC T-HEMT: the scale bar is 100  $\mu\text{m}$ .

These RF T-HEMTs consisted of 200  $\mu\text{m}$  (RF T-HEMT-1) or 300  $\mu\text{m}$  (RF T-HEMT-2)-wide two-finger transistors, each of drain-source distance  $L_{SD} = 14 \mu\text{m}$ , gate length  $L_G = 5 \mu\text{m}$ , and gate-source distance  $L_{SG} = 5 \mu\text{m}$ . For comparison, the T-HEMTs with rectangular-type electrodes (see Figure 4), labelled here as DC T-HEMT, were also investigated (see also reference [9]). Similar to RF T-HEMTs, all DC T-HEMTs had the same gate length and gate-source distance of 5  $\mu\text{m}$ , but the channel width was of 200  $\mu\text{m}$  and the drain-source distances were 17.5  $\mu\text{m}$ , 15  $\mu\text{m}$ , and 12.5  $\mu\text{m}$  for three sample transistors labelled DC T-HEMT-1, DC T-HEMT-2, and DC T-HEMT-3, respectively.

All transistors were measured on the wafer in DC and RF regimes by using Süss Microtech probe station PM8 (SUSS MicroTec SE, Garching, Germany). For the RF measurements, the G-S-G (ground–signal–ground) 150- $\mu\text{m}$  pitch high frequency probes, Agilent E8364B PNA Network Analyzer (Agilent, Santa Clara, CA, USA), and E5270B Precision IV Analyzer with IC-CAP software were used (Keysight Technologies, Santa Rosa, CA, USA). The two-step open-short de-embedding method was implemented, and small signal S-parameters were obtained. The unity current gain cut-off frequency ( $f_T$ ) and the unity maximum unilateral power gain frequency ( $f_{max}$ ) were found from de-embedded S-parameter frequency characteristics.

The SBDs were investigated using EPS150 probe station (Cascade Microtech, Beaverton, OR, USA), high voltage source-meter Keithley 2410 (Tektronix, Beaverton, OR, USA), and impedance analyser Agilent 4294A (Agilent, Santa Clara, CA, USA).

The low-frequency noise in transistors was measured in the linear regime with the source grounded. The voltage fluctuations from the drain load resistor,  $R_L$ , were amplified by a low-noise amplifier and analysed using “PHOTON” spectrum analyser (Bruel & Kjaer, Nærum, Denmark). The spectral noise density of drain current fluctuations was calculated in the usual way with  $S_I = S_V((R_L + R_{DS})/R_L R_{DS})^2$ , where  $S_V$  is the drain voltage fluctuations and  $R_{DS}$  is the total drain to source resistance.

### 3. Experimental Results and Discussions

The 2DEG density ( $N_{2DEG}$ ), mobility ( $\mu_{2DEG}$ ), and sheet resistance ( $R_{Sh}$ ) were determined in the Hall experiments using Van der Pauw (VdP) geometry. The results are summarized in Table 1. Good agreement between the calculated carrier density, an integral of electron distribution in the quantum well (see Figure 1b), measured sheet resistance using contactless eddy current method, and the results of the Hall experiment were found within a deviation interval of 7%.

**Table 1.** Parameters of 2DEG in T-HEMT heterostructures at 300 K and 77 K.

Parameter	Hall Measurements		Simulation	Eddy Current Measurements
	300 K	77 K	300 K	300 K
$N_{2DEG}, \times 10^{13} \text{ cm}^{-2}$	1.00	0.96	1.0	-
$\mu_{2DEG}, \text{ cm}^2/\text{V}\cdot\text{s}$	$1.7 \times 10^3$	$1.0 \times 10^4$	-	-
$R_{Sh}, \Omega/\square$	375	64	-	$380 \pm 10$

These values are typical for the state-of-the-art AlGaIn/GaN heterostructures [23–27]. Therefore, we can conclude that elimination of the buffer layer did not worsen the parameters of the 2DEG.

### 3.1. Performance of SBDs

Typical capacitance–voltage ( $C$ - $V$ ) characteristics of SBD measured at frequencies 100 kHz and 1 MHz are shown in Figure 5a. One can see that frequency dispersion is negligible, indicating that deep levels do not affect the  $C$ - $V$  characteristics. The pinch-off voltage ( $V_{po}$ ) needed to fully deplete a 2DEG channel was found to be about  $-3.1$  V. The density of 2DEG under Schottky contact was calculated using the integral capacitance technique [28]:

$$N_{G-2DEG} = \frac{1}{eA} \int_{V_{po}}^0 C_P(V) dV, \quad (1)$$

where  $e$  is the elementary charge,  $A$  is the area of Schottky contact, and  $C_P(V)$  is the capacitance. The carrier density  $N$  dependence on the distance from the surface  $W$  was found from  $C$ - $V$  data using the following formulas [28]:

$$W = \frac{\varepsilon \varepsilon_0 A}{C_P}, \quad (2)$$

$$N = \frac{C_P^3}{e \varepsilon \varepsilon_0 A^2} \left( \frac{dC_P(V)}{dV} \right)^{-1}, \quad (3)$$

where  $\varepsilon = 8.9$  is the relative permittivity of GaN and  $\varepsilon_0$  is the vacuum permittivity. The obtained  $N$  dependence on the parameter  $W$  is shown in Figure 5b. The density of 2DEG was found to be  $N_{G-2DEG} = 0.69 \times 10^{13} \text{ cm}^{-2}$  at 300 K. This density is smaller than that found from the Hall measurements due to depletion by the Schottky barrier built-in voltage [29,30].

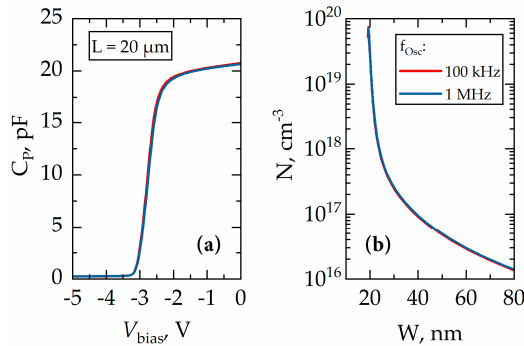


**Figure 5.** (a) Capacitance–voltage ( $C$ - $V$ ) characteristics of SBD with  $L = 20 \mu\text{m}$  at modulation frequencies of 100 kHz (red line) and 1 MHz (blue line), and (b) carrier distribution  $N(W)$  calculated from  $C$ - $V$  data using Equations (2) and (3).

Figure 6 shows examples of the forward and reverse current–voltage characteristics of SBDs. The forward current–voltage characteristics demonstrated an ideality factor of  $n \cong 1.7$ . The barrier height found based on the thermionic emission (TE) model was  $\phi = 0.75$  eV. These values are typical for Ni/AlGaIn Schottky barriers [31]. Under reverse bias, leakage currents were saturated at approximately  $-5$  V and remained constant until the breakdown (see Figure 6b). Moreover, SBDs demonstrated a sufficiently high  $j_{ON}/j_{OFF}$  ratio; for example, for SBD with  $L = 40 \mu\text{m}$ , the highest achieved value was found to be more than three orders of magnitude,  $j_{ON}/j_{OFF} \geq 3200$ , taking into account also the reverse-current densities prior to a breakdown which occurred at a voltage of  $-780$  V. Furthermore,



a 2.5 times improvement in the maximum current density was obtained in comparison with previously reported SBDs fabricated on standard AlGaIn/GaN HEMT structures with a thick GaN:C buffer [8]. Note the dependence of forward current on the distance between ohmic and Schottky contacts indicating good performance of the fabricated ohmic contacts with negligible losses.

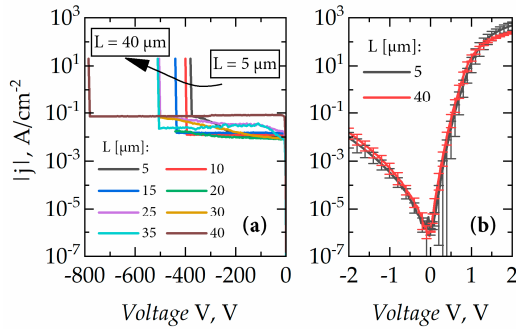


**Figure 6.** (a) Reverse current-voltage characteristics of SBDs and (b) current-voltage characteristics of SBDs with  $L = 5$  and  $40 \mu m$  at low voltages.

GaN–AlN–SiC buffer-free structures with a thin AlN layer may potentially exhibit a higher concentration of the threading dislocations, which may deteriorate the breakdown characteristics. On the other hand, as discussed in References [17,18], high-quality AlN NL in a T-HEMT structure can serve as a back barrier which enhances the critical breakdown field. Figure 7 shows the breakdown voltage and critical electric field dependences on the distance between ohmic and Schottky contacts.

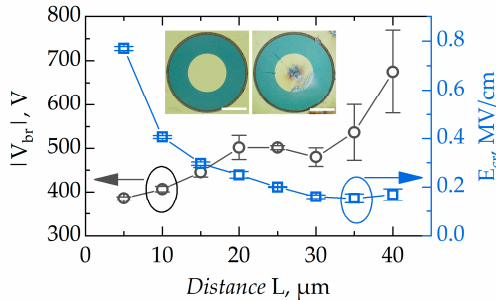


**Figure 7.** Breakdown voltage and critical electric field dependences on the distance between ohmic and Schottky contacts: error bars in the critical field data are depicted by the size of the symbols. Inset: images of  $L = 40 \mu m$  SBD before and after breakdown (scale bar is  $50 \mu m$ ).

As seen in Figure 7, the breakdown voltage depends on the distance,  $L$ , between contacts and ranges from 800 V to 400 V for  $L = 40 \mu m$  and  $L = 5 \mu m$ , respectively. The average breakdown field for  $L = 5 \mu m$  devices was found to be 0.8 MV/cm. It is worth noting that the maximum critical field asymptotically decreased down to 0.2 MV/cm with distance increasing from 5  $\mu m$  to 30  $\mu m$  and was independent of the distance for larger  $L$  values. The inset in Figure 7 shows the optical microscope images of a Schottky diode before and after breakdown. One can see that the inner contact is mostly damaged. Lateral breakdown occurs close to the inner Schottky contact, where the electric field has its maximum. A similar reverse breakdown field dependence on the distance between two ohmic contacts fabricated on the T-HEMT with locally removed 2DEG was reported previously in Reference [18]. There, the critical breakdown field values reached 2 MV/cm for a short distance of  $L = 5 \mu m$  between

two isolated devices. In our work, realistic devices—SBDs—were investigated in the reverse bias regime, demonstrating similar behaviour for the breakdown field with maximum values close to 0.8 MV/cm for the short distance (5  $\mu\text{m}$ ) between Schottky and ohmic contacts. Therefore, we conclude that the actual breakdown field is higher than 0.8 MV/cm and the absence of the thick GaN buffer does not deteriorate the breakdown characteristics by much.

### 3.2. Performance of T-HEMTs

Typical DC characteristics of representative T-HEMT are shown in Figure 8. As seen in Figure 8a, RF T-HEMT demonstrated drain current saturation at the level of 266 mA/mm under DC biases of  $V_D = 10$  V and  $V_G = +1$  V. This translates into an input power value of 2.6 W/mm for T-HEMT with a channel width of 0.4 mm. The drain current in the saturation region fell by 1–2% only. This indicates the advantages of efficient heat removal from the 2DEG channel in AlGaIn/GaN with AlN NL that exploits the absence of the buffer layer and high thermal conductivity of the SiC substrate.

The transfer and transconductance ( $g_m$ ) characteristics at  $V_D = 5$  V for various T-HEMTs are shown in Figure 8b,c. The impact of mesa on the device performance can be identified from the transfer characteristics. Indeed, the circular DC T-HEMT devices demonstrated up to two orders of magnitude larger leakage currents in comparison to those measured for RF T-HEMTs. Both the maximum drain current and the transconductance values were found to be higher for the DC T-HEMTs demonstrating values up to 507 mA/mm and 154 mS/mm, respectively. Meanwhile, RF T-HEMTs demonstrated only 266 mA/mm and 77 mS/mm. The pinch-off region is observed beyond a gate bias of  $-3$  V, which is in good agreement with  $V_{po}$  obtained from  $C$ - $V$  measurements.

One of the most effective ways to evaluate the quality of the material and the deep level traps is the low-frequency noise measurements. It is well known that low-frequency noise may differ significantly for the devices with almost identical DC characteristics. Elevated noise level is an indication of lower quality of the material, higher concentration of the deep level traps, lower reliability, and reduced lifetime of the devices. In the majority of cases, the low-frequency noise in field effect transistors complies with the McWhorter model [32,33]. In accordance with the model, the  $1/f$  low-frequency noise is a result of tunnelling of the carriers to the layers adjacent to the channel. The model allows for estimation of the effective trap density responsible for noise, which is a good figure of merit for the noise level and overall quality of the material.

The spectra of the drain current fluctuations had the form of  $1/f'$  noise with exponent  $\gamma = 0.9$ – $1.1$ . The dependences of the noise  $S_I/I^2$  on the gate voltage swing ( $V_G - V_T$ ) at  $f = 10$  Hz for three representative devices are shown in Figure 9a (here,  $V_T$  is the threshold voltage determined from the transfer current voltage characteristics in the linear regime). As seen, noise depends on the gate voltage as  $(V_G - V_T)^2$  or steeper. It is known that, in many cases, this dependence at high gate voltages may become flat, indicating a contribution of the contact noise. It is seen from Figure 9a that this is not the case for the studied devices and that contacts do not contribute to noise significantly. The effective trap density  $N_T$  in the McWhorter model can be estimated from gate voltage noise as follows [9]:

$$S_{V_G} = \frac{S_I/I^2}{(g_m/I)^2} \quad (4)$$

$$S_{V_G} = \frac{kTN_T e^2}{\gamma f W_{Ch} L_G C^2} \quad (5)$$

where  $k$  is the Boltzmann constant,  $T$  is the temperature,  $W_{Ch}$  and  $L_G$  is the channel area,  $C$  is the gate capacitance per unit area, and  $\gamma$  is the attenuation coefficient of the electron wave function under the barrier, taken to be  $10^8 \text{ cm}^{-1}$ .

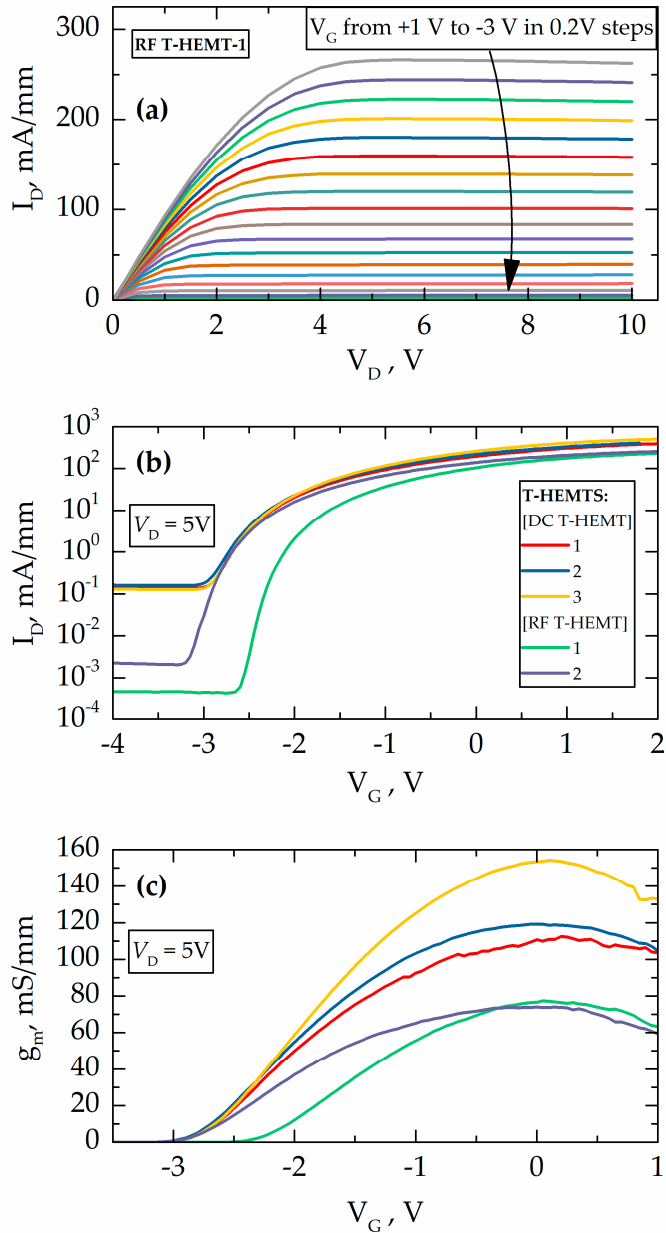


**Figure 8.** DC characteristics of T-HEMTs under study: (a) DC output characteristics of 0.4 mm wide RF T-HEMT-1 and comparisons of transfer (b) and transconductance (c) characteristics of the RF T-HEMTs and DC T-HEMTs with various values of the channel widths  $W_{Ch}$ . The gate length for all devices is 5  $\mu\text{m}$ .

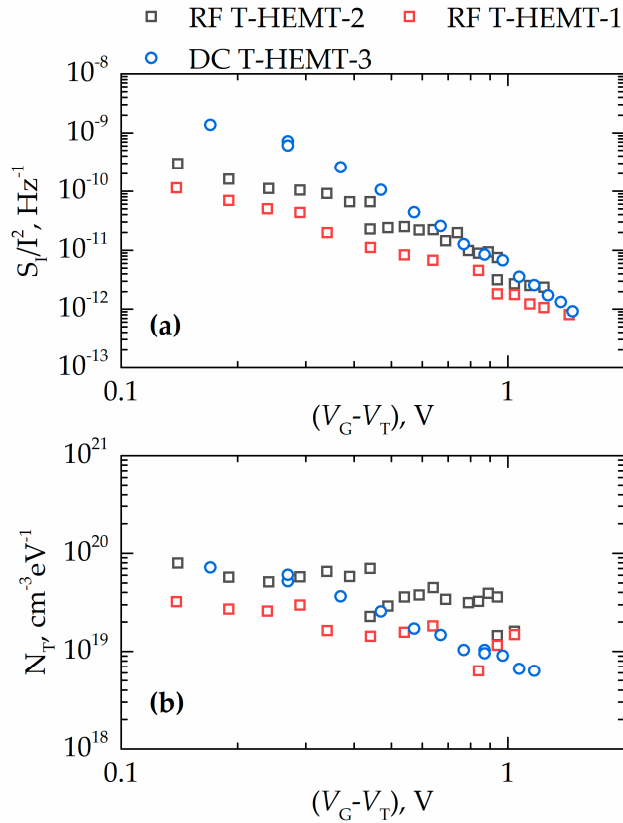


**Figure 9.** (a) Drain current noise  $S_I/I^2$  at frequency  $f = 10$  Hz for T-HEMTs of different channel widths ranging from 0.2 mm to 0.6 mm and (b) the effective trap density  $N_T$  as a function of the gate voltage swing  $(V_G - V_T)$  for the same transistors.

According to the McWhorter model, input gate voltage noise does not depend on access resistance and carrier concentration in the channel [9]. The dependence of the effective trap density on the gate voltage in Figure 9b can be attributed to the dependence of the trap density on energy. The number of traps in this T-HEMT structure was found to be in the range  $10^{19}$ – $10^{20}$   $\text{cm}^{-3}$   $\text{eV}^{-1}$ . Some of the devices demonstrated  $N_T < 10^{19}$   $\text{cm}^{-3}$   $\text{eV}^{-1}$ . These values are of the same order or even smaller than those reported earlier for AlGaIn/GaN HEMTs with a thick buffer layer [9]. Therefore, we conclude that studied T-HEMTs are characterized by the same quality as or even better quality than regular devices with thick buffers.

The unity current gain cut-off frequency ( $f_T$ ) and the unity maximum unilateral power gain frequency ( $f_{max}$ ) were found at various voltages down to the threshold voltage. The results are shown in Figure 10. The RF T-HEMTs with a 0.4-mm channel width demonstrated the highest operational frequencies, with values reaching  $f_T = 1.33$  GHz at  $V_{GS} = 0$  V with  $V_D = 5$  V and  $f_{max} = 6.7$  GHz at the bias of  $V_G = -0.8$  V and  $V_D = 7$  V. These results revealed a figure of merit (FOM) factor  $f_T \times L_G$  up to  $6.7$  GHz  $\times$   $\mu\text{m}$ , which is comparable with the best value of  $9.2$  GHz  $\times$   $\mu\text{m}$  reported for the T-HEMTs in Reference [19]. The performance of RF T-HEMTs can be further improved in our processing via optimization of ohmic contact/access resistance and the reduction of channel length  $L_{SD}$  in tandem

with gate length  $L_G$  [34,35]. Note that there is up to 3 times difference between the FOM factor of T-HEMTs and that of standard HEMTs, which requires more detailed investigations in the future [36].

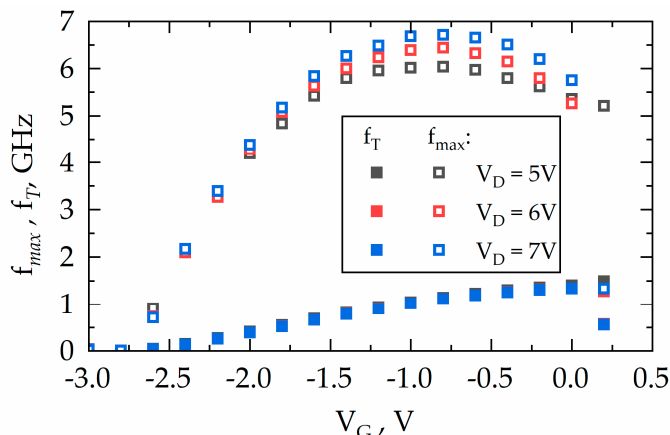


**Figure 10.** Frequencies  $f_T$  and  $f_{max}$  at different biasing conditions extracted from S-parameters measurements of RF T-HEMT-1 with  $W_{Ch} = 0.4$  mm and  $L_G = 5$   $\mu$ m.

#### 4. Conclusions

AlGaIn/GaN SBDs and HEMTs without GaN buffer layers have been fabricated on SiC substrates. 2DEG densities of  $1 \times 10^{13}$   $\text{cm}^{-2}$  with mobility of  $1.7 \times 10^3$   $\text{cm}^2/\text{V}\cdot\text{s}$  and  $1.0 \times 10^4$   $\text{cm}^2/\text{V}\cdot\text{s}$  at 300 K and 77 K, respectively, were found from the Hall measurements. The unterminated and unpassivated SBDs fabricated on these heterostructures exhibited high breakdown voltages up to  $-780$  V, with the critical breakdown field reaching  $0.8$  MV/cm. Transistors on these heterostructures, so-called T-HEMTs, demonstrated maximum current density and transconductance values up to  $0.5$  A/mm and  $150$  mS/mm, respectively, with a negligible reduction in the drain current. This indicates improved thermal management due to a heterostructure design on the SiC substrate without a GaN buffer layer. By systematic low-frequency noise measurements, we estimated the effective trap density, which in T-HEMT structures was below the level of  $10^{19}$   $\text{cm}^{-3}$   $\text{eV}^{-1}$ . This value is similar to or even smaller than previously reported trap densities in heterostructures with thick GaN:C buffers. This means that avoiding a GaN:C buffer in GaN–AlN–SiC material does not lead to an increase in active (dislocation-related) trap density. The unity current gain cut-off and unity maximum unilateral power gain were measured to be  $1.3$  GHz and  $6.7$  GHz, respectively. Using this data, the figure of merit  $f_T \times L_G$  is estimated at  $6.7$  GHz  $\times$   $\mu$ m. Therefore, we conclude that a buffer-free design did not compromise the quality of the structures or the performance of the devices. Our results confirm the potential of a GaN–SiC hybrid material for the development of HEMTs and SBDs for high-frequency and high-power applications with improved thermal stability.

**Author Contributions:** I.K., J.J., and S.R. conceived the idea. J.J., P.P., S.I., and V.K. characterized the material and prepared the samples. J.J., A.Š., and I.K. conducted the electrical characterization. J.J., M.D., and S.R. performed the noise characterization. M.S., S.R., W.K., and I.K. acquired funding. All authors contributed to the discussion, data analysis, and manuscript preparation. All authors have read and agreed to the published version of the manuscript.

**Funding:** The work was supported by the Research Council of Lithuania (Lietuvos mokslo taryba) under the “TERAGANWIRE” project (grant No. S-LL-19-1), by the National Science Centre of Poland (grant no. 2017/27/L/ST7/03283), and by the “International Research Agendas” program of the Foundation for Polish Science co-financed by the European Union under the European Regional Development Fund (Nos. MAB/2018/9).

**Conflicts of Interest:** The authors declare no conflict of interest.

## References

1. Koksaldi, O.S.; Haller, J.; Li, H.; Romanczyk, B.; Guidry, M.; Wienecke, S.; Keller, S.; Mishra, U.K. N-Polar GaN HEMTs Exhibiting Record Breakdown Voltage Over 2000 V and Low Dynamic On-Resistance. *IEEE Electron. Device Lett.* **2018**, *39*, 1014–1017. [[CrossRef](#)]
2. Choi, U.; Kim, H.-S.; Lee, K.; Jung, D.; Kwak, T.; Jang, T.; Nam, Y.; So, B.; Kang, M.-J.; Seo, K.-S.; et al. Direct Current and Radio Frequency Characterizations of AlGa<sub>N</sub>/AlN/GaN/AlN Double-Heterostructure High-Electron Mobility Transistor (DH-HEMT) on Sapphire. *Phys. Status Solidi* **2020**, *217*, 1900695. [[CrossRef](#)]
3. Chandrasekar, H.; Uren, M.J.; Eblabla, A.; Hirshy, H.; Casbon, M.A.; Tasker, P.J.; Elgaid, K.; Kuball, M. Buffer-Induced Current Collapse in GaN HEMTs on Highly Resistive Si Substrates. *IEEE Electron. Device Lett.* **2018**, *39*, 1556–1559. [[CrossRef](#)]
4. Romanczyk, B.; Mishra, U.K.; Zheng, X.; Guidry, M.; Li, H.; Hatui, N.; Wurm, C.; Krishna, A.; Ahmadi, E.; Keller, S. W-Band Power Performance of SiN-Passivated N-Polar GaN Deep Recess HEMTs. *IEEE Electron. Device Lett.* **2020**, *41*, 349–352. [[CrossRef](#)]
5. SaifAddin, B.K.; Almogbel, A.S.; Zollner, C.J.; Wu, F.; Bonef, B.; Iza, M.; Nakamura, S.; DenBaars, S.P.; Speck, J.S. AlGa<sub>N</sub> Deep-Ultraviolet Light-Emitting Diodes Grown on SiC Substrates. *ACS Photonics* **2020**, *7*, 554–561. [[CrossRef](#)]
6. Alshahed, M.; Heuken, L.; Alomari, M.; Cora, I.; Toth, L.; Pecz, B.; Wachter, C.; Bergunde, T.; Burghartz, J.N. Low-Dispersion, High-Voltage, Low-Leakage GaN HEMTs on Native GaN Substrates. *IEEE Trans. Electron. Devices* **2018**, *65*, 2939–2947. [[CrossRef](#)]
7. Pashnev, D.; Kaplas, T.; Korotyeyev, V.; Janonis, V.; Urbanowicz, A.; Jorudas, J.; Kašalynas, I. Terahertz time-domain spectroscopy of two-dimensional plasmons in AlGa<sub>N</sub>/GaN heterostructures. *Appl. Phys. Lett.* **2020**, *117*, 051105. [[CrossRef](#)]
8. Jakštas, V.; Jorudas, J.; Janonis, V.; Minkevičius, L.; Kašalynas, I.; Prystawko, P.; Leszczynski, M. Development of AlGa<sub>N</sub>/GaN/SiC high-electron-mobility transistors for THz detection. *Lith. J. Phys.* **2018**, *58*, 135–140. [[CrossRef](#)]
9. Sai, P.; Jorudas, J.; Dub, M.; Sakowicz, M.; Jakštas, V.; But, D.B.; Prystawko, P.; Cywinski, G.; Kašalynas, I.; Knap, W.; et al. Low frequency noise and trap density in GaN/AlGa<sub>N</sub> field effect transistors. *Appl. Phys. Lett.* **2019**, *115*, 183501. [[CrossRef](#)]
10. Chang, S.-J.; Bhuiyan, M.A.; Won, C.-H.; Lee, J.-H.; Jung, H.W.; Shin, M.J.; Do, J.-W.; Cho, K.J.; Lee, J.-H.; Ma, T.P.; et al. Investigation of GaN channel thickness on the channel mobility in AlGa<sub>N</sub>/GaN HEMTs grown on sapphire substrate. In Proceedings of the 2017 IEEE International Symposium on Radio-Frequency Integration Technology (RFIT), Seoul, Korea, 30 August–1 September 2017; pp. 87–89.
11. Selvaraj, S.L.; Suzue, T.; Egawa, T. Breakdown Enhancement of AlGa<sub>N</sub>/GaN HEMTs on 4-in Silicon by Improving the GaN Quality on Thick Buffer Layers. *IEEE Electron. Device Lett.* **2009**, *30*, 587–589. [[CrossRef](#)]
12. Poblenz, C.; Waltereit, P.; Rajan, S.; Heikman, S.; Mishra, U.K.; Speck, J.S. Effect of carbon doping on buffer leakage in AlGa<sub>N</sub>/GaN high electron mobility transistors. *J. Vac. Sci. Technol. B Microelectron. Nanom. Struct.* **2004**, *22*, 1145. [[CrossRef](#)]
13. Manoi, A.; Pomeroy, J.W.; Killat, N.; Kuball, M. Benchmarking of Thermal Boundary Resistance in AlGa<sub>N</sub>/GaN HEMTs on SiC Substrates: Implications of the Nucleation Layer Microstructure. *IEEE Electron. Device Lett.* **2010**, *31*, 1395–1397. [[CrossRef](#)]
14. Cho, J.; Bozorg-Grayeli, E.; Altman, D.H.; Asheghi, M.; Goodson, K.E. Low Thermal Resistances at GaN–SiC Interfaces for HEMT Technology. *IEEE Electron. Device Lett.* **2012**, *33*, 378–380. [[CrossRef](#)]
15. Uren, M.J.; Moreke, J.; Kuball, M. Buffer Design to Minimize Current Collapse in GaN/AlGa<sub>N</sub> HFETs. *IEEE Trans. Electron. Devices* **2012**, *59*, 3327–3333. [[CrossRef](#)]
16. Fang, Z.-Q.; Claffin, B.; Look, D.C.; Green, D.S.; Vetry, R. Deep traps in AlGa<sub>N</sub>/GaN heterostructures studied by deep level transient spectroscopy: Effect of carbon concentration in GaN buffer layers. *J. Appl. Phys.* **2010**, *108*, 063706. [[CrossRef](#)]
17. Chen, J.-T.; Bergsten, J.; Lu, J.; Janzén, E.; Thorsell, M.; Hultman, L.; Rorsman, N.; Kordina, O. A GaN–SiC hybrid material for high-frequency and power electronics. *Appl. Phys. Lett.* **2018**, *113*, 041605. [[CrossRef](#)]

18. Lu, J.; Chen, J.-T.; Dahlqvist, M.; Kabouche, R.; Medjdoub, F.; Rosen, J.; Kordina, O.; Hultman, L. Transmorphic epitaxial growth of AlN nucleation layers on SiC substrates for high-breakdown thin GaN transistors. *Appl. Phys. Lett.* **2019**, *115*, 221601. [[CrossRef](#)]
19. Chen, D.-Y.; Malmros, A.; Thorsell, M.; Hjelmgren, H.; Kordina, O.; Chen, J.-T.; Rorsman, N. Microwave Performance of ‘Buffer-Free’ GaN-on-SiC High Electron Mobility Transistors. *IEEE Electron. Device Lett.* **2020**, *41*, 828–831. [[CrossRef](#)]
20. Tan, I.; Snider, G.L.; Chang, L.D.; Hu, E.L. A self-consistent solution of Schrödinger—Poisson equations using a nonuniform mesh. *J. Appl. Phys.* **1990**, *68*, 4071–4076. [[CrossRef](#)]
21. Snider, G.L.; Tan, I.-H.; Hu, E.L. Electron states in mesa-etched one-dimensional quantum well wires. *J. Appl. Phys.* **1990**, *68*, 2849–2853. [[CrossRef](#)]
22. Kruszewski, P.; Prystawko, P.; Kasalynas, I.; Nowakowska-Siwinska, A.; Krysko, M.; Plesiewicz, J.; Smalc-Koziorowska, J.; Dwilinski, R.; Zajac, M.; Kucharski, R.; et al. AlGaIn/GaN HEMT structures on ammono bulk GaN substrate. *Semicond. Sci. Technol.* **2014**, *29*, 75004. [[CrossRef](#)]
23. Narang, K.; Bag, R.K.; Singh, V.K.; Pandey, A.; Saini, S.K.; Khan, R.; Arora, A.; Padmavati, M.V.G.; Tyagi, R.; Singh, R. Improvement in surface morphology and 2DEG properties of AlGaIn/GaN HEMT. *J. Alloys Compd.* **2020**, *815*, 152283. [[CrossRef](#)]
24. Yang, C.; Luo, X.; Sun, T.; Zhang, A.; Ouyang, D.; Deng, S.; Wei, J.; Zhang, B. High Breakdown Voltage and Low Dynamic ON-Resistance AlGaIn/GaN HEMT with Fluorine Ion Implantation in SiNx Passivation Layer. *Nanoscale Res. Lett.* **2019**, *14*, 191. [[CrossRef](#)] [[PubMed](#)]
25. Nifa, I.; Leroux, C.; Torres, A.; Charles, M.; Reimbold, G.; Ghibaudo, G.; Bano, E. Characterization and modeling of 2DEG mobility in AlGaIn/AlN/GaN MIS-HEMT. *Microelectron. Eng.* **2019**, *215*, 110976. [[CrossRef](#)]
26. Geng, K.; Chen, D.; Zhou, Q.; Wang, H. AlGaIn/GaN MIS-HEMT with PECVD SiNx, SiON, SiO2 as Gate Dielectric and Passivation Layer. *Electronics* **2018**, *7*, 416. [[CrossRef](#)]
27. Lutsenko, E.V.; Rzhetski, M.V.; Vainilovich, A.G.; Svitsiankou, I.E.; Tarasuk, N.P.; Yablonskii, G.P.; Alyamani, A.; Petrov, S.I.; Mamaev, V.V.; Alexeev, A.N. Investigation of Photoluminescence, Stimulated Emission, Photorefectance, and 2DEG Properties of Double Heterojunction AlGaIn/GaN/AlGaIn HEMT Heterostructures Grown by Ammonia MBE. *Phys. Status Solidi* **2018**, *215*, 1700602. [[CrossRef](#)]
28. Schroder, D.K. Carrier and Doping Density. In *Semiconductor Material and Device Characterization*; John Wiley & Sons, Inc.: Hoboken, NJ, USA, 2005; pp. 61–125.
29. Pashnev, D.; Korotyeyev, V.V.; Jorudas, J.; Kaplas, T.; Janonis, V.; Urbanowicz, A.; Kašalynas, I. Experimental evidence of temperature dependent effective mass in AlGaIn/GaN heterostructures observed via THz spectroscopy of 2D plasmons. *Appl. Phys. Lett.* **2020**, *117*, 162101. [[CrossRef](#)]
30. Hoon Shin, J.; Je Jo, Y.; Kim, K.-C.; Jang, T.; Sang Kim, K. Gate metal induced reduction of surface donor states of AlGaIn/GaN heterostructure on Si-substrate investigated by electroreflectance spectroscopy. *Appl. Phys. Lett.* **2012**, *100*, 111908. [[CrossRef](#)]
31. Kruszewski, P.; Grabowski, M.; Prystawko, P.; Nowakowska-Siwinska, A.; Sarzynski, M.; Leszczynski, M. Properties of AlGaIn/GaN Ni/Au-Schottky diodes on 2°-off silicon carbide substrates. *Phys. Status Solidi* **2017**, *214*, 1600376. [[CrossRef](#)]
32. Handler, P.; Farnsworth, H.E.; Kleiner, W.H.; Law, J.T.; Garrett, C.G.B.; Autler, H.; McWhorter, A.L. Electrical Properties of a Clean Germanium Surface. In *Semiconductor Surface Physics*; Kingston, R.H., Ed.; University of Pennsylvania Press: Philadelphia, PA, USA, 1957; pp. 23–52.
33. Christensson, S.; Lundström, I.; Svensson, C. Low frequency noise in MOS transistors—I Theory. *Solid State Electron.* **1968**, *11*, 797–812. [[CrossRef](#)]
34. Chavarkar, P.; Mishra, U.K. High Electron Mobility Transistors. In *RF and Microwave Semiconductor Device Handbook*; CRC Press: Boca Raton, FL, USA, 2017; pp. 8.1–8.32.

35. Schwierz, F.; Liou, J.J. RF transistors: Recent developments and roadmap toward terahertz applications. *Solid State Electron.* **2007**, *51*, 1079–1091. [[CrossRef](#)]
36. Shinohara, K.; Regan, D.C.; Tang, Y.; Corrion, A.L.; Brown, D.F.; Wong, J.C.; Robinson, J.F.; Fung, H.H.; Schmitz, A.; Oh, T.C.; et al. Scaling of GaN HEMTs and Schottky Diodes for Submillimeter-Wave MMIC Applications. *IEEE Trans. Electron. Devices* **2013**, *60*, 2982–2996. [[CrossRef](#)]

**Publisher’s Note:** MDPI stays neutral with regard to jurisdictional claims in published maps and institutional affiliations.



© 2020 by the authors. Licensee MDPI, Basel, Switzerland. This article is an open access article distributed under the terms and conditions of the Creative Commons Attribution (CC BY) license (<http://creativecommons.org/licenses/by/4.0/>).



**Development of Quaternary InAlGaN Barrier Layer for High Electron Mobility Transistor Structures**





**J. Jorudas** P. Prystawko, A. Šimukovič, R. Aleksiejūnas, J. Mickevičius,  
M. Kryško, P.P. Michałowski, I. Kašalynas  
*Materials*, vol. 15, no. 3, 1118 (2022).  
DOI: 10.3390/ma15031118

This is an open access article distributed under the Creative Commons Attribution License (CC-BY).

The article may be accessed online at <https://doi.org/10.3390/ma15031118>

Article

# Development of Quaternary InAlGaN Barrier Layer for High Electron Mobility Transistor Structures

Justinas Jorudas <sup>1,\*</sup>, Paweł Prystawko <sup>2</sup>, Artūras Šimukovič <sup>1</sup>, Ramūnas Aleksiejūnas <sup>3</sup>, Jūras Mickevičius <sup>3</sup>, Marcin Kryško <sup>2</sup>, Paweł Piotr Michałowski <sup>4</sup> and Irmantas Kašalynas <sup>1,5,\*</sup>

- <sup>1</sup> Terahertz Photonics Laboratory, Center for Physical Sciences and Technology (FTMC), Saulėtekio al. 3, LT-10257 Vilnius, Lithuania; arturas.simukovic@ftmc.lt
  - <sup>2</sup> Institute of High Pressure Physics PAS (UNIPRESS), ul. Sokolowska 29/37, 01-142 Warsaw, Poland; pprysta@unipress.waw.pl (P.P.); krysko@unipress.waw.pl (M.K.)
  - <sup>3</sup> Institute of Photonics and Nanotechnology, Vilnius University, Saulėtekio al. 3, LT-10257 Vilnius, Lithuania; ramunas.aleksiejunas@ff.vu.lt (R.A.); juras.mickevicius@ff.vu.lt (J.M.)
  - <sup>4</sup> Lukaszewicz Research Network-Institute of Microelectronics and Photonics, al. Lotników 32/46, 02-668 Warsaw, Poland; pawel.michalowski@imif.lukasiewicz.gov.pl
  - <sup>5</sup> Institute of Applied Electrodynamics and Telecommunications, Vilnius University, Saulėtekio al. 3, LT-10257 Vilnius, Lithuania
- \* Correspondence: justinas.jorudas@ftmc.lt (J.J.); irmantas.kasalynas@ftmc.lt (I.K.); Tel.: +370-5-231-2418 (I.K.)

**Abstract:** A quaternary lattice matched InAlGaN barrier layer with an indium content of  $16.5 \pm 0.2\%$  and thickness of 9 nm was developed for high electron mobility transistor structures using the metalorganic chemical-vapor deposition method. The structural, morphological, optical and electrical properties of the layer were investigated planning realization of microwave power and terahertz plasmonic devices. The measured X-ray diffraction and modeled band diagram characteristics revealed the structural parameters of the grown  $\text{In}_{0.165}\text{Al}_{0.775}\text{Ga}_{0.06}\text{N}/\text{Al}_{0.6}\text{Ga}_{0.4}\text{N}/\text{GaN}$  heterostructure, explaining the origin of barrier photoluminescence peak position at 3.98 eV with the linewidth of 0.2 eV and the expected red-shift of 0.4 eV only. The thermally stable density of the two-dimension electron gas at the depth of 10.5 nm was experimentally confirmed to be  $1.2 \times 10^{13} \text{ cm}^{-2}$  ( $1.6 \times 10^{13} \text{ cm}^{-2}$  in theory) with the low-field mobility values of  $1590 \text{ cm}^2/(\text{V}\cdot\text{s})$  and  $8830 \text{ cm}^2/(\text{V}\cdot\text{s})$  at the temperatures of 300 K and 77 K, respectively.

**Keywords:** InAlGaN; GaN; high electron mobility transistor structures; III-nitride heterostructures; microwave power devices; THz plasmonic devices



**Citation:** Jorudas, J.; Prystawko, P.; Šimukovič, A.; Aleksiejūnas, R.; Mickevičius, J.; Kryško, M.; Michałowski, P.P.; Kašalynas, I. Development of Quaternary InAlGaN Barrier Layer for High Electron Mobility Transistor Structures. *Materials* **2022**, *15*, 1118. <https://doi.org/10.3390/ma15031118>

Academic Editor: Alexander A. Lebedev

Received: 29 December 2021

Accepted: 28 January 2022

Published: 31 January 2022

**Publisher's Note:** MDPI stays neutral with regard to jurisdictional claims in published maps and institutional affiliations.



**Copyright:** © 2022 by the authors. Licensee MDPI, Basel, Switzerland. This article is an open access article distributed under the terms and conditions of the Creative Commons Attribution (CC BY) license (<https://creativecommons.org/licenses/by/4.0/>).

## 1. Introduction

Currently, III-nitride high electron mobility transistor (HEMT) structures based on the AlGaN/GaN heterostructure are extensively used in various applications such as gas sensors [1,2], THz detectors [3–6] and emitters [7,8], and high-power microwave devices [9–12]. A combination of InN and AlN alloys with very different bandgaps, lattice and spontaneous polarization constants can be used to implement a wide range of electric and optic properties in the heterostructure [13–15]. In particular, the lattice-matched (LM) InAlN/GaN heterostructures are very attractive for the development of HEMTs as they possess no degradation due to mechanical stress and exhibit high chemical and thermal stability, demonstrated at up to 1000 °C [16,17]. The use of thinner LM-InAlN barrier allows for the achievement of much higher two-dimensional electron gas (2DEG) densities than that in standard AlGaN/GaN HEMT structures with the same barrier thickness [18]. Moreover, barrier-layer scaling in InAlN/GaN HEMT structures down to 3 nm was demonstrated, exhibiting thermal stability (up to 1000 °C) of the barrier interface with a GaN buffer and with surface metals, used for electric contacts [19]. All of the reported features of the LM-InAl(Ga)N/GaN HEMT structures were found to be very

attractive for high power GaN-based electronic [11,20–22] and plasmonic devices [23,24]. In particular, optimal conditions for the excitation of 2D plasmons in standard AlGaIn/GaN HEMT structures up to the room temperature were revealed recently [25]. Among other aspects, a shallow depth and a high density of 2DEG in grating-gated heterostructures allow for efficient plasmonic device operation in the THz regime [26]. In this work, the quaternary LM-InAlGaIn barrier layer with indium content of  $16.5 \pm 0.2\%$  and thickness of only 9 nm was developed for GaN-based heterostructures on sapphire substrate and investigated studying material structural properties, optical and electrical characteristics of the test devices.

## 2. Samples

The heterostructure was developed on 2" diameter 430  $\mu\text{m}$  thick single-side polished sapphire substrate. The layers with a nominal thickness of 0.5 nm of GaN cap, 8.7 nm of  $\text{In}_x\text{Al}_{1-x}\text{N}$  barrier, 1.2 nm of  $\text{Al}_{0.66}\text{Ga}_{0.34}\text{N}$  spacer, 600 nm of undoped GaN channel, and 3.2  $\mu\text{m}$  GaN:C buffer on 25 nm low temperature GaN nucleation layer were grown along the polar  $c$ -axis using the metalorganic chemical vapor deposition (MOCVD) method in a Close Coupled Showerhead (CCS) Flip Top 3  $\times$  2 inch reactor (Aixtron, Herzogenrath, Germany). A schematic diagram of the heterostructure layers is also discussed in Section 3.3. Of note, if the thickness of the AlN spacer is larger than 1 nm, its role in the formation of 2DEG layer is not as significant due to the polarization discontinuity with the barrier, which was estimated to be of 0.73 eV from the effective conduction band offset between the LM-InAlN and GaN [18]. Moreover, the target of a  $\sim 9$  nm thickness of the barrier was chosen as optimum for high values of 2DEG density and mobility [19], with an expectation for higher transconductance values due to the short distance between the transistor gate and a 2DEG channel.

The AFM image of an as-grown heterostructure was measured with Dimension 3100 AFM instrument (Veeco, TX, USA). The results are shown in Figure 1. The RMS roughness over the whole image area ( $4 \times 4 \mu\text{m}^2$ ) was found to be 1.2 nm. The threading dislocation density (TDD) was estimated over the area of  $2 \times 2 \mu\text{m}^2$ , counting the pits, which are seen as the black color points in Figure 1. The value of TDD was around  $2 \times 10^9 \text{ cm}^{-2}$ .

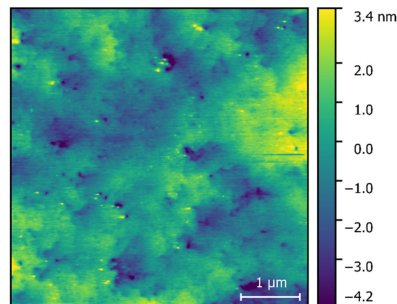


**Figure 1.** AFM image of the as-grown heterostructure.

The sheet resistance was measured by the microwave single-post dielectric resonator QWED SiPDR (QWED, Warsaw, Poland). At room temperature, the as-grown heterostructure demonstrated sheet resistance values of  $350 \pm 1 \Omega/\text{sq}$ .

Mesas for test devices were fabricated using inductively coupled plasma reactive ion etching (ICP-RIE) (Oxford Instruments, Bristol, UK) via Cl plasma. For ohmic contacts, Ti/Al/Ni/Au metal stack of thicknesses 30/90/20/150 nm were deposited and annealed in nitrogen ambient for 30 s at 850  $^\circ\text{C}$ . Schottky contacts were formed of 25/150 nm Ni/Au stack. The set of the test devices consisted of Van der Pauw (VdP) structures, transmission

line method (TLM) resistor array, HEMTs and Schottky barrier diodes (SBDs). Furthermore, test devices were left with an unpassivated nitride surface. More details about the device processing have been reported elsewhere [12,27].

Test TLM structures were used to estimate the resistance of ohmic contacts and the sheet resistance of the 2DEG layer. Their values were found to be of  $1 \Omega \text{ mm}$  and  $385 \Omega/\text{sq.}$ , respectively. The ideality factor and Schottky barrier height were determined from forward biased current-voltage characteristics of the SBDs applying the thermionic emission model [28], demonstrating the values of about 2.3 and 0.7 eV, respectively.

### 3. Results

#### 3.1. Secondary-Ion Mass Spectrometry (SIMS) of the Heterostructure

A SIMS analysis of as-grown heterostructure was performed in order to determine impurity density and distribution of atomic fractions in the layers. In this work SIMS depth profiles were performed employing the SC Ultra instrument (CAMECA, Gennevilliers, France) under ultra-high vacuum. The amount of residual oxygen, carbon, and silicon impurities in the GaN channel layer were found from the calibrated SIMS data to be of  $(3.7 \pm 1.3) \times 10^{16} \text{ cm}^{-3}$ ,  $(5.1 \pm 0.3) \times 10^{16} \text{ cm}^{-3}$ , and  $(1.0 \pm 0.6) \times 10^{16} \text{ cm}^{-3}$ , respectively. The amount of these impurities was close to that obtained by the low-frequency noise and THz electroluminescence spectroscopy methods in the AlGaIn/GaN HEMT on sapphire [27,29].

Figure 2 demonstrates the very uniform distribution of each atomic fraction along the growth direction of the heterostructure layers. A small fraction of Ga was found in the barrier, which occasionally occurs during the growth of the InAlN barrier in MOCVD reactor [30–32]. However, the CCS tools are known to accumulate the gallium-containing material on the inlet showerhead flange upstream the substrates. This deposit can be the unintentional source of the gallium incorporated into the main barrier layer grown and enhanced by TMIn and hydrogen carrier gas delivery [30].

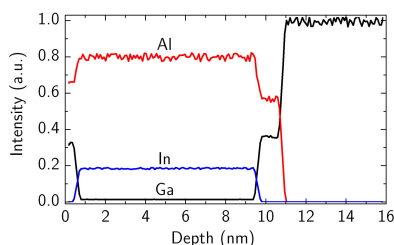
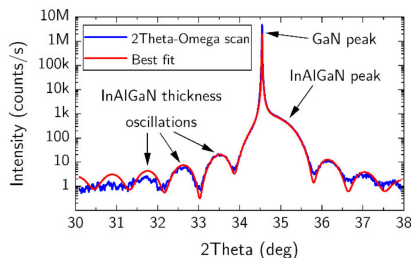


Figure 2. SIMS profile of Ga, In, and Al in the heterostructure under study.

#### 3.2. X-ray Diffraction (XRD) Analysis of the Heterostructure

The crystal quality, layer thicknesses and composition of as-grown heterostructure were investigated by HR-XRD analysis (Malvern Panalytical X'pert MRD, Almelo, Netherlands). The XRD results of as-grown heterostructure are shown in Figure 3. With the assumption that the Ga concentration was 6%, other concentrations were found to be of  $16.5 \pm 0.2\%$  In (error coming from fitting of the simulation) and  $77.5 \pm 0.2\%$  Al. To calculate the fitted curve the dynamical diffraction theory was used. Errors coming from uncertainty of elastic constants were negligible as the layer was not strained. Additionally, lattice constant,  $a$ , of the quaternary barrier was calculated with Nextnano++ software (Nextnano GmbH, München, Germany). The lattice matching to GaN with deviation of  $a_{\Delta} = ((a_{\text{Barrier}} - a_{\text{GaN}})/a_{\text{GaN}}) \times 100\%$  was found to be as small as  $-0.03\%$ . Moreover, a single layer of 30 nm thick InAl(Ga)N was grown on the GaN template using the same

growth conditions as for the investigated heterostructure. The XRD experiment confirmed that the barrier layer is lattice matched to GaN.



**Figure 3.** Experimental HR-XRD curve (blue line) and the best fit (red line) of the heterostructure with quaternary barrier composition of  $16.5 \pm 0.2\%$ ,  $77.5 \pm 0.2\%$ , and  $6\%$  for In, Al, and Ga, respectively, and thickness of  $8.6$  nm.

It is worth discussing the algorithm used in our work for the development of the LM barrier layers. Our method to assess the InAlN (In = 18%, AlN = 82%) barrier composition the path was as follows:

- (i). we made expected calculations of the gas-phase with surplus indium and aluminum precursors only, without flowing the gallium,
- (ii). we grew 30–50 nm thick calibration samples on GaN/Sapphire increasing the growth temperature and checking for lattice-matching to GaN in-plane lattice compatibility by HR-XRD,
- (iii). we applied the preferred high growth temperature and the growth rate to the HEMT final structure, growing a 9 nm thick LM-InAlGaN barrier.

We assumed that some gallium was incorporated into the barrier as expected from similar studies in literature while using the CCS reactors [30]. Therefore, the density of 2DEG and the band gap of barrier layer were experimentally investigated and simulated using Nextnano++ software (see details in next sections). Based on the Nextnano++ results, much higher 2DEG density for nominal ternary composition was expected, therefore, in simulation of HR-XRD data, we iteratively added Ga to the barrier, removing some In and Al but keeping the original Al/In ratio. In this way, the polarization influence on actual 2DEG concentration was decreased until a reasonable agreement between simulation and measurement values were obtained.

### 3.3. Band Diagram of the Heterostructure

Nextnano++ software was used to calculate the bandgap, lattice constant, 2DEG density in the heterostructure using the layers thicknesses from the growth protocol and quaternary barrier composition from the XRD analysis. The results of modeling are shown in Figure 4. It has been shown that for the best lattice-matching the Al/In ratio should be 4.63 [33,34]. The composition of the modeled quaternary heterostructure demonstrated a very similar Al/In ratio of 4.70. Furthermore, its bandgap of 4.36 eV (Figure 4a) was found to be very close to that of ternary  $\text{In}_x\text{Al}_{1-x}\text{N}$  barrier with an In fraction of 18% with  $E_G = 4.39$  eV (not shown). Finally, the calculated 2DEG density in the quaternary heterostructure was found to be of about  $1.6 \times 10^{13} \text{ cm}^{-2}$ .

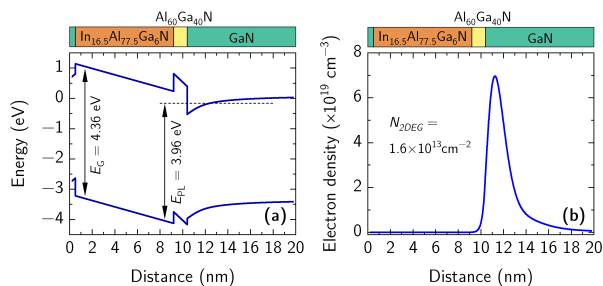


**Figure 4.** Band diagram (a) and 2DEG distribution (b) in the heterostructure calculated using the barrier composition determined from XRD measurements. A schematic representation of the heterostructure layout is provided above the figures.

#### 3.4. Two-Dimensional Electron Gas (2DEG)

The carrier density, mobility, and sheet resistance of the 2DEG were determined in Hall experiment using Van der Pauw structures at two temperatures, 77 K and 300 K. The sheet carrier density at both temperatures was  $1.2 \times 10^{13} \text{ cm}^{-2}$ , with an uncertainty of 3%. Meanwhile, the mobility increased with the decrease in temperature from  $1590 \text{ cm}^2 \text{ V}^{-1} \text{ s}^{-1}$  at 300 K to  $8830 \text{ cm}^2 \text{ V}^{-1} \text{ s}^{-1}$  at 77 K, resulting in the change in sheet resistance from  $320 \text{ } \Omega/\text{sq.}$  to  $60 \text{ } \Omega/\text{sq.}$ , respectively. A small difference in the 2DEG density between calculated  $1.6 \times 10^{13} \text{ cm}^{-2}$  and measured  $1.2 \times 10^{13} \text{ cm}^{-2}$  values can be explained by the heterostructure material sensitivity to the device fabrication steps such as chemical treatment, ion plasma etching, metal electrode deposition, and non-controlled surface unintentional passivation [12,27].

#### 3.5. Schottky Contact to 2DEG

The capacitance-voltage (C-V) characteristics of the fabricated Schottky contacts to the 2DEG layer were measured on the EPS150 probe station (Cascade Microtech, Beaverton, OR, USA) using precision impedance analyzer Agilent 4294A (Agilent, Santa Clara, CA, USA). Typical C-V characteristic of the circular SBD with  $5 \text{ } \mu\text{m}$  separation between ohmic-Schottky contacts and  $80 \text{ } \mu\text{m}$  diameter of inner Schottky pad are shown in Figure 5a. Data linear extrapolation to abscissa allowed us to determine the pinch-off voltage,  $V_{p-o}$ , which was found at  $-1.74 \text{ V}$ . The C-V results allowed us to estimate the dependence of carrier density,  $N$ , on the distance from the surface,  $W$ , employing the method described elsewhere [35]. The position of the 2DEG under the Schottky contact was found to be  $10.5 \text{ nm}$  from surface, which is very close to the nominal value of  $10.4 \text{ nm}$  defined from the growth protocol. It is worth noting that the high 2DEG density was achieved with a barrier thickness of only  $9 \text{ nm}$ . This is less than a half of the AlGaIn barrier layer thickness, which usually varies from  $20$  to  $25 \text{ nm}$  in standard AlGaIn/GaN HEMT structures [12,27].

#### 3.6. Photoluminescence of the Heterostructure

The photoluminescence (PL) spectra of as-grown heterostructure were measured using an optical parametric oscillator (OPO, Ekspla NT342B, Vilnius, Lithuania) for the excitation, generating four ns-pulses with peak power density of about  $200 \text{ kW}/\text{cm}^2$  and  $3 \text{ MW}/\text{cm}^2$  at the selected wavelength of  $300 \text{ nm}$  and  $250 \text{ nm}$ , respectively. Measured PL spectra are shown in Figure 6. At the excitation wavelength of  $300 \text{ nm}$  (black line in Figure 6), electron recombination in GaN barrier was probed only, demonstrating a Lorentz-shape band at the position of  $3.42 \text{ eV}$  with full width at half maximum (FWHM) of  $90 \text{ meV}$ . At the excitation wavelength of  $250 \text{ nm}$ , the broad band centered at around  $3.98 \text{ eV}$  with FWHM =  $200 \text{ meV}$  was measured in the PL spectrum (red line in Figure 6), revealing the contribution of InAlGaIn barrier [36,37].

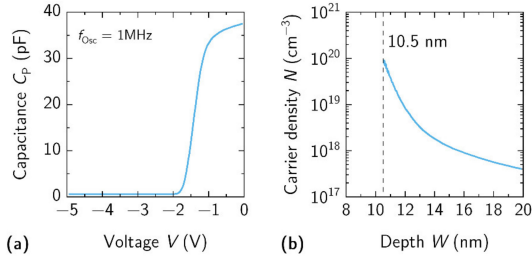


**Figure 5.** (a) Capacitance-voltage (at 1 MHz) measurements for circular SBD with  $\text{\O}80\ \mu\text{m}$  inner Schottky contact pad which is separated from outer ohmic contact by  $5\ \mu\text{m}$ . (b) Measured distribution of carrier density in the heterostructure. The position of 2DEG was found at  $10.5\ \text{nm}$  as marked by dashed vertical line.

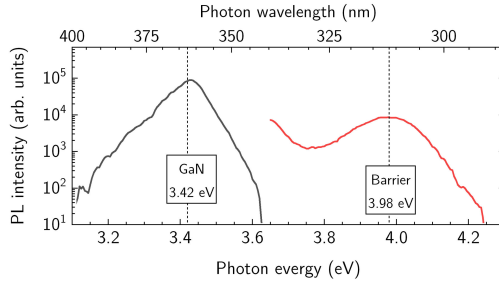


**Figure 6.** PL spectra of the heterostructure measured using different excitation wavelength and peak power density of  $300\ \text{nm}$  and  $200\ \text{kW}/\text{cm}^2$  (black line) and  $250\ \text{nm}$  and  $3\ \text{MW}/\text{cm}^2$  (red line), respectively.

The results of the PL measurements (see Figure 6) demonstrate a  $0.40\ \text{eV}$  red-shift from the expected bandgap energy of the quaternary barrier (see Figure 4a). Such a red-shift of the PL peak was sufficiently small in comparison to the Stokes shifts reported for similar heterostructures with InAlN barrier exhibiting values in the range of  $0.4\text{--}1\ \text{eV}$  [36–40]. Various explanations of the Stokes shift were proposed such as the introduction of sub-band edge states near the band edge minima which induce strain and related alloy composition fluctuations [41], local variations of the number of Al and In atoms surrounding nitrogen atom [42] or radiative recombination between the electrons in the triangular quantum well (2DEG) and photoexcited holes efficiently transferred from InAlN to GaN via sub-band-gap states [37].

Taking into account the energy levels of the barrier conduction band in the vicinity of  $\text{Al}_{0.66}\text{Ga}_{0.34}\text{N}$  spacer ( $237\ \text{meV}$ ) and of 2DEG ( $-162\ \text{meV}$ ) with respect to the barrier bandgap ( $4.36\ \text{eV}$ ), the modified bandgap was estimated to be of about  $E_{\text{PL}} = 3.96\ \text{eV}$ , which is close to the measured PL peak position at  $3.98\ \text{eV}$ . Additionally, the evaluation of the transition energies in *c*-plane grown heterostructure is somehow affected by carrier confinement and the built-in electric field. Therefore, the developed quaternary heterostructure requires a more detailed investigation of photo-carrier transport and a direct comparison of PL spectra with the results of other methods able to determine the bandgap of barrier layer such as a photoluminescence excitation (PLE), cathode photoluminescence (CL), and reflection modulated spectroscopy.

### 3.7. Application of the Heterostructure for Electronic Devices

The SBDs were processed without surface passivation and investigated in the reverse bias regime in order to find the breakdown fields. The results are shown in Figure 7. For the 5  $\mu\text{m}$  contact separation, SBD breakdown occurred at the electric field of 0.43 MV/cm (Figure 7 solid line). For the largest contact separation of 40  $\mu\text{m}$ , the breakdown field value decreased to 0.05 MV/cm (Figure 7 dashed line). The breakdown of the SBD was found to occur via the surface defects and threading dislocations, both of which create shunting paths for the leakage current, the value of which before the breakdown (at  $(-200)$ – $(-230)$  V) was up to 2.14 mA/mm. Furthermore, the SBDs with larger contact separation had a larger active area, which includes more defect and threading dislocations [43–46]. We would think that large leakage currents could cause a thermal breakdown of the device.

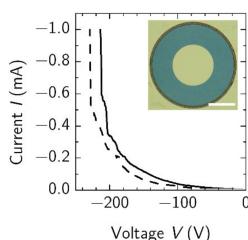


**Figure 7.** Breakdown of two SBDs with contact spacings of 5  $\mu\text{m}$  (solid line) and 40  $\mu\text{m}$  (dashed line). Current was limited to 1 mA level. Inset—microscope image of the SBD with diameter of central Schottky contact and distance to ohmic contact being of 80  $\mu\text{m}$  and 40  $\mu\text{m}$ , respectively.

The HEMTs were also processed and studied on the wafer in DC and RF regimes using the Süss Microtech probe station PM8 (FormFactor Inc., Livermore Inc., Livermore, CA, USA). For the RF measurements the G-S-G (ground–signal–ground) high frequency probes, an E8364B PNA Network Analyzer (Keysight Technologies, Santa Rosa, CA, USA), and E5270B Precision IV Analyzer with IC-CAP software were used (Keysight Technologies, Santa Rosa, CA, USA). The two-step open-short de-embedding method was implemented, and small signal S-parameters were obtained. The unity current gain–cut-off frequency ( $f_T$ ) and the unity maximum unilateral power gain frequency ( $f_{\text{max}}$ ) were found from de-embedded S-parameter frequency characteristics.

Each HEMT was developed in G-S-G device configuration with  $W_{\text{ch}} = 2 \mu\text{m} \times 200 \mu\text{m}$ ,  $L_{\text{ds}} = 12 \mu\text{m}$  and  $L_{\text{g}} = 5 \mu\text{m}$ . The results for HEMTs characterization in DC and RF regimes are shown in Figure 8. Output characteristics demonstrate (see Figure 8a) the effect of very low pinch-off voltage, where the channel is fully closed at  $V_{\text{gs}} = -2$  V. The highest output drain current was recorded at  $V_{\text{ds}} = 6$  V and  $V_{\text{gs}} = 1$  V, reaching up to 200 mA/mm, which deteriorate with further increase in drain voltage due to excess heat accumulation in the conductive channel. The transfer curve for the same device at  $V_{\text{ds}} = 5$  V is shown in Figure 8b. Large leakage currents were observed both in the drain and gate contacts under negative gate bias. The  $I_{\text{on}}/I_{\text{off}}$  ratio for the HEMT was limited to the value of 26 dB. The small-signal transconductance values for this device were measured to be up to 117 mS/mm at  $V_{\text{gs}} = +0.6$  V. The results of RF characterization are shown in Figure 8c. The highest  $f_T$  and  $f_{\text{max}}$  values at  $V_{\text{ds}} = 5$  V and  $V_{\text{gs}} = 0.2$  V were estimated to be up to 0.95 GHz and 4.5 GHz, respectively. The figure of merit value  $f_T \times L_{\text{g}}$  for the investigated HEMT was of 4.3 GHz  $\times \mu\text{m}$ , which is about two times lower than 10 GHz  $\times \mu\text{m}$ , reported for the scaled HEMTs made of similar InAl(Ga)N/GaN heterostructures [10,47]. The difference can be explained by a simplified design of our transistors due to the usage of standard UV photolithography instead of e-beam lithography.



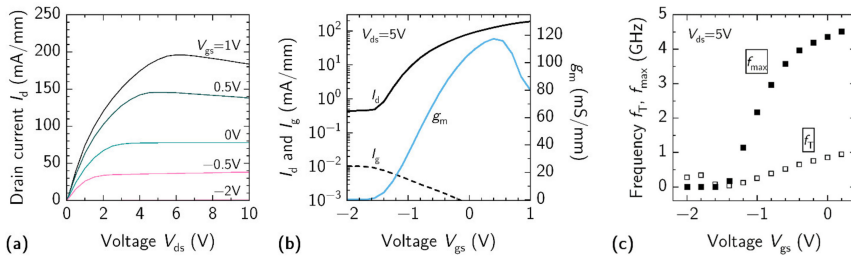


**Figure 8.** (a) Output characteristics, (b) transfer characteristics and (c)  $f_T$  and  $f_{max}$  frequencies measured for the same HEMT with  $L_g = 5 \mu\text{m}$  and  $L_{ds} = 12 \mu\text{m}$ .

#### 4. Conclusions

A quaternary LM InAlGaN barrier layer with an indium content of  $16.5 \pm 0.2\%$  and thickness of only 9 nm has been developed for high electron mobility transistor structures by metalorganic chemical vapor deposition method. A detailed analysis of the structural, morphological, optical and electrical properties revealed the composition of the barrier layer to be  $16.5 \pm 0.2\%$  of In,  $77.5 \pm 0.2\%$  of Al, and 6% of Ga, and allowed us to explain the origin of barrier photoluminescence peak position observed at 3.98 eV with the linewidth of 0.2 eV and the expected red-shift of 0.4 eV only. The thermally stable density of the two-dimension electron gas at the depth of 10.5 nm was experimentally confirmed to be of  $1.2 \times 10^{13} \text{ cm}^{-2}$  ( $1.6 \times 10^{13} \text{ cm}^{-2}$  in theory) with low-field mobility values of  $1590 \text{ cm}^2/(\text{V}\cdot\text{s})$  and  $8830 \text{ cm}^2/(\text{V}\cdot\text{s})$  at the temperatures of 300 K and 77 K, respectively. The fabricated Schottky barrier diodes allowed us to determine the pinch-off voltage to be  $-1.74 \text{ V}$  and breakdown field to be  $0.4 \text{ MV/cm}$  for this heterostructure. The HEMTs fabricated of this heterostructure were tested both in dc and rf regimes and show similar performance to the standard AlGaIn/GaN HEMTs, considering that a substantially thinner barrier layer was used. Overall, the results presented in our work indicate that the developed heterostructure with quaternary LM-InAlGaN barrier is a promising candidate for microwave power electronic and plasmonic devices operating in the THz range.

**Author Contributions:** Conceptualization, P.P. and I.K.; investigation, J.J., P.P., A.Š., R.A., J.M., M.K., P.P.M. and I.K.; data curation, J.J., P.P. and I.K.; writing—original draft preparation, J.J. and I.K.; writing—review and editing, J.J., P.P., R.A. and I.K.; visualization, J.J. and I.K.; supervision, P.P. and I.K.; project administration, I.K.; funding acquisition, P.P. and I.K. All authors have read and agreed to the published version of the manuscript.

**Funding:** The work was supported by the Research Council of Lithuania (Lietuvos mokslo taryba) under the “TERAGANWIRE” project (Grant No. S-L-19-1), by the National Science Center of Poland (Grant No. 2017/27/L/ST7/03283), by “International Research Agendas” program of the Foundation for Polish Science co-financed by the European Union under the European Regional Development Fund (Nos. MAB/2018/9), and partially supported by the Polish National Center for Research and Development through projects No. WPC/20/DefeGaN/2018 and No. TECHMATSTRATEG-III/0003/2019.

**Institutional Review Board Statement:** Not applicable.

**Informed Consent Statement:** Not applicable.

**Data Availability Statement:** The data presented in this study are available on request from the corresponding author. The data are not publicly available due to privacy.

**Conflicts of Interest:** The authors declare no conflict of interest.

## References

- Ahn, J.; Kim, D.; Park, K.-H.; Yoo, G.; Heo, J. Pt-Decorated Graphene Gate AlGaN/GaN MIS-HEMT for Ultrahigh Sensitive Hydrogen Gas Detection. *IEEE Trans. Electron Devices* **2021**, *68*, 1255–1261. [\[CrossRef\]](#)
- Nguyen, V.C.; Kim, K.; Kim, H. Performance Optimization of Nitrogen Dioxide Gas Sensor Based on Pd-AlGaN/GaN HEMTs by Gate Bias Modulation. *Micromachines* **2021**, *12*, 400. [\[CrossRef\]](#) [\[PubMed\]](#)
- Sun, J.; Feng, W.; Ding, Q.; Zhu, Y.; Zhang, Z.; Li, X.; Qin, H.; Zhang, J.; Li, X.; Shangguan, Y.; et al. Smaller Antenna-Gate Gap for Higher Sensitivity of GaN/AlGaN HEMT Terahertz Detectors. *Appl. Phys. Lett.* **2020**, *116*, 161109. [\[CrossRef\]](#)
- Yang, L.; Yao, W.; Liu, Y.; Wang, L.; Dai, Y.; Liu, H.; Wang, F.; Ren, Y.; Wu, Z.; Liu, Y.; et al. Low Capacitance AlGaN/GaN Based Air-Bridge Structure Planar Schottky Diode with a Half through-Hole. *AIP Adv.* **2020**, *10*, 045219. [\[CrossRef\]](#)
- Bauer, M.; Ramer, A.; Chevtchenko, S.A.; Osipov, K.Y.; Cibraite, D.; Pralgauskaitė, S.; Ikamas, K.; Liasauskas, A.; Heinrich, W.; Krozer, V.; et al. A High-Sensitivity AlGaN/GaN HEMT Terahertz Detector With Integrated Broadband Bow-Tie Antenna. *IEEE Trans. Terahertz Sci. Technol.* **2019**, *9*, 430–444. [\[CrossRef\]](#)
- Jorudas, J.; Malakauskaitė, J.; Subačius, L.; Janonis, V.; Jakštas, V.; Kovalevskij, V.; Kašalynas, I.; Malakauskaitė, J.; Subačius, L.; Janonis, V.; et al. Development of the Planar AlGaN/GaN Bow-Tie Diodes for Terahertz Detection. In Proceedings of the 2019 44th International Conference on Infrared, Millimeter and Terahertz Waves (IRMMW-THz), Paris, France, 1–6 September 2019; pp. 1–2. [\[CrossRef\]](#)
- El Fatimy, A.; Dyakonova, N.; Meziani, Y.; Otsuji, T.; Knap, W.; Vandembrouck, S.; Madjour, K.; Théron, D.; Gaquiere, C.; Poisson, M.A.; et al. AlGaN/GaN High Electron Mobility Transistors as a Voltage-Tunable Room Temperature Terahertz Sources. *J. Appl. Phys.* **2010**, *107*, 24504. [\[CrossRef\]](#)
- Janonis, V.; Pashnev, D.; Grigelionis, I.; Korotiev, V.; Balagula, R.M.; Minkevicius, L.; Jorudas, J.; Alexeeva, N.; Subačius, L.; Valušis, G.; et al. Electrically-Pumped THz Emitters based on Plasma Waves Excitation in III-Nitride Structures. In *Terahertz Emitters, Receivers, and Applications XI*; Razeghi, M., Baranov, A.N., Eds.; SPIE: Washington, DC, USA, 2020; Volume 11499, p. 8. [\[CrossRef\]](#)
- Romanczyk, B.; Mishra, U.K.; Zheng, X.; Guidry, M.; Li, H.; Hatui, N.; Wurm, C.; Krishna, A.; Ahmadi, E.; Keller, S. W-Band Power Performance of SiN-Passivated N-Polar GaN Deep Recess HEMTs. *IEEE Electron Device Lett.* **2020**, *41*, 349–352. [\[CrossRef\]](#)
- Shinohara, K.; Regan, D.C.; Tang, Y.; Corrión, A.L.; Brown, D.F.; Wong, J.C.; Robinson, J.F.; Fung, H.H.; Schmitz, A.; Oh, T.C.; et al. Scaling of GaN HEMTs and Schottky Diodes for Submillimeter-Wave MMIC Applications. *IEEE Trans. Electron Devices* **2013**, *60*, 2982–2996. [\[CrossRef\]](#)
- Hassan, A.; Savaria, Y.; Sawan, M. GaN Integration Technology, an Ideal Candidate for High-Temperature Applications: A Review. *IEEE Access* **2018**, *6*, 78790–78802. [\[CrossRef\]](#)
- Jorudas, J.; Šimukovič, A.; Dub, M.; Sakowicz, M.; Prystawko, P.; Indrišūnas, S.; Kovalevskij, V.; Rumyantsev, S.; Knap, W.; Kašalynas, I. AlGaN/GaN on SiC Devices without a GaN Buffer Layer: Electrical and Noise Characteristics. *Micromachines* **2020**, *11*, 1131. [\[CrossRef\]](#)
- Kuzmík, J. InAlN/(In)GaN High Electron Mobility Transistors: Some Aspects of the Quantum Well Heterostructure Proposal. *Semicond. Sci. Technol.* **2002**, *17*, 540–544. [\[CrossRef\]](#)
- Kuzmík, J.; Kostopoulos, A.; Konstantinidis, G.; Carlin, J.F.; Georgakilas, A.; Pogány, D. InAlN/GaN HEMTs: A First Insight into Technological Optimization. *IEEE Trans. Electron Devices* **2006**, *53*, 422–426. [\[CrossRef\]](#)
- Kuzmík, J. Power Electronics on InAlN/(In)GaN: Prospect for a Record Performance. *IEEE Electron Device Lett.* **2001**, *22*, 510–512. [\[CrossRef\]](#)
- Maier, D.; Alomari, M.; Grandjean, N.; Carlin, J.-F.; Diforte-Poisson, M.-A.; Dua, C.; Delage, S.; Kohn, E. InAlN/GaN HEMTs for Operation in the 1000 C Degrees Regime: A First Experiment. *IEEE Electron Device Lett.* **2012**, *33*, 985–987. [\[CrossRef\]](#)
- Medjdoub, F.; Carlin, J.-F.; Gonschorek, M.; Feltin, E.; Py, M.A.; Ducaudeau, D.; Gaquiere, C.; Grandjean, N.; Kohn, E. Can InAlN/GaN Be an Alternative to High Power/High Temperature AlGaN/GaN Devices? In Proceedings of the 2006 International Electron Devices Meeting, San Francisco, CA, USA, 11–13 December 2006; pp. 1–4. [\[CrossRef\]](#)
- Gonschorek, M.; Carlin, J.-F.; Feltin, E.; Py, M.A.; Grandjean, N.; Darakchieva, V.; Monemar, B.; Lorenz, M.; Ramm, G. Two-Dimensional Electron Gas Density in  $Al_{1-x}In_xN$ /AlN/GaN Heterostructures ( $0.03 \leq x \leq 0.23$ ). *J. Appl. Phys.* **2008**, *103*, 093714. [\[CrossRef\]](#)
- Medjdoub, F.; Alomari, M.; Carlin, J.F.; Gonschorek, M.; Feltin, E.; Py, M.A.; Grandjean, N.; Kohn, E. Barrier-Layer Scaling of InAlN/GaN HEMTs. *IEEE Electron Device Lett.* **2008**, *29*, 422–425. [\[CrossRef\]](#)
- Liu, Y.; Jiang, H.; Arulkumar, S.; Egawa, T.; Zhang, B.; Ishikawa, H. Demonstration of Undoped Quaternary AlInGaN/GaN Heterostructure Field-Effect Transistor on Sapphire Substrate. *Appl. Phys. Lett.* **2005**, *86*, 223510. [\[CrossRef\]](#)
- Wang, R.; Li, G.; Karbasian, G.; Guo, J.; Song, B.; Yue, Y.; Hu, Z.; Laboutin, O.; Cao, Y.; Johnson, W.; et al. Quaternary Barrier InAlGaN HEMTs With FT/Fmax of 230/300 GHz. *IEEE Electron Device Lett.* **2013**, *34*, 378–380. [\[CrossRef\]](#)
- Lecourt, F.; Agboton, A.; Ketteniss, N.; Behmenburg, H.; Defrance, N.; Hoel, V.; Kalisch, H.; Vescan, A.; Heuken, M.; de Jaeger, J.-C. Power Performance at 40 GHz on Quaternary Barrier InAlGaN/GaN HEMT. *IEEE Electron Device Lett.* **2013**, *34*, 978–980. [\[CrossRef\]](#)
- Shur, M.S. Terahertz Plasmonic Technology. *IEEE Sens. J.* **2021**, *21*, 12752–12763. [\[CrossRef\]](#)
- Shur, M.; Aizin, G.; Otsuji, T.; Ryzhii, V. Plasmonic Field-Effect Transistors (TeraFETs) for 6G Communications. *Sensors* **2021**, *21*, 7907. [\[CrossRef\]](#) [\[PubMed\]](#)

Pashnev, D.; Korotyeyev, V.V.; Jorudas, J.; Kaplas, T.; Janonis, V.; Urbanowicz, A.; Kašalynas, I. Experimental Evidence of Temperature Dependent Effective Mass in AlGa<sub>N</sub>/Ga<sub>N</sub> Heterostructures Observed via THz Spectroscopy of 2D Plasmons. *Appl. Phys. Lett.* **2020**, *117*, 162101. [\[CrossRef\]](#)

Pashnev, D.; Kaplas, T.; Korotyeyev, V.; Janonis, V.; Urbanowicz, A.; Jorudas, J.; Kašalynas, I. Terahertz Time-Domain Spectroscopy of Two-Dimensional Plasmons in AlGa<sub>N</sub>/Ga<sub>N</sub> Heterostructures. *Appl. Phys. Lett.* **2020**, *117*, 051105. [\[CrossRef\]](#)

Sai, P.; Jorudas, J.; Dub, M.; Sakowicz, M.; Jakštas, V.; But, D.B.; Prystawko, P.; Cywinski, G.; Kašalynas, I.; Knap, W.; et al. Low Frequency Noise and Trap Density in Ga<sub>N</sub>/AlGa<sub>N</sub> Field Effect Transistors. *Appl. Phys. Lett.* **2019**, *115*, 183501. [\[CrossRef\]](#)

Schroder, D.K. Contact Resistance and Schottky Barriers. In *Semiconductor Material and Device Characterization*; John Wiley & Sons, Inc.: Hoboken, NJ, USA, 2005; pp. 127–184.

Grigelionis, I.; Jorudas, J.; Jakštas, V.; Janonis, V.; Kašalynas, I.; Prystawko, P.; Kruszewski, P.; Leszczyński, M. Terahertz Electroluminescence of Shallow Impurities in AlGa<sub>N</sub>/Ga<sub>N</sub> Heterostructures at 20 K and 110 K Temperature. *Mater. Sci. Semicond. Process.* **2019**, *93*, 280–283. [\[CrossRef\]](#)

Kim, J.; Lochner, Z.; Ji, M.-H.; Choi, S.; Kim, H.J.; Kim, J.S.; Dupuis, R.D.; Fischer, A.M.; Juday, R.; Huang, Y.; et al. Origins of Unintentional Incorporation of Gallium in InAlN Layers during Epitaxial Growth, Part II: Effects of Underlying Layers and Growth Chamber Conditions. *J. Cryst. Growth* **2014**, *388*, 143–149. [\[CrossRef\]](#)

Naresh-Kumar, G.; Vilalta-Clemente, A.; Pandey, S.; Skuridina, D.; Behnenburg, H.; Gamarra, P.; Patriarche, G.; Vickridge, I.; di Forte-Poisson, M.A.; Vogt, P.; et al. Multicharacterization Approach for Studying InAl(Ga)N/Al(Ga)N/GaN Heterostructures for High Electron Mobility Transistors. *AIP Adv.* **2014**, *4*, 127101. [\[CrossRef\]](#)

Hiroki, M.; Oda, Y.; Watanabe, N.; Maeda, N. Unintentional Ga Incorporation in Metalorganic Vapor Phase Epitaxy of In-Containing III-Nitride Semiconductors. *J. Cryst. Growth* **2013**, *382*, 36–40. [\[CrossRef\]](#)

Rahimzadeh Khoshroo, L.; Ketteniss, N.; Mauder, C.; Behnenburg, H.; Woitok, J.F.; Booker, I.; Cruis, J.; Heuken, M.; Vescan, A.; Kalisch, H.; et al. Quaternary Nitride Heterostructure Field Effect Transistors. *Phys. Status Solidi C* **2010**, *7*, 2001–2003. [\[CrossRef\]](#)

Ketteniss, N.; Khoshroo, L.R.; Eickelkamp, M.; Heuken, M.; Kalisch, H.; Jansen, R.H.; Vescan, A. Study on Quaternary Alln-GaN/GaN HFETs Grown on Sapphire Substrates. *Semicond. Sci. Technol.* **2010**, *25*, 75013. [\[CrossRef\]](#)

Schroder, D.K. Carrier and Doping Density. In *Semiconductor Material and Device Characterization*; John Wiley & Sons, Inc.: Hoboken, NJ, USA, 2005; pp. 61–125.

Butt , R.; Carlin, J.-F.; Feltin, E.; Gonschorek, M.; Nicolay, S.; Christmann, G.; Simeonov, D.; Castiglia, A.; Dorsaz, J.; Buehlmann, H.J.; et al. Current Status of AllnN Layers Lattice-Matched to GaN for Photonics and Electronics. *J. Phys. D Appl. Phys.* **2007**, *40*, 6328–6344. [\[CrossRef\]](#)

Liulio, V.; Marcinkevičius, S.; Billingsley, D.; Shatalov, M.; Yang, J.; Gaska, R.; Shur, M.S. Photoexcited Carrier Dynamics in AllnN/GaN Heterostructures. *Appl. Phys. Lett.* **2012**, *100*, 242104. [\[CrossRef\]](#)

Gonschorek, M.; Simeonov, D.; Carlin, J.-F.; Feltin, E.; Py, M.A.; Grandjean, N. Temperature Mapping of Al<sub>0.85</sub>In<sub>0.15</sub>N/AlN/GaN High Electron Mobility Transistors through Micro-Photoluminescence Studies. *Eur. Phys. J. Appl. Phys.* **2009**, *47*, 30301. [\[CrossRef\]](#)

Marcinkevičius, S.; Liulio, V.; Billingsley, D.; Shatalov, M.; Yang, J.; Gaska, R.; Shur, M.S. Transient Photoreflectance of AllnN/GaN Heterostructures. *AIP Adv.* **2012**, *2*, 042148. [\[CrossRef\]](#)

Marcinkevičius, S.; Sztejn, A.; Nakamura, S.; Speck, J.S. Properties of Sub-Band Edge States in AllnN Studied by Time-Resolved Photoluminescence of a AllnN/GaN Heterostructure. *Semicond. Sci. Technol.* **2015**, *30*, 115017. [\[CrossRef\]](#)

Mouti, A.; Rouvière, J.-L.; Cantoni, M.; Carlin, J.-F.; Feltin, E.; Grandjean, N.; Stadelmann, P. Stress-Modulated Composition in the Vicinity of Dislocations in Nearly Lattice Matched Al<sub>x</sub>In<sub>1-x</sub>N/GaN Heterostructures: A Possible Explanation of Defect Insensitivity. *Phys. Rev. B* **2011**, *83*, 195309. [\[CrossRef\]](#)

Schulz, S.; Caro, M.A.; Tan, L.-T.; Parbrook, P.J.; Martin, R.W.; O'Reilly, E.P. Composition-Dependent Band Gap and Band-Edge Bowing in AllnN: A Combined Theoretical and Experimental Study. *Appl. Phys. Express* **2013**, *6*, 121001. [\[CrossRef\]](#)

Wahab, Q.; Ellison, A.; Henry, A.; Janzén, E.; Hallin, C.; di Persio, J.; Martinez, R. Influence of Epitaxial Growth and Substrate-Induced Defects on the Breakdown of 4H-SiC Schottky Diodes. *Appl. Phys. Lett.* **2000**, *76*, 2725–2727. [\[CrossRef\]](#)

Muzykov, P.G.; Bolotnikov, A.V.; Sudarshan, T.S. Study of Leakage Current and Breakdown Issues in 4H-SiC Underminated Schottky Diodes. *Solid State Electron.* **2009**, *53*, 14–17. [\[CrossRef\]](#)

Lee, K.-Y.; Capano, M.A. The Correlation of Surface Defects and Reverse Breakdown of 4H-SiC Schottky Barrier Diodes. *J. Electron. Mater.* **2007**, *36*, 272–276. [\[CrossRef\]](#)

Saito, W.; Kuraguchi, M.; Takada, Y.; Tsuda, K.; Omura, I.; Ogura, T. Influence of Surface Defect Charge at AlGa<sub>N</sub>-Ga<sub>N</sub>-HEMT Upon Schottky Gate Leakage Current and Breakdown Voltage. *IEEE Trans. Electron Devices* **2005**, *52*, 159–164. [\[CrossRef\]](#)

Gaska, R.; Shur, M.S.; Hu, X.; Yang, J.W.; Tarakji, A.; Simin, G.; Khan, A.; Deng, J.; Werner, T.; Rumyantsev, S.; et al. Highly Doped Thin-Channel Ga<sub>N</sub>-Metal-Semiconductor Field-Effect Transistors. *Appl. Phys. Lett.* **2001**, *78*, 769–771. [\[CrossRef\]](#)

**Low Frequency Noise and Trap Density in GaN/AlGaN Field Effect Transistors**

P. Sai, **J. Jorudas**, M. Dub, M. Sakowicz, V. Jakštas, D.B. But, P. Prystawko,  
G. Cywinski, I. Kašalynas, W. Knap  
*Applied Physics Letters*, vol. 115, no. 18, 183501 (2019).  
DOI: 10.1063/1.5119227

This is an open access article distributed under the Creative Commons Attribution  
License (CC-BY).

The article may be accessed online at <https://doi.org/10.1063/1.5119227>

# Low frequency noise and trap density in GaN/AlGaN field effect transistors

Cite as: Appl. Phys. Lett. **115**, 183501 (2019); doi: 10.1063/1.5119227

Submitted: 9 July 2019 · Accepted: 17 October 2019 ·

Published Online: 29 October 2019



P. Sai,<sup>1,2</sup> J. Jorudas,<sup>3</sup> M. Dub,<sup>1,2</sup> M. Sakowicz,<sup>4</sup> V. Jakštas,<sup>3</sup> D. B. But,<sup>1,2,5</sup> P. Prystawko,<sup>4</sup> G. Cywinski,<sup>1,5</sup> I. Kašalynas,<sup>3,a)</sup> W. Knap,<sup>1,5,6</sup> and S. Rumyantsev<sup>1,a)</sup>

## AFFILIATIONS

<sup>1</sup>CENTERA Laboratories, Institute of High Pressure Physics PAS, ul. Sokołowska 29/37, 01-142 Warsaw, Poland

<sup>2</sup>V. Ye. Lashkaryov Institute of Semiconductor Physics, National Academy of Sciences of Ukraine, 41 pr. Nauki, 03680 Kyiv, Ukraine

<sup>3</sup>Terahertz Photonics Laboratory, Center for Physical Sciences and Technology (FTMC), Saulėtekio al. 3, LT-10257 Vilnius, Lithuania

<sup>4</sup>Institute of High Pressure Physics PAS, ul. Sokołowska 29/37, 01-142 Warsaw, Poland

<sup>5</sup>CEZAMAT, Warsaw University of Technology, 02-822 Warsaw, Poland

<sup>6</sup>Laboratoire Charles Coulomb, University of Montpellier and CNRS UMR 5221, 34950 Montpellier, France

<sup>a)</sup>Authors to whom correspondence should be addressed: [irmantas.kasalynas@ftmc.lt](mailto:irmantas.kasalynas@ftmc.lt) and [roumis4@gmail.com](mailto:roumis4@gmail.com)

## ABSTRACT

We report experimental results on the low-frequency noise in GaN/AlGaN transistors fabricated under different conditions and evaluate different methods to extract the effective trap density using the McWhorter model. The effective trap density is found to be below  $10^{19} \text{ cm}^{-3}$  for some of the wafers. This trap density is of the same order of magnitude as that reported in Si MOSFETs with a high-k dielectric. One of the structures manifested about two orders of magnitude higher noise level. These measurements correlate with the results of secondary ion mass spectroscopy and terahertz electroluminescence measurements which indicated a  $\sim 30\%$  higher concentration of uncompensated oxygen in this structure. Effective trap density extracted from noise measurements is proven to be a very sensitive figure of merit parameter for the GaN/AlGaN field effect transistors and material quality assessment.

© 2019 Author(s). All article content, except where otherwise noted, is licensed under a Creative Commons Attribution (CC BY) license (<http://creativecommons.org/licenses/by/4.0/>). <https://doi.org/10.1063/1.5119227>

The low frequency noise in GaN-based field effect transistors (FETs) has been studied for more than 20 years (see Refs. 1–7 and references therein). In the majority of publications, the amplitude of the  $1/f$  noise is characterized by the Hooge parameter  $\alpha_H = S_f/f^2 \times N \times f^3$ . Here,  $S_f/f^2$  is the relative spectral noise density of the drain current fluctuations,  $N$  is the total number of carriers in the channel, and  $f$  is the frequency. Although there is no theory behind this formula, it is a simple and convenient way to characterize the amplitude of noise and compare the noise level of different devices. The value of the Hooge parameter reported in publications in GaN/AlGaN high electron mobility field effect transistors (HEMTs) is within the range  $\alpha_H \cong 10^{-1}-10^{-5}$ .<sup>1,2,5,6,9,10</sup> However, the Hooge parameter in GaN/AlGaN HEMTs usually depends on the gate voltage, i.e., on the electron concentration in the channel. Therefore, it is not clear how to choose the electron concentration (gate voltage) to compare noise in different HEMTs.

Another method to characterize noise in FETs is based on the McWhorter model of noise in Si MOSFETs.<sup>11,12</sup> In this model, the  $1/f$

noise originates from the tunneling of electrons from the channel to oxide and their capture at different distances from the channel.

The mechanism of noise in GaN/AlGaN transistors can be quite similar. Electrons can tunnel from the channel to the AlGaN barrier layer or to the GaN and be captured there by the traps. The McWhorter model allows to calculate the trap density responsible for the  $1/f$  noise, which is a good figure of merit for the noise amplitude and HEMT quality. However, there are just a limited number of publications where the trap density in GaN/AlGaN transistors was estimated based on the McWhorter model and compared with the other FETs.<sup>7,13,14</sup>

In this work, we study the  $1/f$  noise in GaN/AlGaN HEMTs fabricated under different conditions, evaluate different methods to extract the trap density, and compare the results with Si MOSFETs.

The epistructures were grown on a high-resistivity GaN:C buffer formed either on a c-axis sapphire ( $\text{Al}_2\text{O}_3$ ) or on semi-insulating (SI) 6H poly-type SiC substrate by the metalorganic chemical vapor deposition (MOCVD) method. The unintentionally doped (UID) GaN

TABLE I. Nominal thickness and some other parameters of epilayers.

Wafer layer	#TG2196	#TG2219	#Hx2688
SiN <sub>x</sub> cap	No	No	1 nm
GaN cap	No	1 nm	2 nm
Al <sub>x</sub> Ga <sub>1-x</sub> N barrier	25 nm	27 nm	19 nm
	$x = 0.20$	$x = 0.23$	$x = 0.25$
AlN spacer	1 nm	1 nm	0.8 nm
UID-GaN	500 nm	500 nm	1000 nm
GaN:C	1000 nm	1000 nm	1300 nm
Substrate	Al <sub>2</sub> O <sub>3</sub>	Al <sub>2</sub> O <sub>3</sub>	SiC

layers were grown at the pressure of  $P = \sim 100, \sim 200, \sim 300$  Torr for the wafers #TG2219, #TG2196, and #Hx2688, respectively, with the compensation of growth temperature for the pressure change. The sequence of layers and their parameters are shown in Table I. The molar fraction,  $x$ , of the Al content and the thickness of the Al<sub>x</sub>Ga<sub>1-x</sub>N barrier were obtained from X-ray diffraction measurements.

The Ohmic and Schottky contacts were fabricated at the FTMC using the Ti/Al/Ni/Au (30/90/20/100 nm) and Ni/Au (25/200 nm) metal stacks, respectively. The Ohmic contacts formed using the rapid thermal annealing method in a nitrogen ambient demonstrated a resistance  $R_c \sim 1 \Omega \text{ mm}$ . More details about the fabrication of contacts can be found in Refs. 15 and 16.

A specific transistor design was chosen in order to avoid the mesa etching step and minimize the process flow to two photolithography procedures. In this design, a square-shaped drain contact is surrounded by a rectangular double gate and double source electrodes. The optical microscope pictures of the transistor and its main dimensions are shown in Fig. 1(a).

The current-voltage characteristics and noise were measured at room temperature on a wafer using a probe station. The noise spectra were measured as a function of the drain,  $V_D$ , and gate,  $V_g$ , voltages with the source grounded. The voltage fluctuations,  $S_v$ , from the drain load resistance  $R_L = 1\text{--}10 \text{ k}\Omega$  were analyzed with a dynamic signal analyzer. The short-circuit current fluctuations were calculated in the usual way as  $S_I = S_v[(R_L + R_d)/(R_L R_d)]^2$ , where  $R_d$  is the differential drain to source resistance obtained from the experimental current-voltage characteristics.

The devices were characterized by a  $\sim 6$  orders of magnitude on/off ratio and a small gate leakage current. The subthreshold slope was within the range of  $\eta = 1.5\text{--}2$ .

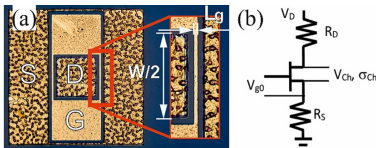


FIG. 1. Optical microscope image of the fabricated HEMT (a) and the equivalent circuit with the notations used in the equations (b).

The noise spectra had the form of  $1/f^\alpha$  noise with  $\alpha = 0.95\text{--}1.05$  without a noticeable contribution of the generation-recombination noise. In the linear regime, the spectral noise density of the drain current fluctuations,  $S_I$ , was always proportional to the current squared. The dependences of noise on the gate voltage swing ( $V_g - V_t$ ) in the linear regime at frequency  $f = 10 \text{ Hz}$  for the representative devices are shown in Fig. 2 ( $V_t$  is the threshold voltage). They have the usual shape for the FETs. At a high gate voltage, the noise slightly increases with the gate voltage increase manifesting the contribution of the contact noise.<sup>17</sup> At a lower gate voltage, noise decreases with the gate voltage increase steeper than  $1/(V_g - V_t)^2$ . Although the McWhorter model predicts the  $1/(V_g - V_t)^2$  slope, the steeper dependences are often observed. There are several possible reasons for that: (i) influence of the drain and source access resistances; (ii) dependence of the trap density on energy; and (iii) contribution of the correlated mobility fluctuations.

In the McWhorter model, the spectral noise density of the drain current fluctuations  $S_I/I^2$  is given by<sup>12</sup>

$$\frac{S_I}{I^2} = \frac{kTN_i}{\gamma f W L_g n_s^2}, \quad (1)$$

where  $k$  is the Boltzmann constant,  $T$  is the temperature,  $N_i$  is the effective trap density,  $f$  is the frequency,  $WL_g$  is the channel area,  $n_s$  is the concentration, and  $\gamma$  is the attenuation coefficient of the electron wave function under the barrier, usually taken equal to  $10^6 \text{ cm}^{-1}$ .

In many publications<sup>18,19</sup> Eq. (1) is complemented by another term for the correlated mobility fluctuations. Mobility fluctuations and correlated mobility fluctuations are indeed the possible mechanisms of noise. However, the relative contribution of the mobility fluctuations is difficult to define. Therefore, we do not include the mobility fluctuations in our analysis and name the  $N_i$  value in Eq. (1) “the effective trap density.”

Equation (1) does not take into account the drain and source access resistances, which are the sum of the contact resistance and resistance of the ungated parts of the channel. Even if the access

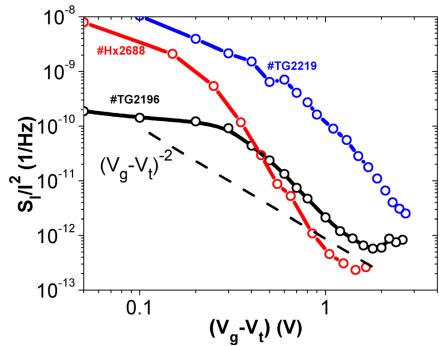


FIG. 2. Dependences of noise on the gate voltage swing ( $V_g - V_t$ ) for the representative devices;  $f = 10 \text{ Hz}$ ; and  $V_D = 0.1 \text{ V}$ .

resistances have a negligible contribution to noise, they still affect the noise properties of the device. First, at nonzero access resistance, the voltage drop on the channel is smaller than the drain voltage. Second, the source access resistance provides a negative feedback to the gate. As a result, the drain current noise is smaller than it would be at zero access resistance, and the correct calculation of the trap density requires the knowledge of this value.

Fluctuations of the current at nonzero access resistance can be written as

$$\delta I = V_D \left( \delta \sigma_t - \frac{d\sigma_t}{dV_{g0}} \delta V_{g0} \right) = V_D \left( \delta \sigma_t - \frac{d\sigma_t}{dV_{g0}} R_S \delta I \right), \quad (2)$$

where  $\sigma_t$  is the total conductance of the transistor including access resistances,  $V_{g0}$  is the gate voltage, and  $R_S$  is the source access resistance [see Fig. 1(b) for the equivalent circuit and notations]. The first term in the brackets,  $\delta \sigma_t$ , describes the fluctuations of the channel conductivity due to physical processes, for example, fluctuations of the number of carriers. The second term describes the negative feedback provided by the fluctuations of the current and corresponding voltage fluctuations on the source access resistance.

The derivative  $d\sigma_t/dV_{g0}$  can be expressed using the internal transconductance  $g_{m0} = dI/dV_{g0}$ :

$$\frac{d\sigma_t}{dV_{g0}} = \frac{d\sigma_{Ch}}{dV_{g0}} \frac{R_{Ch}^2}{(R_{Ch} + R_S + R_D)^2} = \frac{g_{m0}}{V_{Ch}} \frac{R_{Ch}^2}{(R_{Ch} + R_S + R_D)^2}. \quad (3)$$

Here,  $\sigma_{Ch} = 1/R_{Ch}$  is the channel conductance, and  $R_S$  and  $R_D$  are the source and drain access resistances.

Combining Eqs. (2) and (3), the expression for the current fluctuation can be written in the following form:

$$\begin{aligned} \delta I &= \frac{V_D \delta \sigma_t}{\left( 1 + \frac{R_{Ch} R_S g_{m0}}{R_{Ch} + R_S + R_D} \right)} \\ &= \frac{1}{(R_{Ch} + R_S + R_D)} \frac{V_{Ch} \delta \sigma_t}{\left( 1 + \frac{R_{Ch} R_S g_{m0}}{R_{Ch} + R_S + R_D} \right)} \frac{\delta \sigma_{Ch}}{\sigma_{Ch}}. \end{aligned} \quad (4)$$

From Eq. (4), it is easy to find how the relative spectral noise density of drain current fluctuations relates to the channel conductance fluctuation spectral noise density:

$$\frac{S_I}{\bar{I}^2} = K^2 \times \frac{S_{\sigma_{Ch}}}{\sigma_{Ch}^2} = \left[ \frac{R_{Ch}}{(R_{Ch} + R_S + R_D)} \frac{1}{\left( 1 + \frac{R_{Ch} R_S g_{m0}}{R_{Ch} + R_S + R_D} \right)} \right]^2 \frac{S_{\sigma_{Ch}}}{\sigma_{Ch}^2}. \quad (5)$$

Here,  $S_{\sigma_{Ch}}/\sigma_{Ch}^2$  is the relative spectral noise density of the channel conductance fluctuations. If the access resistance is negligible in comparison with the channel resistance, the relative spectral noise density of the current fluctuations is equal to  $S_{\sigma_{Ch}}/\sigma_{Ch}^2$ . In the opposite case of high access resistance, one needs to calculate  $S_{\sigma_{Ch}}/\sigma_{Ch}^2$  using Eq. (5) and find the trap density as

$$N_t = \frac{S_{\sigma_{Ch}} \gamma f W L_g \hbar^2}{\sigma_{Ch}^2 k T}. \quad (6)$$

Another way to estimate the effective trap density is using the input gate voltage noise  $S_{V_g} = (S_I/\bar{I}^2)/(g_m/L)^2$ . Here,  $g_m = K \times g_{m0}$  is the external transconductance, which can be easily measured. The expression for the coefficient  $K$ , which relates the internal and external transconductances, can be found in Ref. 20, for example. It can be expressed exactly as the term in the square brackets in Eq. (5). Therefore, the input gate voltage “does not depend” on the access resistance.

From Eqs. (1) and (5) and the expression for the internal transconductance in the linear regime,  $g_{m0} = C \mu V_{Ch}(W/L)$ , it is easy to obtain the well-known expression for the input gate voltage noise:

$$S_{V_g} = \frac{k T N_t q^2}{\gamma f W L_g C^2}, \quad (7)$$

where  $q$  is the electron charge and  $C$  is the gate capacitance per unit area. Since  $S_{V_g}$  does not depend on the access resistance, it can be used directly to calculate the effective trap concentration without knowing the access resistance. Note also, that in accordance with the McWhorter model,  $S_{V_g}$  does not depend on the carrier’s concentration in the channel, i.e., on the gate voltage.

Figure 3 shows the gate voltage dependence of the effective trap density for the HEMTs fabricated on different epitaxial structures and calculated using Eq. (7). Although all the three wafers were fabricated by a similar technology and have similar layer parameters, the effective trap densities,  $N_t$ , in these structures are quite different. Particularly, the effective trap density at a high gate voltage for the #TG2219 structure is about two orders of magnitude higher than that for the other two structures.

In order to find out what is specific in this wafer, we characterized all the wafers by secondary ion mass spectroscopy (SIMS) and compared the results with the previously published data on the terahertz electroluminescence of impurities.

Special surface-cleaning procedures were employed before the SIMS measurements. This enabled a determination of the doping level well below  $10^{17} \text{ cm}^{-3}$ . Table II shows the oxygen, silicon, and carbon impurity concentrations in the UID GaN layers obtained by the SIMS technique. Oxygen and silicon act as donors in GaN, and carbon is a

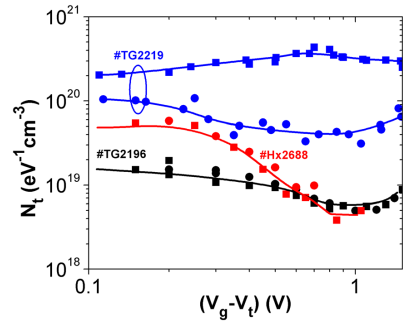


FIG. 3. Effective trap density  $N_t$  as a function of the gate voltage swing  $(V_g - V_t)$  for the studied devices.

**TABLE II.** Concentration of oxygen, silicon, and carbon atoms at the UID GaN layer.

Wafer	Oxygen, $N_D \times 10^{16} \text{ cm}^{-3}$	Silicon, $N_D \times 10^{16} \text{ cm}^{-3}$	Carbon, $N_A \times 10^{16} \text{ cm}^{-3}$
#TG2196	$2.0 \pm 1.0$	$0.9 \pm 0.6$	$1.4 \pm 0.2$
#TG2219	$2.5 \pm 1.1$	$1.0 \pm 0.7$	$1.1 \pm 0.2$
#Hx2688	$2.1 \pm 1.2$	$1.0 \pm 0.8$	$1.3 \pm 0.2$

compensating acceptor<sup>21–23</sup>. As follows from Table II, the #TG2219 structure has the highest concentration of uncompensated donors ( $N_D - N_A$ ). Just this structure is characterized by the highest effective trap density,  $N_t$ . Although we cannot state that these particular donors (oxygen or silicon) are responsible for the high noise level, a higher concentration of the uncompensated donors leads to a higher conductivity and a lower quality of the layer. Traps, which are responsible for the high noise level, might be associated with the defects which accompany these donor dopants. However, these defects cannot be directly observed by the SIMS.

The terahertz electroluminescence of impurities at the cryogenic temperature was studied in Refs. 24 and 25 for the same #TG2196 and #TG2219 structures (marked as U26 and U28, respectively). Indeed, the electroluminescence spectroscopy indicated a  $\sim 30\%$  higher oxygen peak intensity in the #TG2219 wafer, which is characterized by the highest noise level. This result agrees with the SIMS measurements indicating that either oxygen or the other accompanying trap levels are responsible for the high noise in this structure. The possible reason for the lower quality of this wafer is the small pressure during the growth, i.e., 100 Torr contrary to 200 and 300 Torr for other wafers. It is known that lowering of the growth pressure deteriorates the material properties.<sup>26</sup>

The concentration of oxygen in the UID-GaN layer of the #TG2219 wafer is higher than that in other wafers just by a few tens of percent. Meanwhile, the noise amplitude and the corresponding effective trap density differ in an order of magnitude or more, indicating that a minor change in technology might induce a high increase in the trap density which is responsible for the noise. Therefore, noise measurements are a very sensitive method for the assessment of the epitaxial technology and the material quality.

Contrary to the McWhorter model prediction, the effective trap density for some devices slightly decreases with the gate voltage increase reflecting the  $S_{V_g}$  dependence on  $V_g$ . As it was discussed several times, this effect can be due to the contribution of the correlated mobility fluctuations<sup>19</sup> which are not taken into account in this estimate. Another reason is the dependence of the trap density on the energy. Since the main contribution to noise comes from the traps near the Fermi energy, the gate voltage dependence of noise reflects the energy profile of the effective trap density.

At a high gate voltage, the trap density in two of the studied GaN/AlGaIn HEMTs is below  $10^{19} \text{ eV}^{-1} \text{ cm}^{-3}$  (see Fig. 2). Similar or higher values of the effective trap density are often found in Si MOSFETs with a high-k dielectric.<sup>27–29</sup>

In conclusion, the effective trap density was extracted from the low frequency noise measurement of GaN/AlGaIn field effect transistors. The extraction method based on the McWhorter model and input gate voltage noise allowed us to take into account the effect of the access resistance on the output noise. The effective trap density can be as low as below  $10^{19} \text{ eV}^{-1} \text{ cm}^{-3}$ , which is of the same order of magnitude as in

Si MOSFETs with a high-k dielectric. It was found that the high effective trap density correlates with SIMS and terahertz electroluminescence spectroscopies, which reveal a slightly higher concentration of uncompensated donors in GaIn in one of the epitaxial structures. The noise level and effective trap density in this structure is orders of magnitude higher confirming that noise is a very sensitive parameter for the material quality and technology of GaN/AlGaIn HEMT structures.

The work was supported by the “International Research Agendas” program of the Foundation for Polish Science cofinanced by the European Union under the European Regional Development Fund (No. MAB/2018/9) and by the National Science Centre, Poland allocated on the basis of Grant Nos. 2016/22/E/ST7/00526 and UMO-2017/27/L/ST7/03283. The research at the Terahertz Photonics Laboratory at Vilnius was supported by the Research Council of Lithuania (Lietuvos mokslo taryba) under the “TERAGANWIRE” project (Grant No. S-LL-19-1). The research was also partially supported by the Foundation for Polish Science through the TEAM project POIR.04.04.00-00-3D76/16 (TEAM/2016-3/25).

## REFERENCES

- M. E. Levinshtein, S. L. Rumyantsev, R. Gaska, J. W. Yang, and M. S. Shur, *Appl. Phys. Lett.* **73**, 1089 (1998).
- A. Balandin, S. Morozov, G. Wijeratne, S. J. Cai, R. Li, J. Li, K. L. Wang, and C. R. Viswanathan, *Appl. Phys. Lett.* **75**, 2064 (1999).
- W. Y. Ho, C. Surya, K. Y. Tong, W. Kim, A. E. Botcharev, and H. Morkoc, *IEEE Trans. Electron Device* **46**, 1099 (1999).
- T. Roy, E. X. Zhang, Y. S. Puzryev, X. Shen, D. M. Fleetwood, R. D. Schrimpf, G. Koblmueller, R. Chu, C. Poblenz, N. Fichtenbaum, C. S. Suh, U. K. Mishra, J. S. Speck, and S. T. Pantelides, *Appl. Phys. Lett.* **99**, 203501 (2011).
- M. R. Hasan, A. Motayed, M. S. Fahad, and M. V. Rao, *J. Vac. Sci. Technol., B* **35**, 052202 (2017).
- M. Rzin, J. Routouze, B. Guillet, L. Méchin, M. Morales, C. Lacam, P. Gamarra, P. Ruterana, and F. Medjdoub, *IEEE Trans. Electron Device* **64**, 2820 (2017).
- K.-S. Im, M. S. P. Reddy, R. Caulmilone, C. G. Theodorou, G. Ghibaudo, S. Cristoloveanu, and J.-H. Lee, *IEEE Trans. Electron Device* **66**, 1243 (2019).
- F. N. Hooge, T. G. M. Kleinpenning, and L. K. J. Vandamme, *Rep. Prog. Phys.* **44**, 479 (1981).
- Y.-K. Su, S.-C. Wei, R.-L. Wang, S.-J. Chang, C.-H. Ko, and T.-M. Kuan, *IEEE Electron Device Lett.* **24**, 622 (2003).
- S. P. Le, T. Ui, T. Q. Nguyen, H.-A. Shih, and T.-K. Suzuki, *J. Appl. Phys.* **119**, 204503 (2016).
- A. L. McWhorter, in *Semiconductor Surface Physics*, edited by R. H. Kingston (University of Pennsylvania Press, Philadelphia, 1957).
- S. Christenson, I. Lundstrom, and C. Svenson, *Solid-State Electron.* **11**, 797 (1968).
- D. Kotchetkov and A. A. Balandin, *MRS Proc.* **680**, E9.13 (2001).
- H.-C. Chiu, C.-W. Yang, C.-H. Chen, and C.-H. Wu, *IEEE Trans. Electron Device* **59**, 3334 (2012).
- V. Jakštas, I. Kašalynas, I. Šimkienė, V. Strazdienė, P. Prystawko, and M. Leszczynski, *Lithu. J. Phys.* **54**, 227 (2014).
- V. Jakštas, J. Jorudas, V. Janonis, L. Minkevičius, I. Kašalynas, P. Prystawko, and M. Leszczynski, *Lith. J. Phys.* **58**, 188 (2018).
- S. L. Rumyantsev, Y. Deng, S. Shur, M. E. Levinshtein, M. Asif Khan, G. Simin, J. Yang, X. Hu, and R. Gaska, *Semicond. Sci. Technol.* **18**, 589 (2003).
- K. K. Hung, K. Ko, H. Chenming, and Y. Cheng, *IEEE Trans. Electron Device* **37**, 654 (1990).
- G. Ghibaudo, O. Roux, C. Nguyen-Duc, F. Balestra, and J. Brini, *Phys. Status Solidi A* **124**, 571 (1991).
- M. Shur, *Physics of Semiconductor Devices* (Prentice Hall, Upper Saddle River, New Jersey, 1990).
- R. Niebuhr, K. H. Bachem, U. Kaufmann, M. Maier, C. Merz, B. Santic, P. Schlotter, and H. Jürgensen, *J. Electron. Mater.* **26**, 1127 (1997).



- <sup>22</sup>S. Heikman, S. Keller, S. P. DenBaars, and U. K. Mishra, *Phys. Status Solidi C* **7**, 2557 (2003).
- <sup>23</sup>*Properties of Advanced Semiconductor Materials: GaN, AlN, InN, BN, SiC, SiGe*, edited by M. E. Levinshtein, S. L. Rumyantsev, and M. S. Shur (John Wiley & Sons, 2001).
- <sup>24</sup>I. Grigelionis, V. Jakštas, V. Janonis, I. Kašalynas, P. Prystawko, P. Kruszewski, and M. Leszczyński, *Phys. Status Solidi B* **255**, 1700421 (2018).
- <sup>25</sup>I. Grigelionis, J. Jorudas, V. Jakštas, V. Janonis, I. Kašalynas, P. Prystawko, P. Kruszewski, and M. Leszczyński, *Mater. Sci. Semicond. Process.* **93**, 280 (2019).
- <sup>26</sup>P. B. Klein, S. C. Binari, K. Ikossi, A. E. Wickenden, D. D. Koleske, and R. L. Henry, *Appl. Phys. Lett.* **79**, 3527 (2001).
- <sup>27</sup>E. Simoen, A. Mercha, L. Pantisano, C. Claeys, and E. Young, *IEEE Trans. Electron Device* **51**, 780 (2004).
- <sup>28</sup>T. Nguyen, M. Valenza, F. Martinez, G. Neau, J. C. Vildeuil, G. Ribes, V. Cosnier, T. Skotnicki, and M. Müller, *AIP Conf. Proc.* **780**, 235 (2005).
- <sup>29</sup>P. Magnone, F. Crupi, G. Giusi, C. Pace, E. Simoen, C. Claeys, L. Pantisano, D. Maji, V. Ramgopal Rao, and P. Srinivasan, *IEEE Trans. Device Mater. Reliab.* **9**, 180 (2009).

**Self-Heating of Annealed Ti/Al/Ni/Au Contacts to Two-Dimensional Electron Gas in AlGa<sub>N</sub>/Ga<sub>N</sub> Heterostructures**




E. Šermukšnis, **J. Jorudas**, A. Šimukovič, V. Kovalevskij, I. Kašalynas  
*Applied Sciences*, vol. 12, no. 21, 11079 (2022).  
DOI: 10.3390/app122111079

This is an open access article distributed under the Creative Commons Attribution License (CC-BY).

The article may be accessed online at <https://doi.org/10.3390/app122111079>

Article

# Self-Heating of Annealed Ti/Al/Ni/Au Contacts to Two-Dimensional Electron Gas in AlGa<sub>N</sub>/Ga<sub>N</sub> Heterostructures

Emilis Šermukšnis <sup>1,†</sup> , Justinas Jorudas <sup>2</sup> , Artūras Šimukovič <sup>1</sup>, Vitalij Kovalevskij <sup>2</sup> and Irmantas Kašalynas <sup>2,\*</sup> 

<sup>1</sup> Fluctuation Research Laboratory, Center for Physical Sciences and Technology, Saulėtekio Ave. 3, LT-10257 Vilnius, Lithuania

<sup>2</sup> Terahertz Photonics Laboratory (THz Atelier), Center for Physical Sciences and Technology, Saulėtekio Ave. 3, LT-10257 Vilnius, Lithuania

\* Correspondence: irmantas.kasalynas@ftmc.lt

† These authors contributed equally to this work.

**Abstract:** In this work, we investigated the self-heating effects of annealed Ti/Al/Ni/Au ohmic contacts and two-dimensional electron gas (2DEG) in AlGa<sub>N</sub>/Ga<sub>N</sub> heterostructures under strong electric field by using the short pulse current–voltage and microwave noise measurement techniques. The experimental results demonstrated that the self-heating phenomena in ohmic contacts with the increase of current may dominate over the electrical performances of 2DEG channel. Moreover, the excess noise temperature of contact resistance was found to be more than four times higher than that of 2DEG channel at the same high current density values. The results reveal the importance of self-heating of the ohmic contacts on the device performance under short-duration (only 100 ns) and low-duty-cycle (only 10<sup>−5</sup>) pulse regime.

**Keywords:** Gallium nitride; AlGa<sub>N</sub>/Ga<sub>N</sub>; TLM; HEMT; contact resistance; 2DEG; hot electrons; microwave noise; self-heating



**Citation:** Šermukšnis, E.; Jorudas, J.; Šimukovič, A.; Kovalevskij, V.; Kašalynas, I. Self-Heating of Annealed Ti/Al/Ni/Au Contacts to Two-Dimensional Electron Gas in AlGa<sub>N</sub>/Ga<sub>N</sub> Heterostructures. *Appl. Sci.* **2022**, *12*, 11079. <https://doi.org/10.3390/app122111079>

Academic Editor: Annunziata Sansaverino

Received: 30 September 2022  
Accepted: 24 October 2022  
Published: 1 November 2022

**Publisher's Note:** MDPI stays neutral with regard to jurisdictional claims in published maps and institutional affiliations.



**Copyright:** © 2022 by the authors. Licensee MDPI, Basel, Switzerland. This article is an open access article distributed under the terms and conditions of the Creative Commons Attribution (CC BY) license (<https://creativecommons.org/licenses/by/4.0/>).

## 1. Introduction

Gallium nitride (Ga<sub>N</sub>) has many attractive properties for high-power electronics and optoelectronic applications due to a wide bandgap of ~3.4 eV and a high electron peak velocity of ~3 × 10<sup>7</sup> cm/s achieved at high fields [1]. High-electron-mobility transistors (HEMTs) with high density (over 10<sup>13</sup> cm<sup>−2</sup>) two-dimensional electron gas (2DEG) formed at the interface of AlGa<sub>N</sub> barrier and Ga<sub>N</sub> channel layers are also resistant to high electric fields without the breakdown of the material [2,3].

The HEMT, operating as a power amplifier or as a switch, dissipates the electric power in the conductive channel [4] and contacts [5]. Joule heating and the associated temperature increase in the transistor channel and contacts will be more intense at high currents achieved in gated [6,7] and ungated [5,8] devices. Self-heating is one of the factors limiting the operation of transistors [9] and plasmonic devices [10]. It can be mitigated by the use of high-thermal-conductivity substrates and the use of Ga<sub>N</sub>–SiC hybrid material developed on SiC substrate without a Ga<sub>N</sub> buffer layer [11]. The voltage drop in the contacts needs to be accounted for when the average electric field in the channel is estimated to be in an ON state of operation of the transistor or especially for the experiments on the ungated devices [12]. At high current densities, the properties of the contacts are important for transistor reliability [13,14]. Robust electrodes for high-current experiments, especially for ungated or floating gate devices, are also needed [4,15–20].

The contact resistance  $R_c$  is usually estimated from the standard transfer length model (TLM) measurements [21,22]. The dependence of the total resistance  $R$  between two electrodes, which is a sum of  $R_c$  and resistance of the channel  $R_{ch}$ , is measured versus the gap length (channel length)  $L$  between the series of the electrodes of the TLM structure. Due to the absence of a gate in the TLM structure, an electric field profile along the channel

is assumed to be homogeneous and current–voltage (I–V) characteristics at low electric fields reveal the ohmicity of the contacts. The structures with H-shaped contacts, where the contact width is wider than the width of the channel, are also employed with the advantage of lower  $R_c$  [23,24]. Therefore, the contact resistance  $R_c$  can be obtained from low-field measurements.

At higher fields, I–V nonlinearity (the deviation from Ohm’s law) of the total resistance is observed and the increase in  $R$  versus the electric field is explained by the increase in the intensity of electron–phonon scattering in GaN [25]. This self-heating-related increase in the total resistance usually is treated as the increase in  $R_{ch}$ , while  $R_c$  is treated as a constant value, estimated from the TLM measurements at low fields [12,24]. Technological efforts have been targeted at achieving an  $R_c$  value as small as possible, and hopefully, the achieved inequality  $R_c \ll R_{ch}$  lets one neglect the role of  $R_c$ . The  $R_c$  dependence on temperature was investigated [26–28]. However, the  $R_c$  dependence on current (and applied electric field) when the temperature of the contacts increases due to Joule heating was not investigated.

The current and the electric field in the channel are controlled by the applied voltage to the electrodes. Virtually homogeneous current and electric field are expected in the channel between electrodes (corresponds to  $R_{ch}$ ), and non-homogeneous distribution of the current (and the electric field), so-called current crowding phenomena, is assumed under the electrodes (corresponds to  $R_c$ ) [29–31]. The qualitatively similar distribution of the current density is considered in different systems, such as organic [32] or graphene transistors [33].

At high fields, the electron temperature  $T_e$  in GaN is higher than the lattice temperature  $T_L$ , even for the DC-mode measurements [34]. It is well known that the Joule heating (self-heating)-related increase in  $T_L$  is lower in pulsed experiments. Hot-electron temperature is also related to the strong electron–LO-phonon coupling in GaN and the associated hot-phonon effect [25,35]. The experiments on microwave noise thermometry conducted at nearly isothermal lattice temperatures over a wide range of electric fields show that the hot-electron temperature (and electron energy relaxation time) depends on the dissipated power and on the 2DEG density in the GaN-based heterostructures with 2DEG channels [36]. An increase in  $T_L$  is related also to the thermal quenching phenomena, when  $T_e$  decreases along the voltage pulse [37]. For higher electron density, especially in the bulk, self-heating is stronger; therefore, the usage of short duration pulses is required [38].

In this paper, the self-heating of annealed Ti/Al/Ni/Au contacts to the 2DEG in AlGaN/(AlN)/GaN heterostructures was investigated under pulsed electric fields ranging up to 12 kV/cm and reaching current density values up to  $\sim 1$  A/mm. For this reason the pulsed current–voltage (I–V) and microwave noise measurements of the TLM test structures were performed.

The paper is organized as follows. In Section 2, the samples’ growth and ohmic contact fabrication are described, also, the measurement techniques are explained. In Section 3, the estimation of current dependent contact resistance is explained. A significant increase in the  $R_c$  with current was found. The change in  $R_c$  relative to its low-field value was found to be proportional to the dissipated electric power in  $R_c$ . In Section 4, the microwave noise measurements are presented and the noise temperatures of  $R_c$  and  $R_{ch}$  are extracted, demonstrating much higher excess noise temperature in contacts than in the channel. In Section 5, the increase in  $R_c(I)$  was analyzed in terms of self-heating. It was found that the self-heating of  $R_c$  is more intense than that of  $R_{ch}$ , resulting in a rapid increase in the ratio  $R_c(I)/R_{ch}(I)$  with the current as the main result of this work. Finally, the results are summarized.

## 2. Samples and Measurement Techniques

Commercial AlGaN/(AlN)/GaN HEMT structures grown along the polar *c*-axis using the metalorganic chemical vapor deposition (MOCVD) method were selected for this study. The detailed description of the growth and characterization of alike structures can be found elsewhere [39,40]. In particular, layers for the AlGaN/AlN/GaN sample were grown on a 500  $\mu\text{m}$  thick 6H-polytype SiC substrate as follows: a 90 nm thick AlN nucleation layer, a 1300 nm thick high resistivity GaN:C buffer, a 900 nm thick UID GaN layer and a 0.8 nm thick AlN spacer. Then, a 19 nm thick  $\text{Al}_{0.25}\text{Ga}_{0.75}\text{N}$  barrier layer was grown capping it with a 2 nm thick GaN and a 1 nm thick  $\text{SiN}_x$  passivation layers. A similar structures, but without an AlN spacer (AlGaN/GaN) was developed on a semi-insulating 4H-polytype SiC substrate where a nominally undoped 20 nm thick  $\text{Al}_{0.25}\text{Ga}_{0.75}\text{N}$  barrier and 2.5  $\mu\text{m}$  thick GaN buffer were capped by a 1.5 nm thick GaN layer. Figure 1b illustrates only top part of the unintentionally doped (UID) GaN layer and AlGaN barrier required for 2DEG formation.

The ohmic contacts were fabricated of a Ti/Al/Ni/Au metal stack with a respective thickness of 30/90/20/100 nm annealed in nitrogen ambient for 30 s at 850  $^\circ\text{C}$ . The mesas were formed either by inductively coupled plasma reactive ion etching (ICP-RIE) using Cl plasma or by implantation of 700 keV energy Al ions into a depth of about 650 nm. More details about the device processing have been reported elsewhere [11,41]. The TLMs were used to evaluate the performance of ohmic contacts [22]. Values for the contact resistance  $R_c$  and specific contact resistivity  $\rho_c$  at low electric fields were minimized to 1  $\Omega\text{mm}$  and  $2 \times 10^{-3} \Omega\text{mm}^2$ , respectively, [11,41,42]. The Hall effect experiments in Van der Paw geometry at temperature of 300 K revealed the density  $n_{2\text{DEG}}$  and mobility  $\mu_{2\text{DEG}}$  values of 2DEG in used samples to be of  $8.3 \times 10^{12} \text{ cm}^{-2}$  and  $9.3 \times 10^{12} \text{ cm}^{-2}$  and of  $1.9 \times 10^3 \text{ cm}^2/\text{Vs}$  and  $1.9 \times 10^3 \text{ cm}^2/\text{Vs}$ , respectively.

Usually, GaN device fabrication is completed with the deposition of dielectric layers to passivate the surface states minimizing their influence on the device/transistor performance [43]. However, good performance of unpassivated HEMTs has also been reported [44,45], exposing issues of the selection and usage of the surface passivants which might deteriorate the performance. In this work, the surfaces of all heterostructures after device processing were left unpassivated.

A microscope photograph of the TLM samples, an illustration of the cross-section of AlGaN/GaN heterostructures with two metal contacts annealed on the surface, and the connection between the sample (device under test (DUT)) in the electronic scheme are shown in Figure 1a–c, respectively. The 2DEG channel formed at the interface of the AlGaN and GaN layers is indicated by the blue line. Different length channels are selected for the pulsed *I*–*V* and microwave noise measurements by placing the two-pin microwave probe on top of the selected two nearby electrodes. The width *W* and the length *D* of rectangular electrodes were 250  $\mu\text{m}$  and 100  $\mu\text{m}$ , respectively. The distance between electrodes *L* for different TLM resistor samples were 6, 12.5, 25, 35, 45, 55, and 65  $\mu\text{m}$ . We assumed that the length of the 2DEG channel is the same as *L* and is independent of the applied voltage. The current distribution under the right-hand side and left-hand side electrodes is considered to be the same. The current crowding phenomena is illustrated by the set of arrows (vectors which roughly show the direction and the magnitude of the current flow) parallel and perpendicular to the plane of 2DEG.

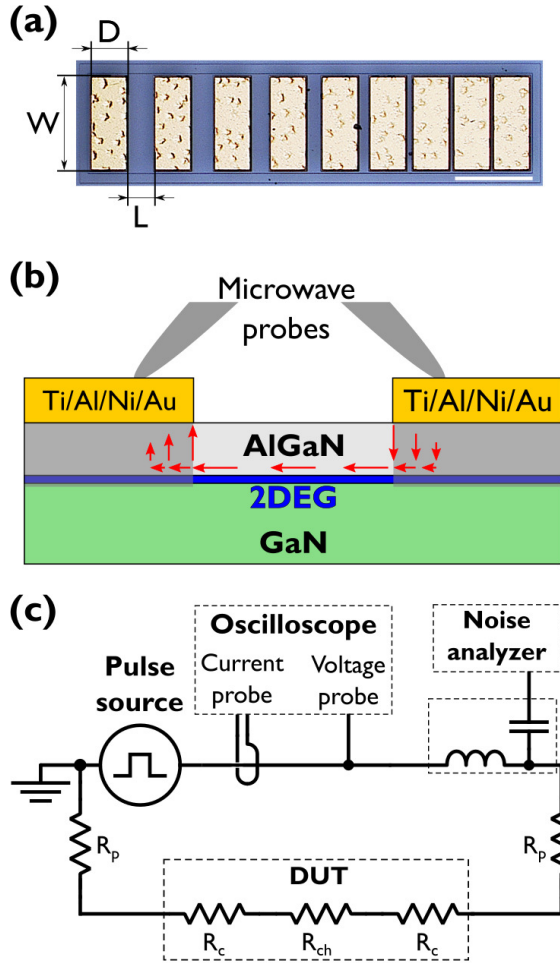


**Figure 1.** Microscope image of the TLM samples of the AlGaIn/GaN channel with electrodes (of width  $W$  and length  $D$ ) (a) and intersection illustration of the AlGaIn/GaN heterostructure with the 2DEG channel, showing the active part of the epitaxial structure and involving only two electrodes (b). Arrows illustrate the current flow. An illustration of the DUT connection in the electronic scheme is presented in (c).

The current–voltage characteristics were measured by applying voltage pulses of width  $\tau_p = 100$  ns and a duty cycle  $\sim 10^{-5}$ . The current–voltage and the hot-electron noise temperature–voltage characteristics were measured by applying voltage pulses to the TLM samples with electric field values reaching up to  $\sim 12$  kV/cm.

A voltage pulse generator (Generator AVL-2A-W-B-P-M, Avtech Electrosystems) was connected to the DUT through a coaxial current probe, a coaxial voltage probe, a microwave diplexer, and a microwave probe (Model 40A with a two-pin ground-signal configuration,

100  $\mu\text{m}$  pitch, GGB Industries), which was mounted on a high-precision probe station with vibration isolation (EPS150, Cascade Microtech). The coaxial voltage probe was realized as a pick-off tee giving 30 times attenuated replica of the voltage pulse. The coaxial current probe (Model 6027, Pearson Electronics) was inductively coupled giving the voltage replica of the current pulse (conversion ratio 1 Volt/Ampere). Signals from both probes were recorded by a digital oscilloscope (DSO1022A, Keysight Technologies).

As the DUT is biased by the voltage pulse, the excess microwave noise  $\Delta T_n = T_n - T_0$  (where  $T_n$  is noise temperature and  $T_0$  is room temperature) of the DUT appears at the pins of the microwave coaxial probe. The microwave diplexer is used to route the microwave noise of the DUT to a noise analyzer, consisting of low-noise amplifiers, a diode detector, and a box-car averager with a gating function (SR250 with modules 240A, 245, Stanford Research Systems). The diplexer was connected in the close vicinity to the DUT; it was connected straight to the coaxial connector of the coaxial microwave (two-pin) probe. The total resistance of the DUT is a sum of contacts resistances and the resistance of the channel,  $R_c + R_{\text{ch}} + R_c$ , while  $R_p + R_p$  is the resistance of the connections between the voltage probe and the DUT, including the resistance of the microwave probe. The description of experimental setups can be found elsewhere [46,47]. In microwave noise temperature experiments, the module of complex  $S_{11}$  parameter (i.e., reflection coefficient in pulsed mode) of the DUT at  $\sim 10$  GHz also was measured and used for the proper estimation of the noise temperature [48,49].

Mesa-isolated TLM electrodes (i.e., channel etched) were used for the leakage current test and for standard  $S_{11}$  parameter spectra measurements by vector network analyzer operating up to 40 GHz. Extracted parasitic capacitance (parallel to the channel) for the shortest channel was less than  $\sim 50$  fF. From  $S_{11}$  spectra measurements of normal TLM structures (i.e., channel not etched), a small serial inductance  $\sim 30$  pH was extracted.

The results of the low-field total resistance measurements of the three heterostructure samples (with and without an AlN thin barrier layer) in the TLM configuration are shown in Figure 2. TLM measurements were conducted with conventional contact-front (two-terminal) method [22]. The total resistance of the DUT is the sum of the channel resistance and contact resistance (see Figure 1c):

$$R = R_{\text{ch}} + 2R_c = (R_{2D}/W) \times L + 2R_c \quad (1)$$

where the resistance of the 2DEG channel (layer)  $R_{\text{ch}}$  is expressed in terms of sheet resistance  $R_{2D}$  of the 2DEG channel between electrodes [22]. If the length  $L$  is reduced to zero, the total resistance approaches  $2R_c$ . The contact resistance can be expressed as:

$$R_c = R_{c2D}L_T/W \quad (2)$$

where  $R_{c2D}$  is the sheet resistance of the 2DEG channel directly under the electrodes and  $L_T$  is a transfer length [50], which is assumed to be  $L_T \ll D$  in our work. Measured total resistance of different length TLM samples (symbols in Figure 2) was fitted by Equation (1) (lines) and both resistances,  $R_{2D}$  and  $R_c$ , were extracted. The interception of lines with the abscissa axis gives  $2R_c$  and the interception with ordinate axis is  $2L_x$  [50]:

$$L_x = (R_c/R_{2D}) \times W = R_{c2D}L_T/R_{2D} \quad (3)$$

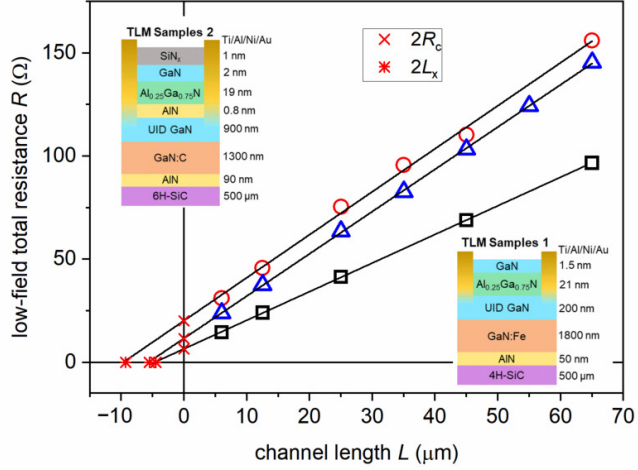


**Figure 2.** The dependence of the low-field total resistance  $R$  on the channel length  $L$ . Data for group of TLM samples 1, fabricated of AlGaN/GaN (bottom inset), are shown by rectangles, meanwhile, the triangles as well as circles demonstrate results for other two groups of TLM samples 2, made of AlGaN/AlN/GaN (top inset).

The total resistance dependencies on the current are shown in Figure 3a. At the current region up to  $\sim 50$ – $100$  mA,  $R$  weakly depends on current, which corresponds to the Ohm's law region. The corresponding electric field range (i.e., low-field range) is up to  $1$ – $2$  kV/cm. This also means that the contact resistance and channel resistance are both ohmic at this region. A deviation from Ohm's law (an increase in  $R$ ) is observed when the current and electric field become higher than  $\sim 100$  mA and  $\sim 2$  kV/cm, respectively. Maximal applied voltages for each length channel are indicated in Figure 3a. Those voltages correspond to an electric field in the channels in excess of  $10$  kV/cm. This nonlinear electron transport phenomena in the AlGaN/GaN channels is explained by the increase in intensity of electron-phonon scattering at higher fields [25]. This is described as a decrease in field-dependent electron drift mobility  $\mu(E)$ , which enters a simple relation  $R_{2D} \propto 1/(n_{2D}\mu(E))$  where  $n_{2D}$  is the sheet electron density. Unexpectedly, at high currents the total resistance for the shorter channels increases more steeply and thus, the ratio  $R(L_2)/R(L_1)$  decreases with current when channel lengths  $L_2 > L_1$  (Figure 3a). Particularly, near Ohm's region, the ratio for longest to shortest channel is  $\sim 6.5$ , while at  $270$  mA it is  $\sim 4.8$ . According to Equation (1), the change (decrease) in the ratio  $R(L_2)/R(L_1) = (L_2 - L_1)/(2WR_c/R_{2D} + L_1) + 1$  with current means that the ratio  $R_c/R_{2D}$  depends (increases) on current. It is worth noting that in most of the experiments, an independent contact resistance on the current density (with a constant value of  $R_{c0}$ ) is assumed. However, a contact resistance vs. current dependence,  $R_c(I)$ , should be considered by using a procedure that is illustrated in Figure 3.



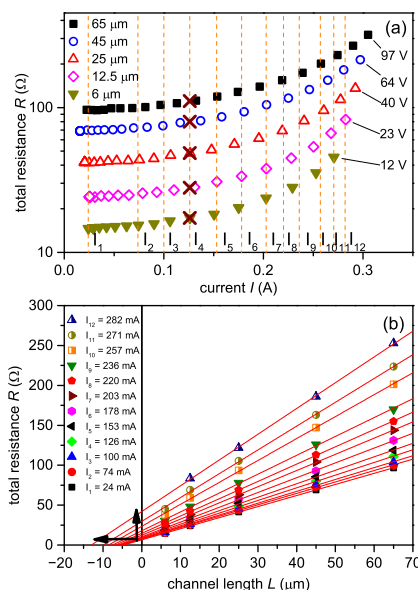


**Figure 3.** The dependence of the total resistance  $R$  on the current  $I$  for the different channel length  $L$  (a) and on channel length for a different current (b).  $L = 6 \mu\text{m}$  (closed triangles),  $12.5 \mu\text{m}$  (open diamonds),  $25 \mu\text{m}$  (open triangles),  $45 \mu\text{m}$  (open circles) and  $65 \mu\text{m}$  (closed rectangles). The measurements are presented for the AlGaIn/GaN channel. The resistance values at a given currents (represented by the vertical dashed lines) are obtained from a linear interpolation; for the particular current  $I = 126 \text{ mA}$  those are indicated as crosses. The applied maximal voltage for each length channel is indicated in the right side of the figure. Interpolated values of different length channels are depicted in the (b) for each current and are used for the estimation of the current dependent contact resistance  $R_c$  and  $L_x$  (see interception with abscissa and ordinate axis in (b)). Solid lines are linearly fit with Equation (1) and arrows show the direction of the increase in  $R_c$  and  $L_x$ .  $I = 24 \text{ mA}$ ,  $74 \text{ mA}$ ,  $100 \text{ mA}$ ,  $126 \text{ mA}$ ,  $153 \text{ mA}$ ,  $178 \text{ mA}$ ,  $203 \text{ mA}$ ,  $220 \text{ mA}$ ,  $236 \text{ mA}$ ,  $257 \text{ mA}$ ,  $271 \text{ mA}$  and  $282 \text{ mA}$ .

### 3. Current-Dependent Contact Resistance

In this work, the contact resistance is defined as:

$$R_c(I) = R_{c0} + \Delta R_c(I) \tag{4}$$

where  $R_{c0}$  is the low-field (at Ohm’s law region) contact resistance and  $\Delta R_c$  represents the change in contact resistance over its low-field value.

Because of the dependence of  $R$  on the bias, the  $R(L)$  plot should be taken at a constant bias in contrast to Figure 2, where any bias for different  $L$  channels could be taken until measurements are done in Ohm’s region. It is convenient to use a constant current for an  $R(L)$  plot because the current is a good quantity to compare the different length channels; the same current in a different  $L$  implies that the electric field also will be the same in those channels. The data points in Figure 3a are not horizontally aligned because the pulsed

voltage generator is not an ideal current source but is rather a voltage source with some internal resistance. Linear interpolation between experimental points was used so that  $R$  values at constant  $I$  (see vertical lines) could be compared. Crosses in Figure 3a illustrate the procedure for a case when  $I = 126$  mA. The  $R(L)$  characteristics obtained in this manner are shown in Figure 3b.

It is worth mentioning that the contact resistance was assumed to be the same for all electrodes of the TLM samples. This assumption also allows for the observation of linear  $R(L)$  characteristics shown in Figures 2 and 3b. An increase in  $R_c$  and  $L_x$  with an increase in  $I$  are observed as indicated in Figure 3b by the vertical arrow and the horizontal arrow, respectively.

The  $R_c$  and  $\Delta R_c$  dependencies on the current density for three samples are depicted in Figure 4a. Here,  $R_c$  and  $\Delta R_c$  values were multiplied by contact width  $W = 250$   $\mu\text{m}$  and the current  $I$  values were divided by  $W$ .

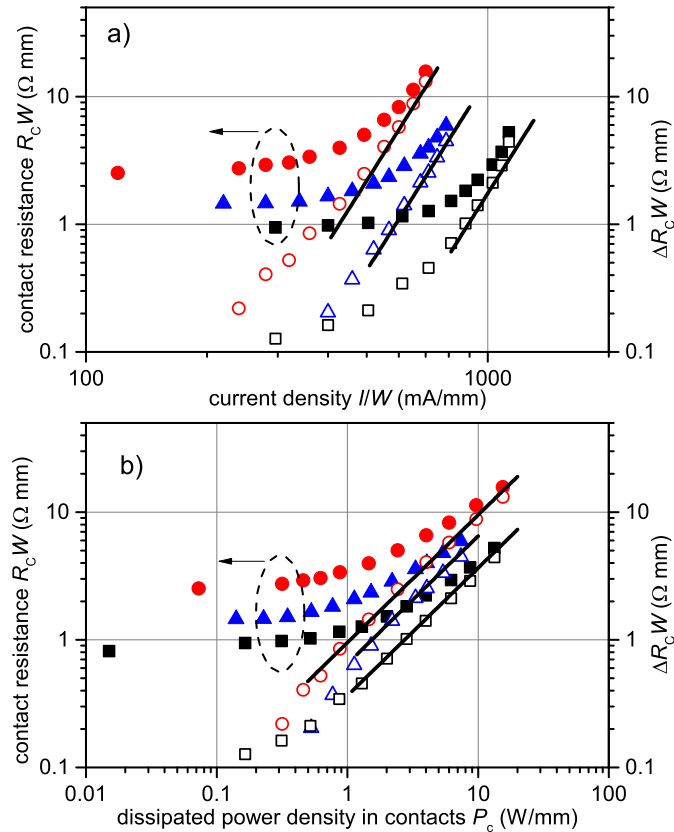


**Figure 4.** The dependence of the contact resistance  $R_c$  on the current density  $I/W$  (a) and on the dissipated electric power density  $P_c$  in contacts (b) for different samples; AlGaIn/GaN (squares), AlGaIn/AlN/GaN (triangles and circles). The dependence of the contact resistance change  $\Delta R_c = R_c - R_{c0}$  relatively to its low-field value is also presented (right-side axis)  $\Delta R_c \propto I^5$  (a) and  $\Delta R_c \propto P_c$  (b), respectively.

At low currents, where Ohm’s law holds,  $R_c$  weakly depends on the current and  $R_c(I) \approx R_{c0}$ . For smaller  $R_{c0}$  (rectangles), the increase in  $R_c$  is slower. Roughly in the range of the measured currents,  $R_c$  increases by more than six times as the current exceeds  $\sim 1$  A/mm (closed rectangles). The same increase (approximately six times, circles) for the sample of higher  $R_{c0}$  is reached at  $\sim 0.6$  A/mm.

The  $R_c(I)$  dependence is nonlinear and develops a steep increase which approaches and exceeds  $\Delta R_c(I) \propto I^5$  (see lines in Figure 4a) at highest currents. This fast increase in  $R_c$  at a high current suggests that, even for very small  $R_{c0}$  values, a noticeable increase in  $R_c$  can be expected at high currents. The dependence of  $\Delta R_c$  and  $R_c$  on the electric power density  $P_c = 2R_c I^2/W$  dissipated in the contact resistances is presented in Figure 4b. It is found that  $\Delta R_c \propto P_c$  in the wide range of  $P_c$ , from  $\sim 0.5$ – $1$  W/mm to  $\gtrsim 10$  W/mm (see the lines in Figure 4b).

The dependence of  $L_x$  on  $I$ , which is obtained similarly to the  $R_c$  in Figure 3 (but from the interception with the ordinate axis) is depicted in Figure 5. The dependencies are qualitatively similar to those of  $R_c$  in Figure 4. Furthermore, the increasing  $L_x$  can thus approach or even exceed some channel lengths used in this work (see Figure 5, circles).

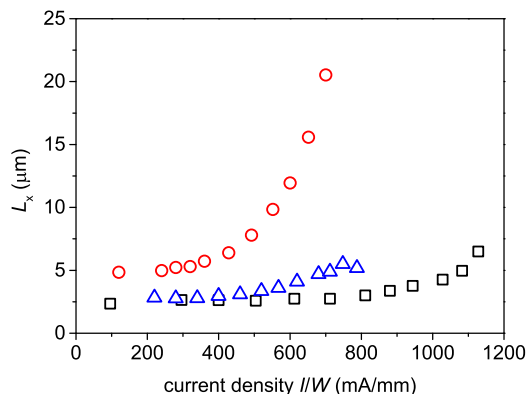


Figure 5. The dependence of  $L_x$  on the current density for different samples; AlGaIn/GaN (squares), AlGaIn/AlN/GaN (triangles and circles).

#### 4. Noise Performance of $R_c(I)$ and $R_{ch}(I)$

Next, we proceed with the noise measurements, the results of which are shown in Figure 6. Higher excess noise temperature  $\Delta T_n$  is obtained for the shorter channel (Figure 6a, closed triangles).

The excess noise temperature  $\Delta T_n$  taken at constant currents for the different length channels is depicted in Figure 6b (symbols). The decrease in  $\Delta T_n(L)$  can be explained by the presence of two distinct noise temperatures  $\Delta T_{nc}$  and  $\Delta T_{nch}$  in the sample where the former is that of the contact resistances  $2R_c$  and the latter is that of the channel resistance  $R_{ch}$ . It is easy to show that  $\Delta T_n$  of the serial connection of  $2R_c$  and  $R_{ch}$  is:

$$\Delta T_n = \frac{\Delta T_{nc} \times 2R_c + \Delta T_{nch} \times R_{ch}}{2R_c + R_{ch}} \tag{5}$$

It follows that if  $\Delta T_{nc} > \Delta T_{nch}$ , then  $\Delta T_n$  decreases from  $\Delta T_{nc}$  to  $\Delta T_{nch}$ , as the ratio  $R_c/R_{ch}$  decreases from infinity to zero, while both temperatures  $\Delta T_{nc}$ ,  $\Delta T_{nch}$  and  $R_c$  do not depend on  $L$  at a given current and only  $R_{ch}(L) = (R_{2D}/W) \times L$  depends on  $L$ . Thus, the

measured  $\Delta T_n(L)$  dependence can be used to extract the temperatures  $\Delta T_{nc}$  and  $\Delta T_{nch}$  by fitting the experimental data with:

$$\Delta T_n(L) = \frac{\Delta T_{nc} \times 2R_c + \Delta T_{nch} \times (R_{2D}/W) \times L}{2R_c + (R_{2D}/W) \times L} \quad (6)$$

where  $R_c$  and  $R_{2D}$  are known (see Figure 3b). The solid curves in Figure 6b are the fit with the  $\Delta T_n(T_{nc}, T_{nch})$  model (Equation (6)). Formally small signal resistances at  $\sim 10$  GHz should be used in Equation (6); however, this simple model gives a good qualitative picture of two different noise temperatures: the noise temperature of  $R_c$  is higher than that of the channel resistance. The extracted  $\Delta T_{nc}$  is indicated by the squares in Figure 6a.

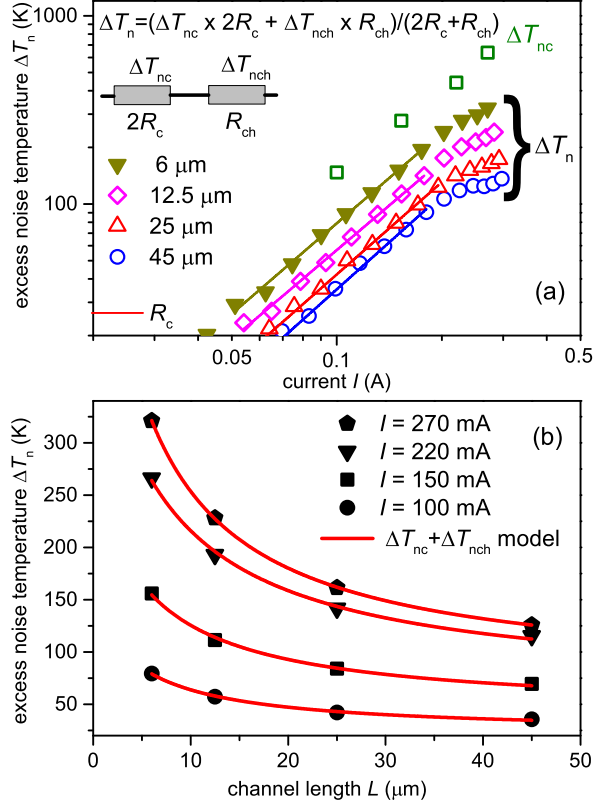


**Figure 6.** The dependence of the microwave excess noise temperature  $\Delta T_n$  on the current for the different channels length of the same TLM in the AlGaIn/GaN sample (a).  $L = 6 \mu\text{m}$  (closed triangles),  $12.5 \mu\text{m}$  (open diamonds),  $25 \mu\text{m}$  (open triangles) and  $45 \mu\text{m}$  (open circles). Lines guide the eyes. Estimated  $\Delta T_n$  at the constant currents is plotted versus channel length (b).  $I = 100$  mA (circles),  $150$  mA (rectangles),  $220$  mA (triangles) and  $270$  mA (pentagons). Curves are the fit by the model (Equation (6)). Excess noise temperature  $\Delta T_{nc}$  of the contact resistance  $R_c$  is estimated as a fitting parameter and its current dependence is depicted by the open rectangles.

### 5. Discussion

The increase in the contact resistance with the current can be treated in terms of self-heating. The nearly linear dependence of  $\Delta R_c$  on dissipated power density  $P_c$  is obtained in Figure 4b. In fact, the dissipated power in the contacts controls the change in  $R_c$ , which is evident from Figure 7, where the relative contact resistance change is plotted. The dependencies of different samples almost coincide when they are plotted versus  $P_c$ .

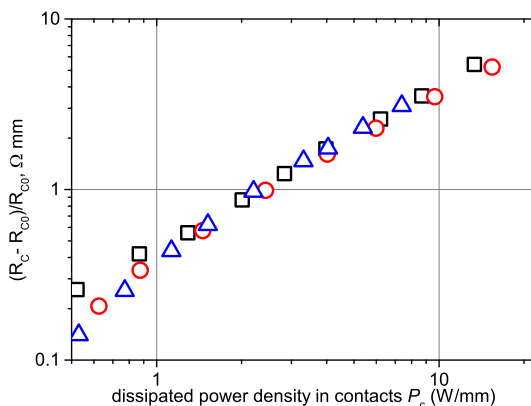


**Figure 7.** The dependence of the relative contact resistance change  $(R_c - R_{c0})/R_{c0}$  on the dissipated electric power density  $P_c$  in contacts for different samples; AlGaIn/GaN (squares), AlGaIn/AlN/GaN (triangles and circles).

Self-heating of the contact resistance also follows from the noise experiment (see Figure 6) under the assumption that noise temperature  $T_{nc}$  is a measure of electron gas temperature  $T_{ec}$  in the contact resistance, i.e.  $T_{nc} \approx T_{ec}$ . The excess noise temperature of contact resistance (squares) approaches  $\sim 700$  K.

The assumption  $T_{nc} \approx T_{ec}$  is realistic because it is based on the experiments with the GaN-based 2DEG channels, where the microwave noise temperature of hot electrons  $T_n$  is approximately equal to hot-electron temperature  $T_h \approx T_e$  [51].

The dependence of channel resistance change  $\Delta R_{2D} = R_{2D} - R_{2D0}$  on dissipated power density  $P_{2D} = R_{2D}(I/W)^2$  in the channel is presented in Figure 8 (closed symbols). It was found, that qualitatively, the change in contact and channel resistances is similar and follows a linear trend at higher power in both cases (see open symbols in Figures 4b and 8, respectively).

The contact resistance  $R_c$  can be described as [50]:

$$R_c = \sqrt{\rho_c \times R_{c2D}}/W \tag{7}$$

where  $\rho_c$  is the specific contact resistance. In actuality,  $\rho_c$  is the resistance from the metal to 2DEG under the electrodes. In Figure 1b, the current flow in  $\rho_c$  and  $R_{c2D}$  is shown as vertical and horizontal current vectors (in shaded areas only), respectively.

Therefore, the observed self-heating of  $R_c$  is related with the self-heating of both resistances  $\rho_c$  and  $R_{c2D}$ . The contact-end (three-terminal) measurement method was developed for the estimation of the  $\rho_c$  and  $R_{c2D}$  values [22,50]. The contact-front (two-terminal in this work) measurements, which are standard measurements of TLM, assume that  $R_{c2D} = R_{2D}$ . The specific resistance obtained by contact-front method are denoted here as  $\rho_{cf}$ . It was found that  $R_{c2D} \neq R_{2D}$  and the temperature dependencies of  $\rho_c$  and  $\rho_{cf}$  were qualitatively different [52]. Disregarding those concerns,  $\rho_{cf}$  was estimated and the results are shown

in the inset of Figure 9. If we assume that the properties of the channel under the electrodes are similar to those between the electrodes ( $R_{c2D} \approx R_{2D}$ ), then the contact-front and contact-end methods give the same results, i.e.,  $\rho_{cf} \approx \rho_c$  and  $L_x \approx L_T$ .

Reiterating, in the present work,  $R_c$ ,  $R_{2D}$ ,  $\rho_{cf}$  and  $L_x$  increase with an increase in the current, while  $\rho_c$  and  $R_{c2D}$  are not known with confidence.

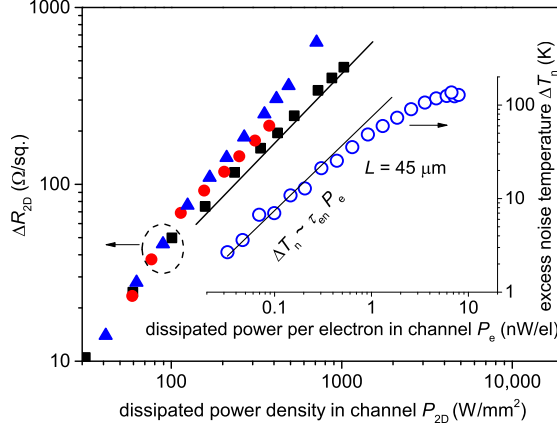


**Figure 8.** The dependence of channel resistance change  $\Delta R_{2D} = R_{2D} - R_{2D0}$  on dissipated power density in channel; AlGaIn/GaN (closed squares), AlGaIn/AlN/GaN (closed triangles and circles). The inset shows the dependence of the excess noise temperature  $\Delta T_n$  on the dissipated power per electron  $P_e$  in the 45  $\mu\text{m}$ -long channel. The lines in the main panel and inset demonstrate the dependencies of  $\Delta R_{2D} \sim P_{2D}$  and  $\Delta T_n \sim P_e$ , respectively.

We also can consider an *unintentionally* formed field-plate-like structure near electrode, which, at higher voltages in the channel, could induce a local high-resistance region near the edge of electrode which also would appear as a increase in  $R$ . In this case, the open symbols in Figure 4a would correspond to the resistance of the high-resistance region and not to the contact resistance change. However, it would be difficult to explain why this resistance is so different (more than 10 times), as it is compared between three channels at a given current.

An interesting correlation is observed in the dependencies of  $\rho_{cf}$  (inset of Figure 9) and  $R_c$  (Figure 4) on the current for different samples. In that case the increase in both starts earlier if low-field resistance  $R_{c0}$  is higher. For example, from Figure 4a it follows that the difference of  $R_{c0}$  between two samples (closed squares and circles) is  $\sim 3$  times, and that correlates with more than  $\sim 12$  times difference in  $R_c$  at an elevated current density of  $\sim 700$  mA/mm (Figure 4a). This makes sense, because  $P_c$  is higher for larger  $R_c$  at the same current, resulting in an increase in self-heating.

In other experiments, when the change in sample temperature was realized by direct heating of the sample (instead of Joule heating), two distinct trends of the change in  $R_c$  and  $\rho_c$  versus temperature were found [26–28,52–59]. The decrease in  $R_c$  was attributed to the metal–semiconductor junction properties and the increase was due to metal-like behavior when electron transport is determined by the “spike mechanism”—metal protrusions directly contacting the 2DEG channel under the electrodes

As it was previously discussed, both  $R_c$  and  $R_{ch}$  increase due to self-heating (Figures 4 and 8). This is also observed in Figure 3a, where the dependence of the total resistance on the current is nonlinear. In terms of sheet resistance  $R_{2D}$ , an increase is observed in Figure 3b, where the slope (which is proportional to  $R_{2D}$ ) changes with the

current. The increase in the resistance of the 2DEG channel at the interface of AlGaIn and GaN is widely acknowledged to be due to electron–phonon scattering, the intensity of which increases with the temperature of the device at a high current. The electron scattering is largely determined by the strong electron–LO–phonon interaction in the GaN and associated hot-phonon effect [25].

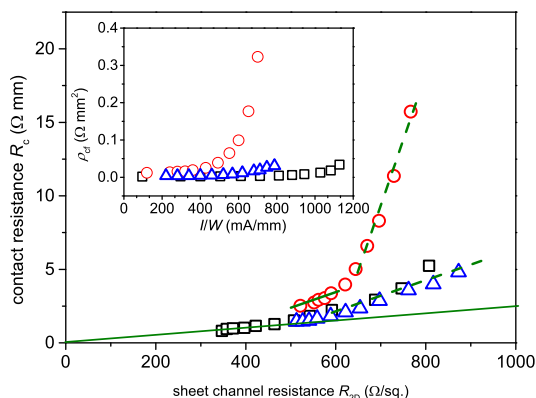


**Figure 9.** The dependence of the contact resistance  $R_c$  on the channel sheet resistance  $R_{2D}$  for different samples: AlGaIn/GaN (squares), AlGaIn/AlN/GaN (triangles and circles). Lines illustrate the slopes of the dependencies. Starting at  $R_{2D} \sim 750 \Omega/\text{sq.}$ , the increase in  $R_c$  becomes faster (dashed lines versus solid lines).

It is natural to expect that the 2DEG channel properties of the area beneath the electrodes (which have a sheet resistance of  $R_{c2D}$ ) at least in part would preserve some features of the channel between the electrodes (which have a sheet resistance of  $R_{2D}$ ). Therefore, we compare the self-heating of  $R_c$  and  $R_{2D}$  by plotting  $R_c(I)$  versus  $R_{2D}(I)$  in Figure 9. Here,  $R_c$  is multiplied by  $W$  as in Figure 4. The channel sheet resistance  $R_{2D}$  is estimated from the  $R(L)$  slope  $\Delta R/\Delta L$  (see Figure 3b) and the channel width  $W$  as  $R_{2D} = (\Delta R/\Delta L) \times W$ . In Figure 9,  $R_c$  is nearly proportional to  $R_{2D}$  at lower currents (see solid lines), but then, it starts to increase faster than  $R_{2D}$  (see dashed lines). The threshold-like increase in  $R_c$  is resolved, revealing the threshold position for all three samples at value of about  $\sim 600 \Omega/\text{sq.}$

The increase in  $R_c$  is not good news for those who fabricate devices with small  $R_{c0}$  and those who believe that it will remain the same small at higher currents (electric fields). The situation is even more dramatic, because the ratio  $R_c/R_{2D}$  (and  $R_c/R_{ch}$ ) also increases with the current. Indeed, from Figure 9 it can be concluded that above the threshold  $R_c$  increases faster than  $R_{2D}$ . We recognize that this is the most important result of the present work. This behavior has many practical consequences, because a fast increase in  $R_c$  depending on  $I$  can deteriorate the performance of electronic devices.

The increase in the ratio  $R_c/R_{2D}$  can be discussed in terms of stronger  $R_c$  self-heating compared to that of  $R_{ch}$ . Excess noise temperature  $\Delta T_{nc}$  in  $R_c$  (Figure 6, squares) is more than four times stronger than  $\Delta T_n$  in the total resistance  $R$  of 45  $\mu\text{m}$ -long channel (circles). The term  $\Delta T_{nc} \times 2R_c$  in Equation (5) is not negligible, even for the 45  $\mu\text{m}$ -long channel (it would be negligible for the infinitely long channel only). Therefore,  $\Delta T_n$  of a 45  $\mu\text{m}$ -long channel reaches  $\sim 130 \text{ K}$  at a  $\sim 0.3 \text{ A}$ , and it is still slightly higher than its  $\Delta T_{ch}$ . Thus, the relation  $\Delta T_{nc} > \Delta T_n \gtrsim \Delta T_{nch}$  holds. This suggests that the temperature  $T_c$  (and thus, the self-heating) of  $R_c$  is higher than the temperature  $T_{ch}$  of  $R_{ch}$ .

Let us first discuss the option that the self-heating of  $R_c$  is caused by the self-heating of  $R_{c2D}$  (see Equation (7)), while  $\rho_c$  self-heating is negligible. The current density in  $R_{c2D}$  is

smaller than in  $R_{2D}$ , therefore, the stronger self-heating of  $R_{c2D}$  compared to  $R_{2D}$ , might seem surprising. The current profile is illustrated in Figure 1b where the horizontal current vector magnitude gradually decreases as the current branches toward the electrodes. A detailed description of the current dependence on the distance can be found elsewhere [22]. We could suppose, that  $R_{c2D} > R_{2D}$  due to lower electron mobility or lower sheet electron density under the electrodes. In this case dissipated power per unit area  $P_{2D}$  at a given current density  $j$  will be higher because  $P_{2D} \propto R_{c2D}j^2$ . Higher dissipated power in the contact resistance results in higher self-heating of  $R_{c2D}$ . The next option is the self-heating of  $\rho_c$ . If the metal-like shunt resistances from the metal to the 2DEG channel under the electrodes persists, the electron mobility in these shunt resistances is expected to be poor due to the high density of electrons and associated intensive electron–electron scattering. However, the high electron density in metals is what could make the specific resistance of those metal protrusions low. The current density in metal protrusion is high if its cross section is small, leading to high resulting values of the dissipated power density per unit volume.

The self-heating model in terms of the two temperatures  $T_c$  and  $T_{ch}$  is oversimplified. In GaN-based 2DEG channels (applicable to  $R_{c2D}$  and  $R_{2D}$ ), excess (hot) electron temperature  $\Delta T_e$  is higher than the excess lattice temperature  $\Delta T_L$  when the constant electric field is applied [34]. In the pulsed mode,  $\Delta T_L$  is lower when compared to the DC mode; therefore, at short voltage pulses a nearly isothermal condition is maintained ( $\Delta T_L \ll T_L$ ), and the self-heating effects related to acoustic phonons are mitigated. Furthermore, in the pulse mode,  $\Delta T_e$  is higher due to the thermal quenching effect when the hot-electron temperature decreases along with the voltage pulse due to the electron mobility decrease [37]; the shorter the pulse, the weaker the thermal quenching. Mainly because of lower  $\Delta T_L$  in the pulsed mode, higher electric fields and currents can usually be reached without the thermal breakdown of the channel. It is also important to mention, that even in the pulsed mode, at higher electric fields the LO-phonon-related self-heating is present. For 2DEG densities, typical for GaN-based heterostructures, the hot-phonon effect is important, as non-equilibrium LO-phonons (hot-LO-phonons) strongly impact the hot-electron transport and temperature [25,35]. At high fields under conditions of strong hot-electron–hot-phonon coupling, when the system is strongly non-equilibrium, the hot-electron temperature  $T_e$  is close to the effective hot-LO-phonon temperature  $T_{LO}$ . In this case, different temperatures  $T_e$ ,  $T_{LO}$  and  $T_L$  are introduced, for which the relation  $T_e \gtrsim T_{LO} \gg T_L$  holds [51]. The hot-electron excess temperature  $\Delta T_e$  is controlled by electron energy relaxation time  $\tau_{en}$ ,  $\Delta T_e \propto \tau_{en}P_e \propto \tau_{en}P_V/n \propto \tau_{en}\rho_j^2/n$ , where  $P_e$  is the dissipated power per electron and  $n$  is the electron density [60]. The dependence of excess noise temperature on dissipated power per electron in the 45  $\mu\text{m}$  long channel  $P_e = U_a I/N$  is shown in the inset of Figure 8 (open circles), where  $N$  is electron number in the channel available from the Hall measurements. The line in the inset is plotted for constant  $\tau_{en}$  in the channel. At a higher power per electron,  $\tau_{en}$  decreases due to enhanced electron–LO-phonon scattering, and experimental points (circles) deviate from that line. If the electron mobility in the 2DEG channel under the electrodes is lower than in the 2DEG channel between electrodes (corresponding to  $R_{c2D}$  and  $R_{2D}$ , respectively), then at a given current,  $\Delta T_e$  in the former channel will be higher. Indeed, at a given current, the electric field (and thus,  $P_e$ ) will be higher for the 2DEG channel with a lower electron mobility. A higher  $P_e$  results in a higher  $\Delta T_e$  (see inset of Figure 8). For the metal-like conductor, the hot-electron effect is not well expressed due to poor electron mobility; therefore,  $T_e \approx T_L$ . In this case,  $\Delta T_e \approx \Delta T_L \propto (1/C_V)\rho_j^2$ , where  $C_V$  is the heat capacity per unit volume. As such, qualitatively both cases (GaN-based channels and metal-like conductors) are similar in that  $\Delta T_e \propto \rho_j^2$ . This is the reason why it is difficult to differentiate between the self-heating of resistances  $R_{c2D}$  and  $\rho_c$  from the temperature–current measurements. Assuming that  $R_{c2D} \approx R_{2D}$  and  $\rho_{cf} \approx \rho_c$ , the data in the inset of Figure 9 indicate the strong self-heating of  $\rho_c$ .

To conclude, we investigated the pulsed current–voltage (I–V) and hot-electron microwave noise (at 10 GHz frequency) characteristics of the TLM samples composed of



AlGaN/(AlN)/GaN heterostructures with annealed Ti/Al/Ni/Au ohmic contacts to the 2DEG channel. From the I-V measurements, the increase in the contact resistance  $R_c$  dependent on the current was found for all samples, with a change up to six times as the current density approached  $\sim 0.6$  A/mm. The comparison of current dependence  $R_c$  and the channel resistance  $R_{ch}$  revealed that  $R_c$  is more sensitive to the current change. It was found that the change in  $R_c$  from its low-field value is proportional to the electric power dissipated in the contacts. The pulsed microwave noise measurements further confirmed that the noise temperature of the contacts is notably higher when compared to the noise temperature of the channel. The increase in the contact resistance (and temperature) was interpreted as a result of self-heating.

**Author Contributions:** Conceptualization, E.Š. and I.K.; investigation, E.Š., J.J., A.Š., V.K. and I.K.; writing—original draft preparation, E.Š. and I.K.; writing—review and editing, E.Š. and I.K.; visualization, E.Š., J.J. and I.K.; supervision, E.Š. and I.K.; project administration, I.K.; funding acquisition, I.K. All authors have read and agreed to the published version of the manuscript.

**Funding:** The work was supported by the Research Council of Lithuania (Lietuvos mokslo taryba) within the framework of the “T-HP” Project (grant No. DOTSUT-184) funded by the European Regional Development Fund according to the Measure No.01.2.2-LMT-K-718-03-0096.

**Institutional Review Board Statement:** Not applicable.

**Informed Consent Statement:** Not applicable.

**Data Availability Statement:** The data presented in this study are available on request from the corresponding author. The data are not publicly available due to privacy.

**Acknowledgments:** The authors are sincerely grateful to J. Malakauskaitė and V. Jakštas for assistance in sample fabrication, to P. Prystawko for fruitful discussions of the various aspects of this work.

**Conflicts of Interest:** The authors declare no conflict of interest.

## References

- Morkoç, H. *Handbook of Nitride Semiconductors and Devices*; Wiley-VCH: Weinheim, Germany, 2008. [\[CrossRef\]](#)
- Abid, I.; Kabouche, R.; Bougerol, C.; Pernot, J.; Masante, C.; Comyn, R.; Cordier, Y.; Medjdoub, F. High Lateral Breakdown Voltage in Thin Channel AlGaIn/GaN High Electron Mobility Transistors on AlN/Sapphire Templates. *Micromachines* **2019**, *10*, 690. [\[CrossRef\]](#) [\[PubMed\]](#)
- Abid, I.; Mehta, J.; Cordier, Y.; Derluyn, J.; Degroote, S.; Miyake, H.; Medjdoub, F. AlGaIn Channel High Electron Mobility Transistors with Regrown Ohmic Contacts. *Electronics* **2021**, *10*, 635. [\[CrossRef\]](#)
- Gonschorek, M.; Carlin, J.F.; Feltin, E.; Py, M.A.; Grandjean, N. Self heating in AlInN/GaN high power devices: Origin and impact on contact breakdown and IV characteristics. *J. Appl. Phys.* **2011**, *109*, 063720. [\[CrossRef\]](#)
- Kuzmík, J.; Bychikhin, S.; Pogany, D.; Gaquière, C.; Morvan, E. Current conduction and saturation mechanism in AlGaIn/GaN ungated structures. *J. Appl. Phys.* **2006**, *99*, 123720. [\[CrossRef\]](#)
- Kuzmík, J.; Tapajna, M.; Valik, L.; Molnar, M.; Donoval, D.; Fleury, C.; Pogany, D.; Strasser, G.; Hilt, O.; Brunner, F.; et al. Self-Heating in GaN Transistors Designed for High-Power Operation. *IEEE Trans. Electron Devices* **2014**, *61*, 3429–3434. [\[CrossRef\]](#)
- Sarua, A.; Ji, H.F.; Kuball, M.; Uren, M.; Martin, T.; Hilton, K.; Balmer, R. Integrated micro-Raman/infrared thermography probe for monitoring of self-heating in AlGaIn/GaN transistor structures. *IEEE Trans. Electron Devices* **2006**, *53*, 2438–2447. [\[CrossRef\]](#)
- Duffy, S.J.; Benbakhiti, B.; Kalna, K.; Boucherta, M.; Zhang, W.D.; Bourzgui, N.E.; Soltani, A. Strain-Reduction Induced Rise in Channel Temperature at Ohmic Contacts of GaN HEMTs. *IEEE Access* **2018**, *6*, 42721–42728. [\[CrossRef\]](#)
- Ranjan, K.; Arulkumar, S.; Ng, G.L.; Sandupatla, A. Investigation of Self-Heating Effect on DC and RF Performances in AlGaIn/GaN HEMTs on CVD-Diamond. *IEEE J. Electron Devices Soc.* **2019**, *7*, 1264–1269. [\[CrossRef\]](#)
- Janonis, V.; Pashnev, D.; Grigelionis, I.; Korotiev, V.; Balagula, R.M.; Minkevicius, L.; Jorudas, J.; Alexeeva, N.; Subacius, L.; Valušis, G.; et al. Electrically-pumped THz emitters based on plasma waves excitation in III-nitride structures. In *Terahertz Emitters, Receivers, and Applications XI*; Razeghi, M., Baranov, A.N., Eds.; SPIE: Washington, DC, USA, 2020; Volume 11499, p. 8. [\[CrossRef\]](#)
- Jorudas, J.; Šimukovič, A.; Dub, M.; Sakowicz, M.; Prystawko, P.; Indrišūnas, S.; Kovalevskij, V.; Rumyantsev, S.; Knap, W.; Kašalynas, I. AlGaIn/GaN on SiC Devices without a GaN Buffer Layer: Electrical and Noise Characteristics. *Micromachines* **2020**, *11*, 1131. [\[CrossRef\]](#)
- Ardaravičius, L.; Matulionis, A.; Liberis, J.; Kiprijanovic, O.; Ramonas, M.; Eastman, L.F.; Shealy, J.R.; Vertiatchikh, A. Electron drift velocity in AlGaIn/GaN channel at high electric fields. *Appl. Phys. Lett.* **2003**, *83*, 4038–4040. [\[CrossRef\]](#)

Cheney, D.J.; Douglas, E.A.; Liu, L.; Lo, C.F.; Xi, Y.Y.; Gila, B.P.; Ren, F.; Horton, D.; Law, M.E.; Smith, D.J.; et al. Reliability studies of AlGaN/GaN high electron mobility transistors. *Semicond. Sci. Technol.* **2013**, *28*, 074019. [[CrossRef](#)]

Meneghini, M.; Meneghesso, G.; Zanoni, E. (Eds.) *Power GaN Devices*; Power Electronics and Power Systems; Springer International Publishing: Cham, Switzerland, 2017. [[CrossRef](#)]

Cai, X.; Du, C.; Sun, Z.; Ye, R.; Liu, H.; Zhang, Y.; Duan, X.; Lu, H. Recent progress of physical failure analysis of GaN HEMTs. *J. Semicond.* **2021**, *42*, 051801. [[CrossRef](#)]

Mohanty, S.K.; Chen, Y.Y.; Yeh, P.H.; Hornig, R.H. Thermal Management of GaN-on-Si High Electron Mobility Transistor by Copper Filled Micro-Trench Structure. *Sci. Rep.* **2019**, *9*, 19691. [[CrossRef](#)] [[PubMed](#)]

Canato, E.; Meneghini, M.; Nardo, A.; Masin, F.; Barbato, A.; Barbato, M.; Stockman, A.; Banerjee, A.; Moens, P.; Zanoni, E.; et al. ESD-failure of E-mode GaN HEMTs: Role of device geometry and charge trapping. *Microelectron. Reliab.* **2019**, *100–101*, 113334. [[CrossRef](#)]

Meneghini, M.; Hilt, O.; Fleury, C.; Silvestri, R.; Capriotti, M.; Strasser, G.; Pogany, D.; Bahat-Treidel, E.; Brunner, F.; Knauer, A.; et al. Normally-off GaN-HEMTs with p-type gate: Off-state degradation, forward gate stress and ESD failure. *Microelectron. Reliab.* **2016**, *58*, 177–184. [[CrossRef](#)]

Zhu, Y.; Cao, W.; Fan, Y.; Deng, Y.; Xu, C. Effects of rapid thermal annealing on ohmic contact of AlGaIn/GaN HEMTs. *J. Semicond.* **2014**, *35*, 026004. [[CrossRef](#)]

Kuzmík, J.; Pogany, D.; Gornik, E.; Javorka, P.; Kordoš, P. Electrical overstress in AlGaIn/GaN HEMTs: Study of degradation processes. *Solid-State Electron.* **2004**, *48*, 271–276. [[CrossRef](#)]

Berger, H. Models for contacts to planar devices. *Solid-State Electron.* **1972**, *15*, 145–158. [[CrossRef](#)]

Schroder, D.K. *Semiconductor Material and Device Characterization*, 3rd ed.; John Wiley and Sons, Inc.: Hoboken, NJ, USA, 2005.

Barker, J.; Akis, R.; Ferry, D.; Goodnick, S.; Thornton, T.; Koleske, D.; Wickenden, A.; Henry, R. High-field transport studies of GaN. *Phys. B Condens. Matter* **2002**, *314*, 39–41. [[CrossRef](#)]

Khan, I.; Cooper, J. Measurement of high-field electron transport in silicon carbide. *IEEE Trans. Electron Devices* **2000**, *47*, 269–273. [[CrossRef](#)]

Ridley, B.K. 379Hot phonons. In *Quantum Processes in Semiconductors*; Oxford University Press: Oxford, UK, 2013. [[CrossRef](#)]

Niranjan, S.; Guiney, I.; Humphreys, C.J.; Sen, P.; Muralidharan, R.; Nath, D.N. Au-free recessed Ohmic contacts to AlGaIn/GaN high electron mobility transistor: Study of etch chemistry and metal scheme. *J. Vac. Sci. Technol. B* **2020**, *38*, 032207. [[CrossRef](#)]

Zhou, D.; Xu, H.; Chen, L.; Lu, H.L.; Huang, W.; Zhang, D.W.; Yan, D. Temperature dependent characteristics of Ti/Al/Ni/Au Ohmic contact on lattice-matched In<sub>0.17</sub>Al<sub>0.83</sub>N/GaN heterostructures. *Solid-State Electron.* **2021**, *183*, 108108. [[CrossRef](#)]

Greco, G.; Iucolano, F.; Roccaforte, F. Ohmic contacts to Gallium Nitride materials. *Appl. Surf. Sci.* **2016**, *383*, 324–345. [[CrossRef](#)]

Zhang, P.; Lau, Y.Y.; Gilgenbach, R.M. Analysis of current crowding in thin film contacts from exact field solution. *J. Phys. D Appl. Phys.* **2015**, *48*, 475501. [[CrossRef](#)]

Zhang, P.; Lau, Y.Y. An exact field solution of contact resistance and comparison with the transmission line model. *Appl. Phys. Lett.* **2014**, *104*, 204102. [[CrossRef](#)]

Duffy, S.J.; Benbakhti, B.; Mattallah, M.; Zhang, W.; Bouchilaoun, M.; Boucherta, M.; Kalna, K.; Bourzgui, N.; Maher, H.; Soltani, A. Low Source/Drain Contact Resistance for AlGaIn/GaN HEMTs with High Al Concentration and Si-HP [111] Substrate. *ECS J. Solid State Sci. Technol.* **2017**, *6*, S3040. [[CrossRef](#)]

Sawada, T.; Yamamura, A.; Sasaki, M.; Takahira, K.; Okamoto, T.; Watanabe, S.; Takeya, J. Correlation between the static and dynamic responses of organic single-crystal field-effect transistors. *Nat. Commun.* **2020**, *11*, 4839. [[CrossRef](#)]

Giubileo, F.; Di Bartolomeo, A. The role of contact resistance in graphene field-effect devices. *Prog. Surf. Sci.* **2017**, *92*, 143–175. [[CrossRef](#)]

Tripathy, S.K.; Xu, G.; Mu, X.; Ding, Y.J.; Wang, K.; Cao, Y.; Jena, D.; Khurgin, J.B. Evidence of hot electrons generated from an AlN/GaN high electron mobility transistor. *Appl. Phys. Lett.* **2008**, *92*, 013513. [[CrossRef](#)]

Khurgin, J.; Jena, D. Isotope Engineering of GaN for Boosting Transistor Speeds. In *High-Frequency GaN Electronic Devices*; Springer International Publishing: Cham, Switzerland, 2020; pp. 43–82. [[CrossRef](#)]

Matulionis, A. GaN-based two-dimensional channels: Hot-electron fluctuations and dissipation. *J. Phys. Condens. Matter* **2009**, *21*, 174203. [[CrossRef](#)]

Ardaravičius, L.; Liberis, J.; Matulionis, A.; Eastman, L.F.; Shealy, J.R.; Vertiatchikh, A. Self-heating and microwave noise in AlGaIn/GaN. *Phys. Status Solidi (a)* **2004**, *201*, 203–206. [[CrossRef](#)]

Šermukšnis, E.; Liberis, J.; Ramonas, M.; Matulionis, A.; Toporkov, M.; Liu, H.Y.; Avrutin, V.; Özgür, Ü.; Morkoç, H. Hot-electron energy relaxation time in Ga-doped ZnO films. *J. Appl. Phys.* **2015**, *117*, 065704. [[CrossRef](#)]

Adamov, R.B.; Pashnev, D.; Shalygin, V.A.; Moldavskaya, M.D.; Vinnichenko, M.Y.; Janonis, V.; Jorudas, J.; Tumėnas, S.; Prystawko, P.; Krysko, M.; et al. Optical Performance of Two Dimensional Electron Gas and GaN:C Buffer Layers in Al-GaN/AlN/GaN Heterostructures on SiC Substrate. *Appl. Sci.* **2021**, *11*, 6053. [[CrossRef](#)]

Pashnev, D.; Koroteyev, V.V.; Jorudas, J.; Kaplas, T.; Janonis, V.; Urbanowicz, A.; Kašalynas, I. Experimental evidence of temperature dependent effective mass in AlGaIn/GaN heterostructures observed via THz spectroscopy of 2D plasmons. *Appl. Phys. Lett.* **2020**, *117*, 162101. [[CrossRef](#)]

Jakštas, V.; Kašalynas, I.; Šimkienė, I.; Strazdienė, V.; Prystawko, P.; Leszczynski, M. Schottky diodes and high electron mobility transistors of 2DEG AlGaIn/GaN structures on sapphire substrate. *Lith. J. Phys.* **2014**, *54*. [[CrossRef](#)]

42. Jorudas, J.; Malakauskaite, J.; Subacius, L.; Janonis, V.; Jakstas, V.; Kasalynas, I. Development of the planar AlGa<sub>N</sub>/Ga<sub>N</sub> bow-tie diodes for terahertz detection. In Proceedings of the IEEE 2019 44th International Conference on Infrared, Millimeter, and Terahertz Waves (IRMMW-THz), Paris, France, 1–6 September 2019; Volume 2019-Septe, pp. 1–2. [\[CrossRef\]](#)
43. Vetry, R.; Zhang, N.; Keller, S.; Mishra, U. The impact of surface states on the DC and RF characteristics of AlGa<sub>N</sub>/Ga<sub>N</sub> HFETs. *IEEE Trans. Electron Devices* **2001**, *48*, 560–566. [\[CrossRef\]](#)
44. Arulkumar, S.; Egawa, T.; Ishikawa, H.; Jimbo, T.; Sano, Y. Surface passivation effects on AlGa<sub>N</sub>/Ga<sub>N</sub> high-electron-mobility transistors with SiO<sub>2</sub>, Si<sub>3</sub>N<sub>4</sub>, and silicon oxynitride. *Appl. Phys. Lett.* **2004**, *84*, 613–615. [\[CrossRef\]](#)
45. Sai, P.; Jorudas, J.; Dub, M.; Sakowicz, M.; Jakstas, V.; But, D.B.; Prystawko, P.; Cywinski, G.; Kašalynas, I.; Knap, W.; et al. Low frequency noise and trap density in Ga<sub>N</sub>/AlGa<sub>N</sub> field effect transistors. *Appl. Phys. Lett.* **2019**, *115*, 183501. [\[CrossRef\]](#)
46. Sermuksnis, E.; Liberis, J.; Simukovic, A.; Matulionis, A.; Ullah, M.B.; Toporkov, M.; Avrutin, V.; Ozgur, U.; Morkoc, H. Hot-electron noise spectroscopy for HFET channels. In Proceedings of the IEEE 2017 International Conference on Noise and Fluctuations (ICNF), Vilnius, Lithuania, 20–23 June 2017; pp. 1–4. [\[CrossRef\]](#)
47. Sermuksnis, E.; Liberis, J.; Matulionis, A.; Toporkov, M.; Avrutin, V.; Ozgur, U.; Morkoc, H. Hot-electron noise and energy relaxation in wurtzite ZnO. In Proceedings of the IEEE 2015 International Conference on Noise and Fluctuations (ICNF), Xi'an, China, 2–6 June 2015; pp. 1–4. [\[CrossRef\]](#)
48. Liberis, J.; Matulionis, A. Microwave noise technique for measurement of hot-electron energy relaxation time and hot-phonon lifetime. *Lith. J. Phys.* **2007**, *47*, 491.
49. Hartmagel, H.; Katilius, R.; Matulionis, A. *Microwave Noise in Semiconductor Devices*; A Wiley-Interscience Publication; Wiley-VCH: Weinheim, Germany, 2001.
50. Reeves, G.; Harrison, H. Obtaining the specific contact resistance from transmission line model measurements. *IEEE Elect. Dev. Lett.* **1982**, *3*, 111. [\[CrossRef\]](#)
51. Liberis, J.; Matulionienė, I.; Matulionis, A.; Ramonas, M.; Eastman, L.F. *Advanced Semiconductor Materials and Devices Research: III-Nitrides and SiC*; Chap Hot Phonons in High-Power Microwave HEMT and FET Channels; Transworld: Kerala, India, 2009.
52. Hajlasz, M.; Donkers, J.J.T.; Sque, S.J.; Heil, S.B.S.; Gravesteyn, D.J.; Rietveld, F.J.R.; Schmitz, J. Sheet resistance under Ohmic contacts to AlGa<sub>N</sub>/Ga<sub>N</sub> heterostructures. *Appl. Phys. Lett.* **2014**, *104*, 242109. [\[CrossRef\]](#)
53. Shi, W.; Huang, S.; Wang, X.; Jiang, Q.; Yao, Y.; Bi, L.; Li, Y.; Deng, K.; Fan, J.; Yin, H.; et al. Low-thermal-budget Au-free ohmic contact to an ultrathin barrier AlGa<sub>N</sub>/Ga<sub>N</sub> heterostructure utilizing a micro-patterned ohmic recess. *J. Semicond.* **2021**, *42*, 092801. [\[CrossRef\]](#)
54. Iucolano, F.; Greco, G.; Roccaforte, F. Correlation between microstructure and temperature dependent electrical behavior of annealed Ti/Al/Ni/Au Ohmic contacts to AlGa<sub>N</sub>/Ga<sub>N</sub> heterostructures. *Appl. Phys. Lett.* **2013**, *103*, 201604. [\[CrossRef\]](#)
55. Kim, S.; Ryou, J.H.; Dupuis, R.D.; Kim, H. Carrier transport mechanism of low resistance Ti/Al/Au ohmic contacts to AlInN/GaN heterostructures. *Appl. Phys. Lett.* **2013**, *102*, 052107. [\[CrossRef\]](#)
56. Sachenko, A.V.; Belyaev, A.E.; Boltovets, N.S.; Konakova, R.V.; Kudryk, Y.Y.; Novitskii, S.V.; Sheremet, V.N.; Li, J.; Vitusevich, S.A. Mechanism of contact resistance formation in ohmic contacts with high dislocation density. *J. Appl. Phys.* **2012**, *111*, 083701. [\[CrossRef\]](#)
57. Fontserè, A.; Pérez-Tomás, A.; Placidi, M.; Llobet, J.; Baron, N.; Chenot, S.; Cordier, Y.; Moreno, J.C.; Gammon, P.M.; Jennings, M.R.; et al. Micro and nano analysis of 0.2 Ω mm Ti/Al/Ni/Au ohmic contact to AlGa<sub>N</sub>/Ga<sub>N</sub>. *Appl. Phys. Lett.* **2011**, *99*, 213504. [\[CrossRef\]](#)
58. Liu, Z.H.; Arulkumar, S.; Ng, G.I. Temperature dependence of Ohmic contact characteristics in AlGa<sub>N</sub>/Ga<sub>N</sub> high electron mobility transistors from –50 to 200 °C. *Appl. Phys. Lett.* **2009**, *94*, 142105. [\[CrossRef\]](#)
59. Blank, T.V.; Gol'Dberg, Y.A. Mechanisms of current flow in metal-semiconductor ohmic contacts. *Semiconductors* **2007**, *41*, 1263. [\[CrossRef\]](#)
60. Dyson, A.; Ridley, B.K. Negative differential resistance associated with hot phonons. *J. Appl. Phys.* **2012**, *112*, 063707. [\[CrossRef\]](#)

**Terahertz Bow-Tie Diode Based on Asymmetrically Shaped AlGaIn/GaN Heterostructures**

**J. Jorudas**, D. Seliuta, L. Minkevičius, V. Janonis, L. Subačius, D. Pashnev, S. Pralgauskaitė, J. Matukas, K. Ikamas, A. Lisauskas, E. Šermukšnis, A. Šimukovič, J. Liberis, V. Kovalevskij, I. Kašalynas  
*Lithuanian Journal of Physics*, vol. 63, no. 4, 191-201 (2023).  
DOI: 10.3952/physics.2023.63.4.1

Reprinted with permission from The Lithuanian Academy of Sciences.

The article may be accessed online at <https://doi.org/10.3952/physics.2023.63.4.1>

## TERAHERTZ BOW-TIE DIODE BASED ON ASYMMETRICALLY SHAPED AlGa<sub>N</sub>/Ga<sub>N</sub> HETEROSTRUCTURES

J. Jorudas <sup>a</sup>, D. Seliuta <sup>a</sup>, L. Minkevičius <sup>a</sup>, V. Janonis <sup>a</sup>, L. Subačius <sup>a</sup>,

D. Pashnev <sup>a</sup>, S. Pralgauskaitė <sup>a</sup>, J. Matukas <sup>a</sup>, K. Ikamas <sup>b</sup>, A. Lisauskas <sup>b</sup>, E. Šermukšnis <sup>c</sup>,

A. Šimukovič <sup>c</sup>, J. Liberis <sup>c</sup>, V. Kovalevskij <sup>d</sup>, and I. Kašalynas <sup>a,b</sup>

<sup>a</sup> Terahertz Photonics Laboratory, Center for Physical Sciences and Technology, Saulėtekio 3, 10257 Vilnius, Lithuania

<sup>b</sup> Institute of Applied Electrodynamics and Telecommunications, Vilnius University, Saulėtekio 3, 10257 Vilnius, Lithuania

<sup>c</sup> Fluctuation Research Laboratory, Center for Physical Sciences and Technology, Saulėtekio 3, 10257 Vilnius, Lithuania

<sup>d</sup> Experimental Nuclear Physics Laboratory, Center for Physical Sciences and Technology,

Saulėtekio 3, 10257 Vilnius, Lithuania

Email: [irmantas.kasalynas@ftmc.lt](mailto:irmantas.kasalynas@ftmc.lt)

Received 3 October 2023; accepted 3 October 2023

Asymmetrical shaping of AlGa<sub>N</sub>/Ga<sub>N</sub> heterostructures containing a conductive layer of two-dimensional electron gas (2DEG) was used for the development of bow-tie (BT) diodes for room temperature terahertz (THz) detection. Considering operation of the THz BT diode in the unbiased mode as preferable for practical applications, we investigated the diodes with an obvious asymmetry of *IV* characteristics, which was found to be more pronounced with the decrease of an apex width, resulting in the sensitive THz detection. A nonuniform heating of carriers in a metalized leaf of the BT diode was attributed as the main mechanism that caused the rectification of THz waves. The responsivity and noise-equivalent power (NEP) at the fundamental antenna frequency of 150 GHz were up to 4 V/W and 2 nW/√Hz, respectively. Such high sensitivity of BT diodes allowed us to measure for the first time the response spectrum of the asymmetric BT antenna demonstrating fundamental and higher order resonances in good agreement with finite-difference time-domain simulation data in a broad spectrum range. The detailed investigation of the low- and high-frequency noise characteristics of AlGa<sub>N</sub>/Ga<sub>N</sub> BT diodes revealed that only thermal noise needs to be considered for the unbiased operation, the value of which was relatively low due to a high density of 2DEG enabling low resistivity values. Moreover, we observed that the responsivity of BT diode scales with its resistance, revealing that tapering of the diode apex below a few microns could be ineffective in applications which require low NEP values.

**Keywords:** THz bow-tie diode, AlGa<sub>N</sub>/Ga<sub>N</sub> heterostructure, 2DEG, asymmetrical BT antenna

### 1. Introduction

The evolution of terahertz (THz) science and technology enable new applications in wireless communication, spectroscopic imaging, chemical and biological sensing, but still requires the development of fast, sensitive and room-temperature THz detectors [1, 2]. Of particular interest are semiconductor based sensors which can be integrated on-chip implementing scalable planar schemes [3–5]. The detectors based on hot-electron effects are attractive due to their high sensitivity and de-

tection capabilities achieved in the broadband spectrum [6–8]. In such devices, the rectification of electromagnetic waves is achieved by thermoelectric effects which are the result of the formation of free-carrier temperature gradients due to asymmetric conditions such as geometrical shaping, doping profile, contact and coupling characteristics [9–11].

Initially, the hot-carrier-based detector was developed as a small area whisker-contact of metal-semiconductor structure, where high-frequency electric fields used to be concentrated in a small

region of active material [12]. Years later, the planar structures of n-n<sup>+</sup>-GaAs possessing a high electron mobility were developed by shaping layers in a bow-tie (BT) antenna geometry and demonstrating the sensor operation in the GHz and THz frequency bands [9]. As a further improvement, the InGaAs layer on the InP substrate was selected together with a more asymmetric planar geometry and a complete one leaf metallization of the diode, representing the form of an asymmetric BT antenna [13]. All these THz sensors were found to be well suited in compact spectroscopic imaging systems operating in the direct detection scheme [14]. The response speed of BT diodes was found to be below nanoseconds [15], which allowed one to record amplitude and phase images quickly in the heterodyne configuration [16]. Different approaches were tested to increase the detector sensitivity such as using a modulation-doped AlGaAs/GaAs heterostructure with a 2D electron gas (2DEG) layer [17], applying the voltage/current bias to BT diode electrodes [14], and providing a field-plate (short-gate) over active part of the BT diode [18, 19]. Moreover, the Fermi-level managed barrier (FMB) diode based on the InGaAs lattice matched to the InP structure was proposed for low-noise THz wave detection at room temperature [20]. In addition, researchers have proposed the high sensitivity In<sub>0.53</sub>Ga<sub>0.47</sub>As photodetector [21] as well as the heterostructured low-barrier diode (HLBD) composed of a composition-graded lattice-matched AlGaInAs triangular barrier in the GaAs/AlGaAs system [22] for room-temperature sensitive sub-THz detection.

The heterostructure-based sensor benefits from the fact that the electron energy relaxation is dominated by the ballistic outflow, which allows one to reduce the electron cooling time and, therefore, the response time of the sensor [23]. The sensitivity and noise-equivalent power (NEP) of BT diodes based on the GaAs material system were found to be up to 10 V/W and down to 4 nW/√Hz, respectively [14, 16]. Utilizing the strong built-in internal electric fields achieved by a specific growth condition of the InGaAs layer on the InP substrate enabled a significant reduction of NEP down to the value of 200 pW/√Hz at a selected frequency of 0.6 THz [24]. Meanwhile, sensitive HLBDs and photodetectors demonstrated a significantly bet-

ter responsivity and NEP values, which at the frequency of around 180 GHz reached up to 6000 and 515 V/W and lower than 0.6 and 20 pW/√Hz, respectively [21, 22].

In this work, we investigated the BT diodes developed of commercially available AlGaIn/GaN heterostructures dedicated to high-electron mobility transistor (HEMT) applications. Compared to previously used GaAs-material systems, the selected material has an advantage of a higher electron density, which is useful for a better match between the THz sensor and asymmetric BT antenna impedances [7]. In addition, the short momentum relaxation time of electrons ensures the THz coupling to the 2DEG layer [25, 26]. Furthermore, good ohmic contacts to 2DEG in AlGaIn/GaN heterostructures can be obtained without the heavy doping of semiconductor layers. This simplifies the interpretation of THz signals caused by carrier heating in the asymmetrically necked contact and semiconductor materials if one takes into account self-heating effects of both ohmic contacts and 2DEG layer, observed even under short-duration (only 100 ns) and low-duty-cycle (only 10<sup>-5</sup>) pulsed electric fields [27].

In this work, we attributed the detected THz signals to the nonuniform heating of carriers in the area of a metallized leaf of the BT diode, resulting in the responsivity and NEP values at 150 GHz frequency and room temperature to be up to 4 V/W and 2 nW/√Hz, respectively. A sufficiently high sensitivity of the BT diode allowed us to record the emission spectrum of the frequency-domain spectrometer source, providing THz powers up to 1 μW in the free space. As a result, the asymmetric BT antenna response spectrum was recorded for the first time. Due to the different device and electrode shaping shown in the designs of Fig. 1(a) and in Refs. [13, 14], the AlGaIn/GaN BT diodes revealed a significantly different frequency characteristic in comparison to that of the InGaAs-BT diodes, results of which will be reported elsewhere. In addition, the noise characteristics and the optical responsivity dependence from the apex width and the resistance of BT diode were investigated. The results indicate that the hot electron effects in the metallized leaf are responsible for the optimal operation of THz BT diodes even without an external bias.

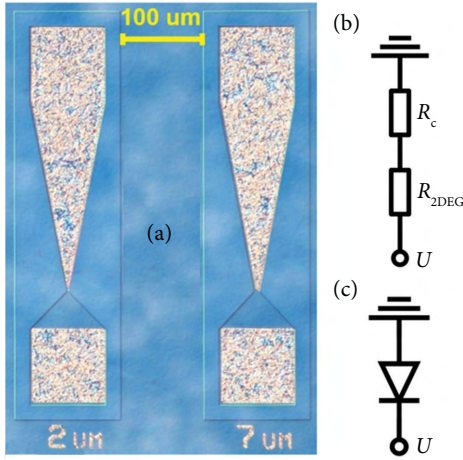


Fig. 1. (a) Nomarski-contrast microscope image of the BT diodes fabricated of asymmetrically shaped AlGaIn/GaN heterostructures with a conductive 2DEG layer. The total length of diode is  $500 \mu\text{m}$ , the width is  $100 \mu\text{m}$ , and the length of metallized and unmetallized heterostructure leaf is  $250$  and  $50 \mu\text{m}$ , respectively. The apex width of shown diodes is  $2$  and  $7 \mu\text{m}$  (as labelled). (b) Suggested equivalent circuit and (c) the symbol of the BT diode, where the resistance  $R_c$  stands for the metallized and  $R_{2\text{DEG}}$  for the unmetallized leaf, which both could be sensitive to the magnitude of the applied electric field.

## 2. Samples

Microscope image of two fabricated BT diodes with the apex width of  $2$  and  $7 \mu\text{m}$  is shown in Fig. 1(a). The samples were fabricated of AlGaIn/GaN heterostructures grown on a  $500 \mu\text{m}$  thick semi-insulating 6H-SiC substrate which were kindly provided for the research by TopGaN (www.topganlasers.com) company. The structure was composed of  $1 \mu\text{m}$  thick unintentionally doped GaN buffer and  $19 \text{ nm}$  thick  $\text{Al}_{0.25}\text{Ga}_{0.75}\text{N}$  barrier layers with a  $1 \text{ nm}$  thick AlN spacer in between. A conductive channel of 2DEG is localized below the AlN spacer in the top part of the buffer layer. DC conductivity and Hall effect measurements at room temperature revealed 2DEG density and low-field mobility values of about  $8.3 \times 10^{12} \text{ cm}^{-2}$  and  $1.9 \times 10^3 \text{ cm}^2/\text{Vs}$ , respectively. From these data the sheet resistivity of the 2DEG layer was estimated to be of about  $400 \Omega$  per square.

The mesas of asymmetrically shaped AlGaIn/GaN heterostructures were developed either by optical photolithography and dry plasma etching or by implantation of Al ions. The ohmic contacts (Ti/Al/Ni/Au:  $30/90/20/100 \text{ nm}$ ) were processed on top of the mesa using e-beam metal evaporation followed by rapid thermal annealing in the  $\text{N}_2$  environment. The metallized leaf is used to concentrate electric field in the apex area, while the unmetallized leaf, a fragment of mesa between two electrodes, is designed as an active part of the sensor, generating a DC signal when exposed to THz radiation. The performance of all BT diodes was investigated in the unbiased mode operation at room temperature unless otherwise specified.

## 3. Results

Two types of the  $IV$  characteristics of AlGaIn/GaN based BT diodes were found after chip fabrication using the same recipe for ohmic contacts [28, 29]. In the first case, the resistance of the metallized BT antenna leaf was found to be insensitive to the magnitude of the applied electric field,  $R_c \approx \text{constant}$ , resulting in the symmetric  $IV$  characteristic of the BT diode. The typical results are shown in Fig. 2 by grey colour short-dash lines. Such type of BT diodes without a bias demonstrated relatively small THz signals

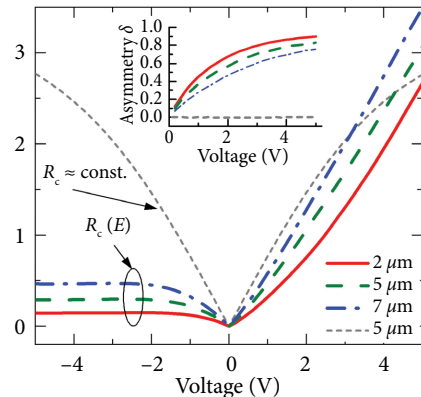


Fig. 2. Current–voltage characteristics of the fabricated BT diodes with different width of the apex (indicated in microns) demonstrating the resistance of metallized leaf's weak and strong dependence on applied electric field (labelled as  $R_c \approx \text{constant}$  and  $R_c(E)$ , respectively). Inset is the asymmetry factor according to Eq. (1).

and responsivity values (see data shown in Fig. 3 by circle symbols) [29].

In another group, the BT diodes demonstrated the resistance of contacts made to be sensitive to the applied electric field  $R_c(E)$ . These BT diodes demonstrated an obvious asymmetry of  $IV$  characteristics, which was more pronounced with the decrease of apex width. The measurement results for BT diodes with different apex sizes are shown in Fig. 2. Here more pronounced carrier heating in the shaped sub-contact area in comparison to the 2DEG channel can be identified [12, 27]. These BT diodes demonstrated a sensitive THz detection in the unbiased regime, thus, only data for those will be discussed further. It is worth to note that the behaviour in the DC regime and the THz performance of such sensors were found to be very similar to those of InGaAs-BT diodes [14], and such facts can be used in the future for the side-by-side comparison of different types of BT diodes.

The transmission line method (TLM) was used to investigate the contact resistance of devices on each AlGaIn/GaN chip after the fabrication process. The contact resistance  $R_c$  and the specific contact resistivity  $\rho_c$  were measured using rectangular shape test TLM structures of  $250 \mu\text{m}$  wide contacts separated by a distance from 3 to  $65 \mu\text{m}$ , revealing the values down to  $1 \Omega \times \text{mm}$  and  $2 \cdot 10^{-5} \Omega \times \text{cm}^2$ , respectively. However, electrode shaping for BT diodes down to the sub-micron size can also modify the contact resistance. Thus, after the device fabrication only the  $IV$  characterization of BT diodes and test TLM structures allowed us to reveal whether the resistance of tapered metallized leaf was dependent on DC voltage or not.

The polarity of bias voltage is determined in respect to the tapered electrode (metallized leaf) which was kept grounded in all experiments. The asymmetry factor of DC currents was defined as [14]

$$\delta = \frac{I_+ - I_-}{I_+ + I_-}, \quad (1)$$

where  $I_+$  and  $I_-$  are the BT diode current measured at positive and negative values of the same bias voltage, respectively. The asymmetry factor of different BT diodes is shown in the inset of Fig. 2. The asymmetry of  $IV$  curves for the BT diodes with  $R_c(E)$  was attributed to the electron heating in the sub-contact area of the metallized leaf. The asymmetry of the current flow is a result of the nonuniform heating of carri-

ers in the vicinity of the apex [7]. Therefore, narrowing of the apex leads to higher electric field values in vicinity of the apex resulting in larger values of the asymmetry factor (see the inset of Fig. 2).

The sensitivity of the BT diode was measured using a quasi-optical setup consisting of an RF signal generator operating at 12.5 GHz and an amplifier-multiplier chain (*Virginia Diodes, Inc.*) with a multiplication factor of 12, 24 and 48 for generating oscillations at 150, 300 and 600 GHz, respectively. A Gunn diode oscillator was used to produce radiation at 94 GHz. The THz beam was emitted to the free space through a horn antenna and was collimated with a  $90^\circ$  off-axis parabolic mirror (OAPM) with a focal length of 10 cm and a diameter of 2 inches. The second OAPM of the same type was used to focus the THz beam onto a hemispherical silicon lens of 12 mm in diameter attached to the back side of a wafer with BT diodes. The power reaching the hemispherical silicon lens was 17, 29, 7 and 0.35 mW at 100, 150, 300 and 600 GHz, respectively. The THz signals were recorded using the lock-in technique.

The responsivity of BT diodes with various apex sizes was measured. The averaged results for 150 GHz frequency are shown in Fig. 3. The responsivity was found by dividing the induced signal voltage over the power of THz beam incident on the BT diode

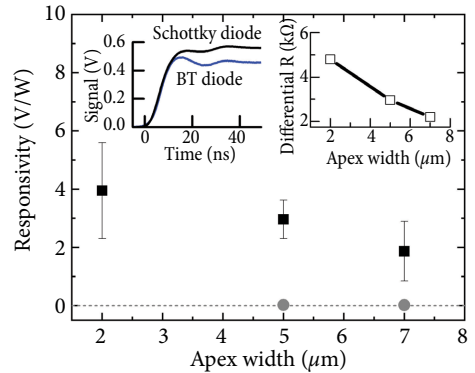


Fig. 3. Measured responsivity dependence on the apex width: squares stand for the BT diodes with  $R_c(E)$  and circles for the BT diodes with  $R_c \approx \text{constant}$  (see also Fig. 2). Right-hand-side inset: the differential resistance of BT diode versus apex width. Left-hand-side inset: comparison of the response speed of BT diode versus Schottky diode.



(power density). As expected, there is a decrease in the voltage sensitivity with an increase in the neck width of the diode. The deviation range of responsivity values was largest for a group of BT diodes with the apex size of  $2\ \mu\text{m}$  independently on the detected THz frequency. It is worth noting that the differential resistance follows a similar trend – decreases with the neck width as it is seen in the right-hand-side inset of Fig. 3.

The detector speed was determined by using mw-field pulses [28]. The response speed of the AlGaIn/GaN BT diode was compared to that of the Schottky barrier diode. The measured pulsed traces are shown in the left-hand-side inset of Fig. 3. The BT diodes showed sub-nanosecond responsivity in a similar manner as the BT diodes developed previously of InGaAs-material [15].

The responsivity spectrum of the BT diodes was measured using the monochromatic radiation of a frequency-domain THz spectrometer TeraScan 780 (*Toptica, Inc.*). The THz beam was electrically modulated at 500 Hz and detected with a lock-in amplifier. The collimating and focusing optics were the same as described previously. The peak THz power of this source was found to be at around the 100 GHz frequency with a value of about  $1\ \mu\text{W}$ , and the sensitivity of developed BT diodes was sufficient to record such power levels.

The normalized responsivity spectrum of the BT diode with a  $2\ \mu\text{m}$  wide apex is shown in Fig. 4. The results obtained using a Gunn oscillator and VDI multiplier chains are also shown by dots. As seen, the data obtained from both experiments show a good agreement. To study the dynamic range of the BT diodes, we gradually attenuated the THz power and measured the resulting voltage signal. The detected signal grew linearly with the power across the range of about 6 orders of magnitude.

The NEP of the detectors is defined as the ratio between the voltage noise and the responsivity. The data of NEP for the AlGaIn/GaN BT diodes are shown in the inset of Fig. 4. For the unbiased operation, only the thermal noise is considered which is relatively low in the AlGaIn/GaN diodes since a high 2D electron density leads to low resistivity values. The NEP dependence on the apex width was found to be relatively weak. The lowest NEP values were obtained at frequencies close to the resonance of BT antenna, with values down to  $2\ \text{nW}/\sqrt{\text{Hz}}$  at an apex width of  $2\ \mu\text{m}$ .

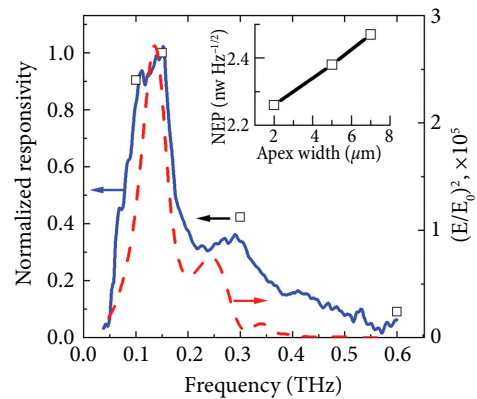


Fig. 4. Responsivity of the BT diode: a solid line shows frequency domain spectroscopy data, dots are the characterization at specific frequencies delivered by Gunn oscillator and frequency multiplier chains, and a dashed line shows the calculated electric field enhancement factor. Apex width of the BT diode is  $2\ \mu\text{m}$ . Inset: NEP of bow-tie diodes at 150 GHz versus apex width.

Finite-difference time-domain simulations were used to find the electric field amplitude distribution in the plane of the BT diode close to the resonant frequency of the THz antenna. The typical results are shown in Fig. 5. In the inset, the colour coding of electric field amplitudes is used to present data. The surface electric field at the antenna apex was calculated modelling a gold on GaN substrate attached to a silicon lens. For comparison, we plot the square of the electric field enhancement factor, assuming that the electron temperature is proportional to the squared electric field amplitude. The results are shown in Fig. 4.

Comparing the experimental and calculated spectra, one can see that the fundamental resonance of the BT antenna is at the frequency of about 150 GHz. The second resonance is observed in the spectrum slightly below 300 GHz. A reasonable agreement between the measured and calculated spectra is achieved; however, the measured responsivity peak was a bit wider, and the second-order resonance was noticeably attenuated compared to the spectrum of the calculated electric field intensity. A possible explanation could be losses introduced by bond wire connections, which are not taken into account in the calculations.

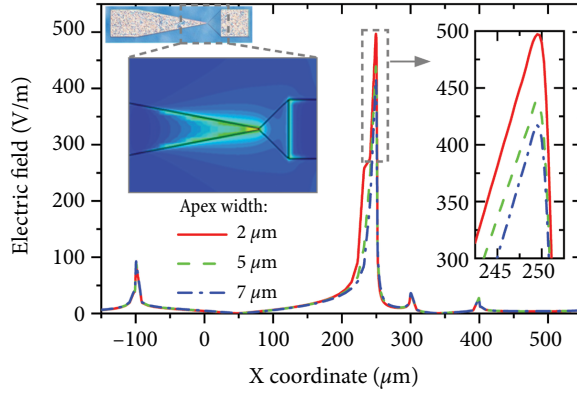


Fig. 5. Modelled surface electric field distributions for the BT diodes with different apex widths. Insets show the characteristic 2D surface electric field distribution and the enlarged plot area near the maximum electric field values.

As seen from Fig. 5, the asymmetric geometry of the BT antenna leads to a strong localization of the THz electric field in the vicinity of the apex and antenna tip. Because of the asymmetry in the carrier temperature, the carrier diffusion brings the charge carriers from the hotter to the colder part of the tapered leaf. As a result, the voltage signal appears at the ends of the BT diode contacts, eliminating the need for an external bias. The direction of the diffusion current is found to be in accordance with the polarity of the signal corresponding to the thermoelectric force of hot electrons [9, 12]. The metallized contacts serve as planar antenna for the normally incident THz wave polarized along the geometric axis of the BT diode. Dimensions of the tapered electrodes result in the resonance at 150 GHz frequency, at which incident radiation is effectively concentrated into the semiconductor. It is worth noting that the response spectrum of the asymmetric BT antenna was recorded for the first time (see Fig. 4), revealing significantly different frequency characteristics from those of the InGaAs-BT diodes, the results of which will be reported elsewhere. A possible reason could be the difference in shaping of the BT diode electrodes fabricated (see Fig. 1(a)) from those described in Refs. [13, 14].

As expected, the narrowing of the diode apex leads to the enhancement of electric field concen-

tration in the metallized leaf tip and apex area (inset of Fig. 5), resulting in the increase of responsivity values (Fig. 3). It is worth to note that the asymmetric shaping of the 2DEG channel can also lead to another detection mechanism, the bi-gradient electromotive force [9].

In general, the response of the hot carrier detector begins to decrease as the detected frequency approaches the inverse of the momentum relaxation time  $\tau_p$  [8]. The measured Drude conductivity of 2DEG in the AlGaIn/GaN structures at room temperature revealed that the carrier relaxation time at low electric field was about 0.3 ps [25]. This suggests that the theoretical cut off frequency for BT diodes could be about 1 THz.

The noise investigations are often used for a more detailed assessment of the quality of THz detector and materials. The results of low-frequency noise measurements at different bias voltages are shown in Fig. 6. The noise spectral density dependence on bias voltage is asymmetric similarly to the current-voltage characteristic (see also Fig. 2). The noise intensity is lowest at the zero bias (see the inset in Fig. 6). The noise spectra of the investigated structures comprise the  $1/f$  fluctuations with the appearance of some Lorentzian type spectral components at specific temperature values. Low frequency noise characteristics of AlGaIn/GaN BT diodes in the temperature range from 78 to 338 K revealed the influence of the defects as

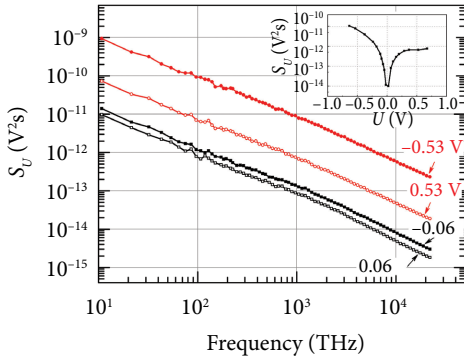


Fig. 6. Voltage noise spectral density at selected bias voltages and the noise spectral density dependence on bias at 1 kHz (in the inset) for the GaN BT diode.

charge carrier capturing centres to the THz detector operation [30]. For the unbiased operation of AlGaIn/GaN BT diodes, only thermal noise needs to be considered, the value of which is relatively low since a high 2DEG density enables low resistivity values.

The microwave noise of the BT diodes and the selected TLM test structures fabricated on the same AlGaIn/GaN sample was investigated using high-frequency measurement setups discussed elsewhere [27]. The excess noise temperature of electrons was measured versus the current density, the values of which were obtained by normalizing the measured charge current to the apex width of BT diode. The results are shown in Fig. 7. The BT diodes demonstrate the asymmetrical behaviour of microwave noise dependent on the bias polarity. The results differed from the characteristics of the rectangular 2DEG layers (TLM resistors), which are shown in Fig. 7 for simplicity with only one polarity. We found that heating of 2D electrons in the BT diode operating in the reverse bias regime is comparable to 2DEG heating in the rectangular shape layer of larger area equipped with large ohmic contacts. Meanwhile, the electron heating was found to be smaller in the BT diode when it operates in the forward bias configuration.

One should note that the BT diodes made of a high electron mobility InGaAs layer [13, 14] showed a similar sensitivity, but the resistance of the samples was more than an order of magnitude larger. The high conductivity of 2DEG channel ena-

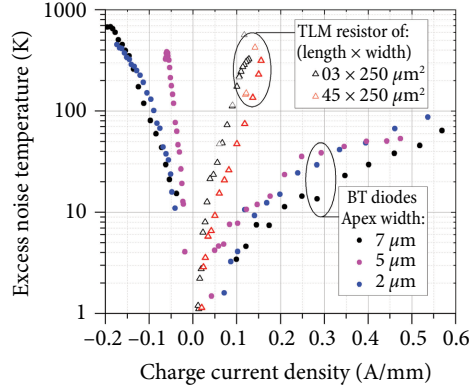


Fig. 7. Excess noise temperature of electrons in the BT diodes with different apex widths (filled-circular symbols) and in the rectangular TLM resistor sample of different indicated size (open-triangular symbols) as a function of charge current density (current normalized to the electrode width).

bles narrowing of the diode apex while maintaining a low diode resistance.

The diode sensitivity at frequencies higher than the fundamental resonance frequency of the BT antenna was found to be almost independent on the apex size. Namely, at 300 GHz frequency, the BT diodes with apexes of 2, 5 and 7  $\mu\text{m}$  demonstrated the average responsivity values of about 1.0, 1.0 and 0.6 V/W, respectively. While at 600 GHz, the sensitivity of BT diodes dropped by another factor of 3 without the pronounced dependence on the apex size. The averaged NEP value of various BT diodes at 300 and 600 GHz frequencies were found at the level of about 10 and 70 nW/ $\sqrt{\text{Hz}}$ , respectively.

Although the NEP values of BT diodes are still inferior to those of the state-of-the-art Schottky diodes, FMB diodes and TeraFET detectors [5, 20, 31], from a technological point of view, the fabrication technology of BT diodes is less demanding. Furthermore, the AlGaIn/GaN BT diodes are expected to have an outstanding chemical and physical stability and electrostatic robustness due to the material properties of gallium nitride. While the narrowing of the diode apex leads to the increased sensitivity, we observe that NEP changes very little, since with decreasing the apex width, the total resistance of the BT diode increases. This

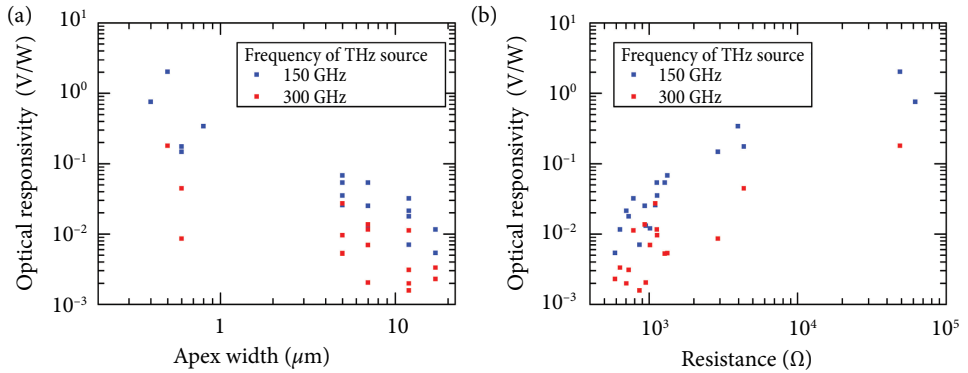


Fig. 8. Responsivity dependence on the apex width (a) and resistance (b) of the BT diode at 150 and 300 GHz frequencies.

suggests that the performance improvement is possible by varying the sheet conductivity of 2DEG layer and by using a different configuration of THz antenna.

Finally, several sets of BT diodes with different apex widths were developed and investigated at the close to resonance frequency of BT antenna in order to obtain more data for statistical analysis. In particular, the planar BT diodes on AlGaIn/GaN HEMT structures were developed considering the variation of apex width from 17 μm down to 0.4 μm [28]. The proposed planar technology is expected to be more suitable for reaching a high range of the THz spectrum as dimensions of the BT diodes can be further scaled down. The optical responsivity dependence on the apex width and the resistance for a number of BT diodes on one chip was measured in the same configuration. The results are shown in Fig. 8. One can see a strong correlation between the resistance and the responsivity values of the BT diode, which depends very little on frequency. Moreover, the responsivity of the BT diode scales nonlinearly with its resistance at values larger than approximately 1000 Ω. Thus, in applications which require low NEP values, tapering the diode apex below a few microns could be ineffective.

#### 4. Conclusions

The BT diodes based on asymmetrically shaped AlGaIn/GaN heterostructures with a 2DEG conductivity layer have been investigated as room tem-

perature THz detectors operating in the unbiased mode, preferable for practical applications. Sensitive THz detection was demonstrated by the diodes with an obvious asymmetry of *IV* characteristics, which was found to be more pronounced with the decrease of apex width. The responsivity and NEP at the fundamental antenna frequency of 150 GHz were up to 4 V/W and down to 2 nW/√Hz, respectively. Such high sensitivity of BT diodes allowed us to measure for the first time the response spectrum of the asymmetric BT antenna demonstrating fundamental and higher order resonances in good agreement with finite-difference time-domain simulation data in a broad spectrum range. The measured low- and high-frequency noise characteristics of the AlGaIn/GaN BT diodes provide new results about electron heating in the BT diode detector and the unbiased operation for which only thermal noise needs to be considered. Moreover, we observed that the responsivity of the BT diode scales nonlinearly with its resistance, demonstrating that the tapering of the diode apex below the range of a few micrometres could be ineffective in applications which require low NEP values.

#### Acknowledgements

The authors are sincerely grateful to J. Malakauskaitė and V. Jakštas for their assistance in the sample fabrication, and to P. Prystawko, R. Venckevičius and G. Valušis for fruitful discussions of various aspects of the research. This

work was supported by the Research Council of Lithuania through the ‘T-HP’ Project (Grant No. DOTSUT-184) funded by the European Regional Development Fund according to the supported activity ‘Research Projects Implemented by World-class Researcher Groups’ under Measure No. 01.2.2-LMT-K-718-03-0096.

## References

- [1] G. Valušis, A. Lisauskas, H. Yuan, W. Knap, and H.G. Roskos, Roadmap of Terahertz Imaging 2021, *Sensors* **21**, 4092 (2021), <https://doi.org/10.3390/s21124092>
- [2] *THz Communications*, eds. T. Kürner, D.M. Mittleman and T. Nagatsuma (Springer International Publishing, Cham, 2022), <https://doi.org/10.1007/978-3-030-73738-2>
- [3] L. Minkevičius, V. Tamošiunas, K. Madeikis, B. Voisiat, I. Kašalynas, and G. Valušis, On-chip integration of laser-ablated zone plates for detection enhancement of InGaAs bow-tie terahertz detectors, *Electron. Lett.* **50**, 1367–1369 (2014), <https://doi.org/10.1049/el.2014.1893>
- [4] S. Goossens, G. Navickaite, C. Monasterio, S. Gupta, J.J. Piqueras, R. Pérez, G. Burwell, I. Nikitskiy, T. Lasanta, T. Galán, et al., Broadband image sensor array based on graphene-CMOS integration, *Nat. Photonics* **11**, 366–371 (2017), <https://doi.org/10.1038/nphoton.2017.75>
- [5] R. Yadav, F. Ludwig, F.R. Faridi, J.M. Klopff, H.G. Roskos, S. Preu, and A. Penirschke, State-of-the-art room temperature operable zero-bias Schottky diode-based terahertz detector up to 5.56 THz, *Sensors* **23**, 3469 (2023), <https://doi.org/10.3390/s23073469>
- [6] C. Liu, L. Wang, X. Chen, A. Politano, D. Wei, G. Chen, W. Tang, W. Lu, and A. Tredicucci, Room-temperature high-gain long-wavelength photodetector via optical-electrical controlling of hot carriers in graphene, *Adv. Opt. Mater.* **6**, 1800836 (2018), <https://doi.org/10.1002/adom.201800836>
- [7] D. Seliuta, J. Vyšniauskas, K. Ikamas, A. Lisauskas, I. Kašalynas, A. Reklaitis, and G. Valušis, Symmetric bow-tie diode for terahertz detection based on transverse hot-carrier transport, *J. Phys. D* **53**, 275106 (2020), <https://doi.org/10.1088/1361-6463/ab831d>.
- [8] A.M. Cowley and H.O. Sorensen, Quantitative comparison of solid-state microwave detectors, *IEEE Trans. Microw. Theory Tech.* **14**(12), 588–602 (1966), <https://doi.org/10.1109/TMTT.1966.1126337>
- [9] A. Sužiedelis, J. Gradauskas, S. Ašmontas, G. Valušis, and H.G. Roskos, Giga- and terahertz frequency band detector based on an asymmetrically necked n-n+-GaAs planar structure, *J. Appl. Phys.* **93**, 3034–3038 (2003), <https://doi.org/10.1063/1.1536024>
- [10] X. Cai, A.B. Sushkov, R.J. Suess, M.M. Jadidi, G.S. Jenkins, L.O. Nyakiti, R.L. Myers-Ward, S. Li, J. Yan, D.K. Gaskill, T.E. Murphy, H.D. Drew, and M.S. Fuhrer, Sensitive room-temperature terahertz detection via the photothermoelectric effect in graphene, *Nat. Nanotechnol.* **9**, 814–819 (2014), <https://doi.org/10.1038/nnano.2014.182>
- [11] L. Vicarelli, M.S. Vitiello, D. Coquillat, A. Lombardo, A.C. Ferrari, W. Knap, M. Polini, V. Pellegrini, and A. Tredicucci, Graphene field-effect transistors as room-temperature terahertz detectors, *Nat. Mater.* **11**, 865–871 (2012), <https://doi.org/10.1038/nmat3417>
- [12] R.I. Harrison and J. Zucker, Hot-carrier microwave detector, *Proc. IEEE*, **54**(4), 588–595 (1966), <https://doi.org/10.1109/PROC.1966.4778>
- [13] D. Seliuta, I. Kašalynas, V. Tamošiunas, S. Balauskas, Z. Martunas, S. Ašmontas, G. Valušis, A. Lisauskas, H.G. Roskos, and K. Köhler, Silicon lens-coupled bow-tie InGaAs-based broadband terahertz sensor operating at room temperature, *Electron. Lett.* **42**, 825–827 (2006), <https://doi.org/10.1049/el:20061224>
- [14] I. Kašalynas, R. Venckevičius, D. Seliuta, I. Grigelionis, and G. Valušis, InGaAs-based bow-tie diode for spectroscopic terahertz imaging, *J. Appl. Phys.* **110**, 114505 (2011), <https://doi.org/10.1063/1.3658017>
- [15] I. Kašalynas, D. Seliuta, R. Simniškis, V. Tamošiunas, K. Köhler, and G. Valušis, Terahertz imaging with bow-tie InGaAs-based diode with broken symmetry, *Electron. Lett.* **45**, 833–835 (2009), <https://doi.org/10.1049/el.2009.0336>

- [16] L. Minkevičius, V. Tamošiūnas, I. Kašalynas, D. Seliuta, G. Valušis, A. Lisauskas, S. Boppel, H.G. Roskos, and K. Köhler, Terahertz heterodyne imaging with InGaAs-based bow-tie diodes, *Appl. Phys. Lett.* **99**, 131101 (2011), <https://doi.org/10.1063/1.3641907>
- [17] D. Seliuta, E. Širmulis, V. Tamošiūnas, S. Balakauskas, S. Ašmontas, A. Sužiedėlis, J. Gradauskas, G. Valušis, A. Lisauskas, H.G. Roskos, and K. Köhler, Detection of terahertz/sub-terahertz radiation by asymmetrically-shaped 2DEG layers, *Electron. Lett.* **40**, 631 (2004), <https://doi.org/10.1049/el:20040412>
- [18] L. Minkevičius, V. Tamošiūnas, M. Kojelis, E. Žąsinas, V. Bukauskas, A. Šetkus, R. Butkutė, I. Kašalynas, and G. Valušis, Influence of field effects on the performance of InGaAs-based terahertz radiation detectors, *J. Infrared Millim. Terahertz Waves* **38**, 689–707 (2017), <https://doi.org/10.1007/s10762-017-0382-1>
- [19] S. Ašmontas, M. Anbinderis, A. Čerškus, J. Gradauskas, A. Sužiedėlis, A. Šilėnas, E. Širmulis, and V. Umansky, Gated bow-tie diode for microwave to sub-terahertz detection, *Sensors* **20**, 829 (2020), <https://doi.org/10.3390/s20030829>
- [20] H. Ito and T. Ishibashi, Low-noise terahertz-wave detection by InP/InGaAs Fermi-level managed barrier diode, *Appl. Phys. Express* **9**, 092401 (2016), <https://doi.org/10.7567/APEX.9.092401>
- [21] Y. Qu, W. Zhou, J. Tong, N. Yao, X. Xu, T. Hu, Z. Huang, and J. Chu, High sensitivity of room-temperature sub-terahertz photodetector based on  $\text{In}_{0.53}\text{Ga}_{0.47}\text{As}$  material, *Appl. Phys. Express* **11**, 112201 (2018), <https://doi.org/10.7567/APEX.11.112201>
- [22] S. Nadar, M. Zaknounge, X. Wallart, C. Coinon, E. Peytavit, G. Ducournau, F. Gamand, M. Thirault, M. Werquin, S. Jonniau, N. Thouvenin, C. Gaquiere, N. Vellas, and J.-F. Lampin, High performance heterostructure low barrier diodes for sub-THz detection, *IEEE Trans. Terahertz Sci. Technol.* **7**, 780–788 (2017), <https://doi.org/10.1109/TTHZ.2017.2755503>
- [23] M. Lee, L.N. Pfeiffer, and K.W. West, Ballistic cooling in a wideband two-dimensional electron gas bolometric mixer, *Appl. Phys. Lett.* **81**, 1243–1245 (2002), <https://doi.org/10.1063/1.1500429>
- [24] V. Palenskis, L. Minkevičius, J. Matukas, D. Jokubauskis, S. Pralgauskaitė, D. Seliuta, B. Čechavičius, R. Butkutė, and G. Valušis, InGaAs diodes for terahertz sensing—effect of molecular beam epitaxy growth conditions, *Sensors* **18**, 1–15 (2018), <https://doi.org/10.3390/s18113760>
- [25] D. Pashnev, V.V. Korotyeyev, J. Jorudas, A. Urbanowicz, P. Prystawko, V. Janonis, and I. Kasalynas, Investigation of electron effective mass in AlGaIn/GaN heterostructures by THz spectroscopy of Drude conductivity, *IEEE Trans. Electron Devices* **69**, 3636–3640 (2022), <https://doi.org/10.1109/TED.2022.3177388>
- [26] J.K. Choi, V. Mitin, R. Ramaswamy, V.A. Pogrebnyak, M.P. Pakmehr, A. Muravjov, M.S. Shur, J. Gill, I. Mehdi, B.S. Karasik, and A.V. Sergeev, THz hot-electron micro-bolometer based on low-mobility 2-DEG in GaN heterostructure, *IEEE Sens. J.* **13**, 80–88 (2013), <https://doi.org/10.1109/JSEN.2012.2224334>
- [27] E. Šermukšnis, J. Jorudas, A. Šimukovič, V. Kovalevskij, and I. Kašalynas, Self-heating of annealed Ti/Al/Ni/Au contacts to two-dimensional electron gas in AlGaIn/GaN heterostructures, *Appl. Sci.* **12**, 11079 (2022), <https://doi.org/10.3390/app122111079>
- [28] J. Jorudas, J. Malakauskaite, L. Subacius, V. Janonis, V. Jakstas, V. Kovalevskij, and I. Kasalynas, Development of the planar AlGaIn/GaN bow-tie diodes for terahertz detection, in: *Proceedings of the 2019 44th International Conference on Infrared, Millimeter, and Terahertz Waves* (IEEE, 2019) pp. 1–2, <https://doi.org/10.1109/IRMMW-THz.2019.8873816>
- [29] J. Jorudas and I. Kasalynas, Terahertz responsivity of AlGaIn/GaN bow-tie diode detectors at the temperatures of 295 K and 80 K, in: *Proceedings of the 2022 47th International Conference on Infrared, Millimeter, and Terahertz Waves* (IEEE, 2022) pp. 1–2, <https://doi.org/10.1109/IRMMW-THz50927.2022.9895472>
- [30] S. Pralgauskaitė, J. Matukas, E. Kazukauskas, I. Kašalynas, V. Janonis, and P. Prystawko, Low

frequency noise spectroscopy of GaN bow-tie THz detectors, in: *Proceedings of the 25th International Conference on Noise Fluctuations (ICNF 2019)*, ed. C. Enz (ICLAB, Neuchâtel, Switzerland, 2019), <https://doi.org/10.5075/epfl-ICLAB-ICNF-269187>

[31] M. Bauer, A. Ramer, S.A. Chevtchenko, K.Y. Osipov, D. Cibiraite, S. Pralgauskaite, K. Ikamas,

A. Lisauskas, W. Heinrich, V. Krozer, and H.G. Roskos, A high-sensitivity AlGaIn/GaN HEMT terahertz detector with integrated broadband bow-tie antenna, *IEEE Trans. Terahertz Sci. Technol.* **9**, 430–444 (2019), <https://doi.org/10.1109/TTHZ.2019.2917782>

## ASIMETRIŠKAI SUSIAURINTŲ AlGaIn/GaN HETEROSTRUKTŪRŲ PETELIŠKĖS TIPO DIODAI TERAHERCINIAMI DAŽNIŲ RUOŽIUI

J. Jorudas <sup>a</sup>, D. Seliuta <sup>a</sup>, L. Minkevičius <sup>a</sup>, V. Janonis <sup>a</sup>, L. Subačius <sup>a</sup>, D. Pashnev <sup>a</sup>, S. Pralgauskaitė <sup>a</sup>, J. Matukas <sup>a</sup>, K. Ikamas <sup>b</sup>, A. Lisauskas <sup>b</sup>, E. Šermukšnis <sup>c</sup>, A. Šimukovič <sup>c</sup>, J. Liberis <sup>c</sup>, V. Kovalevskij <sup>d</sup>, I. Kašalynas <sup>a,b</sup>

<sup>a</sup> Fizinijų ir technologijos mokslų centro Terahercų fotonikos laboratorija, Vilnius, Lietuva

<sup>b</sup> Vilniaus universiteto Taikomosios elektrodinamikos ir telekomunikacijų institutas, Vilnius, Lietuva

<sup>c</sup> Fizinijų ir technologijos mokslų centro Fliuktuacinių reiškinių laboratorija, Vilnius, Lietuva

<sup>d</sup> Fizinijų ir technologijos mokslų centro Eksperimentinės branduolio fizikos laboratorija, Vilnius, Lietuva

### Santrauka

Asimetriškai susiaurintos AlGaIn/GaN heterostruktūros su laidžiu dvimačių elektronų dujų (2DEG) sluoksniu panaudotos sukurti peteliškės tipo (BT) diodus, tinkančius terahercinio dažnių ruožo (THz) bangoms registruoti kambario temperatūroje. Atsižvelgiant į tai, kad be išorinės postūmio įtampos THz BT diodo veikimas yra labiau tinkamas praktiniams taikymams, ištyrėme diodus su didele srovės ir įtampos (*IV*) charakteristikų asimetriją, kuri buvo tuo ryškesnė, kuo mažesnis kakliuko plotis, parodant didelį diodų jautrumą THz bangoms. Krūvininkų kaitinimas metalizuotame diodo lapelyje buvo išskirtas kaip pagrindinis mechanizmas, lemiantis THz bangų lyginimą BT diode. Jautris ir triukšmo ekvivalentinė galia (NEP) ties pagrindiniu antenos dažniu 150 GHz siekė iki 4 V/W ir atitinka-

mai 2 nW/ $\sqrt{\text{Hz}}$ . Toks didelis BT diodų jautrumas leido mums pirmą kartą išmatuoti asimetrinės BT antenos dažninę charakteristiką, stebint pagrindinį ir aukštesnės eilės antenos rezonansus, parodant gerą sutapimą su baigtinių skirtumų laiko skalėje atliktais modeliavimo rezultatais plačiame dažnių ruože. Išsamus AlGaIn/GaN BT diodų žemo ir aukšto dažnio triukšmo charakteristikų tyrimas atskleidė, kad nenaudojant įtampos postūmio reikia atsižvelgti tik į šiluminį triukšmą, kurio vertė buvo santykinai maža dėl didelio 2DEG tankio, lemiančio nedidelę diodo varžą. Taip pat nustatėme, kad BT diodo jautrumas netiesiniu dėsniumi priklauso nuo jo varžos, dėl to diodo kakliuko siaurinimas žemiau kelių mikronų vertės gali būti mažai veiksmingas, kai tikimasi mažų NEP verčių.

**Green Removal of DUV-Polarity-Modified PMMA for Wet Transfer of CVD Graphene**

**J. Jorudas**, D. Pashnev, I. Kašalynas, I. Ignatjev, G. Niaura, A. Selskis,  
V. Astachov, A. Alexeeva

*Nanomaterials*, vol. 12, no. 22, 4017 (2022).

DOI: 10.3390/nano12224017

This is an open access article distributed under the Creative Commons Attribution License (CC-BY).

The article may be accessed online at <https://doi.org/10.3390/nano12224017>





Article

# Green Removal of DUV-Polarity-Modified PMMA for Wet Transfer of CVD Graphene

Justinas Jorudas <sup>1,\*</sup> , Daniil Pashnev <sup>1</sup> , Irmantas Kašalynas <sup>1</sup> , Ilja Ignatjev <sup>2</sup>, Gediminas Niaura <sup>2</sup>, Algirdas Selskis <sup>3</sup>, Vladimir Astachov <sup>4</sup> and Natalia Alexeeva <sup>1,\*</sup>

- <sup>1</sup> THz Photonics Laboratory of Optoelectronics Department, Center for Physical Sciences and Technology (FTMC), Saulėtekis Ave. 3, LT 10257 Vilnius, Lithuania
  - <sup>2</sup> Department of Organic Chemistry, Center for Physical Sciences and Technology (FTMC), Saulėtekis Ave. 3, LT 10257 Vilnius, Lithuania
  - <sup>3</sup> Department of Structural Analysis of Materials, Center for Physical Sciences and Technology (FTMC), Saulėtekis Ave. 3, LT 10257 Vilnius, Lithuania
  - <sup>4</sup> Department of Physical Technologies, Center for Physical Sciences and Technology (FTMC), Saulėtekis Ave. 3, LT 10257 Vilnius, Lithuania
- \* Correspondence: justinas.jorudas@ftmc.lt (J.J.); natalia.alexeeva@ftmc.lt (N.A.)

**Abstract:** To fabricate graphene-based high-frequency electronic and optoelectronic devices, there is a high demand for scalable low-contaminated graphene with high mobility. Graphene synthesized via chemical vapor deposition (CVD) on copper foil appears promising for this purpose, but residues from the polymethyl methacrylate (PMMA) layer, used for the wet transfer of CVD graphene, drastically affect the electrical properties of graphene. Here, we demonstrate a scalable and green PMMA removal technique that yields high-mobility graphene on the most common technologically relevant silicon (Si) substrate. As the first step, the polarity of the PMMA was modified under deep-UV irradiation at  $\lambda = 254$  nm, due to the formation of ketones and aldehydes of higher polarity, which simplifies hydrogen bonding in the step of its dissolution. Modification of PMMA polarity was confirmed by UV and FTIR spectrometry and contact angle measurements. Consecutive dissolution of DUV-exposed PMMA in an environmentally friendly, binary, high-polarity mixture of isopropyl alcohol/water (more commonly alcohol/water) resulted in the rapid and complete removal of DUV-exposed polymers without the degradation of graphene properties, as low-energy exposure does not form free radicals, and thus the released graphene remained intact. The high quality of graphene after PMMA removal was confirmed by SEM, AFM, Raman spectrometry, and by contact and non-contact electrical conductivity measurements. The removal of PMMA from graphene was also performed via other common methods for comparison. The charge carrier mobility in graphene films was found to be up to  $6900 \text{ cm}^2/(\text{V}\cdot\text{s})$ , demonstrating a high potential of the proposed PMMA removal method in the scalable fabrication of high-performance electronic devices based on CVD graphene.



**Citation:** Jorudas, J.; Pashnev, D.; Kašalynas, I.; Ignatjev, I.; Niaura, G.; Selskis, A.; Astachov, V.; Alexeeva, N. Green Removal of DUV-Polarity-Modified PMMA for Wet Transfer of CVD Graphene. *Nanomaterials* **2022**, *12*, 4017. <https://doi.org/10.3390/nano12224017>

Academic Editor: Christian Falconi

Received: 3 October 2022

Accepted: 13 November 2022

Published: 15 November 2022

**Publisher's Note:** MDPI stays neutral with regard to jurisdictional claims in published maps and institutional affiliations.



**Copyright:** © 2022 by the authors. Licensee MDPI, Basel, Switzerland. This article is an open access article distributed under the terms and conditions of the Creative Commons Attribution (CC BY) license (<https://creativecommons.org/licenses/by/4.0/>).

**Keywords:** graphene; DUV; PMMA; THz-TDS

## 1. Introduction

Graphene is a unique material with distinctive characteristics that has shown great potential for a wide range of applications, particularly involving its electronic structure and transport properties [1–3]. The successful isolation of monolayer graphene by mechanical exfoliation performed in 2004 [4] made it possible to achieve electron mobility, at room temperature, of  $\sim 10,000 \text{ cm}^2/(\text{V}\cdot\text{s})$ . In a free-standing graphene layer, the electron mobility can even reach  $200,000 \text{ cm}^2/(\text{V}\cdot\text{s})$  at room temperature, the highest value ever known in pure semiconductors [5,6]. Unfortunately, exfoliation typically produces graphene flakes of only tens of micrometer in size, which is not practical for most applications. Different synthesis processes have been intensively studied to provide a route toward the fabrication of graphene of a quality similar to that of exfoliated graphene, but on

an industrial scale. The fact that the electronic properties of graphene are altered if it is transferred to a substrate [7], and that the charge carrier mobility drops accordingly by orders of magnitude, makes this task really challenging. Chemical vapor deposition (CVD) is among the most utilized synthesis techniques for the manufacture of single-layer graphene on a large substrate [2,3]; however, the choice of substrate is limited to a very small number of transition metals, such as copper or nickel [8–10]. To fabricate graphene-based electronic or optoelectronic devices that require substrates other than these transition metals, additional operations are needed to transfer CVD graphene to the application-compatible substrate [11,12]. This is generally accomplished by dissolving the metal substrate via a wet etching process to release graphene [13–17]. As free-standing graphene is fragile, typically, a supporting layer such as polymethyl methacrylate (PMMA) is used [18,19]. After the transfer process the polymeric transfer agent must be eventually removed via extensive cleaning. However, because PMMA interacts strongly with graphene, complete removal of the PMMA is a difficult task. The residues of PMMA and its products, which are formed during and remain after processing in a solvent, cannot later be removed and will inevitably affect the graphene performance [20,21]. It has been acknowledged by many researchers [22] that the PMMA and its residuals cannot be completely removed by any solvent alone [21], even strong, toxic, and carcinogenic solvents such as anisole [23], acetic acid [24], chlorobenzene [25], and chloroform [26]. Graphene is extremely sensitive to adsorbates and molecules in contact with its surface; hence, the residues tend to act as a dominant source of free charge carriers and scattering centers, suppressing charge transport in graphene [21,27–29]. For example, the carrier mobility of as-prepared CVD graphene,  $10^3$  to  $10^4$   $\text{cm}^2/(\text{V}\cdot\text{s})$ , decreased to  $2 \times 10^2$ – $2.5 \times 10^3$   $\text{cm}^2/(\text{V}\cdot\text{s})$  after the transfer and PMMA removal in acetone [30]. Therefore, thorough removal of the PMMA residues is crucial for improving the electrical and optoelectronic characteristics of graphene-based devices.

Various strategies have been proposed to ensure effective PMMA removal after graphene transfer and preservation of the unique properties of graphene by maintaining its structural integrity [31–33]. One way to overcome incomplete PMMA removal is to reduce the strong interaction of PMMA with graphene by breaking the chain of polymers into lower molecular weight fragments, increasing their solubility as solvent molecules penetrate more easily. Polymer decomposition can be initiated thermally by its depolymerization at 300–400 °C into volatile monomers [34,35] under annealing conditions, including an air, vacuum, or inert atmosphere [36–39]. However, many reports claim that annealing could not completely remove PMMA residues or other contaminants from the graphene surface [22]. Moreover, defects and doping can be introduced into the graphene lattice during the post-annealing process [39]. Polymer decomposition can also be achieved by oxygen plasma treatment [40], which is a standard method of suppressing PMMA residues in the device processing, with the exception of carbon electronics, since it etches carbon material in the form of graphene, damaging it, introducing strains and distorting the graphene lattice, thus causing both topological and chemical defects. It is possible to break the polymer chain into fragments with a lower molecular weight by irradiating it, which leads to so-called PMMA degradation. Various radiation sources with high energy, such as gamma rays, X-rays, electron beams, proton beams, and ion beams, are used for this purpose [25,41–44]. However, along with chain scission, another chemical reaction occurs at larger doses, known as crosslinking, which reduces solubility. The resulting net effect on the polymer is determined by the dominance of one reaction over the other [42]. In addition, defects in graphene can be generated if high radiation doses are used. Moreover, the low-electric field electron mobility, achieved using the techniques described earlier, remains mainly at the level of  $3 \times 10^3$ – $4 \times 10^3$   $\text{cm}^2/(\text{V}\cdot\text{s})$ , which until now was the upper limit of the devices fabricated of CVD-grown graphene [45].

In order to ensure the stability of graphene's chemical composition and structure, and achieve reasonable mobility, scientists have turned attention to the degradation of the polymer under relatively mild processing conditions [39]. As early as the 1990s, researchers

have studied the use of deep-ultraviolet (DUV) exposure of PMMA as an alternative to high-energy exposure methods [46,47], demonstrating that mainly the main-chain scissions occur in PMMA during the exposure of polymer to light with wavelengths shorter than 320 nm. Deep-UV exposure with a wavelength of 254 nm is relatively mild compared to other PMMA exposure techniques, which allows one to ensure the integrity of graphene [25,48]. Furthermore, the DUV method excels in terms of simplicity and cost-effectiveness because DUV of 254 nm can be produced using inexpensive low-pressure mercury vapor lamps [25] or UV-C light emitting diodes, which currently are developing rapidly for germicidal applications [49]. A few papers have reported different UV treatment methods already, showing good cleaning [12,22,25,50,51] of DUV-exposed PMMA by acetone, as a liquid [25] or a vapor [52], and by methyl isobutyl ketone (MIBK) mixed or unmixed with IPA [51]. A clean, uniform, and continuous graphene, with typical low sheet resistance and improved contact between graphene and electrodes, was obtained following DUV exposure [25]. However, the aforementioned solvents themselves introduce additional *p*-doping into graphene, changing its electrical properties in an undesirable way.

On the other hand, regarding the quality of graphene detected after the removal of PMMA, an aqueous solution of isopropyl alcohol (IPA) looks promising as a solvent, since by its nature it does not introduce additional residuals that dope graphene, as it can be seen after using other solvents for PMMA removal [53]. The aqueous mixture of IPA, a binary polar solvent, in a certain range of relative concentrations, was introduced in 1988 [54], and it was shown to be an excellent developer for PMMA [55], exposed to an electron beam [55–57] or X-ray radiation [44,58], when used as a positive resist in e-beam lithography for the micro- and nanoelectronics. In general, such IPA/water solution has found its wide applications in many areas, as personal care, biomedical, e.g., drug delivery [59] and in principle, mixtures of various alcohols with water can be used [60]. Another important advantage of the aqueous alcohol solvent is non-toxicity. Global production of chemicals has increased fiftyfold since 1950 and is projected to triple again by 2050 compared to 2010 [61]. Humanity is currently operating outside the planetary boundary based on the weight-of-evidence for several of the control variables established by scientists [62]. Under these conditions, reducing the burden of chemicals on the environment in general is becoming critical. Unlike acetone, chloroform, anisole, toluol, MIBK, traditionally used to dissolve PMMA, alcohol-water solvents have much less environmental impact or no effect in the case of ethanol and look very appealing.

In this work, we propose a new approach for the efficient removal of the DUV-exposed PMMA from the surface of wet transferred CVD graphene. Traditionally, the removal of the PMMA film during wet transferring of the CVD graphene implies the dissolution of the polymer (a chain of compounds of the ester type) or the MMA monomer, after thermal or radiational decomposition, with solvents such as acetone (refers to the type of ketones). We propose here to modify this scheme by dissolving the DUV-exposed PMMA with a binary polar solvent of isopropyl alcohol and water. We show that complete dissolution of PMMA is achieved on CVD graphene. As far as we know, the investigation of modification in the polarity of the PMMA under the action of DUV [46–48] as well as the mechanism of aqueous isopropyl alcohol advantages as a solvent of the PMMA [59,63] were carried out but independently of each other. The novelty of this work is related to analysis of the mechanism of joint action of these two factors on complete removal of DUV-exposed PMMA from CVD graphene in wet transfer process. Scanning electron microscopy (SEM) and atomic force microscopy (AFM) images, Raman spectra and electrical properties of CVD graphene after PMMA removal were investigated and compared with the samples where PMMA was dissolved using other commonly used solvents such as acetone and chloroform. The proposed new approach is environmentally friendly and does not introduce additional damage to graphene. Regarding impact on environment, the proposed approach uses a low-pressure mercury lamp as a source of DUV radiation, while mercury is known to be a toxic metal that affects public health and the environment [64] through bioaccumulation, which can harm humans in various ways [65]. We have used this source for only academic

purposes to clearly compare with previous research. We suggest to use UV LEDs as a source that does not contain toxic mercury and have many advantages in terms of energy consumption, lifetime, and compactness [49,66].

## 2. Materials and Methods

To investigate the effects of DUV exposure on PMMA, 996 K molar mass PMMA (Sigma-Aldrich, St. Louis, MO, USA) layers were prepared by spin coating a 4% PMMA solution (0.53 g/10 mL) in anisole (99%, Cole-Parmer, Vernon Hills, IL, USA) to the desired substrate and drying at 180 °C resulting in PMMA film of about 250 nm. For various experimental investigations we have used different substrates. The pristine and DUV-exposed PMMA samples were prepared on a 2 mm-thick fused silica substrates (Eksma Optics, Vilnius, Lithuania) for the investigation of absorbance spectra in UV spectrum range using a UV/VIS spectrometer (Perkin Elmer Lambda 25, Waltham, MA, USA) in the transmission geometry. Changes in IR absorbance in PMMA after DUV exposure were investigated using the FTIR spectrometer (Bruker Vertex v80, Ettlingen, Germany) in the transmission geometry with 1 mm aperture in a vacuum environment with PMMA samples on CaF<sub>2</sub> substrates of 1 mm thickness (Eksma Optics, Vilnius, Lithuania). To expose PMMA to DUV we have employed commercial crosslinker (Spectronics Corporation XL-1000 UV spectrolinker, Melville, NY, USA) equipped with 254 nm illumination source (UVC Philips TUV T5 lamps), with exposure time of 8 h at the distance between a source and a sample of 16 cm. To characterize the change in the polarity of the exposed PMMA, the optical contact angle meter (KSV Instruments KSV CAM-101, Espoo, Finland) was used to assess the degree of hydrophilicity of the surface.

Finally, sets of graphene samples were prepared for a proof-of-concept of the proposed approach by taking a commercial monolayer CVD graphene synthesized on a copper foil with protective PMMA coating (Graphenea, San Sebastián, Spain) and transferring it on float zone high resistivity (HR) (>10 kΩ·cm) silicon wafers (Microchemicals, Ulm, Germany). The IPA (≥99.5%, Sigma-Aldrich, St. Louis, MO, USA), acetone (≥99.5%, Chempur, Karlsruhe, Germany) and chloroform (≥99.0%, VWR Chemicals, Radnor, PA, USA) were used as solvents. The quality of the prepared graphene samples was determined by optical microscopy, SEM, atomic force microscopy (AFM), Raman spectroscopy, THz time-domain spectroscopy (TDS), and Hall effect measurements. Scanning electron microscopy images were obtained using secondary electrons at 2 kV and 25 pA beam current in a dual-beam system (FEI Helios Nanolab 650, Hillsboro, OR, USA). The conductive microscopy was performed using scanning probe microscope system (Bruker Dimension 3100, Ettlingen, Germany). Sample bias was set to value of 20 mV using tunneling AFM (TUNA) module under ambient conditions. For these measurements the PtIr cantilever, 300 μm length and 0.8 N/m spring constant (type RMN-12PT300B) was used. The samples were characterized by a Raman spectrometer (Renishaw inVia, Wotton-under Edge, UK) using a 1800 lines/mm grating, a microscope equipped with a 50×/0.8 NA objective, and a continuous-wave 532 nm excitation laser operating at a power of 0.6 mW. The beam was focused to the size of a spot with a diameter of 0.8 μm on the sample surface. The position of the Raman spectrum bands on the wavenumber axis was calibrated by a silicon peak at 520.7 cm<sup>-1</sup>. For each sample, 10 spectra were recorded with an integration time of 60 s and used for statistical analysis. The electrical characteristics of graphene were investigated using contactless optical and contact methods. For optical contactless characterization, terahertz time-domain spectroscopy (THz-TDS) was performed with the commercial THz-TDS spectrometer (Teravil T-SPEC 800, Vilnius, Lithuania) in the transmission geometry of a focused beam with a spot size around 2–3 mm. Since THz-TDS measurements only provide information about the conductance of the graphene sheet, contact Hall measurements in a 0.5 T magnetic field (Ecopia HMS-3000, Anyang, Republic of Korea) were also carried out to gain insight into the doping type of the samples.

### 3. Results

#### 3.1. Mechanism of Solvation of Exposed PMMA

One of the main points of the proposed method is the change in the properties of PMMA, both chemical and physical, when the polymer is exposed to UV radiation. We show that deep-UV irradiation with a wavelength of 254 nm, used for this purpose, leads not only to photodegradation of the polymer due to the main-chain scissions, as occurs with more powerful irradiation sources, but also the appearance of new species, the formation of which is more pronounced in the case of photodegradation at 254 nm.

Since DUV exposure of PMMA takes longer due to the lower energy of irradiation, some products formed after main-chain scissions further absorb UV photons and contribute to the degradation of the polymer by side-chain scissions that are occurring in parallel with the main-chain scissions. As a result, new chemical species are formed, including ketone-type and aldehyde-type carbonyl compounds [47]. To confirm this statement, both pristine and DUV-exposed PMMA was investigated using UV-VIS and FTIR spectroscopy. The changes in UV absorption spectra are shown in Figure 1. Pristine PMMA shows an absorption peak at about 215 nm that, after DUV exposure, becomes more intense and blueshifts out of the range of spectrometer, which makes its exact position hard to evaluate. However, similar behavior was obtained by Shirai et al. [67] using an exposure of 195 nm. Moreover, an absorption band (shoulder) was observed in the pristine PMMA at  $\lambda = 275$  nm, which is attributed to the carbonyl group in the ester side chain. This feature coincides with that obtained by Torikai et al. [47], where exposure of 254 nm from a low-pressure mercury lamp was used. These results indicate the main-chain scissions in the PMMA sample and the formation of new compounds due to side-chain scissions. To investigate whether our DUV illumination introduces free radicals, which are harmful to graphene, we irradiated PMMA in ambient air and argon environments. The UV-VIS spectra for these samples are shown in Figure 1 as red and blue lines, respectively. The fact that they do not show qualitative differences supports the idea that the observed processes are precisely light-induced, and not chemically induced, for example, by ozone generated by DUV source. Since ozone or free radicals are not formed under such irradiation, the released graphene is expected to remain intact, unlike in higher energy PMMA decomposition methods.

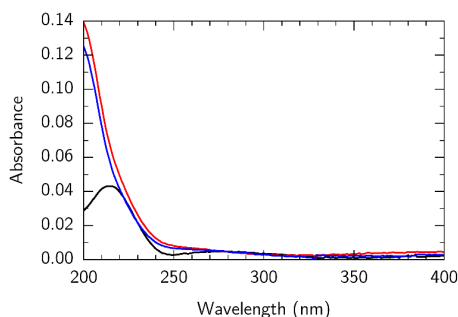


**Figure 1.** Optical absorption spectra of pristine PMMA/quartz (black line), DUV-exposed PMMA/quartz irradiated in air (red line), DUV-exposed PMMA irradiated in argon (blue line). PMMA film thickness, 0.25  $\mu\text{m}$ .

To gain insight into the molecular changes of DUV exposure induced in PMMA film, we performed an analysis of FTIR transmission spectra (Figure 2). The dominant absorption bands are associated with the C–H stretching of  $\text{CH}_3$  and  $\text{CH}_2$  groups (2845, 2922, 2951, and 2992  $\text{cm}^{-1}$ ), C=O stretching (1729  $\text{cm}^{-1}$ ), and stretching vibration of the C–O–C group (1148 and 1193  $\text{cm}^{-1}$ ). The vibrational spectrum of PMMA has been analyzed in detail in

previous publications [68–74]. The difference spectrum reveals the appearance of radiation-induced new absorption bands (positive-going features) and decrease in relative intensity of PMMA bands due to cleavage of some chemical bonds (negative-going features). In the fingerprint spectral region (800–1450  $\text{cm}^{-1}$ ), the relative intensity of the 1148  $\text{cm}^{-1}$  band associated with the symmetric stretching vibration of the C–O–C group decreases the most, indicating DUV-radiation-induced cleavage of ester bonds. The negative-going feature at 1729  $\text{cm}^{-1}$  due to the C=O stretching vibration of the ester group confirms this scenario. In the C–H stretching vibration spectral region, one can find direct evidence of radiation-induced destruction of  $\text{CH}_2$  groups, as two intense negative-going bands at 2851 and 2919  $\text{cm}^{-1}$ , associated with symmetric and asymmetric stretching vibrations of the methylene group, respectively, appear in the difference spectrum. In addition, the negative-going band, due to  $\text{CH}_2$  scissoring deformation vibration, is visible near 1486  $\text{cm}^{-1}$ . These spectral changes indicate cleavage in the vicinity of the  $-\text{CH}_2-$  moiety (main chain). The positive-going feature near 1710  $\text{cm}^{-1}$  reveals the DUV-exposure-induced formation of new species, most likely containing C=O of aldehyde and/or ketone functional groups. The positive-going broad feature near 1618  $\text{cm}^{-1}$  is consistent with the formation of  $\text{sp}^2$ -hybridized carbon bonds, aromatic carboxyl groups, and hydroxyl groups [74]. In addition, positive-going features near 1107 and 1217  $\text{cm}^{-1}$  support the formation of compounds containing C–O bonds or/and hydroxyl groups. Earlier works investigating similar FTIR spectra of DUV-exposed PMMA also concluded that bands of newly produced species were observed in the IR spectrum, and were attributed to ketone-type and aldehyde-type compounds [47].

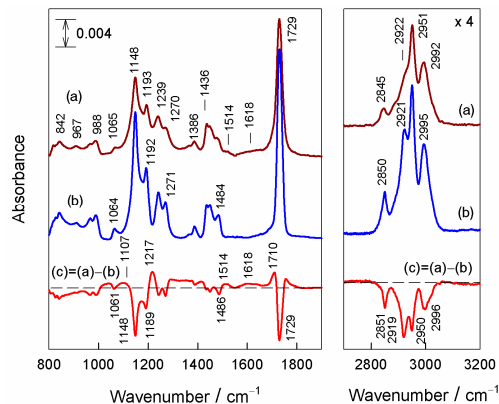


**Figure 2.** Transmission FTIR spectra of (a) DUV-irradiated PMMA/CaF<sub>2</sub> sample and (b) pristine PMMA/CaF<sub>2</sub> sample. The difference of the two spectra is shown as (c). Spectra are shifted vertically for clarity.

Chemical changes in the exposed PMMA structure are manifested in the modification of the physical properties of the final products after the photochemical reaction, specifically in polarity. Namely, the increase in polarity is the first basis of the improved solubility mechanism of PMMA exposed to DUV. After exposure, the newly produced ketone and aldehyde type compounds with a polarity higher than that of the original ester functional group can form H-bonds more efficiently, when acting as an acceptor, namely a carbonyl oxygen acceptor, upon subsequent dissolution.

Assessing the polarity of the material is not an easy task, but the water contact angle has been proven to be directly linked to the polarity of the surface [75]. Contact angle mea-

surement is a qualitative way to evaluate whether the surface is hydrophobic or hydrophilic, which is linked to the intermolecular interactions between the surface and a small drop of water. The evaluation of this value gives a clear indication of the modification in polarity of PMMA under the DUV exposure. The contact angles of PMMA were measured before and after exposure to DUV (Figure 3a). The contact angle measurements confirmed that the DUV exposure modified the surface to be more hydrophilic. The decrease in contact angle from the  $73.1^\circ$  on pristine PMMA to  $60.2^\circ$  on exposed PMMA confirms that the initial products of PMMA (ester functional group) are modified into higher polarity products, presumably ketones and aldehydes.

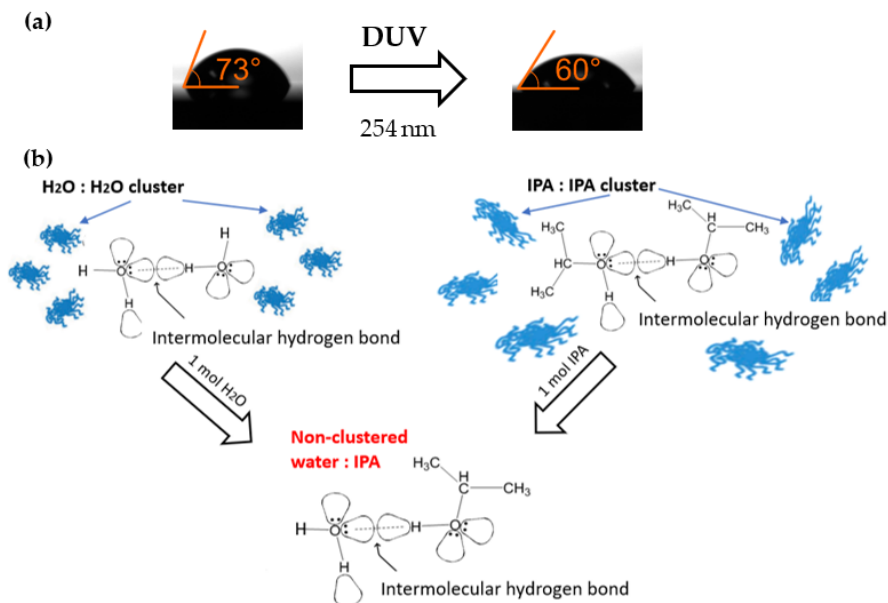


**Figure 3.** (a) Water contact angle on PMMA before (left) and after (right) DUV exposure. Increased hydrophilicity observation corresponds to increasing polarity of new chemical products received after DUV exposure of PMMA. (b) Schematic representation of reconstruction of water: water and IPA: IPA clusters into non-clustered water: IPA mixture to act as an effective solvent, where under specific water: IPA mixture due to formation of hydrogen bonds connect effectively to the polymer.

Since higher polarity products form hydrogen bonds, which are much easier than those of pristine PMMA upon subsequent dissolution, it is expected that this will result in the improved removal of PMMA when using a solvent of suitably high polarity. One could expect that the most effective dissolution will be achieved when the solvent with the highest polarity is used, namely, water (relative polarity 0.998) instead of solvents historically used for this purpose such as acetone ( $C_3H_6O$  0.355), chloroform ( $CHCl_3$  0.259), anisole ( $C_7H_8O$  0.198), or toluene ( $C_7H_8$  0.099). However, it is known that PMMA is practically insoluble in water at ambient temperature [59], since water molecules are highly polar, and they form intermolecular connections, hydrogen-bonded clusters, with other water molecules (Figure 3b). Therefore, they have a small physical surface to effectively interact with PMMA (generally, the host polymer), which leads to the insolubility of the polymer [76]. A similar situation occurs between isopropyl alcohol (IPA), or more generally alcohols,

and organic compounds with polarity higher than ketones and aldehydes. Alcohols, being organic derivatives of water with one hydrogen atom replaced by an alkyl group, are less polar than water, but can also form intermolecular hydrogen bonds with other IPA molecules, as shown in Figure 3b. Thus, IPA itself is also a poor solvent of PMMA. However, when IPA and water are mixed, the breaking of the intermolecular hydrogen bonds in the water and IPA clusters occurs. The energy required to break the bonds comes from the formation of hydrogen bonds between water and the -OH group of the IPA (hydration of the hydroxyl function of the alcohol/IPA by H-bonding). It is expected that the obtained non-clustered water molecules, as shown in the bottom part of Figure 3b, will have more efficient interactions with PMMA through the “localization” mechanism [76,77], leading to increased polymer solubility. Thus, a binary mixture of polar solvents with an equal number of water and IPA molecules for the formation of a water–alcohol hydrogen bond demonstrates an increased solubility of PMMA. For the IPA/water mixture, the 1:1 molar ratio corresponds to the 7:3 volumetric ratio, the exact ratio at which the maximum solubility of PMMA for IPA/water mixtures has been reported previously [55,63]. Overall, the final products formed after DUV exposure to PMMA (aldehyde and ketone groups) have a higher polarity than the pristine PMMA, and a smaller molecular size, which allows them to form hydrogen bonds with IPA/water mixtures more easily.

### 3.2. DUV-Assisted Wet Transfer of Graphene

CVD graphene was transferred onto HR Si substrates using a standard wet transfer procedure using PMMA as a support layer [78,79]. The approach is shown schematically in steps 1–3 in Figure 4a, and with the final steps 4 and 5 referred to later in the text as the proposed “DUV method”. First, a Cu foil is etched away in a dilute room temperature RCA standard cleaning 2 (SC-2) solution of 60:5:2 H<sub>2</sub>O/HCl/H<sub>2</sub>O<sub>2</sub>, adapted from [78]. Then, the translucent PMMA/graphene stack is rinsed thoroughly in DI water and wet transferred to a substrate of choice. The prepared PMMA/graphene samples are first dried in ambient conditions for 20 min, then dried in an oven at 130 °C for 30 min. The thickness of the PMMA film was about 60 nm, according to the manufacturer (Graphenea). The PMMA was removed in steps 4 and 5. We used DUV exposure to modify PMMA, and then IPA/water development, expecting no chemical doping of graphene. Namely, after PMMA was exposed to DUV at 254 nm for 3 h (distance between a source and the sample was 16 cm), it was developed in 7:3 volumetric ratio IPA/water mixture for 30 s and dried with N<sub>2</sub>. The result of the entire procedure of transferring and removing of PMMA is shown in Figure 4b, where a clean graphene sample is visible at a purposefully selected graphene edge area on an HR Si wafer.

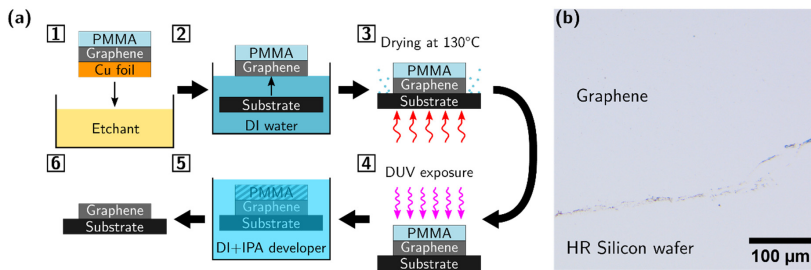


**Figure 4.** (a) Schematic of graphene wet transfer and PMMA removal processing steps. (b) Optical microscope image of graphene edge area.



To compare the discussed method of PMMA removal, additional PMMA/graphene samples were prepared using the same wet transfer process (steps 1–3), but with PMMA removed with common solvents: acetone and chloroform. A total of five samples were prepared: three samples with DUV treatment and development in aqueous IPA (samples DUV1–DUV3), and one sample each for PMMA removal for 18 h at 23 °C with acetone and chloroform, respectively. As a reference, the standard commercially transferred graphene film to SiO<sub>2</sub>/p-Si substrate was also studied. To evaluate the effectiveness of our cleaning procedure, the surfaces of the graphene released with the DUV method and via traditional solvents (chloroform and acetone) were studied via SEM and AFM. SEM images of graphene films prepared by different PMMA removal methods are shown in Figure 5. Comparing the SEM images in Figure 5a–c, graphene processed using chloroform exhibited the highest number of PMMA residuals on the surface. The DUV (Figure 5a) and acetone (Figure 5c) processes showed lower numbers of residuals on the surface.

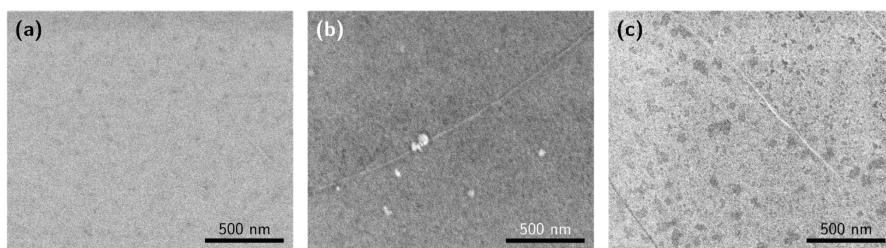


**Figure 5.** SEM images of the graphene films after different PMMA removal methods: (a) DUV exposure and dissolution in IPA/water, (b) dissolution in chloroform, (c) dissolution in acetone.

Figure 6 shows topography and simultaneously obtained tunneling current images. Gwyddion software was used to process the AFM images and to extract the surface roughness. The topographical images are shown in Figure 6a for DUV, Figure 6b for chloroform, and Figure 6c for acetone. The DUV cleaning protocol revealed a flat and homogeneous graphene surface with only occasional wrinkles, similar to samples processed with chloroform (18 h soaking). In Figure 6d–f, conductive areas correspond to the graphene film, while non-conductive zones are either the substrate, residuals of the PMMA, or other contaminants. Profiles A (black lines) in Figure 6g–i represents graphene surfaces that were used to calculate root-mean-square roughness values of 0.26 nm for DUV, 0.30 nm for chloroform, and 0.65 nm for acetone. Profile B (red lines) shows the height of the graphene surface contaminants, which were 13.4 nm for DUV, 18.3 nm for chloroform, and 9.8 nm for acetone. The graphene–substrate distances were estimated from profile C (blue lines) to be around 3.9 nm for DUV and chloroform, but for acetone the distance was approximately twofold larger, at 7.9 nm. These results indicate that DUV and chloroform techniques both reveal clean graphene with the roughness of the graphene surface around 0.26–0.30 nm in contrast to standard acetone cleaning.

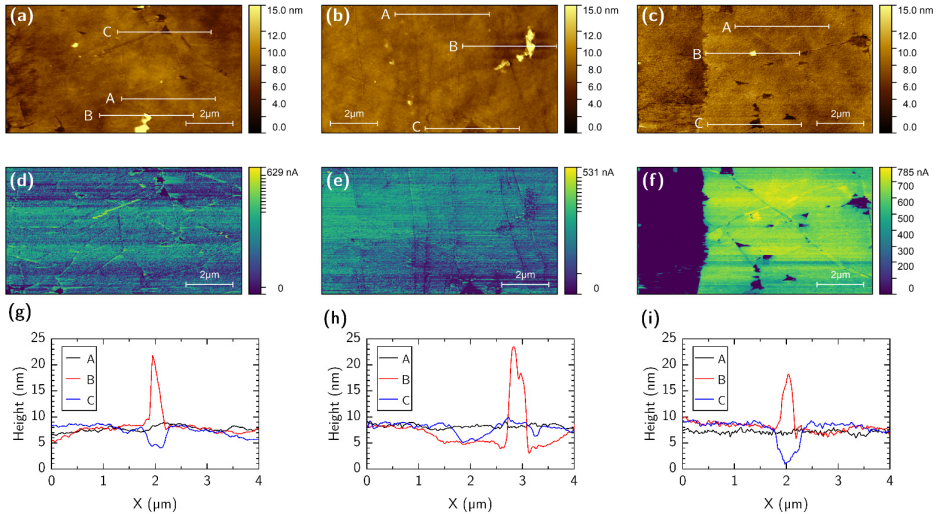


**Figure 6.** Topography and conductivity images ( $10 \times 5.4 \mu\text{m}^2$ ) and topography profiles obtained via AFM microscopy of the graphene samples after different PMMA removal methods: (a,d,g) DUV exposure and IPA/water dissolution; (b,e,h) dissolution in chloroform; (c,f,i) dissolution in acetone. Topography profiles (g–i): A—graphene surface roughness, B—height of contaminants on the graphene, C—hole in graphene showing distance to substrate.

### 3.3. Raman Spectroscopy of Graphene after PMMA Removal

The Raman spectra for the selected sample DUV3 are shown in Figure 7a. The spectra exhibit two distinct peaks at  $1583 \text{ cm}^{-1}$  (G peak) and  $2674 \text{ cm}^{-1}$  (2D peak). It is worth noting that the D peak at around  $1350 \text{ cm}^{-1}$  falls into elevated background, and was not included in the analysis. To obtain the precise position and FWHM of G and 2D lines, a Lorentz function was used to fit each peak obtaining the mean and standard deviation values of peak intensity and FWHM. The results for all the samples are provided in Table 1. The samples prepared by the DUV method demonstrated a high 2D/G intensity ratio and a low FWHM of the 2D line, found to be up to  $2.9 \pm 0.22$  and below  $30 \text{ cm}^{-1}$ , respectively. The samples prepared using chloroform and acetone exhibited a high 2D/G intensity ratio ( $>2.4$ ), but their FWHM was larger in comparison with DUV samples, namely,  $\text{FWHM} \geq 30 \text{ cm}^{-1}$ . To consider the repeatability of our process in the fabrication of DUV samples, we fabricated three DUV samples over two separate processing runs, the results of which are listed in the Table 1. While the 2D/G ratio and FWHM values of the 2D line fluctuated slightly between the samples, the mean values of FWHM were found in the range of 28 to  $30 \text{ cm}^{-1}$ . Additionally, the fitted positions of the 2D and G lines are used in correlational position analysis, between the 2D and G peaks, which makes it possible to investigate strain and doping in graphene films [80]. The results for the samples obtained in this study and commercially transferred graphene are shown in Figure 7b. The theoretical location ( $G_0; 2D_0$ ) of free-standing undoped graphene is marked with a large black cross, the position of which is at  $1581, 2671 \text{ cm}^{-1}$ . The distribution of positions extends to a line in undoped graphene under biaxial strain, and is plotted as a black line, which is the usual case for graphene transferred onto Si [81]. If a graphene film is *p*-doped and under biaxial strain, this will cause the G peak position to move towards higher Raman shifts and parallel to the strain line. Since the data of the samples prepared in this study (DUV,

chloroform, acetone) are distributed between the theoretical lines of undoped graphene and  $5 \times 10^{12} \text{ cm}^{-2}$  doping, this shows a low doping of the prepared graphene samples. A different behavior is observed for a commercially transferred graphene sample. A significant shift in the data points indicates a high doping of graphene films, which was found to be close to  $2 \times 10^{13} \text{ cm}^{-2}$ , demonstrating a low sheet resistance of the graphene according to the manufacturer data sheet.

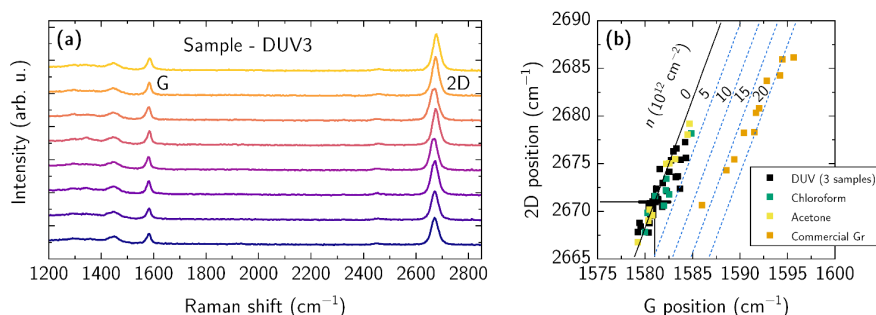


**Figure 7.** Raman measurements of wet-transferred CVD graphene after PMMA removal: (a) Raman spectra of the selected sample DUV3 demonstrating shape and position of G and 2D lines (spectra are shifted vertically for visual clarity). Spectra were measured every  $10 \mu\text{m}$  steps along a line on the graphene. (b) Correlation analysis of the G and 2D peak positions for all samples under study, i.e., 3 DUV method samples (black squares), chloroform sample (green squares), acetone sample (yellow squares), and commercially transferred sample (orange squares). The black solid line demonstrates the dependence correlation between the frequencies of the G and 2D lines in the Raman spectrum of undoped graphene under biaxial strain. Blue dashed lines show correlation dependence for doped graphene under biaxial strain. Black cross marks G and 2D line positions in undoped and unstrained graphene.

**Table 1.** Properties of graphene Raman spectra prepared by different methods.

Sample	$I_{2D}/I_G$	FWHM ( $\text{cm}^{-1}$ )	Processing Run
DUV1	$2.74 \pm 0.31$	$30.2 \pm 1.3$	#1
DUV2	$3.00 \pm 0.41$	$27.8 \pm 1.0$	#1
DUV3	$2.90 \pm 0.22$	$27.9 \pm 1.3$	#2
Chloroform	$2.45 \pm 0.35$	$29.5 \pm 2.2$	#2
Acetone	$3.13 \pm 0.36$	$31.4 \pm 1.2$	#2

### 3.4. Electrical Properties of Graphene after PMMA Removal

Any future applications of CVD graphene require contactless methods of graphene film electrical properties that can conduct large-area mapping and function rapidly [82]. One of such methods is the THz-TDS system, which has been adapted for such applications [83–86]. The THz transmission spectra were analyzed considering graphene on the dielectric substrate as the delta-thin conductive layer, which is described by the Drude conductivity model, with fitting parameters of sheet conductivity  $\sigma_s$ , scattering time  $\tau_{SC}$ , and substrate thickness  $d_s$  [84,85,87]. The transmission spectrum of the graphene sample is shown in Figure 8 by red circles and a fitted curve (black line), which coincide well with experimental points. There are several points (ejections) near the frequencies of 1.1 THz and 2.6 THz, which were caused by natural water vapor variation in ambient air. The transmission spectra of HR silicon were also measured before graphene transfer, demonstrating

less dispersion behavior over the frequency range of interest. All measured time-domain characteristics were averaged 500 times.

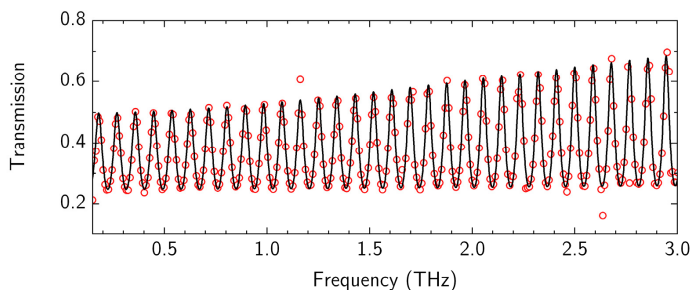


**Figure 8.** The THz transmission spectrum of graphene on HR Si wafer (DUV3 sample). The experimental data (red circles) was described by Drude conductivity model (black line), the usage of which allows one to estimate the electrical conductivity of the graphene.

Relevant electrical properties of the graphene films, such as sheet resistance  $R_S$ , sheet carrier density (unintentional doping)  $N_S$ , and carrier mobility  $\mu$ , were found from fitting results using the respective definitions:

$$R_S = \frac{1}{\sigma_S} \quad (1)$$

$$N_S = \frac{\pi \hbar^2}{q v_f^2} \left( \frac{\sigma_S}{\tau_{SC}} \right)^2 \quad (2)$$

$$\mu = \frac{\sigma_S}{q N_S} \quad (3)$$

The results for all samples are summarized in Table 2. It is important to note that the parameters extracted from THz-TDS results represent statistical averages of any microscale properties over the 2–3 mm spot size of the focused THz beam. All the samples prepared with various PMMA removal techniques exhibited carrier densities below  $3.2 \times 10^{12} \text{ cm}^{-2}$  and mobilities higher than  $2410 \text{ cm}^2/(\text{V}\cdot\text{s})$ . The best overall result was achieved for sample DUV3, which demonstrated very low residual doping and very high mobility values, found to be at the level of  $0.8 \times 10^{12} \text{ cm}^{-2}$  and  $6900 \text{ cm}^2/(\text{V}\cdot\text{s})$ , respectively.

**Table 2.** Electrical properties of graphene samples prepared by different methods.

Sample	Sheet Resistance $R_S$ ( $\Omega/\text{sq.}$ )	Sheet Carrier Density $N_S$ ( $\times 10^{12} \text{ cm}^{-2}$ )	Carrier Mobility $\mu$ ( $\text{cm}^2/(\text{V}\cdot\text{s})$ )	Carrier Type	Processing Run
DUV1	670	2.5	3720	<i>p</i>	#1
DUV2	840	2.0	3650	<i>p</i>	#1
DUV3	1110	0.8	6910	<i>n</i>	#2
Chloroform	850	1.3	5890	<i>n</i>	#2
Acetone	850	3.1	2410	<i>p</i>	#2

Remote THz characterization is a powerful tool; however, it does not provide information on the type of free-charge carriers that interact with THz radiation. To gain more insight into this, we added Ag epoxy contacts to each corner of the rectangular graphene samples and performed Hall experiments. Two of the three samples prepared using DUV treatment

exhibited *p*-type conductivity (DUV1 and DUV2), while the last one demonstrated *n*-type conductivity (DUV3). Samples prepared using chloroform and acetone solvents showed *n* and *p*-type conductivity, respectively. The varying conductivity type for the DUV samples could be a result of slight unintentional doping during PMMA removal, since for all the samples analyzed, carrier density was below  $2.5 \times 10^{12} \text{ cm}^{-2}$ . These results indicate that DUV-assisted PMMA removal in an IPA/water solution makes it possible to obtain clean CVD graphene with high charge carrier mobility values, which are required in the field of high-frequency electronics.

#### 4. Conclusions

In conclusion, a green and cost-efficient method has been developed for PMMA supportive layer removal from the surface of CVD graphene wet transferred onto an application-compatible substrate of choice, which allows one to obtain scalable graphene with high electron mobility for the needs of high-frequency graphene-based electronics and optoelectronics. In terms of the method, we propose to first modify the polarity properties of PMMA via exposure to deep-ultraviolet (DUV) radiation with a wavelength 254 nm, so that not only the decomposition of PMMA polymer to MMA monomer occurs, as typically happens after thermal or photo-irradiation, but also the formation of final products (ketones and aldehydes) with polarities higher than those of the initial products (esters). Such products form hydrogen bonds much more easily upon subsequent dissolution, which would allow for better removal of PMMA using a solvent of high polarity. We propose to use a binary solvent mixture of isopropyl alcohol and water, which is not only extremely polar, but is also a more environmentally friendly solvent. Generally, an aqueous alcohol—such as ethanol—can be used, especially since it has no environmental impact at all. Another advantage of the method is that low-energy irradiation does not form free radicals, thus the released graphene remains intact, unlike in higher-energy PMMA decomposition methods, such as with an electron beam or even DUV at 195 nm.

The high quality of graphene after the removal of PMMA using our method was confirmed with SEM, AFM, and Raman spectrometry. Electrical transport properties of released graphene, which are of special interest to current research, were fulfilled by means of contactless optical (THz-TDS) and contact (Hall measurements) techniques. It was found that the mobility of charge carriers in graphene films reaches up to  $6900 \text{ cm}^2/(\text{V}\cdot\text{s})$ , which makes the proposed method suitable for removing PMMA from the graphene surface in the industry of high-performance large-scale electronic devices based on graphene.

#### 5. Patents

N.A. and I.K. are inventors on a provision patent application filed by the Valstybinis mokslinių tyrimų institutas Fizinių ir technologijos mokslų centras (no. EP3936476A1, published 12 January 2022).

**Author Contributions:** Conceptualization, N.A. and I.K.; formal analysis, J.J., I.K., G.N. and N.A.; investigation, J.J., D.P., I.K., I.L., A.S., V.A. and N.A.; data curation, J.J., I.K. and N.A.; writing—original draft preparation, N.A., J.J. and I.K.; writing—review and editing, N.A., J.J., I.K. and G.N.; visualization, J.J. and N.A.; funding acquisition, I.K. All authors have read and agreed to the published version of the manuscript.

**Funding:** This work received funding from European Regional Development Fund (project No 01.2.2-LMT-K-718-03-0096) under a grant agreement (No. DOTSUT-184) with the Research Council of Lithuania (LMT).

**Data Availability Statement:** Data available on request.

**Acknowledgments:** The work was supported from the Research Council of Lithuania (Lietuvos mokslo taryba) through the “Hybrid plasmonic components for THz range (T-HP)” Grant (No. DOTSUT-184) funded by the European Regional Development Fund according to the supported activity “Research Projects Implemented by World-class Researcher Groups” under the project No.

01.2.2-LMT-K-718-03-0096. The authors thank Virginijus Bukauskas and Arūnas Šetkus for discussion of AFM setup needed for graphene characterization.

**Conflicts of Interest:** N.A. and I.K. are inventors on a provision patent application filed by the Valstybinis mokslinių tyrimų institutas Fizinių ir technologijos mokslų centras (no. EP3936476A1, published 12 January 2022). The other authors declare no conflict of interest.

## References

- Geim, A.K.; Novoselov, K.S.; Falko, V.I.; Colombo, L.; Gellert, P.R.; Schwab, M.G.; Kim, K.; Ferrari, A.C.; Bonaccorso, F.; Falko, V.I.; et al. Science and Technology Roadmap for Graphene, Related Two-Dimensional Crystals, and Hybrid Systems. *Nature* **2012**, *7*, 192–200. [\[CrossRef\]](#)
- Novoselov, K.S.; Falko, V.I.; Colombo, L.; Gellert, P.R.; Schwab, M.G.; Kim, K. A Roadmap for Graphene. *Nature* **2012**, *490*, 192–200. [\[CrossRef\]](#) [\[PubMed\]](#)
- Geim, A.K.; Novoselov, K.S. The Rise of Graphene. *Nat. Mater.* **2007**, *6*, 183–191. [\[CrossRef\]](#)
- Novoselov, K.S.; Geim, A.K.; Morozov, S.V.; Jiang, D.; Zhang, Y.; Dubonos, S.V.; Grigorieva, I.V.; Firsov, A.A. Electric Field Effect in Atomically Thin Carbon Films. *Science* **2004**, *306*, 666–669. [\[CrossRef\]](#) [\[PubMed\]](#)
- Bolotin, K.I.; Sikes, K.J.; Jiang, Z.; Klima, M.; Fudenberg, G.; Hone, J.; Kim, P.; Stormer, H.L. Ultrahigh Electron Mobility in Suspended Graphene. *Solid State Commun.* **2008**, *146*, 351–355. [\[CrossRef\]](#)
- Morozov, S.V.; Novoselov, K.S.; Katsnelson, M.I.; Schedin, F.; Elias, D.C.; Jaszczak, J.A.; Geim, A.K. Giant Intrinsic Carrier Mobilities in Graphene and Its Bilayer. *Phys. Rev. Lett.* **2008**, *100*, 016602. [\[CrossRef\]](#)
- Ni, Z.H.; Ponomarenko, L.A.; Nair, R.R.; Yang, R.; Anissimova, S.; Grigorieva, I.V.; Schedin, F.; Blake, P.; Shen, Z.X.; Hill, E.H.; et al. On Resonant Scatterers as a Factor Limiting Carrier Mobility in Graphene. *Nano Lett.* **2010**, *10*, 3868–3872. [\[CrossRef\]](#)
- Backes, C.; Abdellkader, A.M.; Alonso, C.; Andrieux-Ledier, A.; Arenal, R.; Azpeitia, J.; Balakrishnan, N.; Banszerus, L.; Barjon, J.; Bartali, R.; et al. Production and Processing of Graphene and Related Materials. *2D Mater.* **2020**, *7*, 022001. [\[CrossRef\]](#)
- Reina, A.; Jia, X.; Ho, J.; Nezech, D.; Son, H.; Bulovic, V.; Dresselhaus, M.S.; Kong, J. Large Area, Few-Layer Graphene Films on Arbitrary Substrates by Chemical Vapor Deposition. *Nano Lett.* **2009**, *9*, 30–35. [\[CrossRef\]](#)
- Li, X.; Zhu, Y.; Cai, W.; Borysiak, M.; Han, B.; Chen, D.; Piner, R.D.; Colombo, L.; Ruoff, R.S. Transfer of Large-Area Graphene Films for High-Performance Transparent Conductive Electrodes. *Nano Lett.* **2009**, *9*, 4359–4363. [\[CrossRef\]](#)
- Ullah, S.; Yang, X.; Ta, H.Q.; Hasan, M.; Bachmatiuk, A.; Tokarska, K.; Trzebicka, B.; Fu, L.; Rummeli, M.H. Graphene Transfer Methods: A Review. *Nano Res.* **2021**, *14*, 3756–3772. [\[CrossRef\]](#)
- Sun, H.; Chen, D.; Wu, Y.; Yuan, Q.; Guo, L.; Dai, D.; Xu, Y.; Zhao, P.; Jiang, N.; Lin, C.-T. High Quality Graphene Films with a Clean Surface Prepared by an UV/Ozone Assisted Transfer Process. *J. Mater. Chem. C* **2017**, *5*, 1880–1884. [\[CrossRef\]](#)
- Qi, P.; Huang, Y.; Yao, Y.; Li, Q.; Lian, Y.; Lin, L.; Wang, X.; Gu, Y.; Li, L.; Deng, Z.; et al. Wax-Assisted Crack-Free Transfer of Monolayer CVD Graphene: Extending from Standalone to Supported Copper Substrates. *Appl. Surf. Sci.* **2019**, *493*, 81–86. [\[CrossRef\]](#)
- de Castro, R.K.; Araujo, J.R.; Valaski, R.; Costa, L.O.O.; Archanjo, B.S.; Fragneaud, B.; Cremona, M.; Achete, C.A. New Transfer Method of CVD-Grown Graphene Using a Flexible, Transparent and Conductive Polyaniline-Rubber Thin Film for Organic Electronic Applications. *Chem. Eng. J.* **2015**, *273*, 509–518. [\[CrossRef\]](#)
- Chen, M.; Stekovic, D.; Li, W.; Arkook, B.; Haddon, R.C.; Bekyarova, E. Sublimation-Assisted Graphene Transfer Technique Based on Small Polyaromatic Hydrocarbons. *Nanotechnology* **2017**, *28*, 255701. [\[CrossRef\]](#) [\[PubMed\]](#)
- Wood, J.D.; Doidge, G.P.; Carrion, E.A.; Koepke, J.C.; Kaitz, J.A.; Datye, I.; Behnam, A.; Hewaparakrama, J.; Aruin, B.; Chen, Y.; et al. Annealing Free, Clean Graphene Transfer Using Alternative Polymer Scaffolds. *Nanotechnology* **2015**, *26*, 055302. [\[CrossRef\]](#) [\[PubMed\]](#)
- Lee, W.H.; Suk, J.W.; Lee, J.; Hao, Y.; Park, J.; Yang, J.W.; Ha, H.-W.; Murali, S.; Chou, H.; Akinwande, D.; et al. Simultaneous Transfer and Doping of CVD-Grown Graphene by Fluoropolymer for Transparent Conductive Films on Plastic. *ACS Nano* **2012**, *6*, 1284–1290. [\[CrossRef\]](#)
- Ali, U.; Karim, K.J.B.A.; Buang, N.A. A Review of the Properties and Applications of Poly (Methyl Methacrylate) (PMMA). *Polym. Rev.* **2015**, *55*, 678–705. [\[CrossRef\]](#)
- Jiao, L.; Fan, B.; Xian, X.; Wu, Z.; Zhang, J.; Liu, Z. Creation of Nanostructures with Poly(Methyl Methacrylate)-Mediated Nanotransfer Printing. *J. Am. Chem. Soc.* **2008**, *130*, 12612–12613. [\[CrossRef\]](#)
- Nasir, T.; Kim, B.J.; Kim, K.-W.; Lee, S.H.; Lim, H.K.; Lee, D.K.; Jeong, B.J.; Kim, H.C.; Yu, H.K.; Choi, J.-Y. Design of Softened Polystyrene for Crack- and Contamination-Free Large-Area Graphene Transfer. *Nanoscale* **2018**, *10*, 21865–21870. [\[CrossRef\]](#)
- Lin, Y.-C.; Lu, C.-C.; Yeh, C.-H.; Jin, C.; Suenaga, K.; Chiu, P.-W. Graphene Annealing: How Clean Can It Be? *Nano Lett.* **2012**, *12*, 414–419. [\[CrossRef\]](#) [\[PubMed\]](#)
- Yang, X.; Yan, M. Removing Contaminants from Transferred CVD Graphene. *Nano Res.* **2020**, *13*, 599–610. [\[CrossRef\]](#)
- Barin, G.B.; Song, Y.; de Fátima Gimenez, I.; Souza Filho, A.G.; Barreto, L.S.; Kong, J. Optimized Graphene Transfer: Influence of Polymethylmethacrylate (PMMA) Layer Concentration and Baking Time on Graphene Final Performance. *Carbon N. Y.* **2015**, *84*, 82–90. [\[CrossRef\]](#)

24. Park, H.; Lim, C.; Lee, C.-J.; Kang, J.; Kim, J.; Choi, M.; Park, H. Optimized Poly(Methyl Methacrylate)-Mediated Graphene-Transfer Process for Fabrication of High-Quality Graphene Layer. *Nanotechnology* **2018**, *29*, 415303. [[CrossRef](#)]
25. Suhail, A.; Islam, K.; Li, B.; Jenkins, D.; Pan, G. Reduction of Polymer Residue on Wet–Transferred CVD Graphene Surface by Deep UV Exposure. *Appl. Phys. Lett.* **2017**, *110*, 183103. [[CrossRef](#)]
26. Cheng, Z.; Zhou, Q.; Wang, C.; Li, Q.; Wang, C.; Fang, Y. Toward Intrinsic Graphene Surfaces: A Systematic Study on Thermal Annealing and Wet-Chemical Treatment of SiO<sub>2</sub>-Supported Graphene Devices. *Nano Lett.* **2011**, *11*, 767–771. [[CrossRef](#)]
27. Pettes, M.T.; Jo, I.; Yao, Z.; Shi, L. Influence of Polymeric Residue on the Thermal Conductivity of Suspended Bilayer Graphene. *Nano Lett.* **2011**, *11*, 1195–1200. [[CrossRef](#)] [[PubMed](#)]
28. Leong, W.S.; Wang, H.; Yeo, J.; Martin-Martinez, F.J.; Zubair, A.; Shen, P.-C.; Mao, Y.; Palacios, T.; Buehler, M.J.; Hong, J.-Y.; et al. Paraffin-Enabled Graphene Transfer. *Nat. Commun.* **2019**, *10*, 867. [[CrossRef](#)]
29. Chen, Y.; Gong, X.; Gai, J. Progress and Challenges in Transfer of Large-Area Graphene Films. *Adv. Sci.* **2016**, *3*, 1500343. [[CrossRef](#)]
30. Pirkle, A.; Chan, J.; Venugopal, A.; Hinojos, D.; Magnuson, C.W.; McDonnell, S.; Colombo, L.; Vogel, E.M.; Ruoff, R.S.; Wallace, R.M. The Effect of Chemical Residues on the Physical and Electrical Properties of Chemical Vapor Deposited Graphene Transferred to SiO<sub>2</sub>. *Appl. Phys. Lett.* **2011**, *99*, 122108. [[CrossRef](#)]
31. Chen, M.; Haddon, R.C.; Yan, R.; Bekyarova, E. Advances in Transferring Chemical Vapour Deposition Graphene: A Review. *Mater. Horiz.* **2017**, *4*, 1054–1063. [[CrossRef](#)]
32. Tan, H.; Wang, D.; Guo, Y. Thermal Growth of Graphene: A Review. *Coatings* **2018**, *8*, 40. [[CrossRef](#)]
33. Lisi, N.; Dikonimos, T.; Buonocore, F.; Pittori, M.; Mazzaro, R.; Rizzoli, R.; Marras, S.; Capasso, A. Contamination-Free Graphene by Chemical Vapor Deposition in Quartz Furnaces. *Sci. Rep.* **2017**, *7*, 9927. [[CrossRef](#)] [[PubMed](#)]
34. Holland, B.J.; Hay, J.N. The Thermal Degradation of Poly(Vinyl Alcohol). *Polymer* **2001**, *42*, 6775–6783. [[CrossRef](#)]
35. Peterson, J.D.; Vyazovkin, S.; Wight, C.A. Stabilizing Effect of Oxygen on Thermal Degradation of Poly(Methyl Methacrylate). *Macromol. Rapid Commun.* **1999**, *20*, 480–483. [[CrossRef](#)]
36. Ahn, Y.; Kim, J.; Ganorkar, S.; Kim, Y.-H.; Kim, S.-I. Thermal Annealing of Graphene to Remove Polymer Residues. *Mater. Express* **2016**, *6*, 69–76. [[CrossRef](#)]
37. Liu, B.; Chiu, I.-S.; Lai, C.-S. Improvements on Thermal Stability of Graphene and Top Gate Graphene Transistors by Ar Annealing. *Vacuum* **2017**, *137*, 8–13. [[CrossRef](#)]
38. Xie, W.; Weng, L.-T.; Ng, K.M.; Chan, C.K.; Chan, C.-M. Clean Graphene Surface through High Temperature Annealing. *Carbon N. Y.* **2015**, *94*, 740–748. [[CrossRef](#)]
39. Zhuang, B.; Li, S.; Li, S.; Yin, J. Ways to Eliminate PMMA Residues on Graphene—Superclean Graphene. *Carbon N. Y.* **2021**, *173*, 609–636. [[CrossRef](#)]
40. Peltekis, N.; Kumar, S.; McEvoy, N.; Lee, K.; Weidlich, A.; Duesberg, G.S. The Effect of Downstream Plasma Treatments on Graphene Surfaces. *Carbon N. Y.* **2012**, *50*, 395–403. [[CrossRef](#)]
41. Fragalà, M.; Compagnini, G.; Torrisi, L.; Puglisi, O. Ion Beam Assisted Unzipping of PMMA. *Nucl. Instrum. Methods Phys. Res. Sect. B Beam Interact. Mater. Atoms* **1998**, *141*, 169–173. [[CrossRef](#)]
42. Lehockey, E.M.; Reid, I.; Hill, I. The Radiation Chemistry of Poly(Methyl Methacrylate) Polymer Resists. *J. Vac. Sci. Technol. A Vac. Surf. Film.* **1988**, *6*, 2221–2225. [[CrossRef](#)]
43. Tinone, M.C.K.; Tanaka, K.; Ueno, N. Photodecomposition of Poly(Methylmethacrylate) Thin Films by Monochromatic Soft X-ray Radiation. *J. Vac. Sci. Technol. A Vac. Surf. Film.* **1995**, *13*, 1885–1892. [[CrossRef](#)]
44. Wollersheim, O.; Zumaqu e, H.; Hormes, J.; Kadereit, D.; Langen, J.; H aubling, L.; Hoessel, P.; Hoffmann, G. Quantitative Studies of the Radiation Chemical Behaviour of PMMA and Poly(Lactides). *Nucl. Instrum. Methods Phys. Res. Sect. B Beam Interact. Mater. Atoms* **1995**, *97*, 273–278. [[CrossRef](#)]
45. Cao, H.; Yu, Q.; Jauregui, L.A.; Tian, J.; Wu, W.; Liu, Z.; Jalilian, R.; Benjamin, D.K.; Jiang, Z.; Bao, J.; et al. Electronic Transport in Chemical Vapor Deposited Graphene Synthesized on Cu: Quantum Hall Effect and Weak Localization. *Appl. Phys. Lett.* **2010**, *96*, 122106. [[CrossRef](#)]
46. Han, C.C.; Corelli, J.C. Mechanism Study of Deep-UV Irradiated Poly(Methyl Methacrylate)-Azide Resist System. *Radiat. Eff. Defects Solids* **1989**, *111–112*, 45–58. [[CrossRef](#)]
47. Torikai, A.; Ohno, M.; Fueki, K. Photodegradation of Poly(Methyl Methacrylate) by Monochromatic Light: Quantum Yield, Effect of Wavelengths, and Light Intensity. *J. Appl. Polym. Sci.* **1990**, *41*, 1023–1032. [[CrossRef](#)]
48. Johnstone, R.W.; Foulds, I.G.; Parameswaran, M. Deep-UV Exposure of Poly(Methyl Methacrylate) at 254 Nm Using Low-Pressure Mercury Vapor Lamps. *J. Vac. Sci. Technol. B Microelectron. Nanom. Struct.* **2008**, *26*, 682. [[CrossRef](#)]
49. Zollner, C.J.; DenBaars, S.P.; Speck, J.S.; Nakamura, S. Germicidal Ultraviolet LEDs: A Review of Applications and Semiconductor Technologies. *Semicond. Sci. Technol.* **2021**, *36*, 123001. [[CrossRef](#)]
50. Jeong, H.J.; Kim, H.Y.; Jeong, S.Y.; Han, J.T.; Baeg, K.-J.; Hwang, J.Y.; Lee, G.-W. Improved Transfer of Chemical-Vapor-Deposited Graphene through Modification of Intermolecular Interactions and Solubility of Poly(Methylmethacrylate) Layers. *Carbon N. Y.* **2014**, *66*, 612–618. [[CrossRef](#)]
51. Deokar, G.; Avila, J.; Razaado-Colombo, I.; Codron, J.-L.; Boyaval, C.; Galopin, E.; Asensio, M.-C.; Vignaud, D. Towards High Quality CVD Graphene Growth and Transfer. *Carbon N. Y.* **2015**, *89*, 82–92. [[CrossRef](#)]

52. Dai, B.; Fu, L.; Zou, Z.; Wang, M.; Xu, H.; Wang, S.; Liu, Z. Rational Design of a Binary Metal Alloy for Chemical Vapour Deposition Growth of Uniform Single-Layer Graphene. *Nat. Commun.* **2011**, *2*, 522. [[CrossRef](#)] [[PubMed](#)]
53. Bobadilla, A.D.; Ocola, L.E.; Sumant, A.V.; Kaminski, M.; Seminario, J.M. PMMA-Assisted Plasma Patterning of Graphene. *J. Nanotechnol.* **2018**, *2018*, 8349626. [[CrossRef](#)]
54. Mohsin, M.A.; Cowie, J.M.G. Enhanced Sensitivity in the Electron Beam Resist Poly(Methyl Methacrylate) Using Improved Solvent Developer. *Polymer* **1988**, *29*, 2130–2135. [[CrossRef](#)]
55. Yasin, S.; Hasko, D.G.; Ahmed, H. Comparison of MIBK/IPA and Water/IPA as PMMA Developers for Electron Beam Nanolithography. *Microelectron. Eng.* **2002**, *61–62*, 745–753. [[CrossRef](#)]
56. Hu, W.; Sarveswaran, K.; Lieberman, M.; Bernstein, G.H. Sub-10 Nm Electron Beam Lithography Using Cold Development of Poly(Methylmethacrylate). *J. Vac. Sci. Technol. B Microelectron. Nanom. Struct.* **2004**, *22*, 1711. [[CrossRef](#)]
57. Olzierski, A. Development and Molecular-Weight Issues on the Lithographic Performance of Poly (Methyl Methacrylate). *Microelectron. Eng.* **2004**, *73–74*, 244–251. [[CrossRef](#)]
58. Meyer, P.; El-Kholi, A.; Schulz, J. Investigations of the Development Rate of Irradiated PMMA Microstructures in Deep X-ray Lithography. *Microelectron. Eng.* **2002**, *63*, 319–328. [[CrossRef](#)]
59. Hoogenboom, R.; Becer, C.R.; Guerrero-Sanchez, C.; Hoeppe, S.; Schubert, U.S. Solubility and Thermoresponsiveness of PMMA in Alcohol-Water Solvent Mixtures. *Aust. J. Chem.* **2010**, *63*, 1173. [[CrossRef](#)]
60. Jewrajka, S.K.; Chatterjee, U.; Mandal, B.M. Homogeneous Atom Transfer Radical Polymerization of Methyl Methacrylate at Ambient Temperature in Aqueous Ethanol. *Macromolecules* **2004**, *37*, 4325–4328. [[CrossRef](#)]
61. European Environment Agency. *Chemicals for a Sustainable Future: Report of the EEA Scientific Committee Seminar*; Copenhagen, 17 May 2017; EU Publications Office: Luxembourg, 2018.
62. Persson, L.; Carney Almroth, B.M.; Collins, C.D.; Cornell, S.; de Wit, C.A.; Diamond, M.L.; Fantke, P.; Hassellöv, M.; MacLeod, M.; Ryberg, M.W.; et al. Outside the Safe Operating Space of the Planetary Boundary for Novel Entities. *Environ. Sci. Technol.* **2022**, *56*, 1510–1521. [[CrossRef](#)] [[PubMed](#)]
63. Ocola, L.E.; Costales, M.; Goszola, D.J. Development Characteristics of Polymethyl Methacrylate in Alcohol/Water Mixtures: A Lithography and Raman Spectroscopy Study. *Nanotechnology* **2016**, *27*, 035302. [[CrossRef](#)] [[PubMed](#)]
64. Rene, E.R.; Sethurajan, M.; Kumar Ponnusamy, V.; Kumar, G.; Bao Dung, T.N.; Brindhadevi, K.; Pugazhendhi, A. Electronic Waste Generation, Recycling and Resource Recovery: Technological Perspectives and Trends. *J. Hazard. Mater.* **2021**, *416*, 125664. [[CrossRef](#)]
65. Anaman, R.; Peng, C.; Jiang, Z.; Liu, X.; Zhou, Z.; Guo, Z.; Xiao, X. Identifying Sources and Transport Routes of Heavy Metals in Soil with Different Land Uses around a Smelting Site by GIS Based PCA and PMF. *Sci. Total Environ.* **2022**, *823*, 153759. [[CrossRef](#)]
66. Suzuki, A.; Eemoto, A.; Shirai, A.; Nagamatsu, K. Ultraviolet Light-Emitting Diode (UV-LED) Sterilization of Citrus Bacterial Canker Disease Targeted for Effective Decontamination of Citrus Sudachi Fruit. *Biocontrol Sci.* **2022**, *27*, 1–7. [[CrossRef](#)] [[PubMed](#)]
67. Shirai, M.; Yamamoto, T.; Tsunooka, M. Ablative Photodegradation of Poly(Methyl Methacrylate) and Its Homologues by 185-Nm Light. *Polym. Degrad. Stab.* **1999**, *63*, 481–487. [[CrossRef](#)]
68. Dybal, J.; Krimm, S. Normal-Mode Analysis of Infrared and Raman Spectra of Crystalline Isotactic Poly(Methyl Methacrylate). *Macromolecules* **1990**, *23*, 1301–1308. [[CrossRef](#)]
69. Huszank, R.; Szilágyi, E.; Szoboszlai, Z.; Szikszai, Z. Investigation of Chemical Changes in PMMA Induced by 1.6 MeV He+ Irradiation by Ion Beam Analytical Methods (RBS-ERDA) and Infrared Spectroscopy (ATR-FTIR). *Nucl. Instrum. Methods Phys. Res. Sect. B Beam Interact. Mater. Atoms* **2019**, *450*, 364–368. [[CrossRef](#)]
70. Szilasi, S.Z.; Huszank, R.; Szikra, D.; Vácz, T.; Rajta, I.; Nagy, I. Chemical Changes in PMMA as a Function of Depth Due to Proton Beam Irradiation. *Mater. Chem. Phys.* **2011**, *130*, 702–707. [[CrossRef](#)]
71. Dirlikov, S.; Koenig, J.L. Infrared Spectra of Poly(Methyl Methacrylate) Labeled with Oxygen-18. *Appl. Spectrosc.* **1979**, *33*, 551–555. [[CrossRef](#)]
72. Dirlikov, S.K.; Koenig, J.L. Assignment of the Carbon-Hydrogen Stretching and Bending Vibrations of Poly(Methyl Methacrylate) by Selective Deuteration. *Appl. Spectrosc.* **1979**, *33*, 555–561. [[CrossRef](#)]
73. Wang, J.; Chen, C.; Buck, S.M.; Chen, Z. Molecular Chemical Structure on Poly(Methyl Methacrylate) (PMMA) Surface Studied by Sum Frequency Generation (SFG) Vibrational Spectroscopy. *J. Phys. Chem. B* **2001**, *105*, 12118–12125. [[CrossRef](#)]
74. Trusovas, R.; Račutkaitis, G.; Niaura, G.; Barkauskas, J.; Valušis, G.; Pauliukaite, R. Recent Advances in Laser Utilization in the Chemical Modification of Graphene Oxide and Its Applications. *Adv. Opt. Mater.* **2016**, *4*, 37–65. [[CrossRef](#)]
75. Giovambattista, N.; Debenedetti, P.G.; Rossky, P.J. Effect of Surface Polarity on Water Contact Angle and Interfacial Hydration Structure. *J. Phys. Chem. B* **2007**, *111*, 9581–9587. [[CrossRef](#)]
76. Cowie, J.M.G.; Mohsin, M.A.; McEwen, I.J. Alcohol-Water Cosolvent Systems for Poly(Methyl Methacrylate). *Polymer* **1987**, *28*, 1569–1572. [[CrossRef](#)]
77. Wolf, B.A.; Blaum, G. Measured and Calculated Solubility of Polymers in Mixed Solvents: Monotony and Cosolvency. *J. Polym. Sci. Polym. Phys. Ed.* **1975**, *13*, 1115–1132. [[CrossRef](#)]
78. Liang, X.; Sperling, B.A.; Calizo, I.; Cheng, G.; Hacker, C.A.; Zhang, Q.; Obeng, Y.; Yan, K.; Peng, H.; Li, Q.; et al. Toward Clean and Crackless Transfer of Graphene. *ACS Nano* **2011**, *5*, 9144–9153. [[CrossRef](#)]
79. Suk, J.W.; Kitt, A.; Magnuson, C.W.; Hao, Y.; Ahmed, S.; An, J.; Swan, A.K.; Goldberg, B.B.; Ruoff, R.S. Transfer of CVD-Grown Monolayer Graphene onto Arbitrary Substrates. *ACS Nano* **2011**, *5*, 6916–6924. [[CrossRef](#)]



80. Lee, J.E.; Ahn, G.; Shim, J.; Lee, Y.S.; Ryu, S. Optical Separation of Mechanical Strain from Charge Doping in Graphene. *Nat. Commun.* **2012**, *3*, 1024. [[CrossRef](#)]
81. Ding, F.; Ji, H.; Chen, Y.; Herklotz, A.; Dörr, K.; Mei, Y.; Rastelli, A.; Schmidt, O.G. Stretchable Graphene: A Close Look at Fundamental Parameters through Biaxial Straining. *Nano Lett.* **2010**, *10*, 3453–3458. [[CrossRef](#)]
82. Melios, C.; Huang, N.; Callegaro, L.; Centeno, A.; Cultrera, A.; Cordon, A.; Panchal, V.; Arnedo, I.; Redo-Sanchez, A.; Etayo, D.; et al. Towards Standardisation of Contact and Contactless Electrical Measurements of CVD Graphene at the Macro-, Micro- and Nano-Scale. *Sci. Rep.* **2020**, *10*, 3223. [[CrossRef](#)] [[PubMed](#)]
83. Bøggild, P.; Mackenzie, D.M.A.; Whelan, P.R.; Petersen, D.H.; Buron, J.D.; Zurutuza, A.; Gallop, J.; Hao, L.; Jepsen, P.U. Mapping the Electrical Properties of Large-Area Graphene. *2D Mater.* **2017**, *4*, 042003. [[CrossRef](#)]
84. Buron, J.D.; Pizzocchero, F.; Jessen, B.S.; Booth, T.J.; Nielsen, P.F.; Hansen, O.; Hilke, M.; Whiteway, E.; Jepsen, P.U.; Bøggild, P.; et al. Electrically Continuous Graphene from Single Crystal Copper Verified by Terahertz Conductance Spectroscopy and Micro Four-Point Probe. *Nano Lett.* **2014**, *14*, 6348–6355. [[CrossRef](#)] [[PubMed](#)]
85. Whelan, P.R.; Shen, Q.; Luo, D.; Wang, M.; Ruoff, R.S.; Jepsen, P.U.; Bøggild, P.; Zhou, B. Reference-Free THz-TDS Conductivity Analysis of Thin Conducting Films. *Opt. Express* **2020**, *28*, 28819. [[CrossRef](#)]
86. Jorudas, J.; Pashnev, D.; Alexeeva, N.; Ignatjev, I.; Urbanowicz, A.; Kasalynas, I. Characterization of Graphene Drude Conductivity by Terahertz and Infrared Spectroscopy Methods. In Proceedings of the 2021 46th International Conference on Infrared, Millimeter and Terahertz Waves (IRMMW-THz), Chengdu, China, 29 August–3 September 2021; IEEE: Manhattan, NY, USA, 2021; pp. 1–2.
87. Pashnev, D.; Korotyeyev, V.V.; Jorudas, J.; Urbanowicz, A.; Prystawko, P.; Janonis, V.; Kasalynas, I. Investigation of Electron Effective Mass in AlGaIn/GaN Heterostructures by THz Spectroscopy of Drude Conductivity. *IEEE Trans. Electron Devices* **2022**, *69*, 3636–3640. [[CrossRef](#)]

P7

**Method for patterning graphene layers through photolithography for a scalable fabrication of graphene devices**

N. Alexeeva, **J. Jorudas**, I. Kašalynas

*European Patent Office application*, EP23205083, 2023-10-23.

This is the European Patent Office (EPO) patent application submitted on 23<sup>rd</sup> of October, 2024.



## Acknowledgement of receipt

We hereby acknowledge receipt of your request for grant of a European patent as follows:

Submission number	12552785	
Application number	EP23205083.1	
File No. to be used for priority declarations	EP23205083	
Date of receipt	23 October 2023	
Your reference	F130-20EP	
Applicant	Valstybinis mokslinių tyrimų institutas Fizinių ir technologijos mokslų centras	
Country	LT	
Title	METHOD FOR PATTERNING GRAPHENE LAYERS THROUGH PHOTOLITHOGRAPHY FOR A SCALABLE FABRICATION OF GRAPHENE DEVICES	
Documents submitted	package-data.xml  application-body.xml  SPECEPO-1.pdf Method for patterning graphene.pdf (15 p.)	ep-request.xml  ep-request.pdf (4 p.)  f1002-1.pdf (1 p.)
Submitted by	CN=secure.epoline.org	
Method of submission	Online	
Date and time receipt generated	23 October 2023, 09:14 (CEST)	
Message Digest	B2:B6:B0:2A:7B:82:DF:38:36:1D:04:8D:67:67:FE:9E:AA:C0:39:E9	

## Form 1002 - 1: Public inventor(s)

### Designation of inventor

User reference: F130-20EP

Application No:

Public

<b>Inventor</b>	Name: Alexeeva Natalia Address: Vilnius Lithuania The applicant has acquired the right to the European patent: As employer
<b>Inventor</b>	Name: Jorudas Justinas Address: Vilnius Lithuania The applicant has acquired the right to the European patent: As employer
<b>Inventor</b>	Name: Kasalynas Irmantas Address: Vilnius Lithuania The applicant has acquired the right to the European patent: As employer

### Signature(s)

Place: **Vilnius, Lithuania**  
Date: **23 October 2023**  
Signed by: **/Ausra Pakeniene/**  
Representative name: **Ausra Pakeniene**  
Capacity: **Representative**  
Function of person signing: **Representative**

**Pyrolyzed Photoresist Thin Film: Effect of Electron Beam Patterning on DC and THz Conductivity**

**J. Jorudas**, H. Rehman, G. Fedorov, M. Cojocari, P. Karvinen, A. Urbanowicz,  
I. Kašalynas, L. Y. Matzui, Y. Svirko, P. Kuzhir  
*Lithuanian Journal of Physics*, vol. 63, no. 3, 155-163 (2023).  
DOI: 10.3952/physics.2023.63.3.6

Reprinted with permission from The Lithuanian Academy of Sciences.

The article may be accessed online at <https://doi.org/10.3952/physics.2023.63.3.6>

## PYROLYZED PHOTORESIST THIN FILM: EFFECT OF ELECTRON BEAM PATTERNING ON DC AND THz CONDUCTIVITY

J. Jorudas <sup>a,b</sup>, H. Rehman <sup>a</sup>, G. Fedorov <sup>a</sup>, M. Cojocari <sup>a</sup>, P. Karvinen <sup>a</sup>, A. Urbanowicz <sup>b</sup>,

I. Kašalynas <sup>b</sup>, L. Yu. Matzui <sup>c</sup>, Y. Svirko <sup>a</sup>, and P. Kuzhir <sup>a</sup>

<sup>a</sup>Department of Physics and Mathematics, Center of Photonics Sciences, University of Eastern Finland, Yliopistokatu 7, 80101 Joensuu, Finland

<sup>b</sup>Department of Optoelectronics, Center for Physical Sciences and Technology (FTMC), Saulėtekio 3, 10257 Vilnius, Lithuania

<sup>c</sup>Faculty of Physics, Taras Shevchenko National University of Kyiv, 64/13 Volodymyrska Street, 01601 Kyiv, Ukraine

Email: justinas.jorudas@ftmc.lt

Received 28 September 2023; accepted 2 October 2023

Pyrolyzed photoresist films (PPFs), which are formed via vacuum annealing of a photoresist without a catalyst, can be employed for fabrication of graphitic nanostructures by using conventional lithographic techniques. Such approach allows for reduction of technological steps required for fabrication of conductive micro- and nanoelectrodes for different applications. However, the operation frequency range of PPF electrodes is still unknown. Here, we report the results of the comparative study of PPF structures fabricated by electron beam lithography prior and after the annealing process with preference to the first approach. By performing the comparative measurements of PPF transport properties we found that both pre- and post-processed PPFs possess the same conductivities at dc-current and in the frequency range from 0.2 to 1.5 THz. Moreover, we achieved the sheet resistance of 150 nm thick PPFs as low as 570  $\Omega/\text{sq}$ , which is comparable to that of commercially available chemical vapour deposited (CVD) graphene. These findings open a path for a simple, reproducible and scalable fabrication of graphitic nanocircuits, nanoresonators and passive components suitable for applications in frequencies up to few terahertz.

**Keywords:** pyrolyzed carbon, pyrolyzed photoresist, terahertz, graphitic film, transport properties

### 1. Introduction

Graphene has received a wide attention due to its remarkable electrical, mechanical and optical properties that open a way for numerous applications [1–4]. However, the integration of a single atom thick graphene sheet into the silicon platform is still a challenge that fuels a search for the graphene alternative in electromagnetics, i.e. for robust graphitic films possessing sheet conductivity comparable with that of graphene in a wide spectrum range [5]. It has been demonstrated in particular that micro- and nano-structuring of such graphitic films deposited onto semiconductor substrates can be used to control microwave and THz radiation [6, 7].

Pyrolyzed polymer films (PPF) made by annealing photoresists in an oxygen free environment [8] comprise highly disordered graphite flakes in

an amorphous carbon matrix having a thickness up to ten times smaller than that of a photoresist used for pyrolysis [9]. PPFs have conductivity of about 10 kS/m, which is several orders of magnitude smaller than that of metals (gold, copper and aluminum) normally used in microelectronics and related areas.

The relatively low electrical conductivity of PPF [10] does not rule out practical applications of these carbon films. Indeed, the chemical stability and robustness of PPFs are beneficial for biomedical [11–13], electrochemical [14–16] and microelectromechanical applications [17–20]. Moreover, PPF can be synthesized on silicon, silicon oxide and other substrates conventionally used in modern electronics and optoelectronics [17, 18]. The micro- and nanopatterned PPF-based structures can be created at a specified location on the substrate by using a pre-patterned photoresist significantly

simplifying incorporating carbon electrodes into the semiconductor environment [21–23]. For example, the fabrication of metallic nanoelectrodes implies spin-coating of the resist either before or after the metal deposition, e-beam exposure and resist developing followed by metal etching or lift-off. Annealing of the resist, i.e. the fabrication of PPF, allows for obtaining the conductive nanostructure in a single step after the e-beam exposure.

Despite the listed advantages, it is not yet clear whether the PPF-based electrodes can be used for high frequency applications. In electrodynamics, the criterion of a ‘metallic’ behaviour in terms of the material dynamic conductivity  $\sigma(\omega)$  can be formulated as  $\sigma(\omega) \gg \epsilon_0\omega$ , where  $\epsilon_0 = 8.85 \cdot 10^{-12}$  F/m and  $\omega$  is the characteristic frequency. The dynamic conductivity of a material in most cases decreases as the frequency is increased. Therefore, it is important to characterize the dynamic conductivity of PPF to estimate the frequency range in which the nano-micro electrodes fabricated using this material can be used.

In this communication, we report on the characterization of transport properties of the graphitic films made via pyrolysis of the negative e-beam resist AZ nLOF 2070 (*MicroChemicals GmbH*). To this end, we fabricated two types of PPF based structures. Structures of the first type are defined by electron beam lithography (EBL) followed by development and annealing. Structures of the second type were made of the as-synthesized uniform PPF by plasma O<sub>2</sub> reactive ion etching through the photomask made using EBL technology. The morphology, structure and intrinsic DC conductivity of PPF were found to be the same in both structures. Transmission spectra of the films obtained via time-domain spectroscopy show that the dynamic conductivity of the fabricated structures matches its DC values up to at least 1.5 THz indicating the superior promise of this material for high frequency applications. Moreover, we compare the transport properties of PPF with commercially available graphene-based field-effect devices (*AMO GmbH*) and discuss possible applications.

## 2. Methods

We fabricated two PPF based structures and compared their transport properties in a wide fre-

quency range. The first structure was defined by EBL followed by development and annealing. We further refer to it as the exposed structure (PPFe). The second structure was made of the as-synthesized uniform PPF by plasma O<sub>2</sub> reactive ion etching through the photomask made of the positive photoresist, polymethyl methacrylate (PMMA), with the help of EBL technology. We further refer to it as the unexposed structure (PPFu). The sketch of PPFe and PPFu fabrication routine is presented in Fig. 1.

The pyrolyzed photoresist films were fabricated on 20 × 20 mm substrates of 525 μm thick p-doped Si wafers coated with 3 μm of SiO<sub>2</sub> and 300 nm of Si<sub>3</sub>N<sub>4</sub> (*Silicon Materials*). Prior to spin-coating of the resist, the substrates were cleaned in acetone, isopropanol and deionized (DI) water in an ultrasonic bath, blow-dried with N<sub>2</sub> and heated to 120°C on a hotplate to remove any moisture. We used the photoresist AZ nLOF 2070 (*MicroChemicals GmbH*) diluted with a solvent AZ EBR (*MicroChemicals GmbH*) which was spin-coated on wafers at different speeds to achieve the desired thickness of the photoresist.

The pyrolysis was performed in a vacuum tube furnace (*Carbolite*) under vacuum of 0.1 mBar at different temperatures from 800 to 1100°C for 60 min.

The thickness of photoresist before ( $D$ ) and after ( $d$ ) pyrolysis was measured by a profilometer (*Veeco Dektak 150*) at 5 locations to verify the film thickness uniformity. To confirm the conversion of the photoresist into a graphitic film, Raman spectra were measured (*Renishaw in Via*) using a 2400 lines/mm grating and a ×50 objective at the excitation wavelength 514 nm. The Raman mapping of PPF was performed in the 40 × 40 μm<sup>2</sup> area with a pixel size of 2 × 2 μm<sup>2</sup> using a ×20 objective. The experimental spectra were fitted as two Lorentz peaks and a linear background to extract the D and G peak parameters for the whole image. The patterned pyrolyzed films were investigated with an SEM (*Zeiss LEO 1550*) to define the lateral dimensions and to check the integrity of the films. The DC conductivity of PPFs was determined by the Van der Pauw (VdP) method on patterned 6 × 6 mm<sup>2</sup> square test structures performing reciprocal and reversed polarity measurements with a probe station (*Signatone*) and a multimeter (*GW Instek*). Finally, both PPFe and PPFu samples were

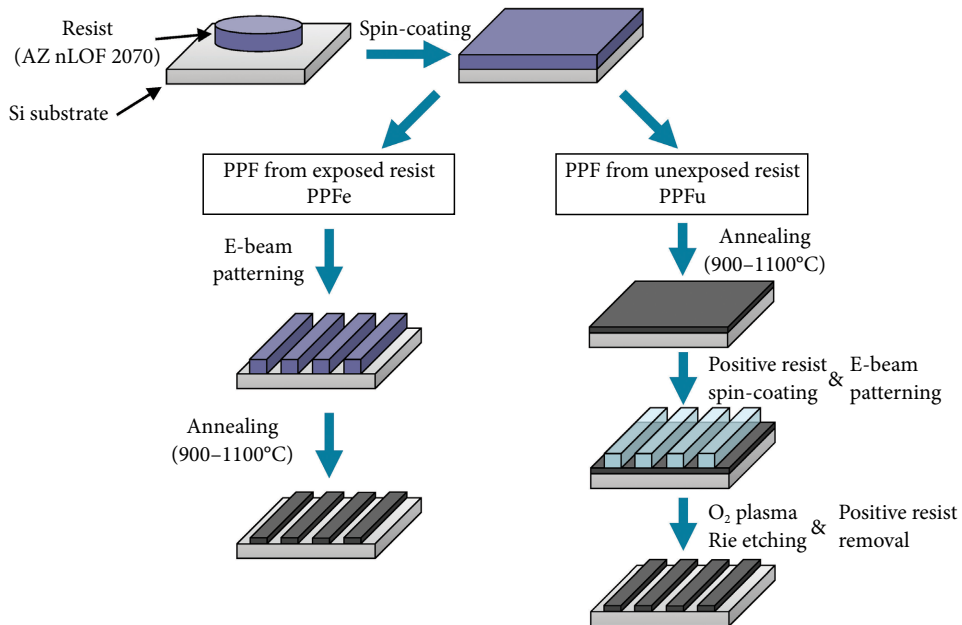


Fig. 1. Illustration of the two fabrication routes for making the two types of PPF gratings: labelled as exposed (PPFe) and unexposed (PPFu) samples.

probed by terahertz time-domain spectroscopy (TDS) (*TeTechS*) in the transmission geometry with an aperture of 4 mm, to investigate the dynamic conductivity of PPF in the THz range.

### 3. Results

#### 3.1. Geometry and morphology of the films

The profiles of a 50  $\mu\text{m}$  wide stripe (marked by a red line in Fig. 2) of the AZ nLOF 2070 resist before and after the pyrolysis at 900°C are shown in Fig. 2. Starting with the thickness of 833 nm, the thickness of the pyrolyzed film reduces down to 162 nm, i.e. the shrinkage ratio is  $S = \frac{D}{d} = 5.1$ . Using the data of two other samples processed with the same starting resist thickness and pyrolyzed under the same conditions, the average shrinkage ratio was estimated to be 5.3. It is consistent with the shrinkage obtained previously for the same resist [9, 21, 24, 25]. Other PPF samples annealed at higher temperatures show a higher shrinkage, for example, at 1100°C we measured  $S = 8.3$ . However,

we did not observe a significant change in the lateral size of both sub-mm and sub- $\mu\text{m}$  resist structures after the pyrolysis.

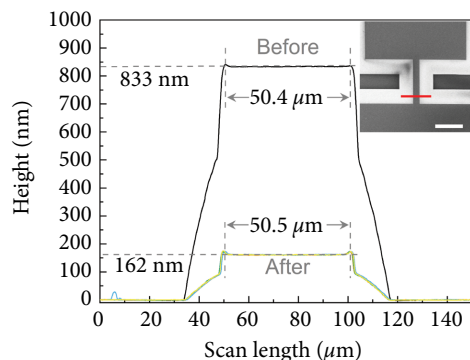


Fig. 2. Profiles of a 50-micron wide resist feature before and after pyrolysis. Inset: SEM image of the PPF Hall bar with a red line marking the areas for profilometer measurement.



The measured Raman spectra after the pyrolysis are dominated by the two broad bands at 1360 and 1600  $\text{cm}^{-1}$  for both PPF<sub>e</sub> and PPF<sub>u</sub>. The G-peak at 1600  $\text{cm}^{-1}$  is the signature of  $\text{sp}^2$  carbon, while the D-peak at 1360  $\text{cm}^{-1}$  is due to crystallographic defects [26]. The ratio of intensities for these two peaks  $I(G)/I(D) = 1.1$  is the same for PPF<sub>e</sub> and PPF<sub>u</sub> samples. The large width of the G-peak as well as the high intensity of the D-peak indicate that in both samples PPF is composed of small monocrystalline graphene flakes. Following Ref. [27] and taking into account  $I(D)/I(G) \sim 1$  at an excitation wavelength of 514 nm, we estimate the in-plane crystallite sizes to be  $L_a \sim 4$  to 5 nm.

The homogeneity of the fabricated films was checked by Raman mapping. The normalized G peak intensity distribution is shown in Fig. 3(b). The observed fluctuations of the signal do not exceed the intrinsic device noise.

### 3.2. Transport properties

By using the Van der Pauw method, the sheet resistance of the films was found to be inversely proportional to the film thickness (see Table 1). This indicates that the carrier scattering at the film surface does not affect the transport characteristics of the film, i.e. the carrier mean free path (MFP), which may be estimated as a crystallite size, is shorter than the film thickness. Importantly, the resistivity of PPFs depends on the annealing temperature [24], but it is the same for the pre-exposed and post-exposed films annealed at the same temperature. The latter circumstances are crucial for using of PPF in practical devices.

To estimate the dynamics of the film conductivity, we measured the transmission spectra of bare and PPF-covered wafers using THz TDS in the range 0.2–1.5 THz. The measured time-traces

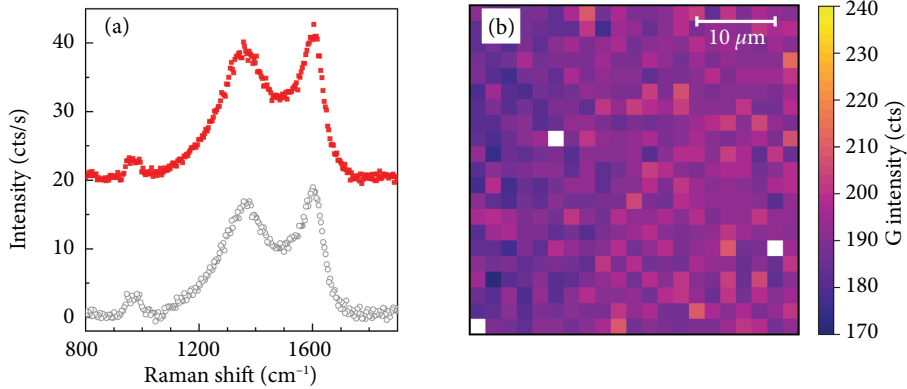


Fig. 3. (a) Raman spectra of PPF<sub>u</sub> (gray circles) and PPF<sub>e</sub> (red squares) samples, note that one spectrum is shifted vertically for clarity. (b) 2D plot of the G-peak intensity as a function of coordinates in the lateral plane of the PPF<sub>e</sub> film.

Table 1. Summary of the results for the PPF<sub>e</sub> and PPF<sub>u</sub> samples.

Sample	Annealing temperature, °C	Thickness after pyrolysis $d$ , nm	Shrinkage $D/d$	Sheet resistance, $\Omega/\text{sq}$	Resistivity, $\text{m}\Omega \text{ cm}$
PPF1u	900	42	6.2	1800	7.6
PPF1e			6.2	1550	6.6
PPF2u		150	5.3	570	8.5
PPF2e		157	5.3	470	7.4
PPF3u	1000	35	7.7	3940	13.8
PPF3e			7.7	2620	9.1
PPF4e	1100	32	8.3	5140	16.1

and the calculated spectra for the Si substrate used are shown in Fig. 4(a, b), respectively. The experimental spectra can be simulated by the standard transfer matrix method using the following relations:

$$\varepsilon(\omega) = \varepsilon_{\infty} + \frac{\sigma(\omega)}{i\omega\varepsilon_0}, \quad (1)$$

$$\sigma(\omega) = \frac{\sigma_{\text{DC}}}{1 - i\omega\tau}, \quad (2)$$

where  $\tau$  is the carrier momentum relaxation time,  $\omega$  is the angular radiation frequency,  $\varepsilon(\omega)$  and  $\sigma(\omega)$  are the dielectric permittivity and conductivity at the frequency  $\omega$ , respectively,  $\varepsilon_0$  is the vacuum permittivity,  $\varepsilon_{\infty}$  is the silicon high frequency dielectric constant, and  $\sigma_{\text{DC}}$  is the DC conductivity of the material.

First, we obtain the scattering time  $\tau$  of Si by fitting the transmission spectrum of the bare Si substrate with  $\sigma_{\text{DC}} = 5 \text{ S/m}$  as measured by the standard 4-probe Van der Pauw method, and  $\varepsilon_{\infty} = 11.6$ . The best fit was found at  $\tau = 0.15 \text{ ps}$ , which is a typical value for the underdoped silicon at room temperature [28].

The transmittance of PPFu and PPFc samples is lower than that of the bare silicon substrate. The relevant transmittance spectra are shown in Fig. 4(c). The fit of PPF-covered wafer transmission spectra gives a very good match between the measured and simulated transmission spectra

with the scattering time less than 10 fs, i.e. when  $\omega\tau \gg 1$  and  $\sigma(\omega) = \sigma_{\text{DC}}$ . That is, in the THz range, the dielectric constant is described by Eq. (1) with the frequency independent conductivity matching the DC conductivity. The fact that the PPF conductivity is frequency independent and coincides with the DC one can be used for designing circuits with PPF nano- or microelectrodes in the frequency range from 0 and up to 1.5 THz.

Based on the Fermi velocity for the  $\text{sp}^2$  carbon material having an order of  $10^6 \text{ m/s}$  and a PPF crystallite size of 5 nm, we estimate the PPF scattering time as 5 fs, which is consistent with the  $\tau < 10 \text{ fs}$  used in the transmission spectra analysis.

### 3.3. Discussion

It is instructive to compare the transport characteristics of PPF to those of the chemical vapour deposition (CVD) grown graphene. While the resistivity of the PPF samples is relatively large, the sheet resistance at the thickness below 200 nm is comparable to that of the CVD graphene. Thus, our experimental findings open a way to employ EBL to fabricate nanostructured graphitic electrodes in very few technological steps, offering a viable alternative to nanostructuring CVD graphene via plasma etching through an EBL fabricated mask in many applications.

Since film DC and THz conductivities are practically the same, the PPF electrodes can be used at

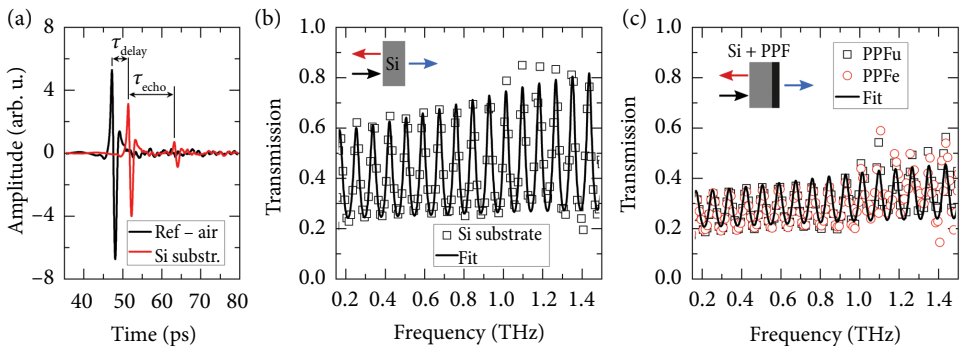


Fig. 4. THz TDS results of PPFc and PPFu samples. (a) Time traces measured after transmission through the aperture (reference) and through the Si substrate. (b) Transmission spectrum of the used wafer (squares) along with the one (solid line) simulated using the model and parameters described in the text. (c) Transmission spectra of the used wafer covered with the pre-exposed (red circles) and post-exposed (black squares) PPF along with the one (solid line) simulated using the model and parameters described in the text.

frequencies lower than  $(RC)^{-1}$ , where  $R$  and  $C$  are the electrode resistance and capacitance, respectively. For a pair of parallel nanoelectrodes having a cross section of  $\sim 10^{-2} \mu\text{m}^2$  with a specific capacitance  $C_s \cong 10^{-17} \text{F}/\mu\text{m}$  and a specific resistance  $R_s \leq 10 \text{ k}\Omega/\mu\text{m}$ , the condition  $(RC)^{-1} = (R_s C_s L^2)^{-1} \geq \omega$  will be met for a few microns ( $L$ ) long electrodes in the THz range and for sub-millimetre electrodes in the GHz range.

Although we did not measure the adhesion of the films using specialized equipment, we observed that the adhesion of both films was good enough to withstand all the technological steps involved and probe station measurements.

To showcase some possible applications for PPFs in the THz range, we fabricated a couple of different structures of PPF, such as nano-grating and split-ring resonators (SRRs). The measured SEM images are shown in Fig. 5(a, b). Figure 5(a) of the periodic nano-grating also demonstrates dark areas between thin grey lines (PPF stripes), two of which on top were marked by a pair of green dotted lines for clarity. These dark regions appear as the result of the charge depletion of the dielectric into the conductive PPF stripes [29]. The Raman mapping of SRRs was performed. The results of the G-peak intensity map are shown in Fig. 5(c) next to its SEM image. We demonstrate that even in the fine features of PPF the structural uniformity is maintained and is similar to the Raman data of the plain PPF (see Fig. 3(b)).

Additionally, biocompatible [13] and much easier to handle PPFs can replace carbon nanotube

nanostructures in multielectrode systems used to study and stimulate neuronal electric activity [30]. Further improvement of the performance of PPF based nano- and microstructures can be achieved by catalyst-assisted pyrolysis as described in our recent work [16].

#### 4. Conclusions

To summarize, we find that the transport properties and morphology of the graphitic films made by annealing of the AZ nLOF 2070 resist used in the EBL do not depend on whether the resist was exposed to the electron beam before annealing or not. Investigating the high frequency characteristics of charge carriers in both PPF<sub>e</sub> and PPF<sub>u</sub> samples we found that the resistivity values of these films were in a range of 7.4–16.1 m $\Omega$  cm and were frequency independent up to at least 1.5 THz. These findings show that based on target application one may use either pre-exposing of the resist or patterning of the already pyrolyzed resist film with no effect on its electrical conductivity up to THz frequencies. Therefore, PPF based conductive structures are applicable in a broad THz range with the benefit of the simple technological process discussed in this paper.

#### Acknowledgements

The study was accomplished with the financial support of the Academy of Finland (Flagship Programme PREIN, Decision 320166, and Mobility

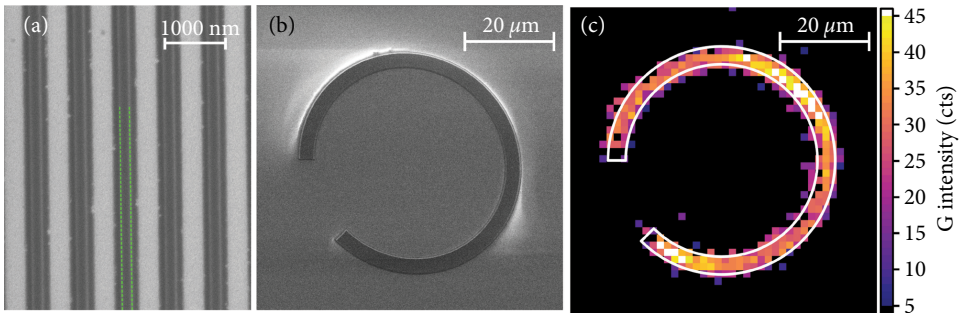


Fig. 5. Demonstration of possible applications of the PPFs: (a) SEM picture of the nano-grating composed of periodic nano-electrodes; (b) SEM picture and (c) the Raman image of the G peak intensity mapping of the unit-cell of split-ring resonator (SRR) designed for waves filtering and beaming in the THz range.

to Finland Decision 334270), Subproject h-cube of EU ATTRACT Phase 2 Research Infrastructure H2020 Project No. 101004462 and Horizon 2020 RISE DiSeTCom (Project No. 823728). The Vilnius Group acknowledges the Research Council of Lithuania for financial support through the ‘T-HP’ Project under Grant DOTSUT-184 funded by the European Regional Development Fund according to the supported activity ‘Research Projects Implemented by World-Class Researcher Groups’ under Contract 01.2.2-LMT-K-718-03-0096.

## References

- [1] R.R. Nair, P. Blake, A.N. Grigorenko, K.S. Novoselov, T.J. Booth, T. Stauber, N.M.R. Peres, and A.K. Geim, Fine structure constant defines visual transparency of graphene, *Science* **320**(5881), 1308–1308 (2008), <https://doi.org/10.1126/science.1156965>
- [2] C. Liao, Y. Li, and S. Tjong, Graphene nanomaterials: synthesis, biocompatibility, and cytotoxicity, *Int. J. Mol. Sci.* **19**(11), 3564 (2018), <https://doi.org/10.3390/ijms19113564>
- [3] Y. Xia, W. Gao, and C. Gao, A review on graphene-based electromagnetic functional materials: electromagnetic wave shielding and absorption, *Adv. Funct. Mater.* **32**(42), 2204591 (2022), <https://doi.org/10.1002/adfm.202204591>
- [4] C.-H. Lin, Y.-S. Chen, J.T. Lin, H.C. Wu, H.T. Kuo, C.F. Lin, P. Chen, and P.C. Wu, Automatic inverse design of high-performance beam-steering metasurfaces via genetic-type tree optimization, *Nano Lett.* **21**(12), 4981–4989 (2021), <https://doi.org/10.1021/acs.nanolett.1c00720>
- [5] T. Kaplas and P. Kuzhir, Ultra-thin pyrocarbon films as a versatile coating material, *Nanoscale Res. Lett.* **12**(1), 121 (2017), <https://doi.org/10.1186/s11671-017-1896-0>
- [6] P.P. Kuzhir, A.G. Paddubskaya, N.I. Volynets, K.G. Batrakov, T. Kaplas, P. Lamberti, R. Kotsilkova, and P. Lambin, Main principles of passive devices based on graphene and carbon films in microwave–THz frequency range, *J. Nanophotonics* **11**(3), 032504 (2017), <https://doi.org/10.1117/1.JNP.11.032504>
- [7] M. Baah, A. Paddubskaya, A. Novitsky, N. Volynets, M. Kumar, T. Itkonen, M. Pekkarinen, E. Soboleva, E. Lahderanta, M. Kafesaki, Y. Svirko, and P. Kuzhir, All-graphene perfect broadband THz absorber, *Carbon* **185**, 709–716 (2021), <https://doi.org/10.1016/j.carbon.2021.09.067>
- [8] A.M. Lyons, Photodefinable carbon films: Control of image quality, *J. Vac. Sci. Technol. B* **3**(1), 447 (1985), <https://doi.org/10.1116/1.583284>
- [9] M. Schreiber, T. Lutz, G.P. Keeley, S. Kumar, M. Boese, S. Krishnamurthy, and G.S. Duesberg, Transparent ultrathin conducting carbon films, *Appl. Surf. Sci.* **256**(21), 6186–6190 (2010), <https://doi.org/10.1016/j.apsusc.2010.03.138>
- [10] M. Baah, P. Obratsov, A. Paddubskaya, A. Biciunas, S. Suvanto, Y. Svirko, P. Kuzhir, and T. Kaplas, Electrical, transport, and optical properties of multifunctional graphitic films synthesized on dielectric surfaces by nickel nanolayer-assisted pyrolysis, *ACS Appl. Mater. Interfaces* **12**(5), 6226–6233 (2020), <https://doi.org/10.1021/acsami.9b18906>
- [11] S.T. Larsen, A. Argyraki, L. Amato, S. Tanzi, S.S. Keller, N. Rozlosnik, and R. Taboryski, Pyrolyzed photoresist electrodes for integration in microfluidic chips for transmitter detection from biological cells, *ECS Electrochem. Lett.* **2**(5), B5–B7 (2013), <https://doi.org/10.1149/2.005305eel>
- [12] H. Zhou, J. Zhou, A. Gupta, and T. Zou, Photoresist derived carbon for growth and differentiation of neuronal cells, *Int. J. Mol. Sci.* **8**(8), 884–893 (2007), <https://doi.org/10.3390/i8080884>
- [13] L. Golubewa, H. Rehman, T. Kulahava, R. Karpič, M. Baah, T. Kaplas, A. Shah, S. Malykhin, A. Obratsov, D. Rutkauskas, et al., Macro-, micro- and nano-roughness of carbon-based interface with the living cells: towards a versatile bio-sensing platform, *Sensors* **20**(18), 5028 (2020), <https://doi.org/10.3390/s20185028>
- [14] D. Sánchez-Molas, J. Cases-Utrera, P. Godignon, and F. Javier del Campo, Mercury detection at microfabricated pyrolyzed photoresist film (PPF) disk electrodes, *Sens. Actuators B Chem.* **186**, 293–299 (2013), <https://doi.org/10.1016/j.snb.2013.06.017>

- [15] Y.M. Hassan, C. Caviglia, S. Hemanth, D.M.A. Mackenzie, T.S. Alström, D.H. Petersen, and S.S. Keller, High temperature SU-8 pyrolysis for fabrication of carbon electrodes, *J. Anal. Appl. Pyrolysis* **125**, 91–99 (2017), <https://doi.org/10.1016/j.jaap.2017.04.015>
- [16] M. Baah, A. Rahman, S. Sibilía, G. Trezza, L. Ferrigno, L. Micheli, A. Maffucci, E. Soboleva, Y. Svirko, and P. Kuzhir, Electrical impedance sensing of organic pollutants with ultrathin graphitic membranes, *Nanotechnology* **33**(7), 075207 (2022), <https://doi.org/10.1088/1361-6528/ac3861>
- [17] J.J. Heikkinen, J. Košir, V. Jokinen, and S. Franssila, Fabrication and design rules of three dimensional pyrolytic carbon suspended microstructures, *J. Micromech. Microeng.* **30**(11), 115003 (2020), <https://doi.org/10.1088/1361-6439/ab9f5b>
- [18] O. Pilloni, M. Madou, D. Mendoza, S. Muhl, and L. Oropeza-Ramos, Methodology and fabrication of adherent and crack-free SU-8 photoresist-derived carbon MEMS on fused silica transparent substrates, *J. Micromech. Microeng.* **29**(2), 027002 (2019), <https://doi.org/10.1088/1361-6439/aaf70f>
- [19] M. Kurek, F. Larsen, P. Larsen, S. Schmid, A. Boisen, and S. Keller, Nanomechanical pyrolytic carbon resonators: novel fabrication method and characterization of mechanical properties, *Sensors* **16**(7), 1097 (2016), <https://doi.org/10.3390/s16071097>
- [20] L.N. Quang, P.E. Larsen, A. Boisen, and S.S. Keller, Tailoring stress in pyrolytic carbon for fabrication of nanomechanical string resonators, *Carbon* **133**, 358–368 (2018), <https://doi.org/10.1016/j.carbon.2018.03.005>
- [21] R. Du, S. Ssenyange, M. Aktary, and M.T. McDermott, Fabrication and characterization of graphitic carbon nanostructures with controllable size, shape, and position, *Small* **5**(10), 1162–1168 (2009), <https://doi.org/10.1002/sml.200801357>
- [22] J.A. Lee, K.-C. Lee, S. Il Park, and S.S. Lee, The fabrication of carbon nanostructures using electron beam resist pyrolysis and nanomachining processes for biosensing applications, *Nanotechnology* **19**(21), 215302 (2008), <https://doi.org/10.1088/0957-4484/19/21/215302>
- [23] K. Malladi, C. Wang, and M. Madou, Fabrication of suspended carbon microstructures by e-beam writer and pyrolysis, *Carbon* **44**(13), 2602–2607 (2006), <https://doi.org/10.1016/j.carbon.2006.04.039>
- [24] A. Singh, J. Jayaram, M. Madou, and S. Akbar, Pyrolysis of negative photoresists to fabricate carbon structures for microelectromechanical systems and electrochemical applications, *J. Electrochem. Soc.* **149**(3), E78 (2002), <https://doi.org/10.1149/1.1436085>
- [25] S. Ranganathan, R. McCreery, S.M. Majji, and M. Madou, Photoresist-derived carbon for microelectromechanical systems and electrochemical applications, *J. Electrochem. Soc.* **147**(1), 277 (2000), <https://doi.org/10.1149/1.1393188>
- [26] A.C. Ferrari and D.M. Basko, Raman spectroscopy as a versatile tool for studying the properties of graphene, *Nat. Nanotechnol.* **8**(4), 235–246 (2013), <https://doi.org/10.1038/nnano.2013.46>
- [27] M.J. Matthews, M.A. Pimenta, G. Dresselhaus, M.S. Dresselhaus, and M. Endo, Origin of dispersive effects of the Raman D band in carbon materials, *Phys. Rev. B* **59**(10), R6585–R6588 (1999), <https://doi.org/10.1103/PhysRevB.59.R6585>
- [28] M. van Exter and D. Grischkowsky, Carrier dynamics of electrons and holes in moderately doped silicon, *Phys. Rev. B* **41**(17), 12140–12149 (1990), <https://doi.org/10.1103/PhysRevB.41.12140>
- [29] Y. Homma, S. Suzuki, Y. Kobayashi, M. Nagase, and D. Takagi, Mechanism of bright selective imaging of single-walled carbon nanotubes on insulators by scanning electron microscopy, *Appl. Phys. Lett.* **84**(10), 1750–1752 (2004), <https://doi.org/10.1063/1.1667608>
- [30] L. Berek-Keren and Y. Hanein, Carbon nanotube-based multi electrode arrays for neuronal interfacing: progress and prospects, *Front. Neural Circuits* **6** (2013), <https://doi.org/10.3389/fncir.2012.00122>

## PLONIEJI PIROLIZUOTO FOTOREZISTO SLUOKSNIAI: STRUKTŪRIZAVIMO ELEKTRONŲ PLUOŠTU ĮTAKA SLUOKSNIO NUOLATINĖS SROVĖS IR THz ELEKTRINIAM LAIDUMUI

J. Jorudas <sup>a,b</sup>, H. Rehman <sup>a</sup>, G. Fedorov <sup>a</sup>, M. Cojocari <sup>a</sup>, P. Karvinen <sup>a</sup>, A. Urbanowicz <sup>b</sup>,  
I. Kašalynas <sup>b</sup>, L. Yu. Matzui <sup>c</sup>, Y. Svirko <sup>a</sup>, P. Kuzhir <sup>a</sup>

<sup>a</sup> Rytų Suomijos universiteto Fotonikos mokslų centro Fizikos ir matematikos skyrius, Joensuu, Suomija

<sup>b</sup> Fizinių ir technologijos mokslų centro Optoelektronikos skyrius, Vilnius, Lietuva

<sup>c</sup> Kyjivo nacionalinio Taraso Ševčenkos universiteto Fizikos fakultetas, Kyjivas, Ukraina

### Santrauka

Pirolizuoto fotorezisto sluoksniai (PPF), sudaromi kaitinant fotorezistą vakuume nenaudojant katalizatoriaus, gali būti panaudoti grafitinių nano darinių gamybai pasitelkiant įprastas litografines technologijas. Toks metodas leidžia supaprastinti technologinį procesą, reikalingą gaminti laidžius mikro- ir nanoelektrodus. Tačiau PPF elektrodų elektrinio laidumo charakteristikos plačiame dažnių ruože vis dar nėra žinomos. Šiame darbe ištirti PPF dariniai pagaminti naudojant elektronų pluošto litografiją arba prieš, arba po fotorezisto pirolizės. Atlikus palyginamuosius PPF laidumo matavimus,

nustatyta, kad dariniai, pagaminti iš PPF, paveikto elektronų pluoštu ar prieš, ar po fotorezisto pirolizės, pasižymi vienodu elektriniu laidumu ir nuolatinės srovės (DC) režime, ir THz dažnių ruože iki 1,5 THz. Pavyko pagaminti 150 nm storio PPF bandinius, kurių sluoksnio varža buvo tik 570  $\Omega$ /sq, – panašios yra komercinio CVD grafeno laidumo vertės. Šie rezultatai atveria galimybių paprastai, atkartojamai gaminti lengvai keičiamo dydžio grafitinius nanograndynus, nanorezonatorius ir pasyviuosius komponentus, kurie gali būti taikomi nuo DC iki keleto terahercų (THz) dažnių ruože.

### Special dedication to prof. Gintaras Valušis

I was really lucky to meet you one day in 2007 in Vilnius, in THz Atelier. We had a lot of fun studying THz features of various nanocarbons. Many good papers were published together, and many projects have been initiated and implemented. Hot discussions, smooth opinions exchanges and lazy coffees form a unique atmosphere around you, stimulating team work. As all your international colleagues, I feel your continuous support and attention. Thanks a lot for 15+ years of our successful collaboration and I do hope we will have more for future scientific endeavours!

Prof. Polina Kuzhir

**Ultra-Broadband Absorbance of Nanometer-Thin Pyrolyzed-Carbon Film on Silicon Nitride Membrane**




**J. Jorudas**, H. Rehman, M. Cojocari, D. Pashnev, A. Urbanowicz, I. Kašalynas, B. Bertoni, L. Vicarelli, A. Pitanti, S. Malykhin, Y. Svirko, P. Kuzhir, G. Fedorov  
*Nanotechnology*, vol. 35, no. 30, 305705 (2024).

DOI: 10.1088/1361-6528/ad4157

This is an open access article distributed under the Creative Commons Attribution License (CC-BY).

The article may be accessed online at <https://doi.org/10.1088/1361-6528/ad4157>

# Ultra-broadband absorbance of nanometer-thin pyrolyzed-carbon film on silicon nitride membrane

Justinas Jorudas<sup>1,2,7</sup> , Hamza Rehman<sup>1,7</sup> , Maria Cojocari<sup>1</sup> , Daniil Pashnev<sup>2</sup> , Andrzej Urbanowicz<sup>2,3</sup> , Irmantas Kašalynas<sup>2,4</sup> , Benedetta Bertoni<sup>5</sup> , Leonardo Vicarelli<sup>5</sup> , Alessandro Pitanti<sup>5,6</sup> , Sergei Malykhin<sup>1</sup> , Yuri Svirko<sup>1</sup> , Polina Kuzhir<sup>1</sup>  and Georgy Fedorov<sup>1,\*</sup> 

<sup>1</sup> Department of Physics and Mathematics, Center of Photonics Research, University of Eastern Finland, Yliopistokatu 7, FI-80101 Joensuu, Finland

<sup>2</sup> Department of Optoelectronics, Center for Physical Sciences and Technology (FTMC), Saulėtekio av. 3, LT-10257 Vilnius, Lithuania

<sup>3</sup> UAB 'TERAVIL', Savanoriu av. 235, LT-02300, Vilnius, Lithuania

<sup>4</sup> Institute of Applied Electrodynamics and Telecommunications, Vilnius University, Saulėtekio al. 3, 10257 Vilnius, Lithuania

<sup>5</sup> Dipartimento di Fisica, Università di Pisa, largo Bruno Pontecorvo 3, I-56127 Pisa, Italy

<sup>6</sup> NEST, CNR—Istituto Nanoscienze, piazza San Silvestro 12, I-56127 Pisa, Italy

E-mail: [alessandro.pitanti@unipi.it](mailto:alessandro.pitanti@unipi.it) and [georgy.fedorov@uef.fi](mailto:georgy.fedorov@uef.fi)

Received 30 November 2023, revised 13 March 2024

Accepted for publication 22 April 2024

Published 9 May 2024



CrossMark

## Abstract

Fifty percents absorption by thin film, with thickness is much smaller than the skin depth and optical thickness much smaller than the wavelength, is a well-known concept of classical electrodynamics. This is a valuable feature that has been numerous widely explored for metal films, while chemically inert nanomembranes are a real fabrication challenge. Here we report the 20 nm thin pyrolyzed carbon film (PyC) placed on 300 nm thick silicon nitride ( $\text{Si}_3\text{N}_4$ ) membrane demonstrating an efficient broadband absorption in the terahertz and near infrared ranges. While the bare  $\text{Si}_3\text{N}_4$  membrane is completely transparent in the THz range, the 20 nm thick PyC layer increases the absorption of the PyC coated  $\text{Si}_3\text{N}_4$  membrane to 40%. The reflection and transmission spectra in the near infrared region reveal that the PyC film absorption persists to a level of at least 10% of the incident power. Such a broadband absorption of the PyC film opens new pathways toward broadband bolometric radiation detectors.

Keywords: ultra-broadband absorption, thin-film absorber, pyrolytic carbon, terahertz, near-infrared

## 1. Introduction

Thin absorptive coatings are widely used in microwave and THz regions as polarizers, filters, attenuators, antennas and electromagnetic interference shielding layers [1–9]. Graphene and carbon-based thin films are very attractive in this respect because their electromagnetic response can be engineered by modifying synthesis conditions [10], doping [11], biasing [12], laser irradiation [13] and mechanical deformation [14]. These also include bolometric detection of radiation in the mid-infrared (MIR) and terahertz (THz) ranges [15–17].

<sup>7</sup> These authors contributed equally.

\* Author to whom any correspondence should be addressed.



Increasing performance of such bolometers in terms of both sensitivity and response time requires reduction of the footprint, that imposes restrictions on the efficiency of converting the radiation energy into heat.

It can be shown that the peak absorption of 50% can be reached when sheet resistance of film  $R_{sh} = \rho/d$ , where  $\rho$  is the material resistivity and  $d$  is the thickness of the film, is equal to half of the vacuum impedance  $Z_0 = \sqrt{\mu_0/\epsilon_0} = 377 \Omega$  [18, 19], when  $d$  is much smaller than the skin depth. This allows to introduce the ‘metallicity’ criterion, which reads:

$$\sigma(\omega) \gg \epsilon_0 \omega, \quad (1)$$

where  $\epsilon_0 = 8.85 \cdot 10^{-12} \text{ F m}^{-1}$  and  $\omega$  is the frequency of the incident electromagnetic wave. Metals used for electronic applications (gold, copper, aluminum, etc.) meet the ‘metallicity’ criterion in a wide range of frequencies. However, their conductivity is very large, so that the thickness of a film having the  $0.5 \times Z_0$  sheet resistance is too small to realize in a reproducible fabrication procedure [20, 21]. In order to avoid this bottleneck there has been suggestions to use metal alloys or doped semiconductor layers compatible with the conventional complementary metal–oxide–semiconductor (CMOS) technology [22].

The conductivity of graphitic films is about two or three orders of magnitude lower than the metal ones [23] however they have not been explored yet. Moreover, advantages of graphitic films include, but are not limited to chemical robustness, low density, ability to fabricate free-standing 3D structures [24] and ability to tune the conductivity in a wide range via the growth parameters. These features make graphitic films a good choice as an absorber material to increase the microbolometer sensitivity [25].

In this work, we report the performance of the 20 nm thin pyrolyzed carbon (PyC) film deposited on a suspended 300 nm thick silicon nitride ( $\text{Si}_3\text{N}_4$ ) membrane for the absorption of radiation in THz and NIR ranges. We show that the 20 nm thick PyC film absorbs between 40% and 10% of the incoming radiation intensity in the THz and NIR ranges, respectively. Our experimental results are in line with describing the PyC film conductivity based on a Drude model with a scattering frequency of about  $10^{15} \text{ Hz}$  and open opportunities for the creation of very sensitive and fast radiation detectors operating in a wide frequency range. The fabrication of the PyC covered silicon nitride membrane rely on much more technologically friendly and reproducible routines (CVD, EBL and etching) in comparison with graphene/polymer sandwiches [26] and hemi-spheres metasurface [8].

## 2. Method

The PyC film was grown on a double-side polished, 250  $\mu\text{m}$  thick Si wafer coated with 300 nm thick layer of high stress  $\text{Si}_3\text{N}_4$  using low pressure chemical vapor deposition (LPCVD). The high growth temperature ( $\sim 800^\circ\text{C}$ ) and the different thermal expansion between Si and  $\text{Si}_3\text{N}_4$  combine to give the film a strong in-plane tensile stress at the room

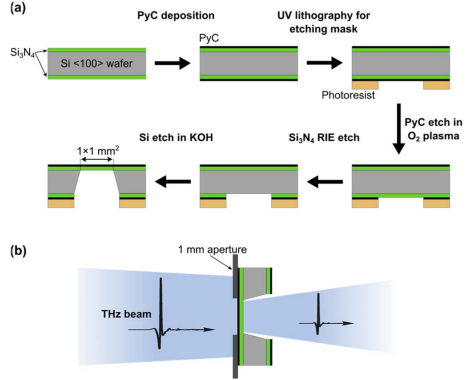


**Figure 1.** (a) Fabrication steps used to make the PyC-coated suspended silicon nitride membrane. (b) Schematic of PyC/ $\text{Si}_3\text{N}_4$  membrane in transmission geometry through aperture.

temperature ( $\sim 900 \text{ MPa}$ ), which is ideal for the realization of mechanical devices. The PyC film was deposited using the standard CVD process of hydrocarbon decomposition [23, 27]. A cleaned  $\text{Si}_3\text{N}_4/\text{Si}$  substrate was loaded into the CVD chamber, which was filled with hydrogen and heated to  $700^\circ\text{C}$ . After that the chamber was pumped down to introduce 1:4 hydrogen–methane gas mixture at the pressure of 25 mBar, heated up to  $1100^\circ\text{C}$  and kept at this temperature for 5 min and then cooled down to  $700^\circ\text{C}$ . The thickness of the deposited PyC film was measured to be 20 nm, with sheet resistance of  $600 \Omega \text{ sq}^{-1}$ , resulting in DC conductivity value of about  $8 \times 10^4 \text{ S m}^{-1}$ . The main steps in the fabrication of the  $1 \times 1 \text{ mm}^2$  PyC/ $\text{Si}_3\text{N}_4$  freestanding membrane are schematically shown in figure 1(a). After the deposition of the PyC film onto both sides of the  $\text{Si}_3\text{N}_4$  coated Si substrate, back surface of the substrate was coated with photoresist and a  $1.3 \times 1.3 \text{ mm}^2$  square opening was realized by standard optical lithography and fluorine-based reaction ion etching (RIE) to remove the PyC film. Afterwards hot 30% KOH wet etching was performed to fully remove the silicon substrate. A special single-sided Teflon holder (Advanced MicroMachining Tools—GmbH) was employed during the KOH bath to protect the PyC coated side.

Transmission spectra of the PyC/ $\text{Si}_3\text{N}_4$  in the range of 0.5–3.0 THz range were measured using a commercial THz-TDS [28] system (T-SPEC 800, TeraVil). The measurement zone was precisely controlled with the positioning PyC membrane on top of 1 mm diameter aperture, as shown in figure 1(b). THz pulse transmitted through the empty aperture was used as the reference. Unfortunately, reflection measurements from the PyC membrane were not possible to conduct due to the small area of the membrane, which is comparable with a wavelength.

PyC/ $\text{Si}_3\text{N}_4$  was characterized using a micro-Fourier transform infrared spectroscopy (micro-FTIR) [29] spectrometer (Jasco FT-IR 6600-IRT 5200), which employs an

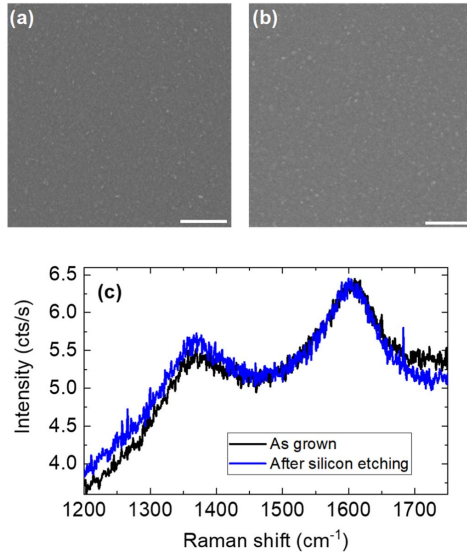


**Figure 2.** PyC film on silicon nitride before and after etching steps of the fabrication process. (a) SEM image of PyC as grown, (b) SEM image of PyC after Si etching process. The scale bar for both SEM images is 500 nm. (c) Raman spectra of the PyC film on silicon nitride before and after Si etching steps of the fabrication process.

interferometric setup with a movable mirror. The advantage of micro-FTIR is that the interferometer is directly mounted on a microscope head, where a broadband mid-infrared and near-infrared (MIR-NIR) source can be precisely focused with a lateral size depending on the magnification stage. In our experimental setup the final  $\times 16$  objective granted for a  $20\ \mu\text{m}$  spot size with an aperture angle of about 35 degree. A simple modification of the optical path of the micro-FTIR can give access to both transmissivity and reflectivity measurements, enabling the direct and local estimation of absorbance.

### 3. Results

#### 3.1. Material characterization: SEM and raman

In order to verify the quality of the PyC film after the fabrication steps described above, we probed its DC sheet resistance using the standard 4-probe Van-der-Pauw method, measured its Raman spectrum and investigated its morphology via scanning electron microscopy (SEM), comparing the obtained parameters with the ones investigated just after deposition. The sheet resistance was found to be  $500 \pm 50\ \text{Ohm sq}^{-1}$ , having a value close to the one measured in as-grown film.

The SEM images for the as-grown PyC film (figure 2(a)) and the PyC/ $\text{Si}_3\text{N}_4$  membrane after Si etching (figure 2(b)) show that the etching did not modify the morphology. This

conclusion is also confirmed by the Raman spectra measured before and after the etching of the Si wafer, as shown in figure 2(c) by matching spectra. It is known that the PyC films fabricated by CVD process consist of few-layer graphene flakes. The relative intensity of the D-peak observed at  $1350\ \text{cm}^{-1}$  and the G-peak observed at  $1600\ \text{cm}^{-1}$  corresponds to the average flake size of about 5 nm [30].

#### 3.2. Electromagnetic response

The transmission spectra of the bare suspended 300 nm thick  $\text{Si}_3\text{N}_4$  membrane and one with a 20 nm thick layer of PyC film in the 0.5–3 THz range are shown in figure 3(a). Due to the dielectric nature of  $\text{Si}_3\text{N}_4$  and small thickness, the membrane is almost completely transparent to the THz radiation, having transmission close to 1. The transmission of the PyC coated  $\text{Si}_3\text{N}_4$  membrane is reduced to  $0.500 \pm 0.025$  and does not change in the whole measurement range of 0.5–3.0 THz. The sharp spikes in the transmission spectra are associated with the fluctuations caused by water vapor.

Following [18], we note that transmission of a thin conductive film is monotonous function of its sheet resistance (figure 3(b)) and the value  $T = 0.5$  corresponds to the sheet resistance of  $\sim 500 \pm 50\ \text{Ohm sq}^{-1}$ , which is consistent with our results obtained by four-probe Van-der-Pauw measurements. As seen from figures 3(b), absorption of 0.4 or more is achieved in a wide range of the sheet resistance values from 75 to  $420\ \text{Ohm sq}^{-1}$ . Also, our data show that the absorption remains the same as the frequency is swept by about an order of magnitude. This implies that performance of the absorbing layer is robust and does not require precise control of the growth parameters.

We now address the question of up to what frequency range the PyC film can be used as an absorber of radiation. The condition (1) is met up to the frequency of  $10^{14}\ \text{Hz}$ . At this frequency, the thickness of silicon nitride membrane is comparable to the wavelength, so it affects the transmission and reflection ( $1.2\text{--}4.2\ \mu\text{m}$ ). Figures 3(c) and (d) show that intrinsic absorption of the  $\text{Si}_3\text{N}_4$  membrane in the NIR range is almost 0, while with the PyC coating it is at least 10% with some variation as a function of frequency. This absorption is less than the 40% value expected for a free-standing conductive PyC with frequency-independent conductivity.

More detailed analysis of the frequency dependence of the PyC absorptivity is based on the Drude–Lorentz model for PyC [31, 32] and Lorentz model for the  $\text{Si}_3\text{N}_4$  membrane. That in the case of the conductive PyC film we approximate the dielectric function as:

$$\varepsilon_{\text{PyC}}(\omega) = \varepsilon_{\infty} + A_{\text{T}} \frac{\omega_{\text{T}}}{\omega_{\text{T}}^2 - \omega^2 - i\omega\gamma_{\text{T}}} - \varepsilon_{\infty} \frac{4\pi\sigma_{\text{DC}}}{i\omega(1 - i\omega\tau)} \quad (2)$$

and in the case of the bare  $\text{Si}_3\text{N}_4$  membrane:

$$\varepsilon_{\text{Si}_3\text{N}_4}(\omega) = \varepsilon_{\infty} + A_{\text{T}} \frac{\omega_{\text{T}}}{\omega_{\text{T}}^2 - \omega^2 - i\omega\gamma_{\text{T}}} \quad (3)$$

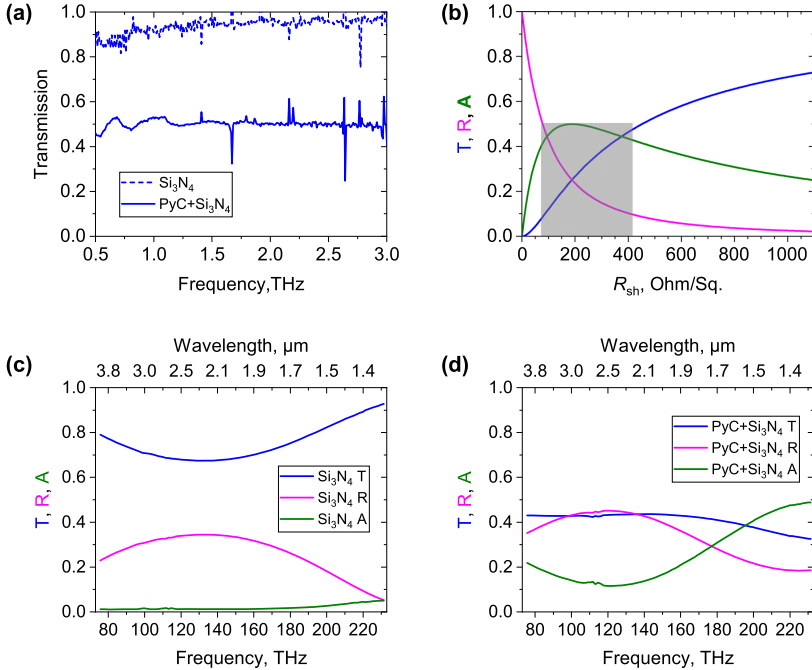


**Figure 3.** (a) Transmission of the bare 300 nm thick Si<sub>3</sub>N<sub>4</sub> membrane (blue dashed line) and a PyC coated Si<sub>3</sub>N<sub>4</sub> membrane (blue solid line) in the THz range. (b) Reflection (R), transmission (T), and absorption (A) of a thin conductive film as a function of its sheet resistance calculated based on the [18]. The shaded region marks the range of the film sheet resistance corresponding to more than 40% absorption. Reflection, transmission, and absorption of a Si<sub>3</sub>N<sub>4</sub> membrane (c) and PyC coated Si<sub>3</sub>N<sub>4</sub> membrane (d) measured in the NIR range.

**Table 1.** Material parameters used for spectra calculation.

	$\epsilon$	$\omega_T$ , Hz	$A_T$	$\gamma_T$ , Hz	$\sigma_{DC}$ , S/m	$\tau$ , fs
Si <sub>3</sub> N <sub>4</sub>	3.85	$1.6 \times 10^{14}$	3	$2.4 \times 10^{13}$	—	—
PyC	1.2	$7 \times 10^{15}$	4	$8.5 \times 10^{15}$	$8 \times 10^4$	2

The second term equation (2) describes the contribution of the  $\pi$ - $\pi^*$  electron transitions ( $E_T = \hbar\omega_T = 4.6$  eV) to the dielectric function. The transition strength  $A_T$  and the full width at half maximum (FWHM)  $\gamma_T$ , as well as the high frequency dielectric permittivity  $\epsilon_\infty$ , have been determined in earlier work [31]. The third term in equation (2) describes the contribution of the free charge carriers via Drude model with DC conductivity  $\sigma_{DC}$  and carrier scattering time  $\tau$ . In the equation (3), the third term responsible for free carrier absorption is zero, while the second term describes the resonant absorption at  $\omega_T \approx 1.6 \times 10^{14}$  Hz due to the optical phonon excitation (see [33, 34]). Note that,  $\omega_T = 2\pi f_T$ , where  $f_T$  is the frequency at which we see the absorption maximum around 26 THz.

The reflection, transmission, and absorption spectra of the bare Si<sub>3</sub>N<sub>4</sub> membrane as well as the PyC coated one can be simulated by the standard transfer matrix method using the above formulae for the dielectric functions. The table 1 summarizes the values of parameters that provide best match between the simulated and measured spectra. The resultant calculated spectra and experimental data are shown in figures 4(a), (b).

Parameters for Si<sub>3</sub>N<sub>4</sub> are consistent with those reported in [33] and [34]. Fitting parameters for the Lorentz term in equation (2) are taken from the [31] while the scattering time  $\tau$  is consistent with an estimation  $\tau \approx l/v_F$  with  $l \sim 5$  nm being the average graphene flake size and  $v_F \approx 10^6$  m s<sup>-1</sup> is the Fermi velocity in the graphene.

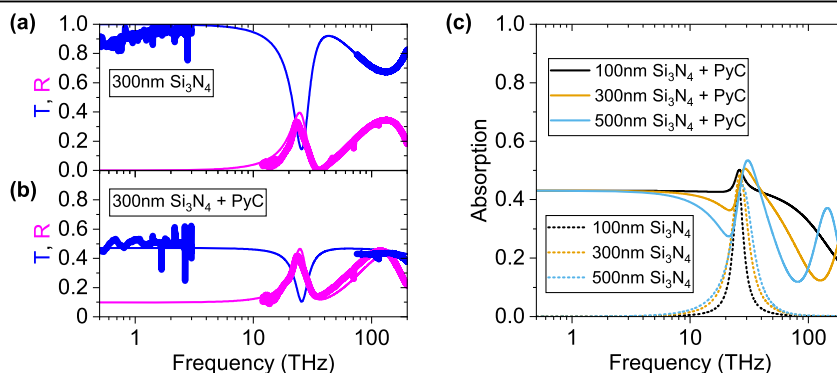


**Figure 4.** Effect of PyC coating on the optical properties of the  $\text{Si}_3\text{N}_4$  membrane. (a) Calculated (lines) and measured (thick lines) transmission  $T$  (blue) and reflection  $R$  (magenta) spectra of a 300 nm  $\text{Si}_3\text{N}_4$  membrane. (b) Same for a 300 nm  $\text{Si}_3\text{N}_4$  membrane with a 20 nm PyC coating. (c) Calculated absorption of bare  $\text{Si}_3\text{N}_4$  membrane and of  $\text{Si}_3\text{N}_4$  membrane with a PyC coating at different  $\text{Si}_3\text{N}_4$  thicknesses.

The good agreement between the calculated and the measured spectra gives confidence in predictions of the simulations in the entire frequency range from 0.5 to 200 THz and in particular the predicted absorption of the  $\text{Si}_3\text{N}_4$ -PyC as shown in the figure 4(c). While radiation absorption by bare  $\text{Si}_3\text{N}_4$  membrane is nonzero only around the optical phonon frequency, the PyC coated membrane is predicted to absorb regardless of the  $\text{Si}_3\text{N}_4$  membrane thickness. Morphology and homogeneity of the PyC films at the interface with different substrates was studied in several earlier works [35–37]. Based on these results we conclude that local changes of the film conductivity at the interface with the membrane cannot cause significant change in the interaction with the electromagnetic radiation in a wide frequency range consistently with our results.

It clearly demonstrates very good performance of a 20 nm PyC film at all frequencies where the  $\text{Si}_3\text{N}_4$  membrane is not absorptive itself and could be including micro-mechanical bolometers, where the thin graphitic film can be safely embedded without degrading the resonator quality [38, 39].

#### 4. Conclusions

To summarize, we report on one of the first successful attempts to fabricate nm-thin graphitic film on the top of optically thin suspended dielectric membrane transparent in the ultrabroad spectral range spanning from THz to IR. The 300 nm thick  $\text{Si}_3\text{N}_4$  membrane was covered with 20 nm thick pyrolytic carbon via chemical vapor deposition process. We have shown that a 20 nm thick PyC film placed on a  $\text{Si}_3\text{N}_4$  membrane absorbs up to 40% of the incident THz radiation, close to the maximum amount possible for the planar thin conductive film, and no less 10% in NIR radiation. The results clearly demonstrates very good performance of a 20 nm PyC film at all frequencies where the  $\text{Si}_3\text{N}_4$  membrane

does not absorb and therefore it can be used with micro-mechanical bolometers. The fabrication of the PyC covered silicon nitride membrane relies on reproducible routines. The transport properties and morphology of the graphitic film remain intact after several fabrication steps including reactive ion etching of the silicon nitride and wet etching of silicon. Given the low density of the PyC film, our results open new opportunities for ultrabroad bolometers. Our experimental data along with a simple model describing the optical response of the PyC film facilitate designing THz/IR optoelectronic devices, based on the chemically robust and bio-compatible PyC film.



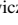
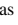




#### Acknowledgments

The study was accomplished with the financial support of subproject H-Cube of EU ATTRACT phase 2 Research infrastructure H2020 (Project № 101004462), Academy of Finland (Flagship Programme PREIN, decision 320166 and 346518, prj. 343393), Horizon 2020 RISE DiSeTCom (Project № 823728), TERASSE Project (Project № 823878) and COST Action NanoSpace (Project № CA21126). The Vilnius Group acknowledges the Research Council of Lithuania for financial support through the ‘T-HP’ Project under Grant DOTSUT-184 funded by the European Regional Development Fund according to the supported activity ‘Research Projects Implemented by World-Class Researcher Groups’ under Contract 01.2.2-LMT-K-718-03-0096.

#### Data availability statement

All data that support the findings of this study are included within the article (and any supplementary files).

## ORCID iDs

Justinas Jorudas  <https://orcid.org/0000-0001-5629-8545>  
 Daniil Pashnev  <https://orcid.org/0000-0002-4648-0957>  
 Andrzej Urbanowicz  <https://orcid.org/0000-0002-2769-452X>  
 Irmantas Kašalynas  <https://orcid.org/0000-0003-1256-9424>  
 Alessandro Pitanti  <https://orcid.org/0000-0002-7027-0300>  
 Sergei Malykhin  <https://orcid.org/0000-0001-7677-0739>  
 Polina Kuzhir  <https://orcid.org/0000-0003-3689-0837>  
 Georgy Fedorov  <https://orcid.org/0000-0002-5224-0474>

## References

- [1] Kuzhir P P, Paddubskaya A G, Volynets N I, Batrakov K G, Kaplas T, Lamberti P, Kotsilkova R and Lambin P 2017 Main Principles of passive devices based on graphene and carbon films in microwave—thz frequency range *J. Nanophotonics* **11** 032504
- [2] Kuzhir P, Celzard A and Chen X 2022 Microwave absorption by carbon-based materials and structures *J. Appl. Phys.* **131** 200401
- [3] Wang X-C, Diaz-Rubio A and Tretyakov S A 2017 An accurate method for measuring the sheet impedance of thin conductive films at microwave and millimeter-wave frequencies *IEEE Trans. Microw. Theory Tech.* **65** 5009–18
- [4] Silva Z J, Valenta C R and Durgin G D 2021 Optically Transparent antennas: a survey of transparent microwave conductor performance and applications *IEEE Antennas Propag. Mag.* **63** 27–39
- [5] Šlegerytė V, Belova-Plonienė D, Katkevičius A and Plonis D 2019 Microwave devices with graphene layers: a review. *In Proc. of the 2019 IEEE Microwave Theory and Techniques in Wireless Communications (MTTW) (Piscataway, NJ) (IEEE)* 87–92
- [6] Wang L, Yu X, Li X, Zhang J, Wang M and Che R 2019 Conductive-network enhanced microwave absorption performance from carbon coated defect-Rich Fe<sub>2</sub>O<sub>3</sub> anchored on multi-wall carbon nanotubes *Carbon* **155** 298–308
- [7] Pang H et al 2021 Research advances in composition, structure and mechanisms of microwave absorbing materials *Composites B* **224** 109173
- [8] Baah M et al 2021 All-graphene perfect broadband THz absorber *Carbon* **185** 709–16
- [9] Novitsky A, Paddubskaya A, Otoo I A, Pekkarinen M, Svirko Y and Kuzhir P 2022 Random graphene metasurfaces: diffraction theory and giant broadband absorptivity *Phys. Rev. Appl.* **17** 044041
- [10] Batrakov K, Kuzhir P, Maksimenko S, Paddubskaya A, Voronovich S, Kaplas T and Svirko Y 2013 Enhanced microwave shielding effectiveness of ultrathin pyrolytic carbon films *Appl. Phys. Lett.* **103** 073117
- [11] Lee H, Paeng K and Kim I S 2018 A review of doping modulation in graphene *Synth. Met.* **244** 36–47
- [12] Chen S et al 2021 Electrically tunable correlated and topological states in twisted monolayer–bilayer graphene *Nat. Phys.* **17** 374–80
- [13] Tasolamprou A C et al 2019 Experimental demonstration of ultrafast THz modulation in a graphene-based thin film absorber through negative photoinduced conductivity *ACS Photonics* **6** 720–7
- [14] Han M, Mu Y, Yuan F, Liang J, Jiang T, Bai X and Yu J 2020 Vertical graphene growth on uniformly dispersed sub-nanoscale SiO<sub>x</sub>/N-doped carbon composite microspheres with a 3D conductive network and an ultra-low volume deformation for fast and stable lithium-Ion Storage *J. Mater. Chem. A* **8** 3822–33
- [15] Sassi U et al 2017 Graphene-based mid-infrared room-temperature pyroelectric bolometers with ultrahigh temperature coefficient of resistance *Nat. Commun.* **8** 14311
- [16] Lee G-H et al 2020 Graphene-based josephson junction microwave bolometer *Nature* **586** 42–6
- [17] Liu Z, Liang Z, Tang W and Xu X 2020 Design and fabrication of low-deformation micro-bolometers for THz detectors *Infrared Phys. Technol.* **105** 103241
- [18] Bosman H, Lau Y Y and Gilgenbach R M 2003 Microwave absorption on a thin film *Appl. Phys. Lett.* **82** 1353–5
- [19] Ling C C, Landry J C, Davee H, Chin G and Rebeiz G M 1994 Large area bolometers for thz power measurements *IEEE Trans. Microw. Theory Tech.* **42** 758–60
- [20] Antonets I V, Kotov L N, Nekipelov S V and Karpushov E N 2004 Conducting and reflecting properties of thin metal films *Tech. Phys.* **49** 1496–500
- [21] Mahan G D and Marple D T F 1983 Infrared absorption of thin metal films: Pt on Si *Appl. Phys. Lett.* **42** 219–21
- [22] Kašalynas I, Adam A J L, Klaassen T O, Hovenier J N, Pandraud G, Iordanov V P and Sarro P M 2008 Design and performance of a room-temperature terahertz detection array for real-time imaging *IEEE J. Sel. Top. Quantum Electron.* **14** 363–9
- [23] McEvoy N, Peltekis N, Kumar S, Rezvani E, Nolan H, Keeley G P, Blau W J and Duesberg G S 2012 Synthesis and analysis of thin conducting pyrolytic carbon films *Carbon* **50** 1216–26
- [24] Heikkinen J J, Košir J, Jokinen V and Franssila S 2020 Fabrication and design rules of three dimensional pyrolytic carbon suspended microstructures *J. Micromech. Microeng.* **30** 115003
- [25] Kuzhir P P, Paddubskaya A G, Maksimenko S A, Kaplas T and Svirko Y 2013 Microwave absorption properties of pyrolytic carbon nanofilm *Nanoscale Res. Lett.* **8** 60
- [26] Kotsilkova R, Todorov P, Ivanov E, Kaplas T, Svirko Y, Paddubskaya A and Kuzhir P 2016 Mechanical properties investigation of bilayer graphene/poly(methyl methacrylate) thin films at macro, micro and nanoscale *Carbon* **100** 355–66
- [27] Benzinger W, Becker A and Hüttinger K J 1996 Chemistry and kinetics of chemical vapour deposition of pyrocarbon: I. fundamentals of kinetics and chemical reaction engineering *Carbon* **34** 957–66
- [28] Nuss M C and Orenstein J 2007 Terahertz time-domain spectroscopy *In Millimeter and Submillimeter Wave Spectroscopy of Solids* (Springer) pp 7–50
- [29] Gaffney J S, Marley N A and Jones D E 2012 Fourier transform infrared (FTIR) spectroscopy *In Characterization of Materials* (Wiley) pp 1–33
- [30] Matthews M J, Pimenta M A, Dresselhaus G, Dresselhaus M S and Endo M 1999 Origin of dispersive effects of the raman D Band in carbon materials *Phys. Rev. B* **59** R6585–8
- [31] Dovbeshko G I, Romanyuk V R, Pidgimyi D V, Cherepanov V V, Andreev E O, Levin V M, Kuzhir P P, Kaplas T and Svirko Y P 2015 Optical properties of pyrolytic carbon films versus graphite and graphene *Nanoscale Res. Lett.* **10** 234
- [32] Adamov R B et al 2021 Optical performance of two dimensional electron gas and gan: C buffer layers in AlGaIn/AlIn/GaN heterostructures on SiC substrate *Appl. Sci.* **11** 6053

- [33] Wada N, Solin S A, Wong J and Prochazka S 1981 Raman and IR absorption spectroscopic studies on  $\alpha$ ,  $\beta$ , and amorphous Si<sub>3</sub>N<sub>4</sub> *J. Non. Cryst. Solids* **43** 7–15
- [34] Knolle W R and Allara D L 1986 Infrared spectroscopic characterization of silicon nitride films—optical dispersion induced frequency shifts *Appl. Spectrosc.* **40** 1046–9
- [35] Baryshevsky V et al 2015 Study of nanometric thin pyrolytic carbon films for explosive electron emission cathode in high-voltage planar diode *Thin Solid Films* **581** 107–11
- [36] Vogel W and Hosemann R 1979 The paracrystalline nature of pyrolytic carbons *Carbon* **17** 41–8
- [37] Zhang X, Zhong L, Mateos A, Kudo A, Vyatskikh A, Gao H, Greer J R and Li X 2019 Theoretical strength and rubber-like behaviour in micro-sized pyrolytic carbon *Nat. Nanotechnol.* **14** 762–9
- [38] Vicarelli L, Tredicucci A and Pitanti A 2022 Micromechanical bolometers for subterahertz detection at room temperature *ACS Photonics* **9** 360–7
- [39] Piller M, Hiesberger J, Wistrela E, Martini P, Luhmann N and Schmid S 2023 Thermal IR detection with nanoelectromechanical silicon nitride trampoline resonators *IEEE Sens. J.* **23** 1066–71

Vilnius University Press  
Saulėtekio al. 9, LT-10222 Vilnius  
e-mail: [info@leidykla.vu.lt](mailto:info@leidykla.vu.lt),  
[www.leidykla.vu.lt](http://www.leidykla.vu.lt)  
Print run copies 25